Université de Montréal

Institut de Génie Biomédical
Faculté de Médecine
Université de Montréal

CENTRALE PARIS

Laboratoire de Mathématiques
Appliquées aux Systèmes
Ecole Centrale Paris

Anatomo-functional magnetic resonance imaging of the spinal cord and its application to the characterization of spinal lesions in cats

Julien COHEN-ADAD

A thesis submitted in fulfillment of the requirements for the degrees of:

Docteur of Philosophy from the Université de Montréal

Docteur of Philosophy from the École Centrale Paris

Université de Montréal – Ecole Centrale Paris

Imagerie par résonance magnétique anatomo-fonctionnelle de la moelle épinière et application à la caractérisation des lésions spinales chez le chat

Julien COHEN-ADAD

Jury

President	Richard D. HOGE	Université de Montreal, Canada
Advisors	Serge ROSSIGNOL	Université de Montréal, Canada
	Habib BENALI	INSERM / Université Paris 6, France
Reviewers	Karla MILLER	University of Oxford, UK
	Cyril POUPON	CEA Neurospin, France
Members	Rachid DERICHE	INRIA Sophia Antipolis, France
	Stéphane LEHÉRICY	Hopital Pitié-Salpêtrière, France
	A. Robert LEBLANC	Université de Montreal, Canada
	Christian SAGUEZ	Ecole Centrale Paris, France

Contents

List of Tables

List of Figures

Glossary

ADC	Apparent diffusion coefficient
A-P	Antero-posterior
ATP	Adenosine triphosphate
BOLD	Blood oxygenation level dependent
C	Cervical
CBF	Cerebral blood flow
CNS	Central nervous system
CPG	Central pattern generator
CPMG	Carr–Purcell–Meiboom–Gill
CST	Corticospinal tract
DOI	Diffuse optical imaging
DTI	Diffusion tensor imaging
DW	Diffusion-weighted
EPI	Echo planar imaging
FA	Fractional anisotropy
fMRI	Functional magnetic resonance imaging
FOV	Field of view
FRT	Funk-Radon transform
FSE	Fast spin echo
FWHM	Full width at half maximum
GLM	General linear model
GRAPPA	Generalized autocalibrating partially parallel acquisitions
HARDI	High angular resolution diffusion imaging
HbO_2	Oxyhaemoglobin
HbR	Deoxyhaemoglobin
HRF	Haemodynamic response function
ICA	Independent component analysis
LSDI	Line scan diffusion imaging
L	Lumbar
MRI	Magnetic resonance imaging
MRO_2	Metabolic rate of O_2
ODF	Orientation distribution function
QBI	Q-ball imaging
PD	Proton density
RARE	Rapid acquisition with relaxation enhancement
R-C	Rostro-caudal
ReST	Reticulospinal tract
RF	Radiofrequency

R-L	Right-left
ROI	Region of interest
RST	Rubrospinal tract
S	Sacral
SAR	Specific absorption rate
SCI	Spinal cord injury
SCT	Spinocerebellar tract
SE	Spin echo
SEEP	Signal enhancement by extravascular proton density
SH	Spherical harmonics
SNR	Signal-to-noise ratio
STT	Spinothalamic tract
T	Tesla (in the context of MRI)
T	Thoracic (in the context of spinal cord)
TE	Echo time
TR	Repetition time
VST	Vestibulospinal tract

Remerciements

Bizarrement la section « remerciements » d'un manuscrit de thèse est celle qui est la plus lue, mais aussi celle qui est généralement écrite après acceptation du manuscrit. Cette incongruité confère aux remerciements une propriété singulière : celle de pouvoir diffuser des sentiments vrais et non censurés.

For de cette liberté d'expression, et par ordre chronologique d'apparition, j'aimerais d'abord remercier Habib de m'avoir accordé sa confiance, de m'avoir reçu dans son laboratoire parisien et présenté avec enthousiasme un projet de doctorat passionnant, de m'avoir accueilli au sein de son équipe fort sympathique (pas seulement au sens de souffrir ensemble), mais aussi pour sa générosité, sa bonne humeur, son bon humour (ou tout au moins compatible avec le mien), sa présence physique et virtuelle (e.g., courriel, visioconférence) et son insatiable curiosité scientifique donnant lieu à de nombreuses investigations mathématico-physiologiques.

J'aimerais également remercier Habib de m'avoir présenté à Serge, mon deuxième papa dans cette aventure académique, à qui je suis extrêmement reconnaissant de m'avoir ouvert la porte de son laboratoire montréalais, enseigné une rigueur scientifique à la fois plaisante et efficace, et transmis sa passion pour l'étude de la moelle épinière, dans un milieu comme les neurosciences où le cerveau règne en monarque. Serge m'a également enseigné une philosophie de vie que j'ai petit à petit adoptée. Par exemple, sa faculté de renvoyer les corrections d'un article en moins de 3 heures ou de répondre aux courriels en moins de 3 minutes. Grâce à lui j'ai réalisé que limiter la procrastination peut avoir des effets bénéfiques sur la santé d'un projet, qu'il soit d'ordre scientifique ou d'ordre privé. Au-delà des sciences, la musique fut également la glie de notre amitié, et je garde un excellent souvenir de notre *Spinal Chord Ensemble.*

Il n'y a pas de mots pour décrire l'influence que peuvent avoir des directeurs de thèse sur le cours d'une vie, mais elle est immense. Je suis conscient de la chance phénoménale qui m'a été donnée d'avoir été guidé par Serge et Habib, sur le plan professionnel mais aussi et surtout sur le plan humain.

Je tiens à remercier Cyril Poupon et Karla Miller d'avoir accepté la révision du présent manuscrit, et à Rick Hoge, Stéphane Lehéricy, Rachid Deriche d'avoir fait partie du jury. Merci à Alain Herment et à Trevor Drew pour leur accueil respectif au sein du Laboratoire d'Imagerie Fonctionnelle et du Groupe de Recherche sur le Système Nerveux Central, ainsi que pour leur support, encouragements et humour très apprécié, respectivement « franchouillard » et « british ». Merci également à Julien Doyon pour son accueil et son support continu au sein de l'Unité de Neuroimagerie Fonctionnelle. Merci à Christian Saguez pour m'avoir autorisé à suivre son programme de l'école doctorale de Centrale Paris, tout comme Robert Leblanc pour son accueil au sein de l'Institut de Génie Biomédical de l'Université de Montréal. Merci également à

Louise Bélanger, Géraldine Carbonel et Catherine Lhopital de nous avoir aidé à gravir les nombreux échelons bureaucratiques afférents à une cotutelle de thèse.

Merci à Rick Hoge, Cyril Poupon et Alexandre Vignaud pour leurs précieux conseils m'ayant permis d'améliorer les acquisition IRM, Rachid Deriche, Maxime Descoteaux et Aurobrata Ghosh pour leurs contributions en imagerie à haute résolution angulaire, Pierre Rainville, Mathieu Piché et Guoming Xie pour leur collaboration en imagerie spinale chez l'humain, Rick Hoge et Claudine Gauthier pour leur collaboration sur l'hypercapnie, Henrik Lundell pour sa collaboration sur l'art de corriger les artefacts de susceptibilité magnétique, Jonathan Brooks pour sa collaboration en imagerie fonctionnelle, Frédéric Lesage, Sarah Chapuisat, Benoît Briau, Eric Beaumont et Simon Dubeau pour leur collaboration en imagerie optique.

Durant les trois dernières années, collègues et amis m'ont beaucoup apporté tant sur le plan scientifique que sur celui du pur divertissement. Au risque d'en oublier, je remercie pèle mêle du côté français : Mélanie, pour ses facultés de tétrapilectomie[1] qu'elle ne cesse d'investiguer, Guillaume pour son aptitude à filtrer ses mauvais calembours, Vincent pour sa capacité à accepter les miens, Saad pour m'avoir accueilli si chaleureusement de nombreuses fois à Oxford, Arnaud, Caroline, Sarah, David, Rémy, Stéphane et Alexandre. Outre atlantique, j'ai particulièrement apprécié les réunions biblio autour d'un « spécial bonjour » et les tournées des cottages québécois avec Pierre et Christophe. Au CRIUGM, j'étais sensible aux fredonnements plaisants de Vo An du bureau d'à côté, à la salsa trépidante d'Oury du bureau de l'autre côté, ainsi qu'aux nombreuses rencontres avec Cécile, Olivia, Ronan, Gaëlle, Johane, Mathieu, Mathieu, Mathieu, Mathieu, Mathieu. La vie au GRSNC fut parsemée de retraites au grand air, sorties anniversaires au Maiko sushi, symposiums, et autres prétextes pour encourager une synergie de convivialité et d'échange scientifique. Je remercie tout particulièrement Hugues, Janyne, Greg, Alain, Hugo, Claude, Maurice, Philippe, René avec qu'il a été fort agréable de passer ces moments agréables.

Enfin, et sur une note plus affective, un grand merci à Claudine, ma mère, mon père, ma petite sœur, Manu, Fred, et autres proches pour leur soutien sans faille, leur amitié et/ou amour. À la manière du Yin et du Yang, en plus d'un environnement scientifique efficace, le bon déroulement d'une thèse nécessite un épanouissement de soi, une sérénité et stabilité autant psychique qu'intellectuelle, pour se concentrer sur la substantifique moelle dont il est question. Un peu comme le Graal du goût parfait dans l'art culinaire, j'ai su trouver le parfait dosage avec ceux qui m'entourent, pour les années passées, celles à venir, et je leur dis merci.

[1] L'art de couper les cheveux en quatre

Abstract

Spinal cord injury has a significant impact on quality of life since it can lead to motor (paralysis) and sensory deficits. These deficits evolve in time as reorganisation of the central nervous system occurs, involving physiological and neurochemical mechanisms that are still not fully understood. Given that both the severity of the deficit and the successful rehabilitation process depend on the anatomical pathways that have been altered in the spinal cord, it may be of great interest to assess white matter integrity after a spinal lesion and to evaluate quantitatively the functional state of spinal neurons.

The great potential of magnetic resonance imaging (MRI) lies in its ability to investigate both anatomical and functional properties of the central nervous system non-invasively. To address the problem of spinal cord injury, this project aimed to evaluate the benefits of diffusion-weighted MRI to assess the integrity of white matter axons that remain after spinal cord injury. The second objective was to evaluate to what extent functional MRI can measure the activity of neurons in the spinal cord.

Although widely applied to the brain, diffusion-weighted MRI and functional MRI of the spinal cord are not straightforward. Various issues arise from the small cross-section width of the cord, the presence of cardiac and respiratory motions, and from magnetic field inhomogeneities in the spinal region. The main purpose of the present thesis was therefore to develop methodologies to circumvent these issues. This development notably focused on the optimization of acquisition parameters to image anatomical, diffusion-weighted and functional data in cats and humans at 3T using standard coils and pulse sequences. Moreover, various strategies to correct for susceptibility-induced distortions were investigated and the sensitivity and specificity in spinal cord functional MRI was studied. As a result, acquisition of high spatial and angular diffusion-weighted images and evaluation of the integrity of specific spinal pathways following spinal cord injury was achieved. Moreover, functional activations in the spinal cord of anaesthetized cats were detected.

Although encouraging, these results highlight the need for further technical and methodological development in the near-future. Being able to develop a reliable neuroimaging tool for confirming clinical parameters would improve diagnostic and prognosis. It would also enable to monitor the effect of various therapeutic strategies. This would certainly bring hope to a large number of people suffering from trauma and neurodegenerative diseases such as spinal cord injury, tumours, multiple sclerosis and amyotrophic lateral sclerosis.

Keywords : Magnetic resonance imaging, diffusion tensor imaging, functional MRI, spinal cord, injury, animal.

Résumé

Les lésions de la moelle épinière ont un impact significatif sur la qualité de la vie car elles peuvent induire des déficits moteurs (paralysie) et sensoriels. Ces déficits évoluent dans le temps à mesure que le système nerveux central se réorganise, en impliquant des mécanismes physiologiques et neurochimiques encore mal connus. L'ampleur de ces déficits ainsi que le processus de réhabilitation dépendent fortement des voies anatomiques qui ont été altérées dans la moelle épinière. Il est donc crucial de pouvoir attester l'intégrité de la matière blanche après une lésion spinale et évaluer quantitativement l'état fonctionnel des neurones spinaux.

Un grand intérêt de l'imagerie par résonance magnétique (IRM) est qu'elle permet d'imager de façon non invasive les propriétés fonctionnelles et anatomiques du système nerveux central. Le premier objectif de ce projet de thèse a été de développer l'IRM de diffusion afin d'évaluer l'intégrité des axones de la matière blanche après une lésion médullaire. Le deuxième objectif a été d'évaluer dans quelle mesure l'IRM fonctionnelle permet de mesurer l'activité des neurones de la moelle épinière.

Bien que largement appliquées au cerveau, l'IRM de diffusion et l'IRM fonctionnelle de la moelle épinière sont plus problématiques. Les difficultés associées à l'IRM de la moelle épinière relèvent de sa fine géométrie (environ 1 cm de diamètre chez l'humain), de la présence de mouvements d'origine physiologique (cardiaques et respiratoires) et de la présence d'artefacts de susceptibilité magnétique induits par les inhomogénéités de champ, notamment au niveau des disques intervertébraux et des poumons. L'objectif principal de cette thèse a donc été de développer des méthodes permettant de contourner ces difficultés. Ce développement a notamment reposé sur l'optimisation des paramètres d'acquisition d'images anatomiques, d'images pondérées en diffusion et de données fonctionnelles chez le chat et chez l'humain sur un IRM à 3 Tesla. En outre, diverses stratégies ont été étudiées afin de corriger les distorsions d'images induites par les artefacts de susceptibilité magnétique, et une étude a été menée sur la sensibilité et la spécificité de l'IRM fonctionnelle de la moelle épinière. Les résultats de ces études démontrent la faisabilité d'acquérir des images pondérées en diffusion de haute qualité, et d'évaluer l'intégrité de voies spinales spécifiques après lésion complète et partielle. De plus, l'activité des neurones spinaux a pu être détectée par IRM fonctionnelle chez des chats anesthésiés.

Bien qu'encourageants, ces résultats mettent en lumière la nécessité de développer davantage ces nouvelles techniques. L'existence d'un outil de neuroimagerie fiable et robuste, capable de confirmer les paramètres cliniques, permettrait d'améliorer le diagnostic et le pronostic chez les patients atteints de lésions médullaires. Un des enjeux majeurs serait de suivre et de valider l'effet de diverses stratégies thérapeutiques. De telles outils représentent un espoir immense pour nombre de personnes souffrant de traumatismes et de maladies

neurodégénératives telles que les lésions de la moelle épinière, les tumeurs spinales, la sclérose en plaques et la sclérose latérale amyotrophique.

Mots-clés : Imagerie par résonance magnétique, imagerie du tenseur de diffusion, IRM fonctionnelle, moelle épinière, lésion, animal.

Publications arising from this work

Journal articles

1. **Cohen-Adad, J.**, Hoge, R.D., Leblond, H., Xie, G., Beaudoin, G., Song, A., Krueger, G., Doyon, J., Benali, H., Rossignol, S., 2009. Investigations in functional MRI of the spinal cord of cats. Neuroimage 44, 328-39.

2. Piché, M., **Cohen-Adad, J.**, Khosh Nejad, M., Perlbarg, V., Xie, G., Beaudoin, G., Benali, H., Rainville, P., Characterization of cardiac-related noise in fMRI of the cervical spinal cord. Magn Reson Imaging (in press).

3. **Cohen-Adad, J.**, Descoteaux, M., Rossignol, S., Hoge, R.D., Deriche, R., Benali, H., 2008. Detection of multiple pathways in the spinal cord using q-ball imaging. Neuroimage, 42, 739-749.

4. **Cohen-Adad, J.**, Benali, H., Barrière, G., Leblond, H., Hoge, R.D., Rossignol, S., 2008. Développement clinique de l'IRM du tenseur de diffusion de la moelle épinière dans un contexte de lésion médullaire. IRBM, 29, 255-260.

5. **Cohen-Adad, J.**, Benali, H., Hoge, R.D., Rossignol, S., 2008. In vivo DTI of the healthy and injured cat spinal cord at high spatial and angular resolution. Neuroimage 40, 685-697.

6. **Cohen-Adad, J.**, Chapuisat, S., Doyon, J., Rossignol, S., Lina, J.M., Benali, H., Lesage, F., 2007. Activation detection in diffuse optical imaging by means of the general linear model. Med Image Anal 11, 616-629.

Conference articles

1. **Cohen-Adad, J.**, Rossignol, S., Benali, H., Hoge, R.D., 2008. In vivo assessment of axonal disruption using diffusion magnetic resonance imaging. In: 31st Canadian Medical and Biological Engineering Conference, Montreal, Canada. Oral presentation (in press).

2. **Cohen-Adad, J.**, Descoteaux, M., Rossignol, S., Hoge, R.D., Deriche, R., Benali, H., 2008. Detection of multiple pathways in the spinal cord white matter using q-ball imaging. In: IEEE International Symposium on Biomedical Imaging, Paris, France, 1380. Oral presentation.

3. **Cohen-Adad, J.**, Benali, H., Rossignol, S., 2007. Methodology for MR diffusion tensor imaging of the cat spinal cord. Conf Proc IEEE Eng Med Biol Soc 1, 323-326. Oral presentation.

4. **Cohen-Adad, J.**, Piche, M., Rainville, P., Benali, H., Rossignol, S., 2007. Impact of realignment on spinal functional MRI time series. Conf Proc IEEE Eng Med Biol Soc 1, 2126-2129. Poster.

5. Chapuisat, S., **Cohen-Adad, J.**, Grova, C., Lina, J.M., Rossignol, S., Doyon, J., Benali, H., Lesage, F., 2007. Application of the general linear model to hemodynamic response estimation in diffuse optical imaging. In: SPIE Photonics North, Ottawa, Canada. Poster.

Conference abstracts

1. **Cohen-Adad, J.**, Gauthier, C., Brooks, J.C.W., Leblond, H., Hoge, R.D., Fisher, J.A., Beaumont, E., Dubeau, S., Lesage, F., Doyon, J., Benali, H., Rossignol, S., 2009. Venous effect in spinal cord fMRI: insights from intrinsic optical imaging and laser speckle. In: 14th Annual Meeting of the Organization for Human Brain Mapping (HBM), San Fransisco, USA.

2. Brooks, J.C.W., **Cohen-Adad, J.**, Gauthier, C., Hoge, R.D., Rossignol, S., 2009. Studying the sensorimotor pathways: brain - brainstem - spinal cord imaging. In: 14th Annual Meeting of the Organization for Human Brain Mapping (HBM), San Fransisco, USA.

3. **Cohen-Adad, J.**, Ghosh, A., Leblond, H., Descoteaux, M., Deriche, R., Benali, H., Rossignol, S., 2009. Comparison of DTI and Q-Ball imaging metrics in a cat model of spinal cord injury. In: 14th Annual Meeting of the Organization for Human Brain Mapping (HBM), San Fransisco, USA.

4. Gauthier, C., **Cohen-Adad, J.**, Brooks, J., Fisher, J.A., Rossignol, S., Hoge, R.D., 2009. Comparison of hypercapnia-induced BOLD changes in the brain and spinal cord. In: 14th Annual Meeting of the Organization for Human Brain Mapping (HBM), San Fransisco, USA.

5. **Cohen-Adad, J.**, Leblond, H., Ghosh, A., Descoteaux, M., Deriche, R., Benali, H., Rossignol, S., 2009. Evaluation of q-ball metrics for assessing the integrity of the injured spinal cord. In: 17th Annual Meeting of the International Society for Magnetic Resonance in Medicine (ISMRM), Honolulu, Hawaii

6. **Cohen-Adad, J.**, Rossignol, S., Hoge, R.D., 2009. Slice-by-slice motion correction in spinal cord fMRI: SliceCorr. In: 17th Annual Meeting of the International Society for Magnetic Resonance in Medicine (ISMRM), Honolulu, Hawaii

7. Gauthier, C., **Cohen-Adad, J.**, Brooks, J., Rossignol, S., Hoge, R.D., 2009. Investigation of venous effects in spinal cord fMRI using hypercapnia. In: 17th Annual Meeting of the International Society for Magnetic Resonance in Medicine (ISMRM), Honolulu, Hawaii

8. **Cohen-Adad, J.**, Lundell, H., Rossignol, S., 2009. Distortion correction in spinal cord DTI: What's the best approach? In: 17th Annual Meeting of the International Society for Magnetic Resonance in Medicine (ISMRM), Honolulu, Hawaii

9. Lundell, H., **Cohen-Adad, J.**, 2009. Point spread function mapping for distortion correction of spinal cord diffusion weighted MRI. In: 17th Annual Meeting of the International Society for Magnetic Resonance in Medicine (ISMRM), Honolulu, Hawaii

10. **Cohen-Adad, J.**, Descoteaux, M., Barrière, G., Hoge, R.D., Deriche, R., Benali, H., Rossignol, S., 2008. Characterization of the healthy and injured spinal cord using q-ball imaging. In: 8th international congress of the IRME, Paris, France. Poster presentation.

11. Xie, G., Piché, M., **Cohen-Adad, J.**, Kosh Nejad, M., Perlbarg, V., Hoge, R.D., Benali, H., Rossignol, S., Rainville, P., 2008. Characterizing and controlling for physiological noise in human cervical spinal fMRI in response to noxious stimuli. In: Society for Neuroscience, Washington, DC, USA, (in press).

12. **Cohen-Adad, J.**, Descoteaux, M., Barrière, G., Hoge, R.D., Deriche, R., Benali, H., Rossignol, S., 2008. Characterization of the healthy and injured spinal cord using q-ball imaging. In: Pathogenesis and Mechanisms of White Matter Injury Workshop, Krakow, Poland. Poster presentation.

13. **Cohen-Adad, J.**, 2008. Diffusion Tensor Imaging and Tractography of the spinal cord in animals and humans. In: Symposium on spinal Cord: Function, Repair and Rehabilitation after Injury, Montreal, Canada. Oral presentation.

14. Barrière, G., **Cohen-Adad, J.**, Benali, H., Rossignol, S., 2008. Locomotor recovery after spinal lesions in the cat using behavioral and imaging techniques. In: Spinal Cord : Function, Repair and Rehabilitation after Injury, Montreal, Canada.

15. Barrière, G., **Cohen-Adad, J.**, Benali, H., Rossigol, S. 2008. A dual lesion paradigm to study spinal cord injury (SCI) in cats using electrophysiological and imaging methods. CDRF's 3rd Spinal Cord Symposium, Atlanta, May 9-11, USA.

16. **Cohen-Adad, J.**, Descoteaux, M., Deriche, R., Rossignol, S., Hoge, R.D., Benali, H., 2008. Q-ball imaging of the spinal cord. In: 16th Annual Meeting of the International Society for Magnetic Resonance in Medicine (ISMRM), Toronto, Canada, 569. Oral presentation.

17. **Cohen-Adad, J.**, Gauthier, C., Benali, H., Rossignol, S., Hoge, R.D., 2008. BOLD signal responses to controlled hypercapnia in human spinal cord. In: 16th Annual Meeting of the International Society for Magnetic Resonance in Medicine (ISMRM), Toronto, Canada, 3403.

18. **Cohen-Adad, J.**, Benali, H., Hoge, R.D., Rossignol, S., 2007. In vivo assessment of spinal cord integrity by diffusion tensor imaging. In: Society for Neuroscience, San Diego, USA, 37, 77.10.

19. **Cohen-Adad, J.**, Hoge, R.D., Benali, H., Rossignol, S., 2007. In vivo diffusion MRI of the cat spinal cord following injury. In: Symposium on Motor Systems, San Diego, USA.

20. **Cohen-Adad, J.**, Benali, H., Hoge, R.D., Leblond, H., Barrière, G., Doyon, J., Rossignol, S., 2007. Spinal cord in vivo diffusion tensor imaging of healthy human and spinalized cats. In: Organization for Human Brain Mapping, Chicago, USA, S887.

21. **Cohen-Adad, J.**, Benali, H., Hoge, R.D., Rossignol, S., 2007. In vivo diffusion tensor imaging of the spinal cord. In: Canadian Physiological Society, Mont Ste-Anne, Quebec, Canada.

22. **Cohen-Adad, J.**, Perlbarg, V., Doyon, J., Hoge, R.D., Beaudoin, G., Song, A., Leblond, H., Provencher, J., Rossignol, S., Benali, H., 2006. Methodology to study functional MRI of the cat lumbar spinal cord. In: Organization for Human Brain Mapping, Florence, Italy, S2851.

23. **Cohen-Adad, J.**, Benali, H., Rossignol, S., 2006. A functional MRI methodology to map the neuronal activity in the spinal cord of cats. In: 28th International Symposium of the Groupe de recherche sur le système nerveux central et le Centre de recherche en sciences neurologiques: "Computational Neuroscience", Montreal, Canada.

Research reports

1. **Cohen-Adad, J.**, 2006. Y a-t-il une variation de la densité de protons associée à l'Imagerie par Résonance Magnétique fonctionnelle ? Université de Montréal, Montréal, Canada (20 pages).

2. **Cohen-Adad, J.**, 2006. Etude des interactions somato-viscérales. Université de Montréal, Montréal, Canada (17 pages).

3. **Cohen-Adad, J.**, 2006. L'énigme des ondes de Mayer : faits et modèles. Université de Montréal, Montréal, Canada (26 pages).

Invited speaker

1. Imaging spinal cord injury and white matter damage. 7th International Symposium on Experimental Spinal Cord Repair and Regeneration, Brescia, Italy, 2009.

2. Q-ball imaging of the spinal cord. FMRIB, Oxford University, Oxford, UK, 2009.

3. Diffusion Tensor Imaging and tractography of the spinal cord in animals and humans. 2nd Symposium on Spinal cord: Function, Repair and Rehabilitation after injury, Montreal, Canada, 2008.

4. DW-MRI and fMRI of the spinal cord. DRCMR center, Copenhagen, Denmark, 2008.

5. MRI of the spinal cord: from white matter organization to neuronal activity. Mass. General Hospital / Harvard University, Boston, USA, 2008.

6. Diffusion Tensor Imaging: Principles and Applications. Functional Neuroimaging Unit, Université de Montréal, Montreal, Canada, 2008.

7. Diffusion and functional MRI of the spinal cord. BIC/MNI, McGill University, Montreal, Canada, 2008.

8. New advances in DTI of the spinal cord. Emory University / Georgia Tech, Atlanta, USA, 2007.

9. Diffusion and functional MRI of the spinal cord. Université de Montréal, Montreal, Canada, 2007.

10. Diffusion MRI of the spinal cord. INSERM / CHU Pitié-Salpêtrière, Paris, France, 2007.

11. Spinal cord imaging: some investigations. FMRIB, Oxford University, Oxford, UK, 2006.

À mes parents,

à ma soeur.

1. Introduction

Spinal cord injury (SCI) induces motor (paralysis) and sensory deficits of varying severity through the disruption of specific ascending and descending spinal pathways. These deficits evolve in time as reorganisation of the central nervous system occurs, both at local and supraspinal sites. This functional compensation may involve various anatomical, physiological and neurochemical mechanisms still under investigation (Rossignol, 2006b). Both the severity of the deficit and the successful rehabilitation process depend on the type and number of axonal tracts that have been altered, as well as changes in the intrinsic properties of the spinal cord. Hence, it may be of great interest to assess white matter integrity at the site of a lesion, to identify anatomical tracts that have been damaged or spared and to quantify the activity of spinal neurons to examine the functional state of the cord.

In clinical routine, evoked potentials and electromyographic measurement already allow to evaluate the integrity of spinal pathways and intrinsic circuits. However, these approaches give only an indirect indication of the actual anatomic integrity. The great potential of magnetic resonance imaging (MRI) lies in its ability to investigate both anatomical and functional properties of biological samples non-invasively. To address the problem of spinal cord injury, MRI appears to be a candidate of choice to evaluate the morphological integrity of the cord, as well as its functional characteristics. The present project aimed to evaluate the benefits of diffusion-weighted (DW) MRI to assess the integrity of remaining white matter axons after spinal cord injury. The second objective was to evaluate to what extent functional MRI (fMRI) can measure the activity of spinal neurons, to be able to observe changes in their activity following injury. These changes could either be related to a spontaneous intrinsic reorganization of spinal circuitry or result from exogenous sensory inputs that aim to improve the recovery of function such as treadmill locomotor training.

However, DW-MRI and fMRI of the spinal cord are not straightforward. Various issues arise from the small cross-section width of the cord, the presence of cardiac and respiratory motions, and from magnetic field inhomogeneities in the spinal region. The purpose of the present thesis was to develop methodologies to circumvent these issues. This work has been conducted is three different laboratories, whose expertises strongly influenced my research priorities. I have been co-supervised by Dr. Serge Rossignol, member of the Groupe de Recherche sur le Système Nerveux Central, Université de Montréal (Montréal, Canada) and a Canada Research Chairholder on Spinal Cord, whose team studies spinal cord neurophysiology in the context of locomotor rehabilitation. I have also been co-supervised by Dr. Habib Benali, based at the Laboratoire d'Imagerie Fonctionnelle – UMR_S 678 INSERM / Université Pierre et Marie Curie (Paris VI), Pitié-Salpêtrière Hospital (Paris, France) whose team's main expertise is to develop methods for the analysis of MRI data. Those two laboratories also collaborate closely with Dr. Richard Hoge, based at the Unité de Neuroimagerie Fonctionnelle,

Centre de Recherche de l'Institut Universitaire de Gériatrie de Montréal (Montréal, Canada), whose main expertise is MR physics. The work presented in this thesis therefore emerges from the input of those three distinctive fields. This conjunction has been essential for conducting such a multi-disciplinary project.

The manuscript is organized as follows. In chapter 2, a literature review will present past studies related to the spinal cord morphology and basic functions and studies related to DW- and fMRI of the spinal cord. Chapter 3 will synthesize past studies related to the topic of interest. Objectives, hypotheses and methods will emerge and will guide the reader through the following chapters. Three published articles presented as the core of this thesis will be provided in chapters 4, 5 and 6. Chapter 7 will briefly summarize the achieved work, discuss its originality and limitations. It will also present additional contributions to this thesis as well as ongoing work and future directions.

2. Literature review

Spinal cord anatomy and function

The present work aims to use MRI to identify spinal pathways, to characterize spinal lesions and to detect neuronal activity evoked by peripheral nerve stimulation in cats. Therefore, the following literature review will focus on these considerations only. For the description of the cord anatomy and function however, the human model will mainly be presented given cat and human share many similarities in terms of spinal structure and function. Also, most spinal MRI studies have been conducted in human, justifying its foreground position. This review has been inspired by the textbooks by W. Kahle *et al.* (Kahle and Frotscher, 2005) and E.D. Schwartz *et al.* (Schwartz and Flanders, 2007) and by other publications.

Anatomy of the cord

The spinal cord is part of the central nervous system (CNS) and participates to the active and passive control of sensorimotor functions (*e.g.*, locomotion, motility, pain perception). An illustration of the CNS is provided in Figure 2.1. The length of the spinal cord is much shorter than the length of the vertebral column around it and its relative size evolves with the age. The human spinal cord extends from the medulla oblongata and ends near the first or second lumbar vertebra, terminating in a fibrous extension known as the filum terminale. It is about 44 cm long in humans. The diameter in cross-section is about 1 cm diameter and ovoid-shaped, with an enlargement in the cervical and lumbar regions. In cross-section, the peripheral region of the cord contains white matter axons forming ascending and descending tracts to and from supraspinal regions. In contrast to the brain, the spinal cord white matter surrounds the butterfly shaped grey matter containing neurons and glial cells. The grey matter surrounds the central canal, which is an anatomic extension of the ventricular system of the brain and also contains cerebrospinal fluid (CSF). Illustration of human spinal cord is provided in Figure 2.2.

The human spinal cord is divided into 31 different segments. Motor nerve roots exit in the ventral aspects and sensory nerve roots enter in the dorsal aspects. The ventral and dorsal roots later join to form paired spinal nerves, one on each side of the spinal cord. There are 31 spinal cord nerve segments in a human spinal cord: 8 cervical (C) segments (the 1st cervical nerve exits the vertebral column above the C1 vertebra and the others below the C1-C7 vertebral bodies), 12 thoracic (T) segments (thoracic nerves exit the spinal column below T1-T12 vertebral bodies), 5 lumbar (L) segments (lumbar nerves exit spinal column below L1-L5), 5 sacral (S) segments (sacral nerves exit spinal column below S1-S5) and 1 coccygeal segment (coccygeal nerves exit spinal column at the coccyx).

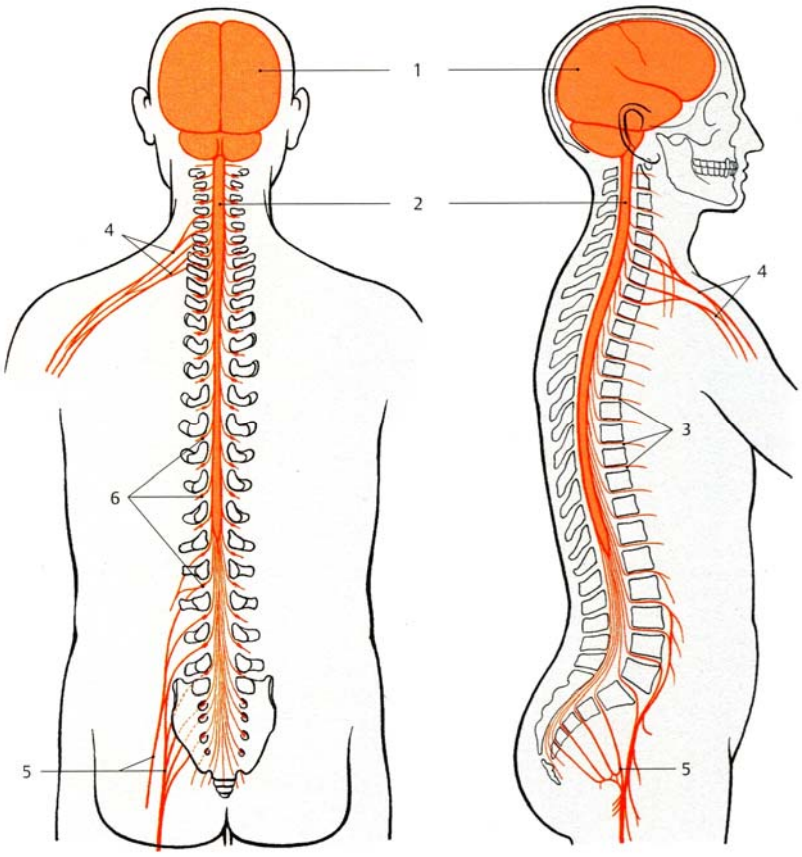

Figure 2.1. Central and peripheral nervous system in human

The CNS includes the brain (1) and the spinal cord (2). Peripheral nerves (3) connect the CNS to muscles and skin and form the brachial plexus (4) and the lumbo-sacral plexus (5). Spinal ganglions (6) are located at the entrance of afferent fibres and contain cell bodies. Adapted from (Kahle and Frotscher, 2005).

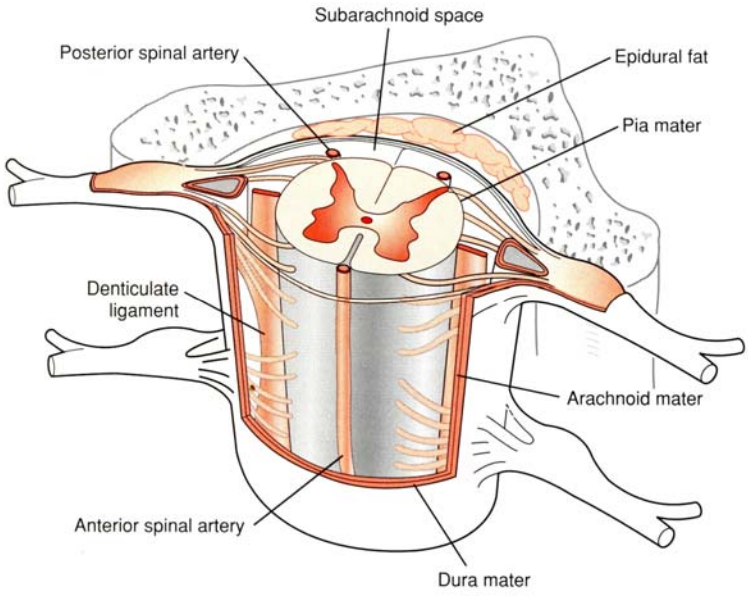

Figure 2.2. Human spinal cord

This figure illustrates the human spinal cord and its relationship with surrounding structures in the spinal canal. Adapted from (Schwartz and Flanders, 2007).

In the cat there are 8 cervical spinal segments, 13 thoracic spinal segments, 7 lumbar spinal segments, 3 sacral spinal segments and 5 coccygeal spinal segments. The spinal cord ends around the S1 vertebral body level. A description of the cat spinal anatomy is provided in (Fletcher and Malkmus, 1999; Hudson and Hamilton, 1993). When imaging the cat spinal cord, the following anatomical and physiological characteristics were useful for the rostro-caudal localization and for the identification of physiological fluctuations in fMRI time series. The cranial and caudal edges of the cat right kidney reach level L1 and L4 vertebral bodies respectively, and cranial and caudal edge of the cat left kidney reach level L2 and L5 vertebral bodies respectively.

White matter tracts are illustrated in Figure 2.3. They mainly consist of ascending and descending tracts. Ascending tracts are involved in the perception of sensory inputs and include the dorsal column, the spinocerebellar tracts (SCT) and the spinothalamic tracts (STT). Descending tracts are responsible for the motor control and include the corticospinal tracts (CST), the rubrospinal tract (RST), the reticulospinal tract (ReST) and the vestibulospinal tract (VST). Partial lesions involving specific tracts therefore lead to specific functional deficits as shown in (Anderson et al., 2007; Barriere et al., 2008; Frigon and Rossignol, 2006; Jiang and Drew, 1996).

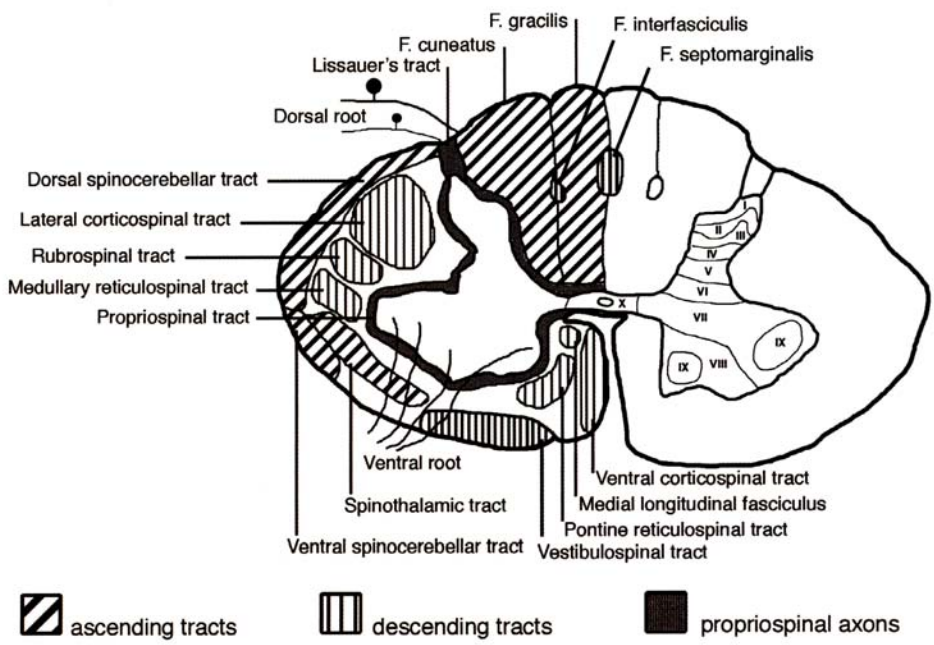

Figure 2.3. White matter tracts in the spinal cord

The left side of the drawing shows major white matter tracts in the human spinal cord. The right side shows the lamination of the grey matter. Adapted from (Schwartz and Flanders, 2007).

Simple reflexes

To provide a better understanding of the stimulations, this section presents the concept of mono- and polysynaptic reflexes. Afferent fibres of the dorsal root – whose cell bodies are located in the spinal ganglion – transmit sensory signals from the periphery to neurons located in the dorsal horn of the cord. Those signals are processed first at the spinal level but are also sent to supraspinal regions through collaterals of the afferents or through projecting interneurons whose axons ascend the spinal cord (see Figure 2.4a). At the spinal level, the information reaches motoneurons in the ventral horn either directly (monosynaptic pathways as in Figure 2.4b) or through interneurons (di-, tri-, or polysynaptic pathways as in Figure 2.4c). When motoneurons are activated, muscles will contract unless the cholinergic transmission is blocked by agents such as pancuronium which acts at the neuromuscular junction.

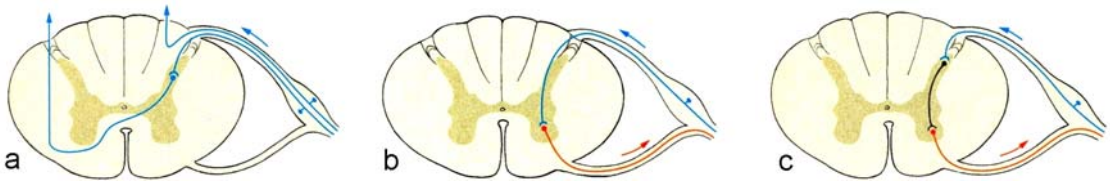

Figure 2.4. Monosynaptic and polysynaptic reflexes
This figure illustrates the transmission of afferent signal to supraspinal regions (a) and reflexes via monosynaptic (b) and polysynaptic pathways (c). Adapted from (Kahle and Frotscher, 2005).

Vascular arborisation of the spinal cord

Given that functional magnetic resonance imaging (fMRI) relies on the recording of haemodynamic changes related to neuronal activity, it is worth describing the vascular architecture providing the blood supply in the spinal cord. An illustration of the spinal cord vascular supply is shown in Figure 2.5. Arterial supply in the cord is provided by vertebral arteries and segmental arteries. Vertebral arteries give rise to two posterior spinal arteries which course along the dorsal side of the cord. At about C2 vertebral body, vertebral arteries merge to form the anterior spinal artery. This artery courses along the medio-ventral side of the cord. Segmental arteries give rise to radicular arteries which supply blood to the cord's roots. Draining veins have a distribution similar to that of the arteries. The venous network gives rise to one anterior spinal vein and two posterior spinal veins.

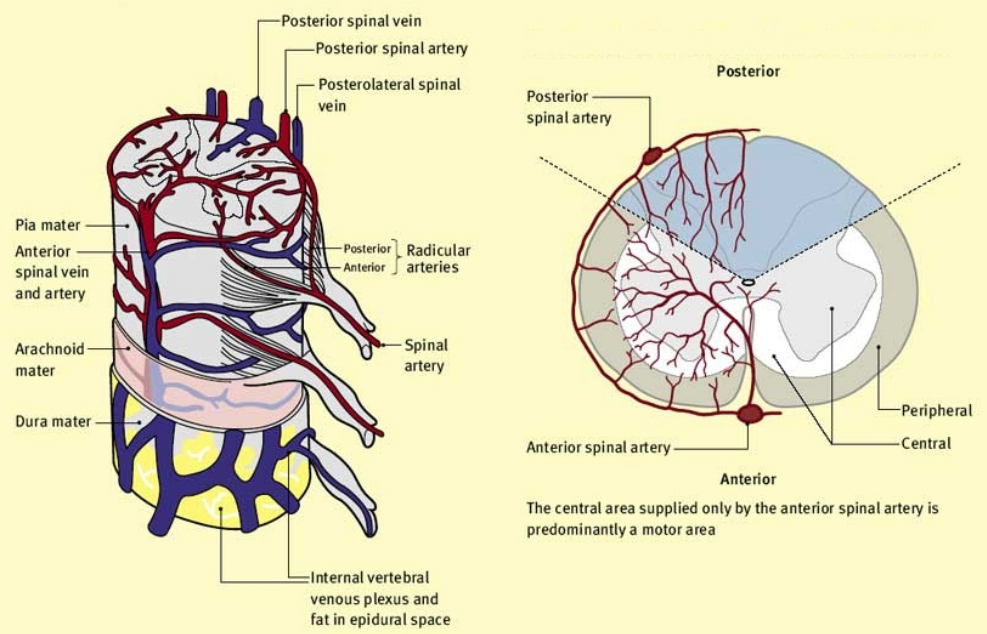

Figure 2.5. Vascular supply in the spinal cord
Left panel shows the general arterial supply and venous drainage. Right panel shows the cross-sectional distribution of arteries. Source: http://www.frca.co.uk/.

Spinal cord injury

Spinal cord injury (SCI) has a significant impact on the quality of life since it can lead to motor deficits (paralysis) and sensory deficits. Throughout the world, about 2.5 million people live with SCI[2]. To date, there is no consensus for fully rehabilitative cure in SCI, although numerous therapeutic approaches have shown benefits (Rossignol et al., 2007; Thuret et al., 2006). It is thus of great importance to develop tools that will improve characterization of spinal lesions as well as the integrity of remaining spinal tracts to eventually establish better prognosis after spinal injury.

Spinal lesions notably induce inflammation, oedema and necrosis at the site of injury (see Figure 2.6). Apart from the lesion, secondary pathological processes including ischemia, inflammation and excitotoxic events may also occur. These so-called 'secondary injuries' follow a first spinal trauma and can be located several vertebral levels from the epicentre of the lesion (Park et al., 2004; Tator and Fehlings, 1991). In the following paragraphs we will briefly describe some spinal anatomo-functional changes triggered by SCI and that are of interest for the present thesis.

[2] http://www.campaignforcure.org

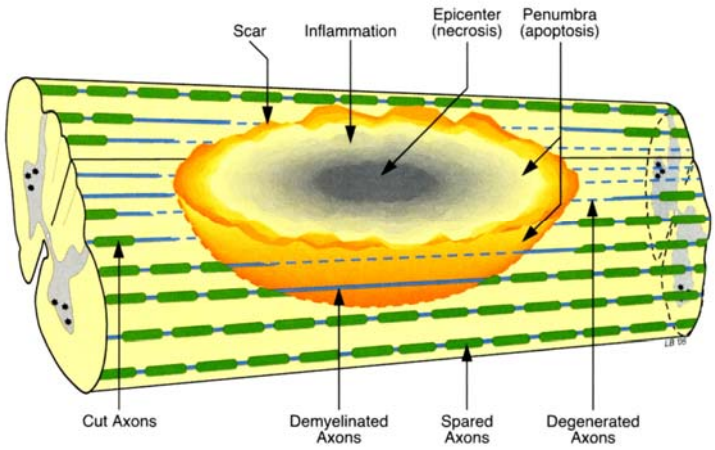

Figure 2.6. Injured spinal cord
The epicentre is characterized by dead cells and surrounded by scar tissue. The lesion could expend with time due to apoptosis and lead to secondary injuries. The lesion directly damages local axons but some closely axons could be spared. Demyelination occurs and further damages axons in physical contact to the injury. This process which last for a few days is called Wallerian degeneration. Adapted from (Schwartz and Flanders, 2007).

Wallerian degeneration

Following spinal lesions, nerve fibres may be disconnected from their cell bodies. As a result, these axons degenerate within a few days. This process is known as Wallerian degeneration. Axon segments which are no longer linked to cell bodies always show degeneration. However, axon collaterals proximal to the lesion can survive. This phenomenon was first observed in 1850 by Waller (Waller, 1850). A recent interpretation of the phenomenon is proposed in (Beirowski et al., 2005). Downstream effects of Wallerian degeneration is the degeneration of ascending and descending pathways in the spinal cord white matter that could potentially be detrimental to intrinsic spinal programs, notably those involved in locomotion.

Axonal regrowth and remyelination

At the site of injury, fibrous scar tissue and myelin are associated with a large number of molecules that inhibit axonal regrowth. It has been shown that limiting the inhibitory effects of these molecules facilitates axonal regeneration, therefore improving recovery of function (Klapka et al., 2005; Schwab, 2004). Besides direct axon damage, some axons may also loose their myelin sheath thereby hampering the conduction of action potentials. Other approaches tend to induce remyelination by several means (McDonald and Belegu, 2006), including cell grafts (stem cells) or interference with immunological mechanisms (Schwartz and Yoles, 2006).

Spinal reorganization

Not only does the spinal cord possess repair mechanisms that could be enhanced, but plastic reorganizations may occur to compensate the loss of functions. For instance, there may be regeneration of damaged axons or collateral sprouting of axons in spared

descending/ascending pathways or primary afferents (Kerschensteiner, 2007). These new growths can project through different spinal paths as they are forming new circuits and adopt unpredicted trajectories as they by-pass the scar tissue (Bareyre et al., 2004; Fouad and Pearson, 2004). This process may play various roles that are illustrated in Figure 2.7. Therefore, apart from directly acting on the lesion site, a large number of studies took advantage of the spinal cord's capacity to change its intrinsic morphological and functional properties. As an illustration of those powerful mechanisms, a cat that has undergone complete spinal cord injury can recover a spinal locomotion after several weeks (Rossignol, 2006b).

Given that both the severity of the deficit and the successful rehabilitation process depend on the type and number of axonal tracts that have been altered, it may be of great interest to assess the white matter integrity at the site of a lesion, to identify anatomical tracts that have been damaged and to quantify the activity of spinal neurons to evaluate the functional state of the cord. Moreover, monitoring the efficiency of the above-mentioned therapeutic strategies is needed to get them accepted in clinical routine. The purpose of the next section is to present a non-invasive technique that appears to be suitable to reach these crucial goals.

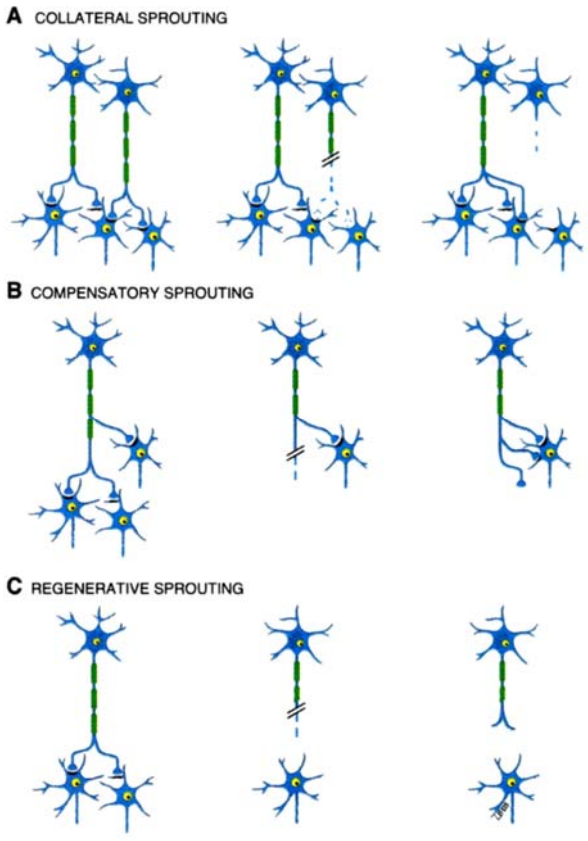

Figure 2.7. Principle of axonal sprouting

New axonal pathways and synaptic terminals can appear in the spinal cord following injury. These new growths can play various roles, notably by innervation of collateral neurons (A), by an accrue number of connections for compensation (B) or by regeneration within an injured axon (C). Adapted from (Schwartz and Flanders, 2007).

Imaging the spinal cord white matter with MRI

Principles of DW-MRI

Magnetic resonance imaging (MRI) is based on absorption and reemission of a radiofrequency signal from resonating hydrogen protons (Purcell et al., 1946). This allows to image water molecules which constitute a great proportion of biological tissues. Proton density (PD), longitudinal (T_1) and transverse (T_2) decays give rise to various contrasts which are used to emphasise specific anatomical structures (*e.g.*, white matter and grey matter). Classical MRI sequences are useful to detect various types of pathologies such as tumours, oedema, ischemia, compression, brain atrophy and multiple sclerosis. Although very useful for many widely-used applications, these types of sequence do not enable specific imaging of white matter axons which would be of interest for assessing the number of disrupted axons and the progression of Wallerian degeneration. The following section will cover an MRI-based technique to image the white matter more specifically.

Diffusion-weighted signal

Diffusion-weighted (DW) MRI allows the measurement of water diffusion anisotropy in biological tissues (Beaulieu, 2002; Hagmann et al., 2006; Le Bihan et al., 2001; Mori and Zhang, 2006). Since the fibrous morphology of white matter restricts water diffusion along white matter axons, DW-MRI allows the indirect localisation of white matter tissue (Douek et al., 1991). The basics of DW-MRI are as follows: water molecules are in constant motion in biological tissues. This state is called Brownian motion. When a particular pulse sequence is applied, it is possible to quantify the extent of water displacement in a given direction (Stejskal and Tanner, 1965). This sequence consists of magnetic gradients applied before and after a 180° refocusing pulse. For motionless molecules, the dephasing induced by the first gradient is compensated by the application of the second gradient. No signal is attenuated. However, if water molecules move during the application of this pair of gradients, spins are dephased more rapidly and signal decreases as a function of the magnitude of displacement. The magnitude by which the diffusion signal is weighted is dictated by the so-called b-value. This value depends on the square of the gradient strength and on the diffusion time interval Δt as defined by

$$b = \gamma^2 \delta^2 \|g\|^2 \left(\Delta t - \frac{\delta}{3} \right) \tag{2.1}$$

where g is the diffusion-encoding gradient, δ is the duration of the encoding gradient, Δt is the delay between application of and γ is the gyromagnetic ratio. DW images hence show hypersignal where water molecules are more static and an apparent diffusion coefficient (ADC) maps can be established. Based on the latter physical process, DW-MRI can be used to quantify axon disruption, myelin integrity and axon swelling (Thurnher and Bammer, 2006a). Principle of DW-MRI is illustrated in Figure 2.8.

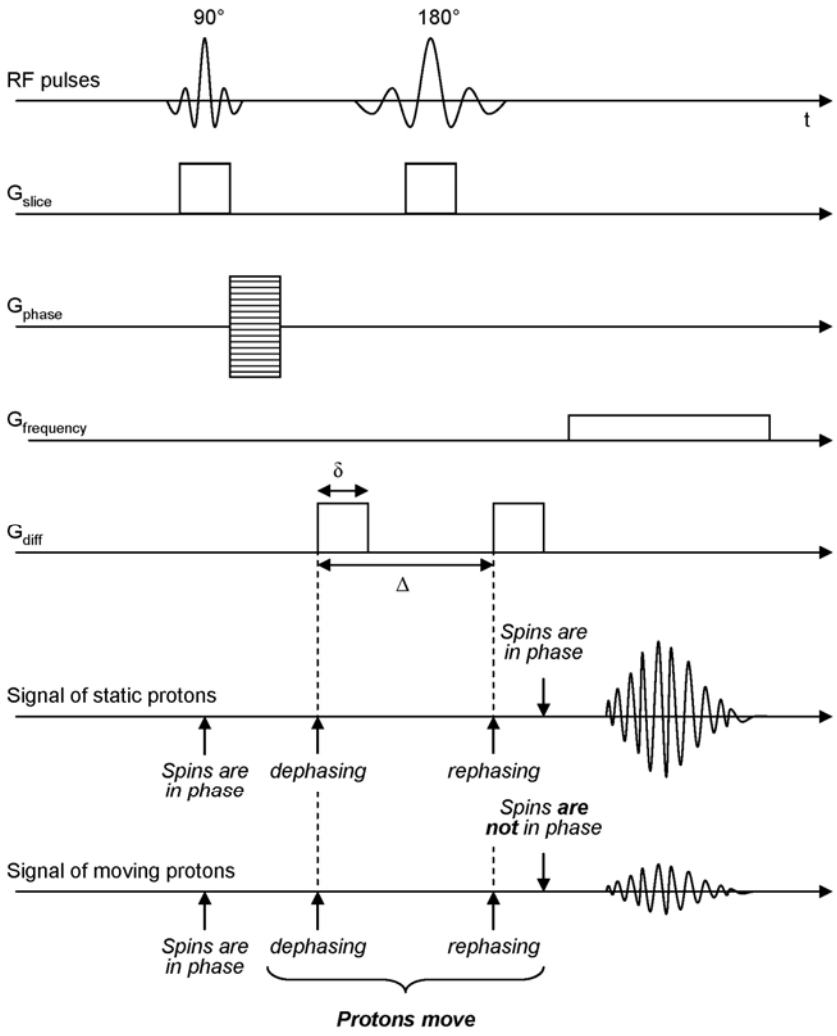

Figure 2.8. Principle of diffusion-weighted MRI

Simplified timeline of RF pulse and gradient events in a standard DW sequence. For motionless molecules, the dephasing induced by the first gradient is compensated by the application of the second gradient: MR signal is mainly T_2-weighted. However, if water molecules move during the application of this pair of gradients, spins are dephased more rapidly and signal decreases as a function of the magnitude of displacement.

Diffusion tensor imaging (DTI) and tractography

By weighting the diffusion signal in several directions, it is possible to compute a parametric model representing the main diffusion direction at each voxel (Basser et al., 1994). This type of model is described by a tensor and is usually represented graphically as a 3D ellipsoid. This technique is known as Diffusion Tensor Imaging (DTI). The purpose of DTI is to estimate the so-called diffusion tensor *D* from the following equation

$$A = e^{-b \cdot D} \tag{2.2}$$

where *A* stands for the signal attenuation and *b* for the diffusion weighting, as defined in Equation (2.1). After multiple regressions are performed to retrieve *D*, the latter matrix is

diagonalized using singular value decomposition to get the three eigenvalues. From each tensor's eigenvalues, several indices characterising the diffusion can be computed. These include fractional anisotropy (FA) and mean diffusivity. Also, the first and second eigenvalues can be of interest as they have been shown to be more specifically informative to characterize some pathologies, as compared to anisotropic measurement (Gulani et al., 2001; Kinoshita et al., 1999; Ono et al., 1995; Song et al., 2002b).

Having modelled the diffusion tensor, it is possible to reconstruct global axonal pathways by linking every voxel with a similar eigenvector to its neighbours. This procedure, known as fibre tractography, allows 3-D mapping of white matter architecture in the mammalian brain (Basser et al., 2000; Ciccarelli et al., 2003; Conturo et al., 1999; D'Arceuil et al., 2007; Descoteaux et al., 2007b; Dyrby et al., 2007; Oppenheim et al., 2007). It should be mentioned however that reconstructed fibre bundles do not represent real axonal tracts but trace the path where water diffuses preferentially. Hence, tractography results should be handled with care since they may not represent the real pathway of axons (Basser et al., 2000; Johansen-Berg and Behrens, 2006). For instance, false negatives could be induced by the presence of crossing fibres which would artificially decrease the FA and stop the tracking procedure. Inversely, false positives could be induced by fibrous structures such as scar tissue in which water diffusion also has anisotropic properties (Schwartz et al., 2005d). Probabilistic methods allow better flexibility in the quantification of white matter directionality and have therefore the potential to limit the number of false negatives (Behrens et al., 2003). Another limitation of tractography is the impossibility of distinguishing anterograde from retrograde conduction (*i.e.*, descending or ascending pathways in the cord).

Application of tractography in the spinal cord demonstrated the feasibility of retrieving major longitudinal pathways, *i.e.*, axon bundles oriented in the rostro-caudal (R-C) direction (Bilgen et al., 2005; Ciccarelli et al., 2007; Ellingson et al., 2007b; Fenyes and Narayana, 1999; Gullapalli et al., 2006; Maier, 2007; Wheeler-Kingshott et al., 2002). Tracking of spinal nerves was also possible using DTI (Benner et al., 2008). An important motivation for tracking specific pathways in the spinal cord is the ability to obtain quantitative measurements along those pathways, to correlate the integrity of specific tracts with the severity of functional deficits (Gullapalli et al., 2006; Schwartz et al., 2005a). To successfully perform these measurements, white and the grey matter in the spinal cord must be segmented accurately, despite the limited spatial resolution in the axial plane. For this purpose, methods based on fuzzy-logic technique have been suggested to automatically and efficiently segment white and grey matter on DTI maps (Ellingson et al., 2007a). Other studies also demonstrated the ability to detect collateral fibres in the *ex vivo* human spinal cord using the second eigenvector of the diffusion tensor (Mamata et al., 2006) or using high angular resolution diffusion imaging techniques (Berens, 2006). Interestingly, the latter study demonstrated particular diffusion properties in the dorsal horn of spinal cord injured rats, such as increased diffusivity in the plane orthogonal to dorso-ventral tracts.

HARDI and q-space techniques

Diffusion tensors quantify mean diffusion within the space of a voxel, *i.e.*, on the order of the millimetre. Knowing that axon diameter is on the order of the micrometer, the computed tensor only gives a macroscopic quantification of the diffusion process. The result is a macroscopic integration including every axon localised in the given voxel. If axons were homogeneously aligned within a voxel, the first eigenvector of the tensor would accurately approximate their direction (Lazar and Alexander, 2003). However, the tensor model is not capable of resolving multiple fibre orientations within one voxel (Campbell et al., 2005; Tuch et al., 2002). Although the use of the second eigenvector has been proposed as a means of resolving crossing fibres in the brain (Wiegell et al., 2000) and in spinal cord (Maier and Mamata, 2005; Mamata et al., 2006), there is some restriction imposed by the tensor itself. Indeed, the three eigenvectors are, by definition orthogonal. Thus, when the primary direction is defined by the first eigenvector – longitudinal fibres in the case of the spinal cord, the second eigenvector is limited in terms of degrees of freedom since its direction is necessarily on the plane orthogonal to longitudinal fibres. In the presence of non orthogonal fibres, the usual way of decomposing the tensor (*i.e.*, in an orthogonal fashion) becomes less efficient (Hagmann et al., 2006).

To overcome this issue, model-free approaches have been proposed to measure the microscopic diffusion without constraining its representation. These methods are known as diffusion spectrum imaging (Wedeen et al., 2005) and have already demonstrated benefits for imaging the brain (Schmahmann et al., 2007). However, long acquisition times are required to adequately sample of q-space and retrieve the three-dimensional diffusion profile. To reduce acquisition times, sampling of q-space in one direction has been proposed (Callaghan et al., 1988), allowing the distinction of diffusion properties of various types of axons (Assaf et al., 2000; Ong et al., 2008). Another approach is to sample the q-space restricted in a single sphere. This method is known as high angular resolution diffusion imaging (HARDI). Some popular HARDI reconstructions include q-ball imaging (QBI) methods (Campbell et al., 2005; Tuch, 2004; Zhan and Yang, 2006) and deconvolution methods (Alexander, 2005; Jian and Vemuri, 2007; Tournier et al., 2004). Originally proposed in (Tuch, 2004), QBI reconstructs the diffusion orientation distribution function (ODF) directly from the raw HARDI measurements on a single sphere using the Funk-Radon transform (FRT). This FRT can be solved analytically, efficiently and robustly with the spherical harmonic (SH) basis (Anderson, 2005; Descoteaux et al., 2007a; Hess et al., 2006). QBI has already shown benefits for imaging micro-diffusion properties in the brain (Mukherjee et al., 2008; Tuch et al., 2005).

Anisotropy and white matter

A few remarks should be made regarding the interpretation of diffusion anisotropy in healthy and injured white matter, given that its origin is still poorly understood. Anisotropy could originate from the myelin sheath, axonal membrane and neurofibrils, or a combination of them (Biton et al., 2007). Although water anisotropy is often attributed to the presence of

myelin around white matter axons (Chenevert et al., 1990), it was shown that similar diffusion anisotropy is observed both in nonmyelinated and myelinated nerves, suggesting that myelin is not a necessary determinant for diffusion anisotropy (Beaulieu and Allen, 1994). Being able to accurately model the diffusion process would increase the accuracy of the estimated ADC (Beaulieu, 2002). Better modelling would allow to distinguish several confounding parameters such as axonal density (Jespersen et al., 2007) and size (Assaf et al., 2008; Ong et al., 2008), oedema (Sen and Basser, 2005), tissue motion (Summers et al., 2006), myelination state (Beaulieu and Allen, 1994) and partial volume effect (Smith et al., 2008). Recently, methodological frameworks have been proposed to quantitatively validate extracted diffusion directions with the actual directions observed through light microscopy in histological samples (Choe et al., 2008; Golabchi et al., 2004). These frameworks represent essential tools for the community developing new methods for white matter imaging.

DW-MRI of the spinal cord

Challenges

Spinal cord DW-MRI has been the subject of intense research for the last ten years (Bammer and Fazekas, 2003; Clark and Werring, 2002; Ducreux et al., 2007; Lammertse et al., 2007; Maier, 2007; Thurnher and Bammer, 2006a; Vargas et al., 2008). Although widely applied to the brain, this method is challenging at the spinal level because of: (i) the small size of the cord relative to the brain (~1 cm diameter in the human) requiring higher spatial resolution and thus decreasing the signal-to-noise ratio (SNR), (ii) physiological motions (respiration, cardiac), which may bias ADC estimation (Kharbanda et al., 2006) and create ghosting artifacts (Clark et al., 2000), (iii) partial volume effects, which are more problematic in the cord due to the surrounding cerebrospinal fluid (CSF) (Nunes et al., 2005), (iv) chemical-shift artifacts arising from the epidural fat and other nearby structures and (v) geometric distortions arising from magnetic field inhomogeneities in nearby inter-vertebral disks and lungs. The latter point is particularly challenging in DW-MRI since standard sequences based on echo-planar imaging (EPI) are very sensitive to this type of artifact (Ardekani and Sinha, 2005; Heidemann et al., 2003; Jeong et al., 2006; Voss et al., 2006).

Coil

Receiving coils deserve careful consideration for the improvement of SNR, which is a particularly important requirement in spinal cord MRI given the need for high spatial resolution. This brief review on coils used for spinal cord imaging also applies to other types of sequences than DW-MRI, such as MRI relaxometry and functional MRI. To image the human spinal cord, people have used standard multi-channel spine coils (Brooks et al., 2008; Dietrich et al., 2001; Ducreux et al., 2007; Holder et al., 2000; Kharbanda et al., 2006; Mamata et al., 2006; Thurnher and Bammer, 2006a; Voss et al., 2006; Wilm et al., 2007), 8-channel head coils – for the upper cervical cord only (Jeong et al., 2005; Ohgiya et al., 2007a; Tsuchiya et al., 2005), single-

channel surface coils (Spuentrup et al., 2003), and custom phased array coils (Maieron et al., 2007b). Phased array receiver coils have two advantages. The first one is related to SNR. The noise in high field MRI predominantly comes from the subject rather than from the coils or electronics. Hence, using small elements arranged in arrays produces high sensitivity with an overall reduction of noise (Roemer et al., 1990). The second advantage of phased array coils is the possibility of using parallel imaging[3], of particular interest for the spinal cord region due to susceptibility effects. An example of advanced coil design is the 16-channel phased-array coil used by Mainero *et al.* in their fMRI experiments (Bodurka et al., 2008).

Surface coils (Kim et al., 2007a; Kim et al., 2007b; Loy et al., 2007; Nevo et al., 2001; Schwartz et al., 2005a; Schwartz et al., 2005b; Schwartz et al., 2005c; Schwartz et al., 2005d; Schwartz et al., 2003; Schwartz et al., 1999; Zhao et al., 2006a) and chronically implanted coils (Bilgen et al., 2001; Deo et al., 2006; Elshafiey et al., 2002; Fenyes and Narayana, 1999; Ford et al., 1994; Madi et al., 2005; Silver et al., 2001; Wirth et al., 1993) have been used for imaging the spinal cord of rodents and cats. Although implanted coils provide much higher SNR than that of surface coils, they may have undesirable effects due to surgical procedure, including scar tissue formation and possible rejection of the coil inducing inflammation (Berens, 2006).

Patient positioning, slice orientation and voxel size

As in the previous section, the following literature also applies to non-DW-MRI sequences. In human spinal acquisitions, subjects are usually positioned head-first supine. There are two main strategies for slice orientation. The first one consists in acquiring thick axial slices with high in-plane resolution, taking advantage of the gross symmetry of the cord along the R-C axis (Backes et al., 2001; Brooks et al., 2008; Elshafiey et al., 2002; Endo et al., 2008; Govers et al., 2007; Gullapalli et al., 2006; Holder et al., 2000; Kim et al., 2007a; Kornelsen and Stroman, 2004; Lilja et al., 2006; Madi et al., 2005; Maieron et al., 2007b; Moffitt et al., 2005; Nevo et al., 2001; Ng et al., 2008; Ohgiya et al., 2007a; Schwartz et al., 1999; Stroman et al., 2001b; Tsuchiya et al., 2005; Wilm et al., 2008; Yoshizawa et al., 1996). The second strategy consists in acquiring sagittal slices parallel to the R-C axis, usually using isotropic voxels (Bammer et al., 2002; Cercignani et al., 2003; Jeong et al., 2005; Kharbanda et al., 2006; Murphy et al., 2001; Shen et al., 2007; Spuentrup et al., 2003; Stroman et al., 2005a; Thurnher and Bammer, 2006b; Tsuchiya et al., 2003). The latter approach offers the benefits of extensive spinal coverage using only a few slices. Moreover, isotropic voxels enable the exploration of the anatomical structure of the white matter without bias (Basser et al., 2000; Jones et al., 2002b). Instead, elongated voxels result in more averaging of the diffusion signal in one specific direction, therefore biasing estimation of DTI metrics.

[3] the basics of parallel imaging will be described in section 'Strategy towards reducing susceptibility artifacts in DW-MRI'

Pulse sequence and acquisition parameters

As it is the case in brain, EPI is the most straightforward approach to obtain fast acquisition of DW spinal cord data. Also, standard EPI sequences allowing diffusion-weighting are implemented in most clinical scanners. However, EPI is very sensitive to susceptibility effects, which are particularly present in the spinal region (Ardekani and Sinha, 2005; Heidemann et al., 2003; Jeong et al., 2006; Voss et al., 2006). To alleviate this issue, strategies have been developed to investigate optimal pulse sequences for spinal cord DW-MRI. Most of them are described in section 'Strategy towards reducing susceptibility artifacts in DW-MRI' of the present manuscript. To optimize the choice of TR and TE, some studies investigated intrinsic T_1 and T_2 relaxation times and relative spin density in the rat spinal cord (Narayana et al., 1999b; Stanisz et al., 2005). It has notably been shown that white and grey matters have different T_2 and proton density (PD) values, but similar T_1 values.

Angular resolution

Angular resolution in DW-MRI is dictated by the b-value and by the number of directions in which magnetic gradients are applied to get the DW signal. At high b-values the signal is more weighted towards its diffusion direction. Therefore the signal is more attenuated yielding low SNR data (Ronen et al., 2005). Hence, a compromise should be found between the angular resolution and the SNR required to get interpretable data – this motivates for example the use of regularization methods for DTI and QBI (Arsigny et al., 2006; Descoteaux et al., 2007a; Lu et al., 2006).

There is an ongoing debate as to whether increasing the number of directions over a certain threshold yields significant benefits for diffusion modelling (Hosey et al., 2005; Jones, 2004; Lee et al., 2006; Ni et al., 2006). An article from Landman *et al.* suggests to increase the number of directions rather than the number of averaging (Landman et al., 2007). A study based on Monte-Carlo simulations showed that optimal DTI reconstruction is made possible when using 20 to 30 directions for gradient encoding (Jones, 2004). Additionally, the way q-space is sampled also has an impact in the estimation of the diffusion tensor (Papadakis et al., 1999). For spinal cord imaging, many studies pointed out the axial symmetry of the cord as an argument for imaging with a reduced number of directions (Gulani et al., 1997; Schwartz et al., 2005a). However, the computed ADC is biased for regions were axons curve or change direction, namely in some complex anatomical projections of nerve roots or following SCI. Furthermore, as mentioned in (Madi et al., 2005), these acquisitions are dependent on subject positioning within the scanner, so that the cord axis is aligned with the longitudinal gradient. When only a small section of the cord is imaged, this may be possible. However, for ADC quantification along a larger extent of the cord, the curvature may induce a bias in the proton signal attenuation where longitudinal fibres are no longer aligned with the gradient. To prevent this, Madi *et al*. used an icosahedral scheme up to 42 gradient directions and showed the benefit of high angular resolved gradient directions. In the case of model-free approaches however, as many directions as possible are needed to robustly reconstruct the ODF (Perrin et al., 2005;

Poupon et al., 2007). However, there is a trade-off with acquisition duration. To minimize this trade-off, researchers try to measure the diffusion profile using non-homogeneous sampling of the q-space. They notably claim that when a particular orientation of fibre bundles is assumed, it becomes beneficial to record more DW data in the plane orthogonal to those fibres. Recent studies proposed methods to estimate the diffusion profile online (Poupon et al., 2007), enabling the dynamic adaptation of q-space sampling using a data-driven loop (Peng and Arfanakis, 2007).

Cardiac-related motion

Significant motion of the spinal cord has been reported in the R-C (Summers et al., 2006) and in the antero-posterior (A-P) direction (Figley and Stroman, 2007; Figley et al., 2008; Kharbanda et al., 2006) along with CSF pulsation. This motion modifies the ADC in specific directions, thus biasing FA quantifications along the cord. Cord motion could arise from two distinct phenomena. The first one is related to the dilation of arteries following cardiac systole, as observed in the brain (Dagli et al., 1999). The second source of motion may be related to CSF pulsation. After cardiac systole, increase of cerebral blood volume causes a compression of the subarachnoid space, yielding abrupt CSF flow in the spinal region (Alperin et al., 1996; Du Boulay et al., 1972). During the diastole, CSF flows back to supraspinal regions at relatively high velocity (Henry-Feugeas et al., 1993). Hence, it has been suggested that data should be acquired at a certain phase of the cardiac rhythm where cord motion is minimal (Summers et al., 2006).

Respiration-related motion

Similarly to cardiac pulsations, motion due to respiration significantly degrades image quality (Cai et al., 2007; Spuentrup et al., 2003). Respiratory gating has been used successfully to limit respiration-related motion artifacts (Fenyes and Narayana, 1999; Kim et al., 2007a; Loy et al., 2007; Madi et al., 2005). More advanced methods rely on the acquisition of expiration and inspiration phases to reduce motion occurring between phase encoding lines, thus allowing faster acquisition (Spuentrup et al., 2003). Additionally to moving structures, respiration could have another negative impact related to susceptibility effects. When imaging the thoracic region, air volume in the lungs regularly changes, its volume, causing variations in local B_0-field homogeneity. This can cause susceptibility effects such as geometric distortions in the phase encoding direction (Brosch et al., 2002; Raj et al., 2001; Van de Moortele et al., 2002). This effect is even more notable at ultra high field but can already be encountered at 3T. To circumvent this issue, dynamic shimming has been proposed (van Gelderen et al., 2007) and has shown encouraging results in the brain at 7T (Duyn et al., 2007).

Strategy towards reducing susceptibility artifacts in DW-MRI

As described in the previous section, DW-MRI is highly challenging in the spinal cord due to various types of artifacts. Among them, susceptibility artifacts are particularly

problematic. The present section will review most strategies used to reduce susceptibility artifacts in the spinal cord. Descriptions of pulse sequence strategies are based on the textbook from Bernstein *et al.* (Bernstein et al., 2004).

Susceptibility artifacts are mainly observed in spin echo (SE) and gradient echo (GE) EPI acquisition. In the presence of magnetic field inhomogeneities – induced by intervertebral disks or lungs – spins experience off-resonance, *i.e.*, they precess at a frequency different than the Larmor frequency. Given that classical EPI schemes consist in filling k-space in one shot, phase errors accumulate during slice acquisition, causing geometric distortions in the image domain. This phenomenon may be formalized by the following MR signal equation

$$S(t) = \int_x \int_y m(x,y) e^{-i2\pi\left[k_x(t)x + k_y(t)y + \Delta B_0 t\right]} dxdy \tag{2.3}$$

where m stands for the total magnetization, k_x and k_y stand for the time dependent k-space trajectories (*i.e.*, area under the gradient waveform) in the frequency x and phase y directions, and ΔB_0 is the undesirable term representing field strength variation of local inhomogeneities. Given that the recorded MR signal codes for the spatial location via the Fourier transform, the phase error term ΔB_0 produces geometric distortions in the image domain along the phase encoding direction. It may also produce significant signal loss in GE-EPI. Two different approaches can be used to limit susceptibility artifacts. One can either optimize the acquisition sequence (Raya et al., 2005) or one can correct distortions using non-linear registration algorithms (Andersson et al., 2003). Limiting susceptibility artifact during acquisition can be achieved by reducing $\Delta B_0 t$ in Equation (2.3). To do this in EPI, the inter-echo spacing – which is defined as the total time between acquisition of two phase lines – can be reduced by increasing the bandwidth, reducing the number of phase lines, or imaging faster by taking advantage of multi-channel coils (parallel imaging) or interleaved k-space acquisitions (multi-shot). The following paragraphs will review these techniques.

Multi-shot acquisition

In multi-shot (or segmented) acquisition, k-space is divided, thereby dividing the total readout time for each slice (Poustchi-Amin et al., 2001). However the problem of multi-shot is the generation of phase errors notably related to physiological motion (Bammer et al., 2002; Bammer et al., 1999). Following inverse Fourier transform, these phase errors cause a repetition of the image pattern in the phase encoding direction (ghosting). To correct for this one can use echo-time shifting (Feinberg and Oshio, 1994), as well as monitoring navigator echoes that monitor phase errors and retrospectively correct them before image reconstruction (de Crespigny et al., 1995; Nunes et al., 2005). One group further improved the latter method by introducing information related to subject motion (Clark et al., 2000). To keep acquisition time short, it has been proposed to acquire scans without gradients blips (Schmithorst et al., 2001). Many studies have shown multi-shot acquisition to be a promising technique for spinal cord DW-MRI (Bammer et al., 2002; Ries et al., 2000; Zhang et al., 2005a). An example of multi-shot acquisition in the spinal cord is provided in Figure 2.9.

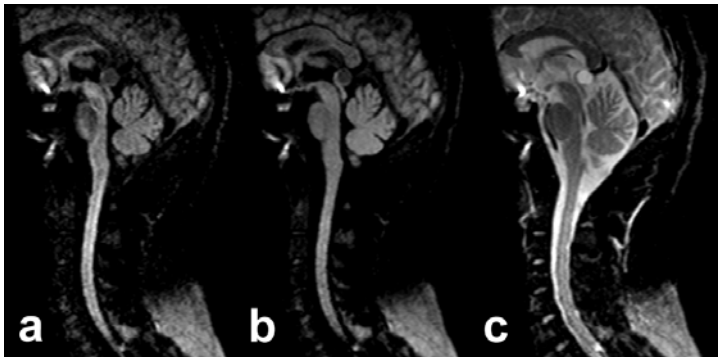

Figure 2.9. Multi-shot EPI acquisition
Example of the interleaved implementation of a multi-shot EPI sequence (11 interleaves of 15 echoes each) showing sagittal DW image with diffusion-encoding gradient oriented R-L (a), trace image (b) and T_2-weighted image (c). Images were obtained on a 1.5T Philips system using a neck-coil. Adapted from (Bammer et al., 2002).

Parallel acquisition

This technique takes advantage of the multiple receiving elements of certain coils to reduce acquisition time. Each element of the antenna acquires in parallel a portion of the k-space. For instance, each channel of an 8-channel coil could simultaneously acquire 1/8 of the k-space. However, due to the limited coil sensitivity profile, it would typically acquire 1/3 of the k-space, thus dividing by three the acquisition time – and also by three the accumulation of phase errors. Two well-known approaches could be used to combine the signal coming from individual coils. One is called GRAPPA (GeneRalized Autocalibrating Partially Parallel Acquisitions) and is primarily implemented on Siemens scanners. It consists in filling missing lines of the k-space prior to image reconstruction. Another approach, developed by Pruessmann *et al.* is called SENSE (SENSitivity Encoding) and consists in correcting aliased patterns in the image domain, given the coils' sensitivity profile (Pruessmann et al., 1999). A review on parallel imaging is presented in (Heidemann et al., 2003). Some comparisons with and without parallel acquisition demonstrate its benefits for imaging the brain (Alexander et al., 2006; Ardekani et al., 2006; Ardekani and Sinha, 2004) and the spinal cord (Cercignani et al., 2003; Noebauer-Huhmann et al., 2006). To further reduce susceptibility artifacts one could combine multi-shot with parallel acquisitions (Skare et al., 2007). An example of parallel imaging in the spinal cord is provided in Figure 2.10.

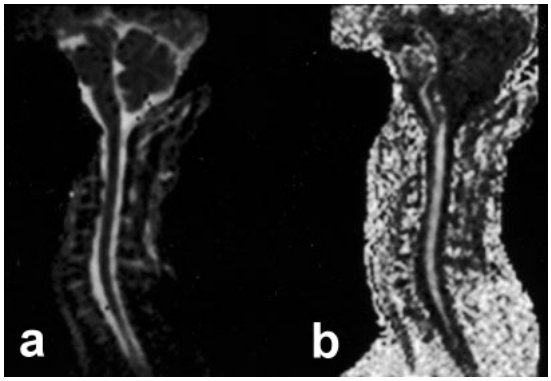

Figure 2.10. Parallel imaging acquisition
Sagittal mean diffusivity (a) and FA map (b) obtained using the SENSE parallel imaging technique, with 2-time acceleration in the A-P direction. Images were obtained on a 1.5T Siemens system using a four-element neck coil. Adapted from (Cercignani et al., 2003).

Reduced FOV

Another way to reduce the $\Delta B_0 t$ term in Equation (2.3) is to decrease the number of phase lines acquired. To keep the same spatial resolution while decreasing matrix size, it is possible to reduce the field of view (FOV) – either in the phase encoding direction only, or in both dimensions. For instance, the proposed ZOOM-EPI technique reduces the echo-spacing duration using a reduced square FOV. This approach has demonstrated benefits in the human cervical spinal cord using sagittal slices (Jeong et al., 2005; Jeong et al., 2006; Wheeler-Kingshott et al., 2002). A drawback of this approach however is that the SNR is reduced. Also, depending on subject size and slice orientation, an additional outer volume suppression pulse might be required to avoid aliasing (Wilm et al., 2007). Advanced outer volume suppression methods demonstrated encouraging results for imaging the whole human spinal cord at high spatial resolution (Wilm et al., 2008). To circumvent the need for outer volume suppression – which might increase the specific absorption rate (SAR) significantly, one can use an excitation pulse restricted in the phase encoding direction, as demonstrated in the human cervical spinal cord (Saritas et al., 2008). An example of the latter method is illustrated in Figure 2.11.

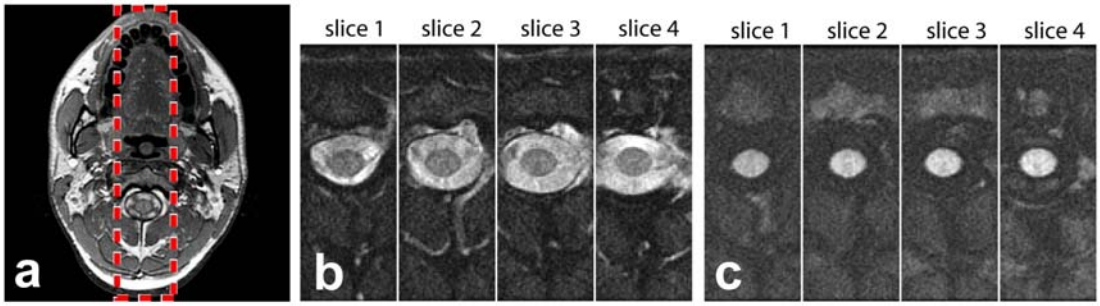

Figure 2.11. Reduced FOV acquisition
Anatomical axial image showing the FOV (a). Resulting T_2-weighted (b) and mean of all three DW images (c). This method introduces a fat saturation pulse and does not need any outer volume suppression. Images were obtained on a 1.5 GE system using an 8-channel head coil. Adapted from (Saritas et al., 2008).

Fast Spin Echo (FSE)

Rapid Acquisition with Relaxation Enhancement (RARE) is a SE sequence with refocusing pulses after radiofrequency (RF) excitation to significantly decrease relaxation time, thus enabling the introduction of more excitation pulses in a given time, in comparison to the standard SE sequence. Therefore, k-space is filled much faster making this sequence less sensitive to off-resonance effects and Eddy-currents[4] (Hennig et al., 1986). A number of variations of the RARE sequence have been developed, including Fast Spin Echo (FSE) and Turbo Spin Echo (TSE). In this thesis, I will refer to this type of sequence with the term 'FSE'. Some studies have demonstrated the benefits of FSE for imaging the human spinal cord with DTI (Sarlls et al., 2005; Tsuchiya et al., 2003; Xu et al., 2004). Although faster than standard SE, this sequence is much slower than EPI. To make DW-FSE applicable in clinical routine, coils with very high sensitivity should be used, requiring less averaging therefore decreasing total acquisition time (Xu et al., 2004). In addition to the long acquisition time, there is another disadvantage of the FSE sequence related to the Carr–Purcell–Meiboom–Gill (CPMG) condition. This condition states that the magnetization following an excitation pulse must be aligned with the axis of the refocusing pulses. Any component that does not follow this condition is suppressed after some echoes. This is important in DW imaging since the application of diffusion gradients violate this condition, therefore producing image artifacts (Clark and Werring, 2002). To overcome this difficulty a non-CPMG technique based on FSE has been proposed (Le Roux, 2002). It has so far yielded promising results in the spinal cord , as shown in Figure 2.12.

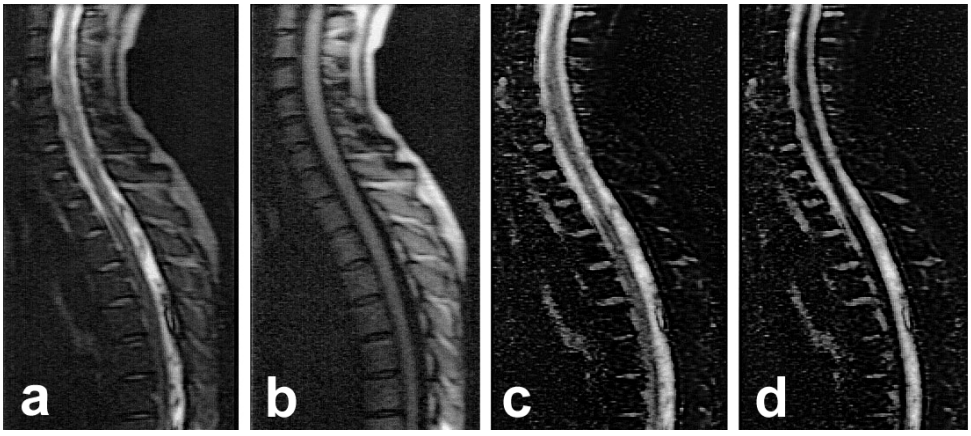

Figure 2.12. Non-CPMG FSE acquisition
Sagittal T_2-weighted image (a), DW trace image (b), ADC map in the R-C (c) and in the A-P direction (d). Sequence developed by P. Le Roux et al. (Le Roux, 2002), figure adapted from (Clark and Werring, 2002).

[4] Eddy-currents are produced by the electric field generated by rapid changes in magnetic flux (Faraday's Law). In accordance with Lenz's Law, these Eddy currents induce magnetic field which can cause image distortions, especially in DW-MRI due to the presence of strong and rapidly switching diffusion gradients (Reese et al., 2003).

Line scan diffusion imaging (LSDI)

LSDI is another alternative to the EPI acquisition scheme. It is a spin-echo technique that relies on the sequential single-shot acquisition of phase encoding lines. LSDI is relatively insensitive to B_0-field inhomogeneities, Eddy-currents, bulk motion, and can provide rectangular DW images (Finsterbusch and Frahm, 1999, 2000; Gudbjartsson et al., 1996). Previous studies have compared single-shot EPI and LSDI (Kubicki et al., 2004). LSDI was applied in children (Robertson et al., 2000), in the human spinal cord (Maier, 2007; Maier and Mamata, 2005; Mamata et al., 2006) and in the spine (Bammer et al., 2003). However, the trade-off of LSDI acquisition scheme is the relatively long acquisition time to image a large volume.

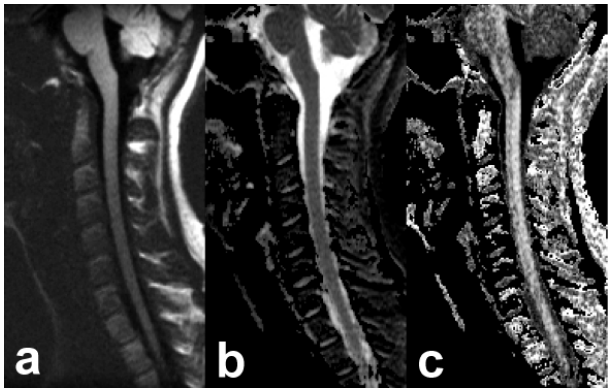

Figure 2.13. LSDI acquisition
Sagittal mean DW image reconstructed from all six DW images (a), ADC trace (b) and FA map (c). Images were obtained in a 1.5T GE system using a phased-array spine coil. Adapted from (Maier and Mamata, 2005).

Radial acquisition

Contrary to the classical Cartesian k-space filling, radial acquisition is made up of phase lines passing through the centre of k-space. Hence, all readout lines are symmetric to the origin of Fourier space and are equivalent with respect to the reconstruction. This is not the case in conventional Cartesian readout schemes, where a single corrupted data line can degrade the complete image (Dietrich et al., 2001). Due to the high density of data at the centre of k-space, the SNR is still acceptable when fewer phase lines are acquired compared to the Cartesian k-space sampling scheme. A disadvantage of radial acquisition however is the presence of streak artifacts due to the undersampling of the azimuthal region in k-space (Bernstein et al., 2004). Instead of rotating single lines, one could also rotate blades consisting of several phase lines (Pipe, 1999; Pipe and Zwart, 2006). This technique is known as periodically rotated overlapping parallel lines with enhanced reconstruction (PROPELLER). A radial EPI technique using this approach has been proposed and yielded very promising results in the abdomen (Deng et al., 2008) and in the spinal cord (Wang et al., 2005). Sarlls *et al.* further improved the radial FSE technique by using wider refocusing slice, to decrease B_1-field inhomogeneities effects (Sarlls and Pierpaoli, 2008a; Sarlls and Pierpaoli, 2008b).

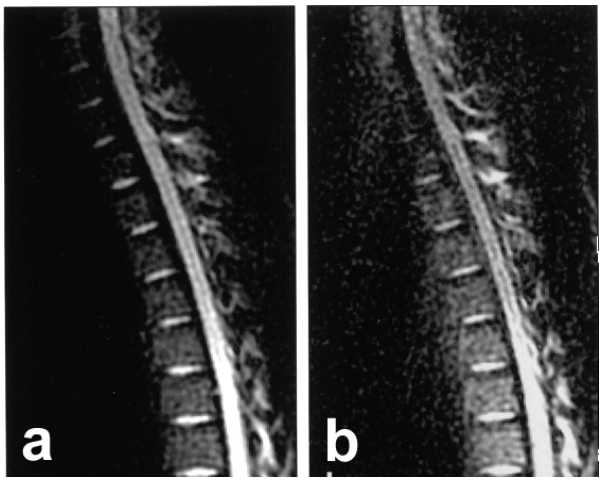

Figure 2.14. Radial acquisition
Sagittal DW image with diffusion-encoding gradients in the R-C direction and b-value of 50 s/mm^2 (a) and 350 s/mm^2 (b). Images obtained on a 1.5T Marconi system with a phased-array coil. Adapted from (Dietrich et al., 2001).

Point spread function

To correct for phase errors in k-space one can use an additional image called the Point Spread Function (PSF). The PSF is obtained by acquiring a certain number of SE signals, while incrementing the phase for each line (Robson et al., 1997). These images provide additional information about distortions in all directions, as well as the intensity distribution for each of voxels. By considering the displacement of the PSF, local distortions due to susceptibility and chemical shift effects can be quantified and subsequently corrected (Zaitsev et al., 2004; Zeng and Constable, 2002). This technique can be combined with other acquisition methods for faster imaging, such as parallel imaging (Zaitsev et al., 2004). Although this technique has shown very encouraging results, its implementation is not straightforward and might lead to computational-related issues during image reconstruction.

Correcting distortions *a posteriori*

As an alternative to modification of acquisition methods, it is possible to correct for susceptibility artifacts following image reconstruction. Given that off-resonance effects are negligible in the frequency-encoding direction due to the fast sampling of RF echoes, one can make the assumption that reconstructed images show susceptibility distortions in the phase encoding direction only. To correct for these distortions in the image domain, various strategies use non-linear registration algorithms constrained in one direction. In the following, we will review four major strategies: the field-map method, the reversed gradient method, the field modelling method and the registration method based on a reference image. Note that all forms of correction procedures reviewed here do not allow the retrieval of lost signal occurring as a result of susceptibility artifacts. In such cases, only an adequate acquisition scheme can handle this difficult issue. For more information on correcting distortions *a posteriori*, Andersson *et al.* wrote a review oriented towards DTI (Andersson et al., 2003).

The field-map approach is based on the acquisition of a phase image resulting from the subtraction of two images acquired at a different TE. This phase image, also known as a 'field-map', is subsequently used to quantify susceptibility differences in the region of interest (Cusack et al., 2003; Schneider and Glover, 1991; Wilson et al., 2002). This method is widely used and is for example implemented in FSL (Smith et al., 2004). The standard procedure consists in (i) acquiring the field-map, (ii) processing it to generate a warping matrix and (iii) applying this warping matrix to EPI series. Although this procedure is relatively straightforward, is requires the acquisition of an additional image – usually done before acquiring the EPI series. For regions particularly prone to inhomogeneities (like in the brainstem or spinal cord), phase field-maps may exceed 2π, therefore producing 'phase wraps'. To correct for these phase wraps, one could use automatic algorithms that identify phase discontinuities based on a standard intensity segmentation, and then correct phase errors at wrap interfaces (Jenkinson, 2003). Two studies demonstrated the benefits of this method in phase imaging at 7T where phase wraps are particularly problematic (Duyn et al., 2007; Hammond et al., 2008).

Another method to correct for image distortion uses an additional EPI volume acquired with the same FOV and matrix, but using reversed phase gradients (*i.e.*, rotated by 180°). This approach uses the fact that susceptibility distortions are directed along with the phase gradient. Rotating the phase gradient by 180° results in a sign reversal of $\Delta B_0 t$ in Equation (2.3). As a result, images acquired with reversed gradients exhibit distortions in the opposite direction. The idea of filling k-space in opposite directions was originally suggested in (Chang and Fitzpatrick, 1992) and has been adapted to correct EPI distortions in (Andersson et al., 2003; Reinsberg et al., 2005; Voss et al., 2006). Using both images acquired with positive and negative phase gradients, geometric and intensity correction fields are estimated and subsequently applied to EPI datasets. The method is robust and relatively straightforward – although requiring implementation of the correction method – and has demonstrated promising results in the human cervical spinal cord (Voss et al., 2006).

Another approach consists in modelling the displacement field, using a linear combination of spline functions estimated from the EPI dataset (Andersson et al., 2001; Kybic et al., 2000; Skare and Andersson, 2005; Studholme et al., 2000). Implemented in SPM package (Friston et al., 1994a), this method has the advantage of not relying on additional acquisition. However, robust estimation of the displacement field may be compromised in cases of strong susceptibility artifacts, like in the spinal cord. Also, this method makes the assumption of a 'susceptibility-by-movement interaction', which implies that knowledge of the subject's motion will allow a robust estimate of the underlying static inhomogeneities. The estimation of a deformation field is similar to the inverse problem. This method is more suitable for fMRI rather than for DW-MRI, where only few T_2-weighted images are acquired.

The fourth and last approach discussed here is based on the non-linear registration of an EPI over a non-distorted reference image (Ardekani and Sinha, 2005). The reference image is typically a T_2-weighted FSE sequence, acquired with the same FOV as the DW-EPI. The

method consists in (i) manually segmenting the region of interest (ROI) to optimize registration procedure, (ii) normalizing intensity histograms for both EPI and FSE images and (iii) estimating a slice-dependent non-rigid deformation field constrained in the phase encoding direction. The deformation field is subsequently applied to all DW volumes. This method is advantageous because no additional volume acquisition is required, except a reference image without distortion – which is incidentally generally acquired by default in standard protocols. In addition, the reference image could be used as a 'gold standard' for validating distortion correction methods.

Applications to spinal cord injury

Although DW-MRI has been applied to various spinal cord pathologies such as tumours, multiple sclerosis and amyotrophic lateral sclerosis, this section will only review applications in spinal cord injury, as this is the main focus of this thesis.

A large number of studies have applied DW-MRI in humans to evaluate the integrity of spinal cord white matter after SCI (Ducreux et al., 2007; Ellingson et al., 2008a; Facon et al., 2005; Fujiyoshi et al., 2007; Lammertse et al., 2007; Plank et al., 2007; Ries et al., 2000; Shen et al., 2007; Thurnher and Bammer, 2006a; Vargas et al., 2008). Some studies namely showed the benefits of DW images in comparison to T_1- and T_2-weighted images for the detection of abnormalities following acute and chronic SCI (Ries et al., 2000; Shen et al., 2007). As an example, Figure 2.15 shows a comparison of T_2-weighted and DW images in chronic spinal cord compression. Investigations of the sensitivity of DTI indices in SCI have been conducted in (Budde et al., 2007; Ellingson et al., 2008b; Herrera et al., 2008; Shanmuganathan et al., 2008; Song et al., 2002c). Results notably showed that the ADC and second eigenvalue are highly sensitive to abnormalities following SCI. More specifically, radial diffusivity (defined by the mean of the two last eigenvalues) correlates well with the degree of myelination (Song et al., 2002c). Some studies have investigated experimental SCI in rats using small bore MRI (DeBoy et al., 2007; Deo et al., 2006; Kim et al., 2007a; Krzyzak et al., 2005; Schwartz et al., 2005d; Schwartz et al., 1999). Importantly, these studies have shown that DTI can detect fibre bundles disruption and can map the orientation of glial scars (Schwartz et al., 2005d).

From a more therapeutic point of view, DW-MRI has already been used in experimental trials to investigate responses to cellular interventions after SCI (Fujiyoshi et al., 2007; Nevo et al., 2001; Peles et al., 2004; Schwartz et al., 2005a; Schwartz et al., 2003). Optimal DTI indices have been investigated in longitudinal studies in the rat with partial SCI (Deo et al., 2006; Kim et al., 2006; Kim et al., 2007a; Loy et al., 2007). Results showed statistically significant correlation between the BBB score (Basso et al., 1995) and the tensor first eigenvalue (Deo et al., 2006). Similar results were observed in dogs with spinal cord ischemia (Zhang et al., 2007). In the latter study, ADC decreased during the first hour following ischemia, then increased gradually.

Wallerian degeneration was investigated using a multimodal approach including DTI, transcranial magnetic stimulations (TMS) and functional tasks (Lindberg et al., 2007). It has been shown that DTI can detect dynamic changes related to degeneration of specific tracts (Becerra et al., 1995; Guleria et al., 2008; Lindberg et al., 2007; Mac Donald et al., 2007; Moller et al., 2007; Thomalla et al., 2004; Werring et al., 2000). Some authors also investigated the question of what would be the most sensitive DTI indices to detect Wallerian degeneration. It was reported that first and second eigenvalues may be the most sensitive parameters (Budde et al., 2007; Herrera et al., 2008; Zhang et al., 2008).

Spinal cord injury has also been imaged using other MRI techniques than DTI. It is worth mentioning them to appreciate the relative benefits of DW-MRI. High resolution MRI of the spinal cord has been conducted in the rat with complete and partial SCI (Berens, 2006; Fraidakis et al., 1998). Several quantitative measurements were reported, including spinal cord atrophy and relaxation parameters. These results showed that high resolution MRI can accurately detect and localize lesions and secondary injuries in the spinal cord (Narayana et al., 1999a; Narayana et al., 2004), as well as the myelination state (Kozlowski et al., 2008). Other studies based on q-space imaging investigated white matter properties in the healthy (Assaf and Cohen, 2000; Assaf et al., 2000; Cohen and Assaf, 2002; Ong et al., 2008) and injured rat spinal cord (Assaf et al., 2002; Assaf et al., 2003). The latter technique allows some inference of mean axon diameter and density in the healthy (Assaf et al., 2008; Ong et al., 2008) and injured spinal cord (Bar-Shir et al., 2008; Chin et al., 2004) as well as on the myelination state (Biton et al., 2006, 2007).

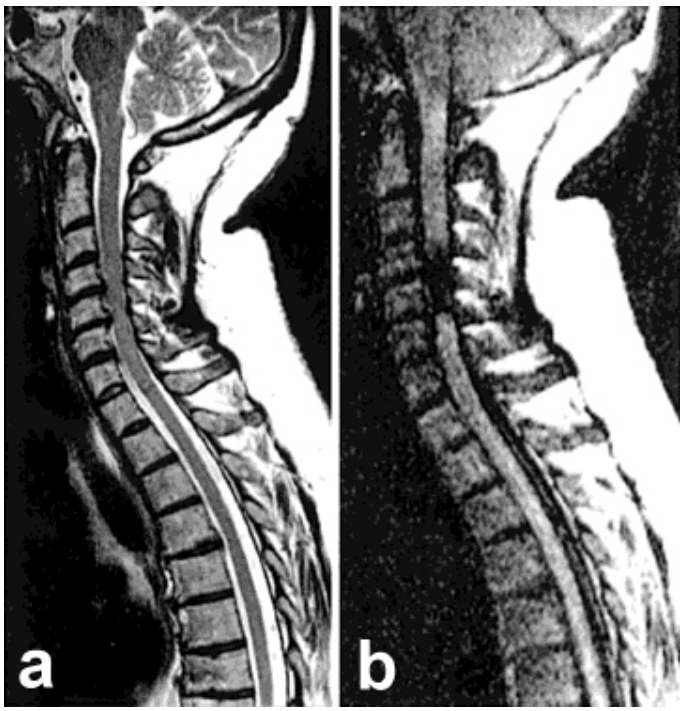

Figure 2.15. DW-MRI in spinal cord compression
Sagittal T_2-weighted FSE image (a) and DW image with a b-value of 300 s/mm^2 (b). One can clearly see the signal loss on the DW image in the region where spinal cord is compressed. Images were obtained on a 1.5T Philips system using a four-channel coil and a multi-shot EPI pulse sequence. Adapted from (Ries et al., 2000).

Functional MRI of the spinal cord

In the previous section we have reviewed an MRI-based technique for quantitative measurements of the characterization of the state of white matter axons. In the followings sections we will review another MRI-based technique called functional MRI (fMRI), which provides insights into neuronal activity in the central nervous system.

Principle of fMRI

BOLD contrast

Based on deoxyhaemoglobin's (HbR) paramagnetic properties, fMRI allows the detection of vascular changes following neuronal activation. Widely used for the last 15 years, this technique is based on a blood oxygenation level dependent (BOLD) signal (Kwong et al., 1992; Ogawa et al., 1990). The basic principle behind the BOLD signal is that following neuronal activation, metabolic demand of oxygen induces a local increase in blood flow and blood volume. However, this blood supply exceeds the actual usage of oxygen, yielding a transient increase of oxyhaemoglobin (HbO_2) in the venous compartment and thus a relative decrease of HbR. Given that the HbR molecule has paramagnetic properties, its presence induces local variations of B_0-field, yielding faster transverse relaxation, also known as T_2^* decay. Since HbR concentration is reduced following neuronal activation, local protons will experience a longer dephasing period resulting in a higher T_2^*-weighted MR signal. Several reviews on BOLD signal are provided in (Bandettini and Ungerleider, 2001; Heeger and Ress, 2002; Logothetis, 2002; Nair, 2005; Raichle, 2001).

Given that fMRI relies on haemodynamic changes to infer on neuronal activity, it is worth understanding basic properties of blood regulation. BOLD signal exists because oxygenated blood supply exceeds the actual demand of activated neurons. Two theories explain this phenomenon. The first one suggests that enzymes responsible for metabolizing the oxygen to produce adenosine triphosphate (ATP) saturate, leaving residual oxygen (*i.e.*, non-metabolized) to be washed out in the venous compartment where BOLD signal is recorded (Fox et al., 1988). The second theory suggests that the low diffusion rate of oxygen through the blood-brain-barrier imposes a disproportionate increase of blood flow (BF) compared to the amount of consumed oxygen (Gjedde et al., 1990). Following the first theory, one should observe a saturation of metabolic rate of oxygen (MRO_2) by gradually increasing BF. In the second theory, one should observe a proportional relationship between the two parameters. Hoge *et al.* have demonstrated the existence of a linear relationship between cerebral BF and MRO_2 using hypercapnia, thereby supporting the hypothesis of a restricting oxygen diffusion (Hoge et al., 1999b).

Like in the brain, spinal neurons require energy supplied by ATP. In their experiment, Marcus *et al.* induced a metabolic response in the lumbo-sacral spinal cord following

stimulation of the femoral and sciatic nerves in dog, lamb and sheep (Marcus et al., 1977). They measured the increase in blood flow using micro-electrodes located in the ipsi- and contra-lateral regions of the white and grey matter. They detected a 50% local increase of blood flow in the ipsi-lateral grey matter, but did not detect any significant blood flow increase in the ipsi-lateral white matter nor in the whole contra-lateral region. The authors therefore concluded that the haemodynamic response following a metabolic stimulus is extremely localized in terms of vascular reaction close to the activated neurons. This observation has been later confirmed by intrinsic optical imaging studies in the cervical cord of rats (Sasaki et al., 2002). Another study did a comparison of the vascular reactivity between the spinal cord and the brain (Nix et al., 1976). Authors measured a brisker vascular response in the cord compared to the brain, under hypercapnia.

SEEP contrast

The signal enhancement by extravascular protons (SEEP) density effect was originally proposed in (Stroman et al., 2001a; Stroman et al., 2001b). Since then, his team and a few other groups have widely supported this theory in various studies and reviews (Kornelsen and Mackey, 2007; Li et al., 2005; Ng et al., 2006; Stroman, 2005). Interestingly, another group suggested the existence of a non-BOLD contrast mechanism based on an increase in water diffusion associated with neuronal firing (Le Bihan et al., 2006).

The hypothesis underlying this new contrast arose from an experiment in which TE was varied to quantify the respective contribution of T_2^* and PD (Stroman et al., 2001b). When extrapolating signal intensity for each voxel at TE = 0 (*i.e.*, to get PD-weighted signal), the authors detected a signal correlated with the paradigm. They supported their finding by quoting past studies in which an increase in ADC, together with neural activity had been detected (Darquie et al., 2001; Le Bihan et al., 2006). This phenomenon was interpreted as an increase of extravascular proton density induced by cellular swelling (Stroman, 2005). The authors then validated this new contrast using various approaches. Among them, they suppressed the BOLD contribution using a 0.2T scanner (Stroman et al., 2003a). They have also studied cellular swelling following activation as a biophysical basis and confirmed the increase of extravascular proton density (Stroman et al., 2008b).

Although very exciting, this technique remains highly controversial. Three studies were not able to reproduce consistent responses using a similar protocol (Bouwman et al., 2008; Jochimsen et al., 2005; Moffitt et al., 2005). Main arguments against the SEEP effect are related to statistical issues (Jochimsen et al., 2005). The method used by Stroman *et al.* to detect activated voxels has been mostly based on temporal correlation analysis, without taking into account physiological-related fluctuations – usually, only linear trends are removed prior to data analysis (Stroman et al., 2004; Stroman et al., 1999; Stroman and Ryner, 2001). It could also be hypothesised that the presence of signal variation related to intravoxel incoherent motion (Le Bihan et al., 1986; Song et al., 2002a) might have contributed to the detection of a task-related signal. Given the great potential of this new contrast for detecting neuronal activity in the spinal

cord, further validation studies seem to be required to make SEEP effect accepted in the community.

Applications in the spinal cord

Originally developed for the brain, fMRI was applied for the first time in the spinal cord at 1.5T using a motor task (Yoshizawa et al., 1996). Since then, it has been applied to the spinal cord of animals and humans for the last twelve years (Lammertse et al., 2007; Stroman, 2005). Such a technological development is of interest in a clinical perspective, namely to determine actual sensorimotor changes in the spinal cord following injury (Kornelsen and Mackey, 2007). Moreover, given the anatomo-functional changes occurring in the injured spinal cord, fMRI would enable longitudinal studies in animals, looking for example at plastic processes leading to locomotor recovery (Frigon and Rossignol, 2006; Rossignol, 2006b).

Previous studies have shown that fMRI can detect motor (Backes et al., 2001; Bouwman et al., 2008; Giulietti et al., 2008; Govers et al., 2007; Komisaruk et al., 2002; Kornelsen and Stroman, 2004, 2007; Madi et al., 2005; Maieron et al., 2007b; Ng et al., 2006; Ng et al., 2008; Stroman and Ryner, 2001; Yoshizawa et al., 1996) and sensory (Brooks et al., 2008; Endo et al., 2008; Lawrence et al., 2004; Lawrence et al., 2008b; Li et al., 2005; Lilja et al., 2006; Mackey et al., 2003; Majcher et al., 2006; Malisza and Stroman, 2002; Moffitt et al., 2005; Porszasz et al., 1997; Stracke et al., 2005; Stroman et al., 2004; Stroman et al., 2005a; Zhao et al., 2008) activation in the spinal cord. Although substantial advances in knowledge have arisen from these studies, the poor reproducibility of the activation patterns and their characteristics – in terms of amplitude and location – have been invoked as significant concerns by several authors (Backes et al., 2001; Bouwman et al., 2008; Brooks et al., 2008; Giove et al., 2004; Govers et al., 2007; Zhao et al., 2008). Similarly to DW-MRI, main difficulties in spinal fMRI arise from the small size of the spinal cord, the presence of large movements due to cardiac pulsation and respiration (Brooks et al., 2008; Figley and Stroman, 2007) and magnetic field inhomogeneities around inter-vertebral disks, which induce significant susceptibility artifacts.

Acquisition parameters

Most studies have used axial orientation with relatively large slice thickness and high in-plane resolution (Backes et al., 2001; Endo et al., 2008; Giulietti et al., 2008; Govers et al., 2007; Kornelsen and Stroman, 2004; Lilja et al., 2006; Madi et al., 2005; Maieron et al., 2007b; Moffitt et al., 2005; Ng et al., 2008; Stroman and Ryner, 2001; Yoshizawa et al., 1996; Zhao et al., 2008). Another strategy is to image in sagittal orientation using isotropic voxels. The latter approach offers the benefits of extensive spinal coverage using only a few slices (Bouwman et al., 2008; Stracke et al., 2005; Stroman et al., 2005a). Also, since BOLD fMRI relies on haemodynamic effects the sagittal approach produces better resolution in the rostro-caudal direction, which is of interest to depict the location of activated clusters. Due to the limited SNR however, one disadvantage of having isotropic voxels is the difficulty to reach high spatial

resolution in the spinal cord cross-section. This is desirable to precisely assess the lateralization of the activation as done in (Lilja et al., 2006; Maieron et al., 2007b; Yoshizawa et al., 1996). Additionally to the BOLD and SEEP contrasts, studies have detected task-related signal in the spinal cord using blood volume measurements in the cat (Zhao et al., 2006a) and in the rat (Zhao et al., 2008). They confirmed previous observations claiming that blood volume has better spatial specificity than that of the BOLD technique (Smirnakis et al., 2007).

Stimulus type

To elicit spinal cord activation, researchers have employed various types of stimulus. We can distinguish two groups of stimulus: passive tasks characterized by sensory activity, and active tasks characterized by motor activity. It is important to distinguish these two types of stimulus since they produce very different patterns of motion artifacts, which are highly problematic in fMRI. Sensory stimuli include skin vibrations, heat and electrical stimuli. Vibrations could be elicited at various frequencies to distinguish activation of Meissner skin receptors (sensitive to low frequencies) from Pacinian receptors (sensitive to high frequencies) (Lawrence et al., 2008b). Tactile stimulations have also been shown to produce robust activation of the cervical cord in humans (Agosta et al., 2007b; Stracke et al., 2005). Similarly, electrical stimulations can be evoked at various intensities to distinguish noxious from non-noxious activity (Lawrence et al., 2008a; Lilja et al., 2006; Zhao et al., 2008). These studies have reported drastic improvement in the reproducibility and sensitivity of BOLD responses, when inducing noxious versus non-noxious stimuli in rats. For motor tasks, people have used fist clenching (Giulietti et al., 2008; Stroman and Ryner, 2001; Yoshizawa et al., 1996), finger tapping (Bouwman et al., 2008; Govers et al., 2007; Maieron et al., 2007b; Ng et al., 2008), tongue tapping (Komisaruk et al., 2002) and lower limb motion (Kornelsen and Stroman, 2004). Although the latter task is of great interest for the study of spinal activity evoked by a locomotor pattern, task-related motion is very problematic and might have induced false positives in the reported activation maps. To better study the locomotor pattern in animal models, one can instead induce fictive locomotion in paralysed animals by the use of pharmacological noradrenergic precursors (l-DOPA) or receptor agonists such as clonidine (Pearson and Rossignol, 1991; Rossignol et al., 1998).

Validation

Evaluating the presence and spatial location of task-related signal is crucial to assess the specificity of activation maps. This can be done using [14C]2-deoxyglucose or c-fos expression mapping. C-fos is an immediate early gene rapidly induced within some neurons upon repetitive stimulations. A mapping of activated neurons is then made possible using immunohistochemistry imaging techniques. Some extensive studies have mapped active neurons during hind limb flexion withdrawal reflex in cats using c-fos expression (Gustafson et al., 2006), and during noxious stimuli in rats using glucose metabolic mapping (Mao et al., 1992; Porro et al., 1991). Other studies validated fMRI results in the rat using c-fos expression (Lawrence et al., 2004; Lawrence et al., 2008a). However, one should always keep in mind that

the BOLD contrast is assumed to detect vascular changes in capillaries and veins, therefore a slight spatial shift of activation maps is expected when comparing c-fos expression with BOLD responses – the latter being more localized in the venous compartment.

Anaesthetic

It is well established that anaesthesia has an impact on the haemodynamic response, shape and timing following neuronal stimuli (Fukuda et al., 2005; Sicard et al., 2003). Although the spinal cord reacts to a large number of anaesthetics (Collins et al., 1995b; De Jong et al., 1968), their specific effects are not fully understood yet. For a review of anaesthetic agents used in the cat, the reader is invited to look at (Jones, 1979; Robertson and Taylor, 2004). Another review on the use of anaesthetics in small animals is provided in (Richardson and Flecknell, 2005).

Halothane and isoflurane are commonly used in animal studies (Antognini et al., 2005). They are inhaled general anaesthetic agents causing hyperpolarization of neurons, inhibition of excitatory synapses and enhancement of inhibitory synapses (Nicoll and Madison, 1982). Isoflurane has well recognized analgesic effects (*i.e.*, pain relief) (Boccara et al., 1998), contrary to halothane (Houghton et al., 1973). Halothane has been used with non-noxious stimulations in the rat (Yamamori et al., 1995) and with graded noxious stimulations in the cat (Namiki et al., 1980). Nitrous oxide (N_2O) is usually mixed with isoflurane, and has been reported to have an impact the cardiovascular system, notably by its vasoconstrictive effects (Pypendop et al., 2003). However, changes in blood volume are highly undesirable when doing fMRI, since basal blood flow – which depends on blood volume – impacts the dynamics of the BOLD signal (Stefanovic et al., 2006; Vazquez et al., 2006). Although the BOLD response has already been detected under isoflurane, its amplitude was drastically reduced (Brevard et al., 2003; Liu et al., 2004; Sicard et al., 2003).

Ketamine, propofol and alpha-chloralose are also commonly used in animals. They are non-opioid intravenous anaesthetic agents. The advantage of intravenous agents for spinal cord fMRI is that their predominant action is at the postsynaptic level, whereas the action of inhaled anaesthetic is at both the pre- and postsynaptic level (Evers and Crowder, 2001). Propofol provides no analgesia in contrast to ketamine (Miner and Burton, 2007; Wright, 1982). Comparing propofol to ketamine in cats, Uchida *et al.* showed that ketamine did not produce any change in responses to non-noxious stimulations (Uchida et al., 1995). Also, ketamine was shown to have little impact on basal blood flow in humans (Abel et al., 2003) and to have relatively low impact on BOLD responses (Rogers et al., 2004). Alpha-chloralose is one of the most commonly used anaesthetics in animals for fMRI studies. One significant advantage of alpha-chloralose is its small effect on neuronal activity and basal blood flow (Ueki et al., 1992). However, it can only be used for acute experiments. One study compared SEEP responses under alpha-chloralose to halothane in the spinal cord (Lawrence et al., 2007). It was shown that both types of anaesthetic give similar responses, although halothane produces slightly higher percent

signal change. Other types of anaesthetic have been used together with fMRI studies, such as opioids (Pattinson et al., 2007) and urethane (Kannurpatti and Biswal, 2004).

Physiological motion

Figley *et al.* have characterized spinal cord motion during heartbeats in the context of fMRI (Figley and Stroman, 2007; Figley et al., 2008). They showed that greatest cord displacement occurs in the A-P direction and therefore suggested to include these motion parameters in the general linear model (GLM, see next section 'Analytical considerations') (Figley and Stroman, 2008). Another study characterized physiological-related noise in the human spinal cord (Brooks et al., 2008). Authors of this study reported the presence of cardiac and respiratory fluctuations as well as a combination of both effects giving rise to very low frequency fluctuations. These low frequency fluctuations may arise from the so-called Mayer waves[5]. J. Brooks *et al.* suggested to include external recording of physiological parameters in the design matrix of the GLM as in the RETROICOR method (Glover et al., 2000). They demonstrated the benefits of this analytical approach to robustly detect BOLD responses in the human spinal cord (Brooks et al., 2008).

Analytical considerations

Widely used in the neuroimaging community, the general linear model (GLM) is implemented in freely available software such as SPM (Friston et al., 1994a) and FSL (Smith et al., 2004). The principle behind the GLM is to perform a linear regression using a repertoire of functions that are assumed to model fMRI time series. It then allows to statistically test the contribution of each regressor, at every voxel of the volume series. The physiological counterpart of this statistical test is that neuronal activity – which is temporally controlled – induces a local change in the haemodynamic steady state, giving rise to the BOLD signal. Let us denote by Y the measured data (*i.e.*, the time course of an MRI voxel), by X a time series describing the response to an experimental paradigm (*e.g.*, the paradigm convoluted to an assumed haemodynamic response function), by β the amplitude of that response, by D a matrix modelling the structured background signal with contribution λ, and by e the residuals. The signal Y can be modelled as follows

$$Y = \beta \cdot X + \lambda \cdot D + e \tag{2.4}$$

Given the following inference, one can compute a T-score defined by the estimated β and the standard deviation of e. In this model, one assumes that the term e is independent and identically normally distributed (i.i.d.). If e was not i.i.d., the variance of the estimator would be underestimated, thus leading to a biased T-score and therefore altering activation detection sensitivity (Dagli et al., 1999; Lund et al., 2006). In the case of spinal fMRI, cardiac signal

[5] Mayer waves are oscillations of arterial pressure occurring spontaneously in mammals at a frequency of about 0.1 Hz in humans (Cohen and Taylor, 2002; Julien, 2006; Mayer, 1876).

significantly contributes to the total variance of time series (Brooks et al., 2008). Hence, when modelling *Y* with the GLM one has to take cardiac signal into account, otherwise residuals *e* would include cardiac fluctuations leading to coloured residuals, *i.e.*, there would be temporal autocorrelations within residuals leading to a biased T-score. As mentioned in section 'Physiological motion', one possibility is to model physiological fluctuations using the RETROICOR method. It is also possible – although less accurate – to account for autocorrelations using autoregressive filter (Friston et al., 2000).

Contrary to brain fMRI studies, not the majority of published articles on spinal cord fMRI were conducted using the GLM (Agosta et al., 2008; Backes et al., 2001; Bouwman et al., 2008; Brooks et al., 2008; Endo et al., 2008; Giulietti et al., 2008; Govers et al., 2007; Li et al., 2005; Lilja et al., 2006; Madi et al., 2005; Maieron et al., 2007b; Ng et al., 2006; Ng et al., 2008; Stroman, 2006; Valsasina et al., 2008). Instead, many studies were conducted using cross-correlation following linear trends removal (Kollias et al., 2004; Kornelsen and Stroman, 2004, 2007; Lawrence et al., 2004; Lawrence et al., 2008a; Lawrence et al., 2008b; Malisza and Stroman, 2002; Stroman, 2005; Stroman et al., 2004; Stroman et al., 2005a; Stroman et al., 2005b; Stroman et al., 2001a; Stroman et al., 2001b, 2002a, b; Stroman et al., 2008b; Stroman et al., 2003a; Stroman et al., 1999; Stroman and Ryner, 2001; Stroman et al., 2002c, 2003b; Stroman et al., 2003c). No physiological-related modelling was done, which may have led to biased correlation coefficients. Moreover, the statistical significance of activations was not always reported and if it was, no correction accounted for the number of voxels included in analysis. Therefore this analytical technique may have led to a large number of false positives as shown in the reported activation maps using the BOLD (Stroman et al., 1999) or the SEEP contrast (Stroman et al., 2002a).

No group study has been extensively conducted in spinal cord fMRI yet. The first issue is that no consensual template has been available so far, preventing the use of a normalization procedure as usually done in the brain (Friston et al., 1995). However, one recent study provided the first template of the human cervical spinal cord, based on the averaging of eight normal subjects (Stroman et al., 2008a). The normalization procedure using this template consists in straightening the cord using manual delineation of the central canal, followed by an homothetic transformation in the R-C direction to account for vertebras' size variability among subjects. Although this method needs more subjects to be included in the template model and requires careful aging considerations (*i.e.*, the correspondence between spinal and vertebral levels evolves with aging), it is a significant step towards the routine use of group analyses in spinal cord fMRI.

Spinal cord activity following injury

Using a model of thoracic lesions in a rat, a study conducted at 4.7T demonstrated an increase of activity in the dorsal horn, caudal and ipsi-lateral to a thoracic lesion (Endo et al., 2008). Another study performed in the rat at 9.7T demonstrated a decrease of BOLD percent signal change in the spinal cord following the section of peripheral nerves (Majcher et al.,

2007). In addition to these animal studies, Kornelsen *et al.* detected the presence of spinal cord activation below the site of cervical and thoracic injury (Kornelsen and Stroman, 2007) and Stroman *et al.* investigated the presence of activation in spinal cord injured patients using noxious stimuli (Stroman et al., 2004; Stroman et al., 2002c).

3. Rationale

Synthesis of past studies

Looking at the literature on DW-MRI of the spinal cord, most methods have been developed in humans. However, many studies have involved rodents in which some challenges were more easily overcome or controlled (*e.g.*, through mechanical ventilation, implanted coils). Also, the use of animal models allows the investigation of the impact of experimental lesions in longitudinal studies. Some animal studies described ADC characteristics at the site of experimental lesions (Deo et al., 2006; Kim et al., 2007a; Krzyzak et al., 2005; Schwartz et al., 1999) while others investigated the impact of cellular intervention after SCI (Nevo et al., 2001; Schwartz et al., 2005a; Schwartz et al., 2003). One important finding is that ADC values correlate with the degree of white matter integrity (Deo et al., 2006; Schwartz et al., 2005d). Although encouraging results arose from this literature, DW-MRI of the injured cord is recent and requires more investigation (Deo et al., 2006; Maier and Mamata, 2005; Tsuchiya et al., 2005).

Conversely, fMRI of the spinal cord appears to be much more problematic than that in the brain (Bouwman et al., 2008; Giove et al., 2004; Govers et al., 2007; Stroman, 2005). Most published studies were conducted using non-standard methodologies including the SEEP contrast and cross-correlation analyses. Furthermore, the use of masking in many studies prevents assessment of the spatial specificity of the reported activations. Given that masks were essentially drawn over the spinal cord, it was not possible to assess the number of false positives in a region outside of the spinal cord, *i.e.*, where neuronal activation was unlikely to occur. Although automatic masking procedures have been widely admitted in brain studies, their use is problematic in the spinal cord where assessment of false positives is needed as a validation tool in non-standard experimental setups. In addition to the SEEP studies, some BOLD-based investigations reported successful results although the robustness of the activation remained problematic (Brooks et al., 2008; Giulietti et al., 2008; Lilja et al., 2006; Maieron et al., 2007b; Zhao et al., 2008). It seems worth understanding why detecting the BOLD effect is so challenging in the spinal cord, given that this technique has been successfully used by neuroscientists in other regions of the central nervous system for the last 18 years.

Objectives

Although significant contributions have arisen from past studies, further improvements are still needed. In this thesis the main objectives were to develop optimal strategies for conducting DW-MRI and fMRI in the spinal cord of healthy and spinal cord injured mammals, as will be detailed hereafter.

In spinal cord DW-MRI, a major objective was to robustly detect and accurately localize the loss of white matter tissue following spinal cord lesions. A direct corollary of this objective would be to correlate physiological impairments with the number and type of axonal pathways that have been damaged, as observed using DW-MRI. Although previous studies have already demonstrated the proof-of-principle to obtain satisfactory images as well as to detect spinal lesions using DW-MRI, limitations in image quality and in animal preparation ask for further improvements. These improvements were focused on the following aspects: using a 3T MRI system with clinical-compatible setup, optimization of coils (*e.g.*, birdcage versus phased-array coil, number and types of elements to use), subject positioning, type of sequence, acquisition parameters (for optimal SNR, susceptibility effects, physiological motions, Eddy currents), data processing (*e.g.*, motion correction, susceptibility-induced distortions, regularization methods for tensor fields, HARDI reconstruction) and interpretation of results (*e.g.*, anisotropic change within lesions, partial volume issues, modelling issues, motion-induced biases in reporting quantitative anisotropic measurements). These objectives have been addressed in the following article:

- Article #1: In vivo DTI of the healthy and injured cat spinal cord at high spatial and angular resolution.

Moreover, it has been shown that DTI can retrieve major longitudinal pathways, *i.e.*, axon bundles oriented in the rostro-caudal direction. However, other types of fibres not oriented longitudinally are also present in some parts of the cord. These are for instance commissural fibres coursing in the medio-lateral direction, and dorso-ventral fibres that may originate from dorsal root afferents or terminal fibres of descending tracts. Since the diffusion tensor can only account for a single principal diffusion direction, these pathways may not be visible using DTI (Hagmann et al., 2006). Furthermore, after lesions or in the presence of tumours or cysts tracts can be displaced so that they are no longer following a longitudinal direction. In the following article, we applied the QBI technique in both *in vivo* and *ex vivo* feline spinal cord. We showed that QBI can recover longitudinal pathways as DTI does, but can also recover medio-lateral and dorso-ventral directions which are consistent with the known architecture of the spinal cord. This study is detailed in the following article:

- Article #2: Detection of multiple pathways in the spinal cord using q-ball imaging

At the beginning of this thesis, the ultimate goal of fMRI was to quantitatively assess change in spinal cord activation following injury. Also, at a more fundamental scale, one goal was to be able to use fMRI as a tool to study the specific nervous levels involved in the control of the locomotion in mammals. However, given the poor reliability of fMRI in the spinal cord the two abovementioned applications needed some preliminary studies to gain more confidence in this technique. In addition, few methodological developments were dedicated to spinal fMRI, including data acquisition and processing, identification of physiological-related noise and validation of neuronal activation. The present project aimed to investigate these issues and to

make new methods available for the research community. More fundamentally, we have also sought a better understanding of the functional relationship between neural activity, energy metabolism and haemodynamic change in the spinal cord. Therefore, in this thesis we aimed to characterize fMRI activations in the cat spinal cord. We have evoked simple spinal reflexes in anaesthetized cats while measuring the BOLD response in a 3T MRI system. The details of the developed methodology and outcomes are provided in the following article:

- Article #3: Investigations on BOLD signal in cats under ketamine

Methodology

Animal preparation

Cats were used in this project. Experiments were conducted in accordance with the Ethical Committee of the Université de Montréal. Animal preparation was achieved by Dr. Janyne Provencher, Dr. Hugues Leblond, Dr. Grégory Barrière and Dr. Alain Frigon at the GRSNC, Physiology Department, Université de Montréal. Most cats were implanted chronically with electrodes to record activity in various hind limb muscles. Care was taken to lead the wires subcutaneously from the head to the hind limbs as laterally as possible to minimise magnetic field inhomogeneities around the vertebral column that can induce geometric distortions and signal loss in EPI data.

For the purpose of DW-MRI, experimental lesions were induced using a micro-knife after unilateral or bilateral laminectomy. In the case of complete section of the cord, the gap between the rostral and caudal parts of the cord was filled with a haemostatic agent (Surgicel®). For the work presented here, three cats received a partial lesion at T11 level, followed by a complete lesion at T13 level one month after. Between both surgical events, cats were daily trained to walk on a treadmill for improving their locomotor rehabilitation (Barbeau and Rossignol, 1987; Barriere et al., 2008). Illustration of complete and partial lesions in one cat is provided in Figure 3.1. One could appreciate the benefits of anatomical MRI for assessing the extent of the lesion non-invasively.

For fMRI experiments, five cats were chronically implanted with *in situ* polymer cuff electrodes around either the superficial peroneal nerve innervating the dorsum of the foot, or the tibial nerve innervating the plantar surface of the foot. Four other cats were implanted with subcutaneous electrodes on the dorsal aspect of the hind feet. During fMRI experiments, all cats were first anaesthetized with isoflurane, then anaesthetic was switched to ketamine. Although alpha-chloralose is one of the commonly used anaesthetics in fMRI studies, we used ketamine so as to keep cats alive after experiments. The stimulation threshold was estimated after positioning the cat in the scanner to avoid any electrode displacement. By varying the stimulation intensity, we evaluated the threshold current needed to evoke a twitch, usually by palpation of the knee flexor muscle semitendinosus. This value was then used as a reference

stimulus (threshold) for each cat. Following stimulus threshold evaluation, cats were paralyzed with pancuronium and ventilated mechanically. End tidal CO_2 was continuously monitored via the output of the endotracheal tube.

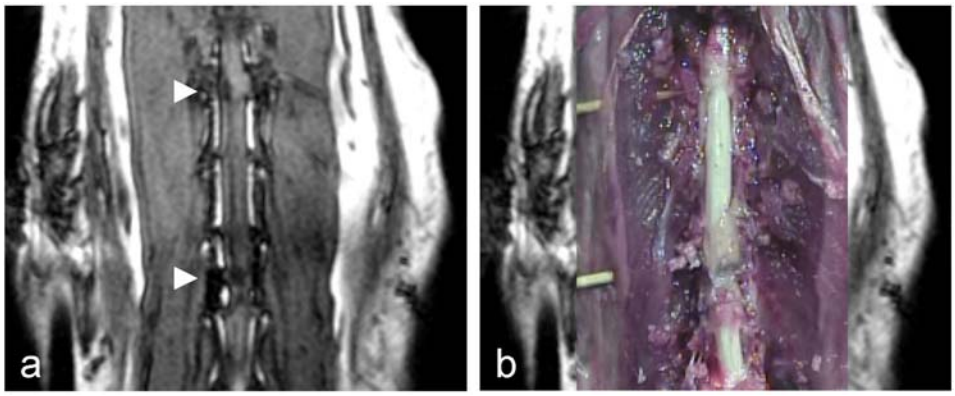

Figure 3.1. Complete and partial lesion on a cat
a: Coronal T_1-weighted (MPRAGE) anatomical image showing both complete (bottom arrow) and partial left (top arrow) lesions, performed at T13 and T11 respectively. **b:** Picture of the same cat during dissection showing actual lesions location (picture is overlaid on the anatomical MRI).

Ex vivo spinal cord

For the purpose of QBI, three biological phantoms were created. They were made up with lumbar spinal cords of cats. Although biological samples are usually fixed with formaldehyde, excised spinal cords were not fixed in that case because this chemical process induces a significant decrease of transverse relaxation time in the white matter (Carvlin et al., 1989; Pfefferbaum et al., 2004). We indeed tried to image a fixed spinal cord sample with the minimum TE achievable (~90 ms) and no or few signal was detected in the white matter. Therefore we put the following extracted spinal cords in saline solution (0.9%). Thirty minutes after extraction, each cord was placed into a gelatine solution (6%). It was imaged five hours later. An illustration of the spinal cord in gelatine is provided in Figure 3.2.

The choice of gelatine versus agarose was guided by the following considerations. First, the gelatine melting point is located at around 40°C versus 85°C for the agarose. The latter temperature could have been harmful to spinal cord tissues. Second, there are less air bubbles with gelatine – when properly prepared. Air bubbles could be problematic because they induce magnetic field inhomogeneities therefore producing distortions in EPI data. Gelatine was prepared as follows: 36 g of gelatine (Vyse, 6%) was poured into 600 mL of cold water and 2 g of ethylenediaminetetraacetic acid (EDTA) (5 mMol/L) was added for conservation purpose. It had been warmed while continuously stirring the container for removing air bubbles. The gelatine was then poured over the spinal cord – which was kept in suspension using two cords. The whole recipient was then put in a regular fridge for four hours.

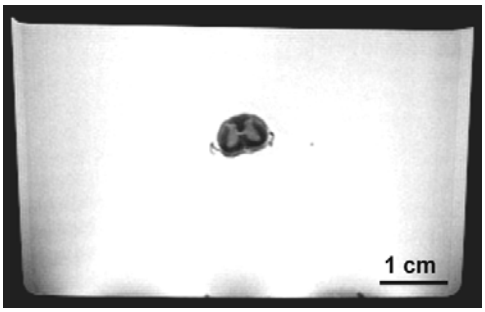

Figure 3.2. Ex vivo spinal cord in gelatine
Axial view of a PD-weighted image showing the spinal cord phantom. Large distance between the cord and the gelatine-air interface was allowed to limit susceptibility effects in the central region when using EPI sequences.

DW-MRI acquisition

All data were acquired on a Siemens Trio system (Erlangen, Germany). During this three years project, the system was upgraded from Syngo version VA25 to VB15. This notably yielded more channels (32 versus 8) and new types of coil (*e.g.*, a flexible body matrix particularly suitable for spinal cord imaging). Regarding cat positioning and acquisition parameters that gave optimal data quality, an exhaustive guideline describing all steps to follow is provided in Appendix A. In the following we will review some of the methodological points that require further explanations. We used the standard SE-EPI sequence provided by Siemens. Although cardiac gating has been suggested to reduce ghosting artifacts (Summers et al., 2006), the relatively high cardiac frequency in cats (~2 Hz) compared to that in humans (~1 Hz), the irregularity of cardiac frequency due to the anaesthetic state, and the high TR and number of slices made it difficult to apply this technique within a reasonable scan time for anaesthetised animals. However we have been using respiratory gating for the late acquisitions. The reason is that the DW-MRI protocol includes acquisition in the thoracic regions, which is prone to large susceptibility artifacts due to the presence of the lungs. Those inhomogeneities induce off-resonance during slice selection, which in turns produce significant signal loss (see Figure 3.3). Lately, we have used respiratory gating by recording MR signal during the expiration phase only, aiming at limiting the volume of air in the close region. Not only did this approach enable to limit motion-related artifact (*e.g.*, ghosting), but it was highly beneficial for limiting signal loss in the thoracic region (see Figure 3.4). Depending on the cat size in the A-P direction, we used a saturation band to avoid aliasing due to the limited FOV in the phase encoding direction – note that we used a reduced FOV to limit the number of phase lines in the k-space, thus reducing susceptibility artifacts. Looking at past studies, we chose to acquire isotropic voxels for two main reasons. The first was to avoid any prior regarding orientation of axonal tracts. The second reason was related to the conditions prevailing in spinal cord injury. If data were averaged along several millimetres in the axial direction using highly anisotropic voxels, a transverse low-width lesion would have not been detected. We acquired most DW data with relatively large number of directions (64) and with a high b-value (1000 s/mm^2) to adequately reconstruct the ODF.

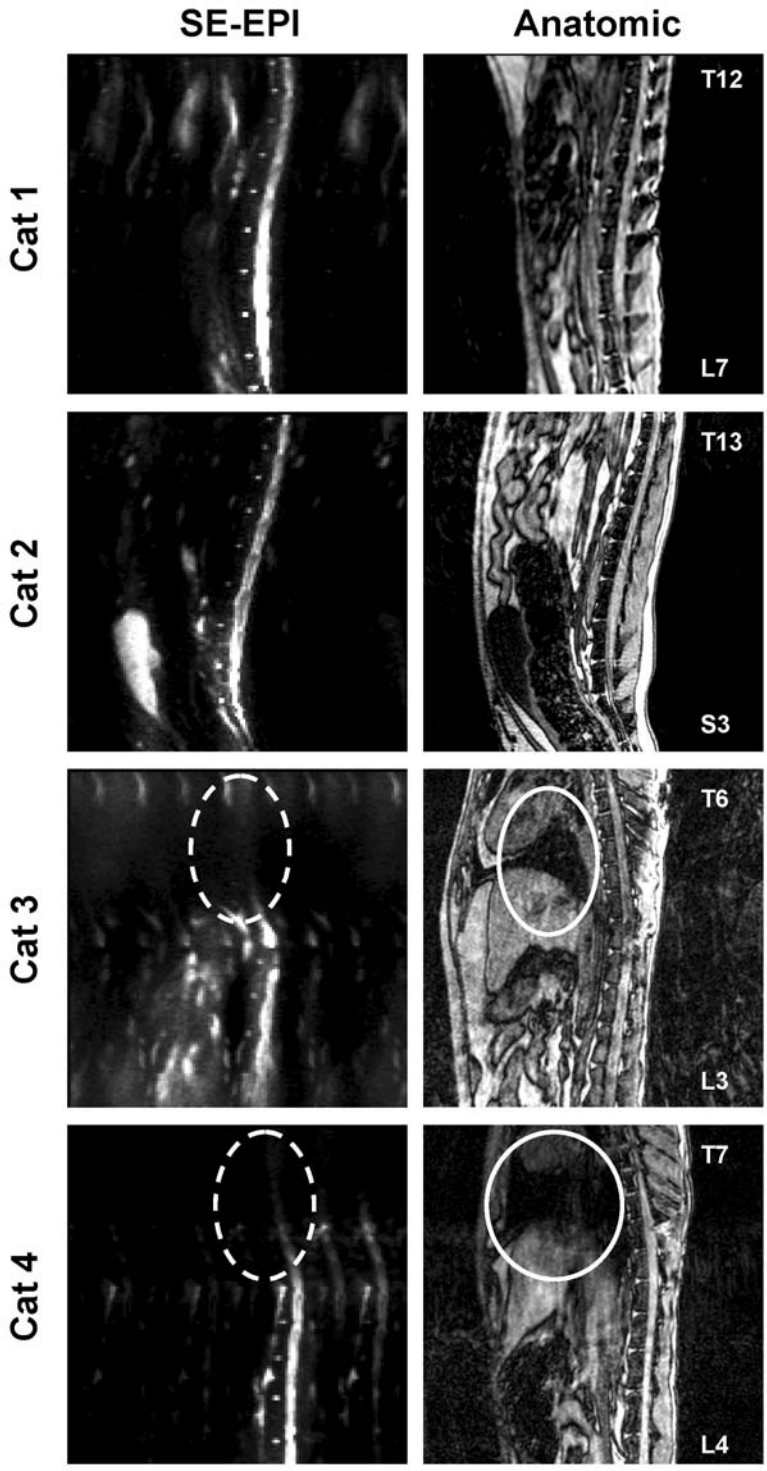

Figure 3.3. Susceptibility artifacts in the thoracic region

This figure illustrates susceptibility-related signal loss in the thoracic spinal cord using SE-EPI sequence (iPAT4 with phase-encoding A-P). The two last cats demonstrate signal loss in the thoracic region (dashed ellipses), which corresponds to a region close to the lungs (continuous ellipses). Signal loss was probably due to off-resonance effect during slice excitation.

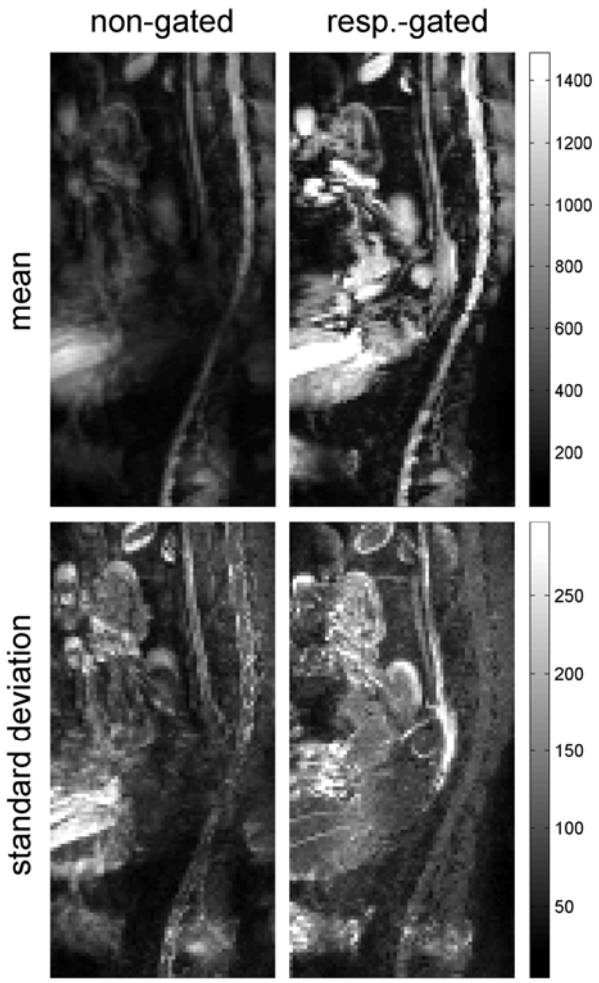

Figure 3.4. Benefits of respiratory gating
Mean and standard deviation computed from time series acquired without and with respiratory gating (same colour scaling). Acquisition was done with the following parameters: PACE sequence, sagittal orientation, TR / TE = 750 / 18 ms, flip angle = 50°, slice thickness = 2 mm, in-plane resolution = 1.5×1.5 mm^2. One can observe a much higher signal in the cord when acquisition is in phase with the respiratory cycle.

To correct for susceptibility artifacts three different methods have been evaluated. Given that most methods were essentially validated using brain data, it is likely that they do not produce similar results in the spinal cord since the latter exhibits significantly larger B_0-field inhomogeneities. Hence, we acquired non-DW FSE images for using the non-linear warping algorithm proposed by S. Ardekani *et al.* (Ardekani and Sinha, 2005). We also acquired EPI using the same matrix and FOV, but with phase encoding gradients switched by 180°. Those scans were used with the method proposed by H. Voss *et al.* (Voss et al., 2006). As a standard way for correcting geometric distortions, we acquired a phase field-map to estimate the actual B_0-field deformation (Cusack et al., 2003). All these approaches required an extensive programming part in MATLAB, especially the reversed gradients method for which there was no existing code in this language. An illustration of the benefits of the reversed gradient method for correcting susceptibility effects is provided in Figure 3.5.

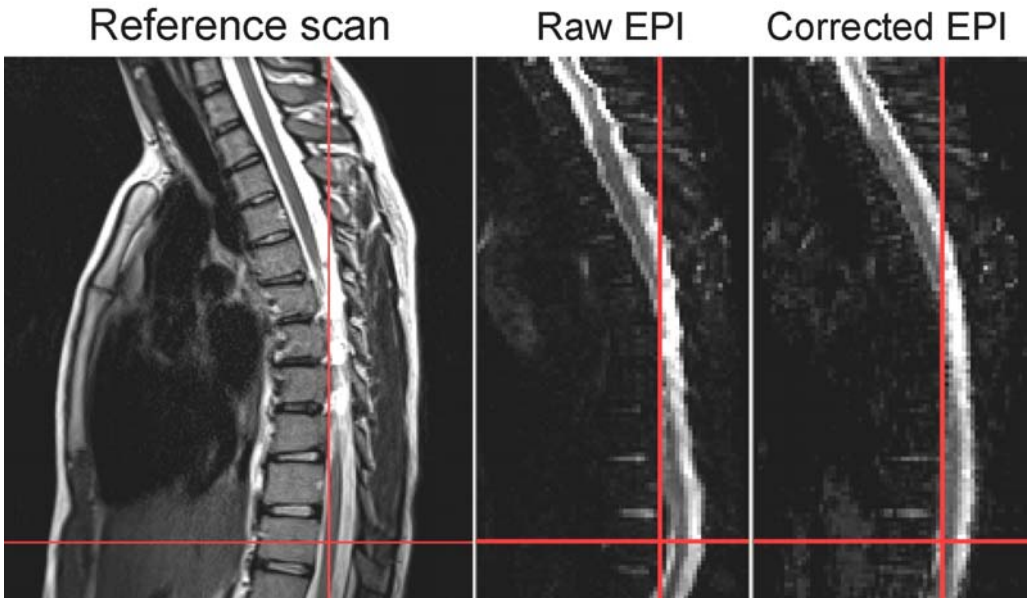

Figure 3.5. Distortion correction using the reversed gradient method
This figure shows results of the reversed gradient method applied to T_2-weighted EPI in the human thoraco-lumbar spinal cord. A reference scan (FSE, left panel) is compared to the raw (middle panel) and corrected EPI (right panel). Phase encoding was A-P.

DW data processing

Following image reconstruction, DICOM data were pre-processed using a custom MATLAB script. This program allows (i) converting mosaic DICOM images to Analyze file format, (ii) to average images respectively to their diffusion-weighting direction[6], (iii) to generate a text file which contains a list of gradient vectors and (iv) to correct the generated gradient list using patient orientation information contained in the DICOM header. The latter process is needed because the gradient vector provided in the DICOM header is in absolute coordinates, therefore it should be corrected if the FOV is tilted – which was often the case in such unorthodox acquisitions. Note that no motion correction was applied for two reasons. First, cats were anaesthetized and motionless in the scanner (except of course passive motions related for instance to the respiration). Second, the relatively low SNR in DW data would have yielded non robust estimation of the rigid-body transformation matrix.

To estimate the diffusion tensor we used the freely available software MedINRIA[7]. Instead of performing the regression in the classical Euclidean space, tensors were computed into the log-Euclidean space which presents the same properties as the affine-invariant family

[6] Instead of using the index of image files, averaging was based on the automatic identification of DW images using their respective DICOM header containing the gradient vector. This was made because some pulse sequence did not respect the gradient list that was provided by Siemens. Moreover this procedure allowed more flexibility for removing DICOM images hampered by all sorts of artifacts (*e.g.*, motion or spiking artifacts).
[7] http://www-sop.inria.fr/asclepios/software/MedINRIA/

but is computationally faster. A Riemannian framework was used assuming Rician noise. This approach presents some advantages, notably for the regularization of tensors in noisy datasets (Arsigny et al., 2006). The tractography algorithm was based on this tri-linear log-Euclidean interpolation and used a standard streamline algorithm (Xu et al., 2002). The tractography procedure was automatic, since every voxel of the reference volume was a seeding point (Fillard et al., 2006).

Tractography was conducted by isolating various regions of interest (ROI) based on the axial view of the PD-weighted volume. Those ROIs were selected in the white matter to isolate various pathways. For the identification of the dorsal and ventral columns, we first extracted all bundles included in the dorsal and ventral part of the cord, respectively. Then, a second ROI was defined for every spinal level, from T12 to L4, left and right. This procedure specifically allowed the identification of the dorsal and ventral columns. For the identification of other tracts, we created an ROI box that we moved around the axial view of the PD volume. The box size was approximately $1.5 \times 1.5 \times 1.5$ mm^3. For either lateral side, we moved the box over two different regions which included the corticospinal tract (CST), the dorso-ventral spinocerebellar tract (SCT), the rubrospinal tract (RST) as well as the spinothalamic tract (STT).

For assessing change in DTI indices at the site of spinal cord injuries we compared various regions of the cord as done by others (DeBoy et al., 2007; Deo et al., 2006). ROIs were manually selected on the left and right side all along the spinal cord. To demonstrate the statistical difference between healthy and injured tissues, we performed a Student's T test based on the robust median (Rousseeuw and Croux, 1993). The median of all FA values was first estimated. Then, the standard deviation centred on the median was calculated. The null hypothesis assessed that population of FA values was homogeneous. We compared each point to the robust median and aberrant points were rejected given two P-value thresholds (95% and 99%). Then, we made a correspondence between aberrant points and their location along the healthy and injured part of the cord.

To reconstruct the ODF based on HARDI measurements we used the method developed by M. Descoteaux *et al.* (Descoteaux et al., 2006, 2007a). It is based on the spherical harmonics (SH) decomposition and enables to retrieve the so-called fibre ODF (*i.e.*, sharp version of the diffusion profile).

FMRI acquisition

Cats were positioned feet first supine. We investigated both the use of a single-channel human knee coil – which provides better homogeneity – and the use of an 8-channel spine array coil – which provides better sensitivity in the spinal cord. Anatomical scans were conducted using a 3D MPRAGE sequence, and functional times series were acquired using a 4-shot GE-EPI sequence. No parallel imaging was used for fMRI scans because the SNR was much lower than that with 4-shots EPI. Moreover parallel imaging was not feasible using the single channel knee coil. Sagittal slices were selected over the whole lumbar spinal cord. Given the

relationship between vertebral and spinal levels, activation was expected primarily at vertebral level L4 and L5. However, recording of the whole lumbar cord allowed us to assess the spatial specificity of the activation by looking at the mean activation at other levels. Also, we chose to image using isotropic voxels at a resolution of $2\times2\times2$ mm^3 to limit partial volume effects along the R-C axis.

A typical fMRI acquisition included 5 sequences of 2 minutes (1 minute of rest and 1 minute of stimulations). Although characterization of the haemodynamic response requires event-related stimuli, we used block design to increase the sensitivity to detect BOLD signal. High intensity electrical stimulations were found to evoke much detectable BOLD signal (Lawrence et al., 2008a; Lilja et al., 2006; Zhao et al., 2008), however we aimed at showing the feasibility of detecting low-level stimuli. Going back to the original context of this work, one motivation was the ability to detect lumbar activity evoked by fictive locomotion in the scanner. This physiological state could be elicited by the use of pharmacological agents and is of great interest for studying the detailed activity of the central pattern generator in chronic spinal cord injury model (Pearson and Rossignol, 1991). Stimulation intensity was therefore twice the activation threshold – evaluated for each cat before pancuronium. Hence, only A-fibres (Aα, Aβ) giving rise to non-noxious stimuli were expected to activated. On the contrary, C-fibres and Aδ fibres which are known to give rise to noxious stimuli were probably not activated at this electrical intensity.

FMRI data processing

Since spinal fMRI time series are not common in the neuroimaging community, the first step was to investigate spatiotemporal properties of such data. For that purpose we used spatial ICA (Cohen-Adad et al., 2006b). This multivariate and data-driven technique enables to spatially and temporally map functional dataset in a given number of components (Bell and Sejnowski, 1995). This is a linear procedure which assumes the spatial independence between each component. It has already been applied to fMRI for the identification of BOLD and other physiological-related structured signals (Calhoun et al., 2001; McKeown et al., 1998). The disadvantage of using ICA however is the impossibility to infer classical hypothesis tests to statistically confirm – or infirm – the presence of any task-related activation (Hu et al., 2005).

To detect and to quantify the haemodynamic response evoked by neuronal activity, we conducted a statistical analysis using the GLM approach. We used the SPM2[8] package with some custom modifications described hereafter. Pre-processing steps included (i) correction for timing errors related to the duration of each slice acquisition within a volume (slice timing) (ii) realignment of functional series to limit the effect of subject motion, (iii) and spatial smoothing of functional series by convolving them with a 2-D Gaussian kernel (FWHM = 4 mm). At step (ii), an appropriate rigid-body realignment was conducted by estimating the transformation matrix based on specific voxels as proposed in (Cohen-Adad et al., 2007g; Stroman et al.,

[8] http://www.fil.ion.ucl.ac.uk/spm/

2004). These voxels were selected over the spine but not in regions which are prone to strong physiological motions, such as in the kidneys and in the air-abdomen interface. Processing of fMRI time series involved a design matrix including cosine drifts (high pass filtering with cut-off at 0.008 Hz) and a 1st order autoregressive model to account for autocorrelations mostly induced by cardiac fluctuations. The regressor of interest was built by convolving the block design matrix with the default canonical haemodynamic response function provided by SPM. This parametric function made of two gamma functions peaks at 6 s and does not include an initial undershoot. Note that part of SPM code has been modified to prevent the software from automatically generating a mask based on the intensity of voxels, which works fine for the brain but not for the spinal cord (this automatic procedure can eliminate voxels close to or within the spinal cord). GLM analysis was therefore conducted within a mask which included not only the spinal cord but also the surrounding fat, the CSF, the spine and adjacent muscles. This large mask enabled to assess the spatial specificity of the activation by examining the number of false positives in regions where no activation was expected to occur, as done previously (Zhao et al., 2008).

Group analysis was conducted between runs, for each cat individually. Fixed-effect analysis was chosen, assuming homoscedasticity in fMRI time series between runs, *i.e.*, the variance of residuals was similar between runs because the cat and the experimental protocol were the same within each group. Hence, we only considered the first level statistic (only intra-run variance was considered). The mean global effect was Student distributed, which allowed testing the null hypothesis. Note that both physiological and system variability were expected to occur within cats, justifying choosing another approach such as the random-effect analysis. Nevertheless, the high sensitivity of fixed-effect plus some preliminary results obtained using random-effect analysis and T-maps average (Lazar et al., 2002) guided our decision.

To evaluate whether the spinal cord showed a spatially consistent pattern of activation, percent signal change has been quantified using ROI selected in the spinal cord at each vertebral segment of the lumbar cord. For that purpose, Student's T-tests were conducted by comparing averaged activations between each adjacent pairs of vertebral levels. To quantify the variability of BOLD response over time, an individual ROI was obtained for each cat by thresholding T-maps obtained from the fixed-effect analysis. Percent signal change was then quantified in each ROI to study the evolution of functional activation across time.

An original contribution to this project was the quantification of static SNR (SNR_0) and temporal SNR (tSNR) in spinal fMRI time series. Previous studies have shown that SNR_0 and tSNR have a significant impact on the sensitivity to detect BOLD activations (Bellgowan et al., 2006; Bodurka et al., 2007; Parrish et al., 2000; Triantafyllou et al., 2005). Therefore, we quantified both noise parameters to evaluate the ability to detect BOLD signal in the spinal cord versus in the brain. Computed measurements were compared with those reported in the literature (Triantafyllou et al., 2005), after adjusting for flip angle and voxel size using simple regressions. It is worth comparing SNR of fMRI dataset in various conditions since BOLD effect is proportional to the baseline signal. Hence, showing differences in the brain versus in

the spinal cord would help to understand the difficulties in finding significant activation in spinal cord fMRI.

Another original contribution was the measurement of basal CO_2 level, and its correlation with the BOLD response. Given that fMRI signal reflects changes in blood oxygenation, blood flow and blood volume, this relative measurement is highly sensitive to the basal vascular state (Stefanovic et al., 2006; Wise et al., 2004). There are many factors that impact the basal state, such as anaesthetics, respiration rate and blood pressure (Sicard et al., 2003). To address possible effects related to blood gas level, end-tidal CO_2 was recorded for each run and each session. The tube directed to the mechanical ventilator was split, and the second extremity was connected to an acquisition system which converted gas pressure into digital values (Datex Normocap 200, Denver, USA). A custom MATLAB program detected CO_2 peak levels and averaged them for each run. Mean CO_2 levels were then compared to the mean percent signal change using a least square-based linear regression. A Fisher F-test was then performed to test the linear relationship between these two parameters.

4. Article #1: In vivo DTI of the healthy and injured cat spinal cord at high spatial and angular resolution

J. Cohen-Adad[1,2,3,4], H. Benali[2,3], R.D. Hoge[3,4] and S. Rossignol[3,4]

[1]*Groupe de Recherche sur le Système Nerveux Central, Department of Physiology, Faculty of Medicine, Université de Montréal, Montreal, QC, Canada*
[2]*INSERM U678, Université Pierre et Marie Curie (Paris VI), CHU Pitié-Salpêtrière, Paris, France*
[3]*Unité de Neuroimagerie Fonctionnelle, CRIUGM, Université de Montréal, Montreal, QC, Canada*
[4]*Institute of Biomedical Engineering, Department of Physiology, Faculty of Medicine, Université de Montréal, Montreal, QC, Canada*

Published in NeuroImage. Received 2 August 2007; revised 2 November 2007; accepted 13 November 2007; Available online 3 December 2007

Preface

The purpose of this article was the development of a methodology for imaging the spinal cord of cats in a 3T scanner at high spatial resolution. The method notably focused on a mean to correct susceptibility artifacts during post-processing, as well as on the identification of anatomical pathways in the spinal cord white matter using the so-called 'selective tractography' method. This article also provides measurements of FA in the healthy and injured spinal cord of cats. This work has been published in NeuroImage (Cohen-Adad et al., 2008b). Part of methodological developments with more emphasis in characterization of artifacts has been published in the French journal IRBM (Cohen-Adad et al., 2008a). This work has also been published as a short article in conference proceedings (Cohen-Adad et al., 2007d; Cohen-Adad et al., 2008i) and in abstract forms (Barrière et al., 2008; Cohen-Adad, 2008; Cohen-Adad et al., 2007a; Cohen-Adad et al., 2007b, c; Cohen-Adad et al., 2007f). My contribution to this article was to develop the methodology, to acquire the data, to process the data and to write the article. Co-authors of this article and their individual contribution are listed hereafter:

Habib Benali is my co-supervisor and has been involved in providing useful comments on data processing.

Richard D. Hoge has provided useful comments on MRI acquisitions.

Serge Rossignol is my co-supervisor and has been involved in actively reviewing the manuscript as well as in providing useful comments on neurophysiology.

Abstract

Spinal cord diffusion tensor imaging (DTI) is challenging in many ways: the small size of the cord, physiological motion and susceptibility artifacts pose daunting obstacles to the acquisition of high-quality data. Here, we present DTI results computed from in vivo studies of the healthy and injured spinal cord of five cats. Both high spatial (1.1 mm^3) and angular (55 directions) resolutions were used to optimise modelling of the diffusion process. Also, particular effort was directed towards a strategy that limits susceptibility artifacts. For validation purposes, acquisitions were repeated in two cats before and after making a spinal lesion. As a result, various axonal trajectories were identified by tractography including dorsal and ventral columns as well as lateral tracts. Also, fibre bundles showed robust disruption at the site of spinal cord injuries (partial and complete) via tractography, accompanied with significantly lower fractional anisotropy values at the site of lesions. Important outcomes of this work are (i) tractography-based localisation of anatomical tracts in the thoraco-lumbar spinal cord and (ii) in vivo assessment of axonal integrity following experimental spinal cord injury.

Keywords: Spinal cord, Thoracic, Lumbar, Injury, MRI, DTI, Tractography

Introduction

Spinal cord injury (SCI) induces motor (paralysis) and sensory deficits through the disruption of specific ascending and descending spinal pathways. These deficits evolve in time as a reorganisation of the central nervous system occurs, both at local and supraspinal sites. Such functional compensation may involve various anatomical, physiological and neurochemical mechanisms that are still under investigation (Rossignol, 2006b). For instance, there may be regeneration of damaged axons or collateral sprouting of axons in spared descending/ascending pathways or primary afferents (Kerschensteiner, 2007). These new growths can project through different spinal paths as they are forming new circuits and adopt unpredicted trajectories as they by-pass the scar tissue (Bareyre et al., 2004; Fouad and Pearson, 2004). Both the severity of the deficit and the successful rehabilitation process depend on the type and number of axonal tracts that have been altered, as well as changes in the intrinsic properties of the spinal cord. Hence, it may be of great interest to assess the white matter integrity at the site of a lesion, to identify anatomical tracts that have been damaged and possibly image the trajectory of new pathways as they evolve.

Magnetic Resonance Imaging (MRI) provides the ability to specifically observe white matter tracts via diffusion-encoded MRI (dMRI) (Le Bihan et al., 2001; Mori and Zhang, 2006). This method measures diffusion anisotropy by applying magnetic gradients in various directions of space. Although widely applied to the brain, this method is challenging at the spinal level

because of: (i) the small size of the cord relative to the brain (~1 cm diameter in the human) requiring higher spatial resolution and thus decreasing the signal-to-noise ratio (SNR), (ii) physiological motions (respiration, cardiac) that may bias anisotropic diffusion coefficient (ADC) estimation (Kharbanda et al., 2006) and create ghosting artifacts (Clark et al., 2000), (iii) partial volume effects that are more problematic in the cord due to the surrounding cerebrospinal fluid (CSF) (Nunes et al., 2005), (iv) chemical-shift artifacts arising from the epidural fat and other nearby structures and (v) geometric distortions arising from magnetic field inhomogeneities in nearby inter-vertebral disks and lungs. The latter point is particularly challenging in dMRI since usual sequences based on echo planar imaging (EPI) are very sensitive to such artifacts (Ardekani and Sinha, 2005; Heidemann et al., 2003; Jeong et al., 2006; Voss et al., 2006).

Spinal cord dMRI has been the subject of intense research for the last 10 years (Bammer and Fazekas, 2003; Clark and Werring, 2002; Ducreux et al., 2007). Although the ultimate goal is to apply this technique in humans, many studies involved rodents in which some challenges might be more easily overcome or controlled (e.g., through mechanical ventilation, implanted coils). Also, the use of animal models allows investigating the impact of experimental lesions in longitudinal studies. These studies might contribute to the understanding of the regeneration process after SCI. Some animal studies described ADC characteristics at the site of experimental lesions (Deo et al., 2006; Kim et al., 2007a; Krzyzak et al., 2005; Schwartz et al., 1999) while others investigated the impact of cellular intervention after SCI (Nevo et al., 2001; Schwartz et al., 2005a; Schwartz et al., 2003). One important finding is that ADC values correlate with the degree of white matter integrity (Deo et al., 2006; Schwartz et al., 2005d). *In vivo* dMRI of the injured cord is recent and requires more investigation (Deo et al., 2006; Maier and Mamata, 2005; Tsuchiya et al., 2005).

In the light of past studies, we ask the following question: To what extent does diffusion MRI give precise information on the integrity of the damage of spinal tracts after spinal cord lesions*?* Here, we characterised the healthy and injured spinal cord of cats using diffusion tensor imaging (DTI). For validation purposes, some acquisitions were repeated on a several cats, before and after the spinal injury. This enabled to compare results within and between animals. In order to compute accurate tensors, we performed high spatial and high angular resolution acquisitions through parallel imaging. Following tensor estimation, we performed tractography to identify various possible anatomical tracts and assess the integrity of axons.

Material and methods

General protocol

Five cats underwent seven MRI sessions. Two cats (A,B) were scanned in the intact state. One cat (C) received a complete lesion at T13 and was scanned at two different times: 104 days and 170 days after the lesion. One cat (D) received a small dorso-lateral lesion on the left

side (T11) and then a complete lesion at T13 16 days later. It was scanned 22 days after this complete lesion. One cat (E) was scanned intact and then received a large hemi-lesion at T11 (left side). It was scanned again 9 days after the lesion.

Animal preparation

All implantations and lesions were performed under general anaesthesia (isoflurane 1-2%) preceded by adequate pre-medications. The experiments were conducted in accordance with the Ethical Committee of the University of Montreal. Cooperative cats were initially selected to walk regularly at defined speeds on a treadmill. Three cats (A,C,E) were implanted chronically with electrodes to record activity in various hindlimb muscles. Care was taken to lead the wires subcutaneously from the head to the hindlimbs as laterally as possible to minimise magnetic field inhomogeneities around the vertebral column that can induce geometric distortions in the phase encoding direction of EPI data, as will be discussed later. A unilateral or bilateral laminectomy was performed at T11 or T13 for unilateral or bilateral spinal lesions respectively. Lesions were made using a micro-knife and, in the case of complete section of the cord, the gap between the rostral and caudal parts of the cord was filled with a hemostatic agent (Surgicel®).

MRI Acquisition

All MRI data were acquired on a Siemens Trio system (3T). We used the spine array coil provided as an accessory on this scanner, which includes a cervical collar attachment, to achieve a spatially homogeneous sensitivity profile. An illustration of the coil arrangement and its relation to the animal is provided in Figure 4.1. The number of elements used in the spine and cervical coil segments were, respectively, five and three. RF transmission was performed using the body coil integrated into the magnet bore. Data acquisition was carried out on the thoraco-lumbar region (T6-L7) with the cat positioned feet-first-supine.

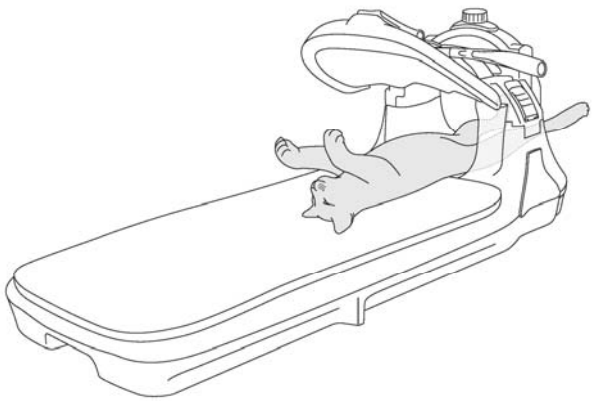

Figure 4.1. Cat in spinal coil
Spine array coil configuration and its relation to the cat placed feet first in the supine position.

Anatomical scans were conducted with the following parameters: 3D inversion recovery T1 weighted sequence, same orientation plane as for diffusion-weighted data (*i.e.*, sagittal or coronal), 256×256 matrix, 112 slices, TR = 1800 ms, TE = 3.53 ms, flip angle = 9°, voxel size = 0.75 mm^3. Proton density (PD) weighted scans were also performed, as these provided better distinction between white and grey matter. The PD scans were used to generate regions of interest (ROIs – see section on data processing). Parameters were: Turbo Spin-Echo (TSE) sequence (turbo factor of 7), axial orientation, 512×512 matrix, 20 slices, TR = 2000 ms, TE = 14 ms, flip angle = 150°, voxel size = 0.35×0.35×3 mm^3.

Additional scans were acquired using a T2-weighted TSE sequence (turbo factor of 13), as a reference for correcting geometric distortions induced in diffusion series by magnetic field inhomogeneities present around intervertebral disks and lungs. The distortion correction method is described in the next section. Acquisition parameters were: same field of view (FOV) as in diffusion-weighted data, 256×256 matrix, 16 slices, TR = 7490 ms, TE = 78 ms, flip angle = 180°, voxel size = 0.55×0.55×1.1 mm^3 (no gap).

Diffusion-weighted (DW) data were acquired using a single-shot spin echo EPI sequence. Parallel acquisition using GRAPPA (GeneRalized Autocalibrating Partially Parallel Acquisition) was used with an acceleration factor of 4 to limit the extent of susceptibility artifacts (Ardekani et al., 2006). To further limit this type of artifact, the readout bandwidth was adjusted to produce the minimum possible echo spacing, usually on the order of 1.1 ms. To limit the effect of eddy-current distortions, we used a twice refocusing pulse sequence (Reese et al., 2003). All DW images were acquired using the following parameters: 128×128 matrix, 16 slices, TR = 9500 ms, TE = 109 ms, flip angle = 90°, b-value = 0 and 800 s/mm^2. Although cardiac-gated dMRI acquisition has been suggested for reducing ghosting artifacts (Summers et al., 2006), the relatively high cardiac frequency in cats (~ 2 Hz) compared to that in humans (~ 1 Hz), the irregularity of cardiac frequency due to the anaesthetic state, and the high TR and number of slices made it difficult to apply this technique within a reasonable scan time for anaesthetised animals. To limit cardiac-related ghosting, we instead optimised slice orientation as follows: two different slice orientations were chosen depending on the location of EMG wires. These were sagittal or coronal, with phase encoding in A-P and L-R direction respectively, as already optimized in (Cohen-Adad et al., 2007d). For cat B, DW images were acquired at 1.3 mm^3 in 12 directions. For cats A, C, D and E, DW images were acquired at 1.1 mm^3 in 55 directions using a polyhedron scheme (Madi et al., 2005). The relatively high b-value was chosen to be consistent with the high number of directions, since a higher b-value increases the sharpness of the tensor ellipsoid by greater attenuation of MRI signal in the diffusion direction (Tuch et al., 2002).

Data processing

After reconstruction in the image domain, DICOM data were averaged respectively to their diffusion-weighting directions. For correcting residual susceptibility-induced distortions we used the framework proposed in (Ardekani and Sinha, 2005). For each session, the non-

weighted EPI volume was 3D interpolated to get a 256×256×32 matrix. The T2-weighted TSE volume was interpolated in the slice direction to get a 256×256×32 matrix as well. The cord and surrounding CSF were manually segmented and intensity histogram normalisation between both volumes was performed. Then, a non-rigid deformation field was estimated to register the EPI on the TSE volume. The deformation field was then applied to all DW volumes. Note that in (Ardekani and Sinha, 2005) they estimated a deformation field for each direction of the DW scans. Here we used a single deformation field for two reasons. First, the DW sequence incorporated a twice refocusing pulse (Reese et al., 2003), which greatly reduced the degree of eddy-current distortions. Second, the very low SNR in some DW volumes would have yielded a non-robust estimation of the deformation field. We therefore preferred a single robust estimation based on the non-weighted EPI. To guide our decision, we compared two variance maps computed from (i) DW scans corrected from a single deformation field, and (ii) DW scans corrected from individual deformation fields, as in (Ardekani and Sinha, 2005). Figure 4.2 illustrates the impact of both approaches by showing slightly more variance for the individual correction approach. This additional variance is located at spinal cord edges, demonstrating the inaccuracy in registering low SNR images on the TSE scan.

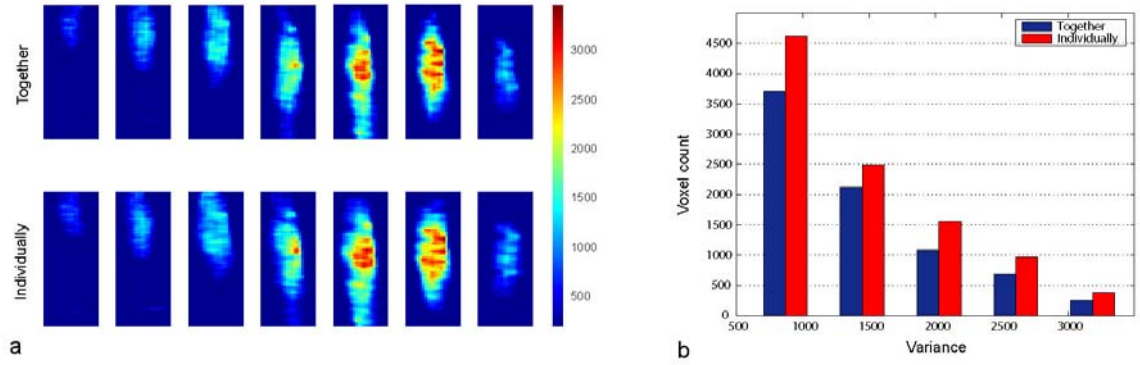

Figure 4.2. Distortion correction – variance maps

Seven coronal slices showing variance maps computed from diffusion-weighted data which have been corrected either using a single deformation field estimated from the non weighted scan (a top), or using deformation fields estimated from each individual diffusion-weighted scan (a bottom). Histogram showing the distribution of variance for both cases (b).

The basics of DTI is to estimate the so-called diffusion tensor D in equation $A = \exp(-b.D)$, where A stands for the signal attenuation and b for the characterisation of the gradient pulse (time, amplitude). A multiple regression is performed to recover D, then the latter matrix is diagonalized to retrieve the three eigenvalues. In the present study we used the freely available software MedINRIA[9]. Instead of performing the regression in the classical Euclidean space, tensors were computed into the log-Euclidean space which presents the same properties

[9] http://www-sop.inria.fr/asclepios/software/MedINRIA/

as the affine-invariant family but is computationally faster. A Riemannian framework was used assuming Rician noise. This approach presented some advantages, notably for the regularization of tensors in noisy datasets (Arsigny et al., 2006). The tractography algorithm was based on this tri-linear log-Euclidean interpolation and used a standard streamline algorithm (Xu et al., 2002). The tractography procedure was automatic, since every voxel of the reference volume was a seeding point (Fillard et al., 2006).

Selective tractography was conducted by isolating various regions of interest based on the axial view of the anatomical volume (see Figure 4.3). White and grey matter contrast was sufficient to identify various regions, including known anatomical tracts. Note that extracted bundles might include various adjacent anatomical tracts and the method does not allow precise isolation of tracts such as only corticospinal or only rubrospinal tracts. Indeed, traditional tracking of such axonal bundles necessitates knowing the start and end points, which are not necessary included in the FOV used during the acquisition. Although the coronal and sagittal FOV was quite large (up to 167 mm), it did not include structures where various tracts originate, e.g., the mesencephalon for the rubrospinal tracts. However, the method did allow the separation of various quadrants in the cord, such as dorsal, ventral and lateral funiculi. To a certain extent, it was also possible to identify various sub-quadrants in the lateral cord, as described hereafter. For the identification of the dorsal and ventral columns, we first extracted all bundles included in the dorsal and ventral part of the cord, respectively. Then, a second ROI was defined for every spinal level, from T12 to L4, left and right. This procedure specifically allowed the identification of the dorsal and ventral columns. For the identification of other tracts, we created an ROI box that we moved around the axial view of the PD volume. The box size was approximately 1.5 mm^3. For either lateral side, we moved the box over two different regions which included the corticospinal tract (CST), the dorso-ventral spinocerebellar tract (SCT), the rubrospinal tract (RST) as well as the spinothalamic tract (STT).

For the assessment of FA changes at the site of injuries on cat D and E, we compared various regions of the cord as done by others (DeBoy et al., 2007; Deo et al., 2006). ROIs were manually selected on the left and right side all along the spinal cord. A total of 45×2 ROI were defined every 3.3 mm along the thoraco-lumbar cord. To demonstrate the statistical difference between healthy and injured tissues, we performed a Student's *T* test based on the robust median (Rousseeuw and Croux, 1993). The median of all FA values was first estimated. Then, the standard deviation centred on the median was calculated. The null hypothesis assessed that population of FA values was homogeneous. We compared each point to the robust median and aberrant points were rejected given two P-value thresholds (95% and 99%). Then, we made a correspondence between aberrant points and their location along the healthy and injured part of the cord.

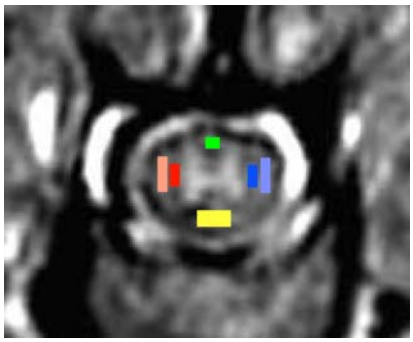

Figure 4.3. Selective tractography – regions of interest
Axial view of a PD-weighted image with overlay of the six ROIs used for selective tractography (top is dorsal). Colour code is consistent with Figure 6. Top ROI includes dorsal columns, bottom ROI includes ventral columns, both lateral-median ROIs overlap the corticospinal tracts (CST) and the rubrospinal tract (RST), both most lateral ROIs overlap the dorso-ventral spinocerebellar tract (SCT), and part of the spinothalamic tract (STT).

Results

Visualisation of anatomical tracts

One motivation of this work was to assess the extent of which tractography can identify known white matter tracts in the *in vivo* spinal cord. This study therefore provides various results of tensor maps, as well as extracted fibre bundles showing specific anatomical tracts. Figure 4.4 shows coronal slices of a T2-weighted TSE image with an overlay of estimated tensor fields. There is good coherence in the longitudinal orientation of principal eigenvectors, without visible distortion in the phase encoding direction (left-right). Since this reduction of distortion might arise from both the acquisition (parallel imaging) and the pre-processing (non-rigid co-registration) methods, it is worth detailing their individual impact. We observed that around structures where local field inhomogeneities were relatively small (e.g., lumbar part, around inter-vertebral disks), parallel imaging alone was sufficient to eliminate almost all distortion. Around structures more severely affected by susceptibility artifacts (e.g., thoracic region due to lungs) however, parallel imaging was not sufficient, and the co-registration procedure was highly beneficial.

From these images, we can appreciate the benefits of such a high spatial resolution for identifying diffusion anisotropy and directionality at specific regions of the cord. This notably enables anatomic localisation of the nerve roots. For instance, one can clearly identify spinal nerves entering on either side of the cord. At this vertebral level (T13-L1), we expect spinal nerves to project almost perpendicularly to the cord. This can be observed in Figure 4.4c.

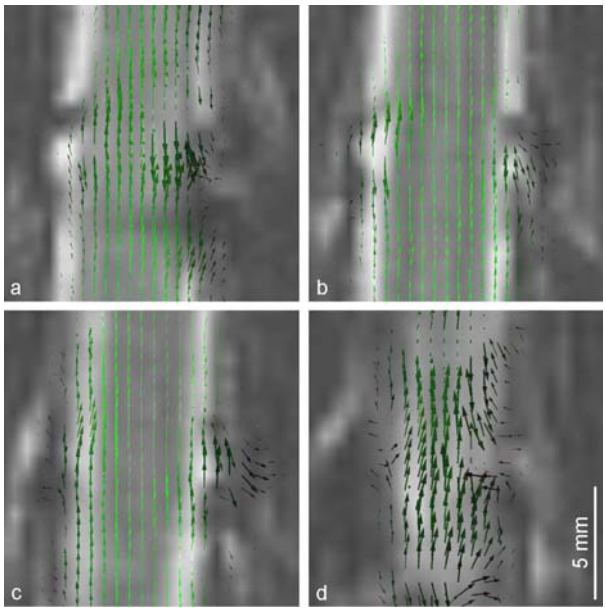

Figure 4.4. Tensor map of the healthy spinal cord of cat

Four tensor fields overlaid on TSE coronal slices. (a) and (d) are more ventral and dorsal, respectively (on each slice, top is rostral). Slices cover an antero-posterior region of 5.5 mm centred at T13-L1. The spatial sampling of the tensor field is the same of the interpolated DW data, *i.e.*, 0.55×0.55×0.55 mm^3. Colour coding for the tensors stands for the principal eigenvector direction, where green corresponds to the rostro-caudal direction. Intensity coding represents FA value. Note that arrows are provided as visual aids, and do not indicate any connection directions.

When performing tractography, spinal nerves were also well defined, and one can note a good correspondence between tractography-derived and schematic organization of axonal tracts (see Figure 4.5bc). Another important point about this figure is the relatively large FOV used (about 14 cm). This enabled consistent tractography throughout several levels of the cord (from T12 to L7), without visible distortions (see Figure 4.5a). Such very long trackings are first steps towards robust identification of specific spinal tracts, because the ability to track fibres from supraspinal to lumbar regions is needed for the inclusion of start and end tract points, as already pointed out in the methods section.

Selective tractography results showed various extracted tracts coursing from T11 to L3 (see Figure 4.6). We were able to distinguish the dorsal and ventral columns, as well as lateral tracts that might include the CST, RST, SCT and the STT right and left. Again, note the absence of geometric distortion in the phase encoding direction (*i.e.*, left-right). Statistics were conducted on each individual tract to assess similar FA quantification among them. In Figure 4.6, each tract is denoted by its letter. FA values are given as mean ± standard deviation: FA(a) = 0.46 ± 0.12, FA(b) = 0.45 ± 0.14, FA(c) = 0.43 ± 0.13, Fa(d) = 0.41 ± 0.14, FA(e) = 0.47 ± 0.12, FA(f) = 0.42 ± 0.11. For assessment of homogeneous FA between all tracts, an ANOVA was conducted on FA means. Hypothesis of homoscedasticity was assumed, and the mean of all variance was considered for computing the F-score. Results of the ANOVA assessing homogeneous FA values between all extracted tracts gave an F-score of 0.035, leading to no significant difference between FA values among spinal tracts (P=0.05).

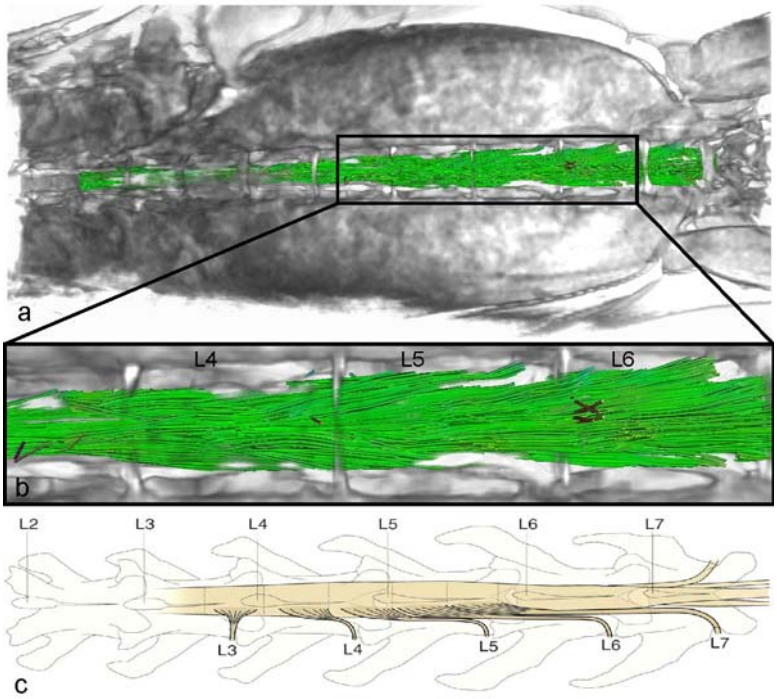

Figure 4.5. Fibre tractography of the healthy spinal cord of cat
Fibre bundles overlaid on a reconstructed anatomical MRI (a) with a zoomed panel showing the lumbar region (b), and schematic spinal nerve topology at lumbar level (c). Orientation is coronal, top-left is right-rostral.

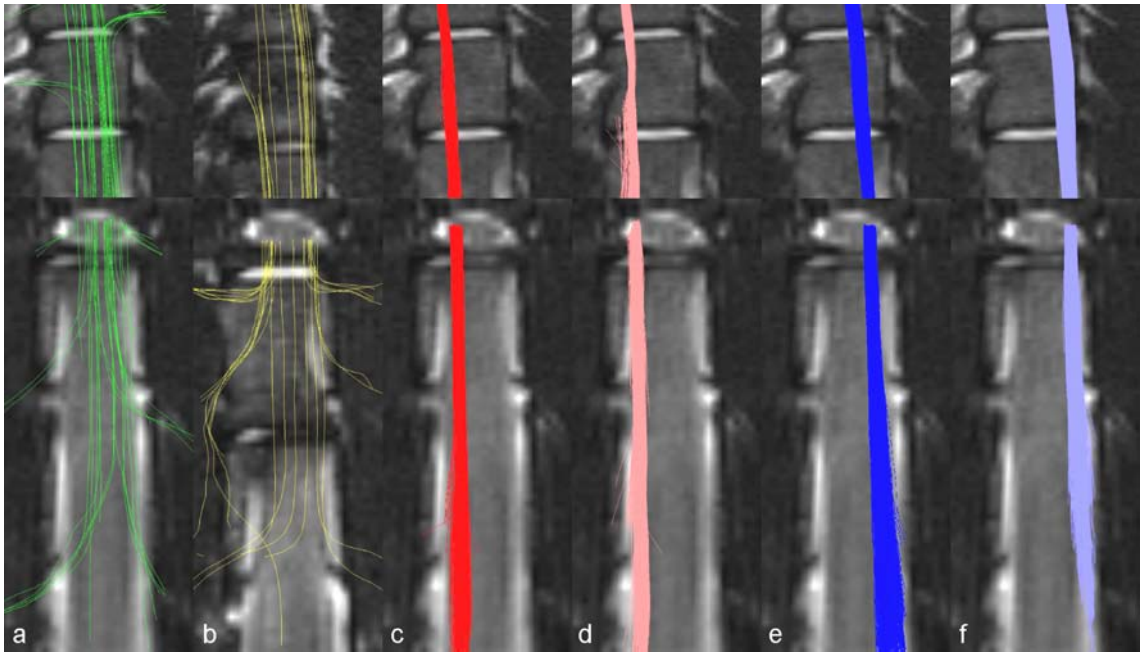

Figure 4.6. Selective tractography – results
Selective tractography showing dorsal column (a), ventral column (b) and lateral tracts (c-f). Orientation is coronal, top-left is rostral-left. ROIs used for the tractography are shown Figure 4.3 with same colour code.

Spinal cord injury

To make the bridge between *in vivo* FA quantification and *post-mortem* state of the cord, histological slices showing healthy, unilateral and bilateral injured cord are reported for cat D in Figure 4.7. Closely rostral to both lesions, Figure 4.7a shows the intact grey and white matter, without apparent scar tissue or oedema. Figure 4.7b shows the dorsal-left localisation of the lesion at T11, with the presence of scar tissue. Figure 4.7c shows the complete section of the cord at T13. Figure 4.7d shows the completeness of the grey and white matter at a level close but caudal to both lesions. Note that degenerated axons due to Wallerian process (Beirowski et al., 2005) would not be visible at this resolution.

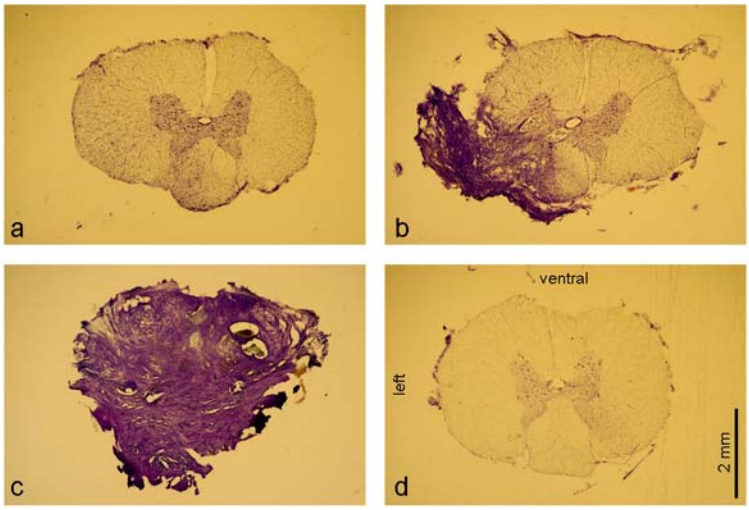

Figure 4.7. Histological slices of spinal cord injury
Histological axial sections of cat D spinal cord centred on T10 (a), on the left hemilesion at T11 (b), on the complete lesion at T13 (c) and at L1 (d).

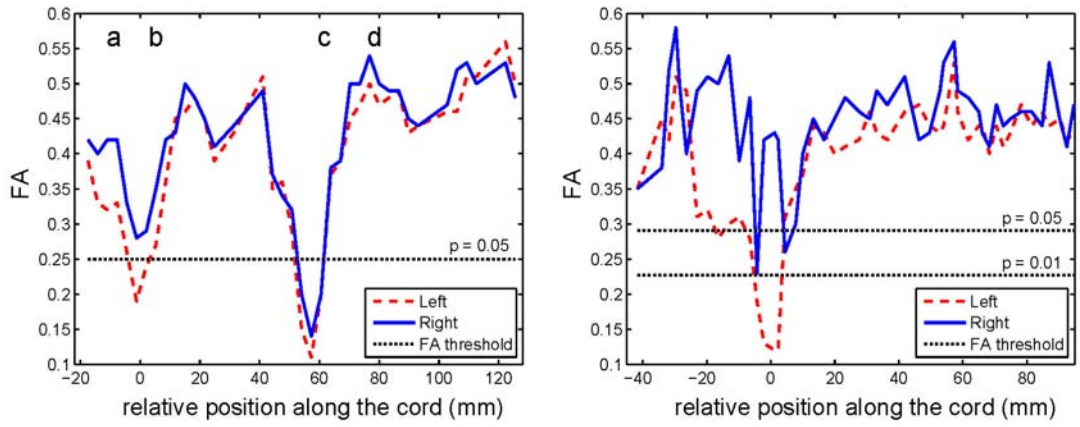

Figure 4.8. FA quantification along the injured spinal cord
Fractional anisotropy quantification along the spinal cord of cat D (left) and cat E after left hemilesion (right). Abscissas show position along the cord relative to the middle of T11 with increasing values towards the caudal direction, ending at L3. Values are reported every 3.3 mm. The location of cat D histological slices are reported on the graph by letters referring to Figure 4.7.

FA quantifications for cat D and E are provided in Figure 4.8. Aberrant points having an FA value statistically different from the median are located below the FA-threshold lines. For cat D, significantly lower values of FA appeared both left and right on the complete lesion and only left on the partial lesion ($P<0.05$). For cat E, significantly lower values of FA appeared ipsilateral to the lesion ($P<0.01$) and closely caudal and rostral contralateral to the lesion ($P<0.05$). For cat D, the location of histological slices are reported on the graph by letters, referring to Figure 4.7. One can observe a good correspondence between FA quantification and the histological data of the cord.

When performing tractography on cats C and D having complete SCI, fibre disruption was complete when adjusting FA threshold (on the order of 0.25). Figure 4.9a shows tractography results from cat C. Two zoomed windows show the actual complete lesion on the T1 weighted anatomical MRI (see Figure 4.9b) and on the tensor field (see Figure 4.9c). Although T1 weighted images enable observation of a lesion-related contrast, they do not provide any quantification of white matter integrity, as does DTI. In that case, the decrease in diffusion anisotropy might reflect the lesion accompanied by scar tissue, the presence of oedema being less probable since the lesion was old (more than 5 months). Within and close to the lesion, tensors tend to have a spherical representation. We can assume that various processes, notably those related to axonal regrowth, are inaccurately described by the tensor model which constrains the modelling of the diffusion in only one principal direction, through the principal eigenvector. Other diffusion processing methods allowing better flexibility notably for crossing fibres might be of interest. This aspect is discussed later. Also note that the spherical representation of the tensors at the edges of the cord might be due to a partial volume effect between CSF and white matter. Moreover, we would expect less anisotropy within grey matter accompanied with more spherical tensors, which is not the case here. We have two explanations. The first is related to a partial volume effect that might have occurred as well between white and grey matter. The second argument is related to the particular property of the spinal cord grey matter, which has been reported to be much more anisotropic than that in the brain (Fenyes and Narayana, 1999; Holder et al., 2000).

Taking advantage of the relatively high spatial resolution, we performed selective tractography on cat E before and after the spinal lesion on the left, by extracting fibre bundles at either side of the cord using two different ROIs located caudal to the lesion (around L3). Results showed a good coherence along several levels of the thoraco-lumbar cord without visible distortion (Figure 4.10). Moreover, fibre disruption was present at the exact lesion location (white arrow), suggesting a lack of residual connections of tracked fibre bundles, between either side of the lesion. FA values for this cat were reported in the right graph of the Figure 4.8.

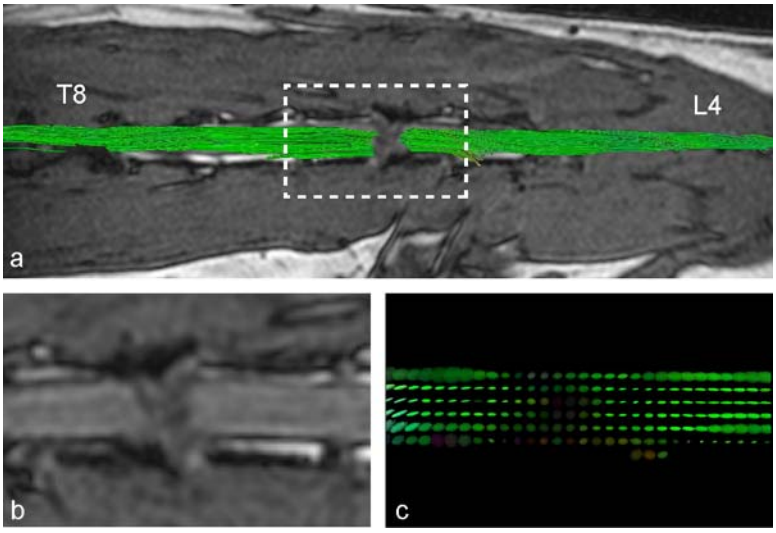

Figure 4.9. Tractography of the injured spinal cord
Tractography result on a cat with complete spinal cord injury, overlaid on an anatomical MRI (a), zoomed window covering T13-L1 levels showing the anatomical (b) and ellipsoid tensors (c). Orientation is coronal, top-left is right-rostral. Colour coding for the tensors stands for the principal eigenvector direction, where green corresponds to the rostro-caudal direction. Intensity coding stands for FA value.

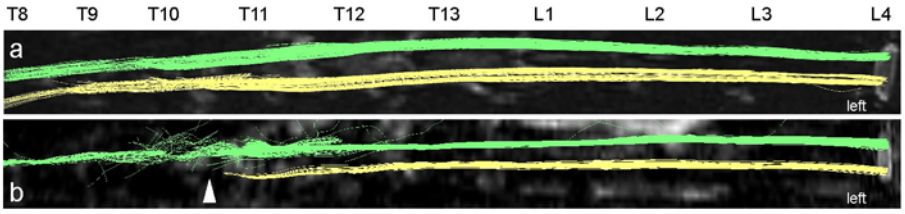

Figure 4.10. Selective tractography of the injured spinal cord
Coronal views of tractography results on a cat before (a) and after (b) left hemilesion at T11. For (a) and (b), top is right side of the cord and bottom is left side of the cord. The segments are indicated above and give the rostro-caudal direction from thoracic (T) to lumbar (L). Boxes for selective tractography where selected on either side of the cord around L3. Lesion location is indicated by the white arrow.

Discussion

After analysis of all datasets, tensor maps showed a consistent directionality of principal eigenvectors all along the cord, as well as spinal nerves projecting on the spinal cord at various vertebral levels. Extrapolating these tensor maps to a streamline-based tractography, large FOV tracking of various axonal tracts was feasible without visible distortion. We showed the feasibility of observing axonal interruption via tractography in complete and partially injured cats. Although this proof of feasibility was already demonstrated during *ex vivo* acquisition on rodents at 9.4T (Schwartz et al., 2005d), the clinical and *in vivo* setup used in the present study represents a major advance.

Originality of the work

Thoraco-lumbar cord

Most studies focused on the cervical (Bammer et al., 2002; Holder et al., 2000; Mamata et al., 2006; Schwartz et al., 2003; Tsuchiya et al., 2005; Voss et al., 2006; Wheeler-Kingshott et al., 2002; Xu et al., 2004) or thoracic (Deo et al., 2006; Elshafiey et al., 2002; Fenyes and Narayana, 1999) regions of the spinal cord. Cervical, thoracic and lumbar regions have a large variability in terms of susceptibility-induced artifacts due to various surrounding organs containing air, especially the lungs (Dietrich et al., 2001). Furthermore, the diameter of the cord varies along its axis. Knowing that most of the literature results focused on the cervical spine and since acquisition challenges vary greatly, it is therefore a worthwhile endeavour to provide dMRI results of the thoraco-lumbar cord.

Large FOV

Many studies have been performed on a clinical scanner using minimal achievable FOV (Jeong et al., 2005; Wheeler-Kingshott et al., 2002; Wilm et al., 2007). However, a large FOV has two main advantages. First, as mentioned before, supraspinal structures are necessary in order to identify some specific axonal tracts such as rubrospinal or corticospinal tracts. Second, observing a large region along the cord is crucial when seeking changes at multisegmental levels, above, across and below a spinal lesion. For instance, the corticospinal tract from the contralateral cortex might sprout below the lesion and participate in the functional recovery following the lesion. The latter argument underlies the importance of observing a large region in the thoraco-lumbar cord, as done in this study.

High spatial and angular resolution

The main focus of this study was the use of high spatial and angular resolution in spinal imaging. Indeed, in order to limit the intra-voxel heterogeneity we performed high spatial resolution acquisitions. Since the acquisition time was still reasonable (less than 45 minutes for acceptable results), the data were relatively noisy. Using an efficient regularization method for the tensors, we were able to drastically reduce outliers and overcome the relatively low SNR (Fillard et al., 2006). One motivation for increasing spatial resolution was to identify major tracts in the spinal cord. We chose to acquire isotropic voxels for two main reasons. First, when no prior is set concerning the orientation of axonal tracts, anisotropic voxels might induce a bias when estimating the principal eigenvector (Basser et al., 2000; Jones et al., 2002b). Although there is a certain axial symmetry in the cord that still allows longitudinal tractography at high in-plane resolution (Gullapalli et al., 2006), we think that the use of isotropic voxels will avoid bias when attempting to track non-longitudinal fibres. The second argument for isotropic voxels is related to the conditions prevailing in spinal cord injury. If data were averaged along several millimetres in the axial direction using highly anisotropic voxels, a transverse low-width lesion would not be detected by dMRI. Indeed, the FA value would be averaged in the axial direction

and only the healthy tissue, which would be highly preponderant, would contribute to the estimation of FA.

Another aspect in this study is the number of gradient directions used. Some recent studies supported the choice of a reduced number of directions (Landman et al., 2007; Lee et al., 2006). Such small angular samplings are certainly valid when the goal of DTI is to obtain a rough description of the diffusion process in the cord at a reasonable scanning time. However, we think that more precise description of subtle phenomena such as axonal sprouting would require higher sampling rate. Also, collateral fibres and anatomical projections, notably from dorsal roots, impose a low radius curve that can be described only with high angular resolution. Many previous studies also pointed the axial symmetry of the cord as an argument for imaging with a reduced number of directions (Gulani et al., 1997; Schwartz et al., 2005a). However, the computed ADC are biased for regions were axons curve or change direction, notably in some complex anatomical projections of nerve roots or following SCI. Furthermore, as pointed out in (Madi et al., 2005), such acquisitions are dependent of the subject positioning within the scanner, so that the cord axis is aligned with the longitudinal gradient. When only a small section of the cord is imaged, this may be possible. However, for quantifying ADC along a larger extent of the cord, the curvature might induce a bias in the protons attenuation where longitudinal fibres are no more aligned with the gradient. For that purpose, Madi *et al*. used an icosahedral scheme up to 42 gradient directions and showed the benefit of high angular resolved gradient directions. Following such considerations, we imaged the cord using a polyhedron scheme of 55 directions to estimate the full tensor with minimum bias and no assumed main direction of diffusion.

In vivo study with clinical imaging system

Many *in vivo* studies providing high spatial resolution were conducted on rats using an implanted coil (Deo et al., 2006; Elshafiey et al., 2002; Fenyes and Narayana, 1999; Madi et al., 2005). Implanted coils allow for a better SNR but have two major disadvantages. First, the surgical implantation might introduce physiological reaction within the region of interest such as oedema. Second, dMRI methodology using implanted coils are de facto incompatible with human studies. In the present study we used a standard human spine array. One next and important step will be the application of the method to human studies.

Limitation of the study

Variability in data quality

All datasets gave DTI results that were consistent for all cats. However, data quality was substantively different between sessions: irregularity in the intensity and number of ghosting artifacts, signal loss in regions around the lungs, inter-slice inhomogeneities in SNR. Inter-subject variability in image quality has already been observed in spinal cord dMRI (Spuentrup et al., 2003). We attributed these differences in data quality to cardiac and

respiratory inter-cat variability, to the presence of EMG wires in some cats and also to the slightly different echo spacing used during the acquisitions. Moreover, the susceptibility-sensitive sequences used are prone to severe distortions and signal loss from T12 to T5 in the cat. Signal loss might be related to susceptibility artifacts inducing inaccuracy in slice excitation, hence leading to the excitation of wrong protons (*i.e.*, located in adjacent slices). The lower data quality in the region around the lungs suggests that respiratory gated or navigated acquisition might lead to improvement.

Another limitation concerns the choice of not employing cardiac gating during the acquisition of diffusion-weighted data. Indeed, cardiac-related motions of the cord in the rostral-caudal direction have been reported in recent dMRI studies (Summers et al., 2006). It has been shown that such motions increase ADC in the rostral-caudal direction, thus biasing FA quantification along the cord. Although we did not employ cardiac gating (for reasons mentioned in the methods section), our quantification results along the cord are mainly considered individually, *i.e.*, there is no attempt to derive absolute FA values in the white / grey matter of cats. Nonetheless, future studies using cardiac gating might be a necessary step for accurate inter-subject FA quantification.

Physiological considerations

The cat with a small partial lesion (cat D, in Figure 7b) showed rapid recovery of locomotor functions after a few days whereas the one with large hemi-lesion (cat E) did not walk at the time it was imaged. Moreover, diffusion MRI results showed higher anisotropy coupled with a higher continuity of white matter axons on the cat with a small spinal lesion. Although based only on two cats, we were able to assess a qualitative correlation between physiological recovery and tractography results. However, some potential biases in this correlation have to be pointed out. First, the possible presence of oedema in the cat with a larger lesion might have altered the quantification of ADC, as mentioned in (Schwartz et al., 2003). Indeed, this lesion was performed only 9 days before imaging. Second, the partial lesion study was conducted on two cats only, which prevented us from coming to any statistical conclusion. The latter point opens the door to the development of a methodological framework for group analysis of DTI in the spinal cord, as already proposed for the brain (Jones et al., 2002a), and also to the development of analytical tools that could quantify the notion of fibre bundle integrity via tractography.

Observation of axonal disruption

Some limitations have to be underlined regarding assessment of axonal disruption via tractography. First, the streamline-based algorithm used in this study required a threshold based on the fractional anisotropy. By modifying the threshold, the fibre disruption at the site of the lesion became more or less evident. This aspect should be overcome using a more objective threshold for tractography. Second, the presented results arise from a relatively small number of cats. This study contributes to the proof of feasibility required for clinical applications,

however, other studies are needed in order to gain statistical confidence (Kinoshita et al., 2005). Third, the disruption observed via tractography did show the site of the complete spinal section in a robust way. However, the lesion was surgically induced and then filled with a synthetic agent which presumably had isotropic properties. One could thus ask whether the sensitivity for obtaining bundle disruption would be similar in non-surgical lesions (such as spinal cord compression), as investigated in (Facon et al., 2005). Also, the presence of oedema and glial scar at the site of the lesion would probably interfere with the fractional anisotropy quantification, as investigated in (Schwartz et al., 2005d).

Limitation of tractography

Some characteristics of the tractography procedure have to be clarified in order not to misinterpret the presented results. Fibre bundles do not represent real axonal tracts but trace the path where water diffuses preferentially. Hence, reconstructed fibres should be handled with care since they may not represent the real pathway of axons (Basser et al., 2000; Johansen-Berg and Behrens, 2006). One way of representing this uncertainty are probabilistic methods which allow better flexibility in the quantification of white matter directionality (Behrens et al., 2003). Limitations of tractography are also discussed in a neurosurgical framework (Kinoshita et al., 2005). Another limitation of tractography is the impossibility of distinguishing anterograde from retrograde connections. Although, anatomical priors might be used in the spinal cord in order to distinguish the type of connection, as already done for the descending rubrospinal tract (Schwartz et al., 2005d), it should again be mentioned that robust identification of specific tracts implies very high spatial resolution, and also implies knowing the start and end of tracts.

Another MRI-based approach allowing imaging of specific tracts relies on the injection of manganese, a paramagnetic agent that diffuses through white matter axons following electrical stimulations. Specific axonal tracts are therefore visible using T1-weighted sequence (Bilgen et al., 2006). Such methods have already been applied to observe CST following SCI in rats, and yield promising results (Bilgen, 2006).

Biophysical modelling

Physiological changes following SCI may be assessed via dMRI (Deo et al., 2006; Kim et al., 2007a). Also, the presence of oedema and glial scar may alter ADC coefficients (Schwartz et al., 2005d). However, some physiological processes following SCI are still unpredictable. For instance, sprouting of undamaged axons may occur at non-precisely identified location, the number and characteristics of new projections may vary, as well as the mean angle between newly grown projections and longitudinal fibres. Hence, the ability to model the diffusion process accurately while studying the injured cord would increase the reliability of the estimated ADC (Beaulieu, 2002). With such modelling, one would be able to distinguish several confound parameters such as axonal density (Jespersen et al., 2007) and extent of oedema (Sen and Basser, 2005). However, even combining high resolution and accurate quantitative diffusion metrics, one might still wonder if today's dMRI would allow for

the identification of sprouting fibres. In future work, it might be worth examining this phenomenon *ex vivo* to get even higher resolution without physiological and susceptibility artifacts. The validity of transposing *in vivo* from *ex vivo* results has already been investigated and accepted in mice (Kim et al., 2007b), in cats (Pattany et al., 1997), as well as in humans (Maier and Mamata, 2005).

Tensor model: pros and cons

Diffusion tensors quantify the mean diffusion within the space of a voxel, *i.e.*, on the order of the millimetre. Knowing that axon diameter is on the order of microns, the computed tensor only gives a macroscopic quantification of the diffusion process. The result is a macroscopic integration including every axon localised in the given voxel. If axons were homogeneously aligned within a voxel, the principal eigenvector of the tensor would accurately approximate their direction (Lazar and Alexander, 2003). However, the tensor model is not capable of resolving multiple fibre orientations within one voxel (Campbell et al., 2005; Tuch et al., 2002). Knowing that the spinal cord white matter contains sites of crossing fibres, e.g., collateral and longitudinal fibres, the tensor model used in this study might limit the ability to distinguish various crossing tracts.

Some manipulations of the tensor have been proposed to overcome the limits imposed by its single diffusion direction. The intra-voxel heterogeneity might be better described by the use of the second eigenvector of the diffusion tensor. The impact of the tensor model for crossing fibres was investigated in the brain (Wiegell et al., 2000). These authors showed that the introduction of the second eigenvector allows a better characterization of the fibre network in some parts of the brain with extensive amounts of crossing fibres. In the spinal cord, another group showed that the second eigenvector could map collateral fibres (Maier and Mamata, 2005; Mamata et al., 2006).

Although it is possible to see other tracts than longitudinal ones in the spinal cord, notably by means of second eigenvectors as seen previously, there is a restriction imposed by the tensor itself. Indeed, the three eigenvectors are, by definition orthogonal. Thus, when the primary direction is defined by the principal eigenvector, *i.e.*, longitudinal fibres in the case of the spinal cord, the second eigenvector is limited in degrees of freedom since its direction is necessary on the plan orthogonal to longitudinal fibres. In the presence of non orthogonal fibres, the usual way of decomposing the tensor (*i.e.*, in an orthogonal fashion) becomes less efficient. In that case, other representations of the acquired diffusion data should be considered, such as qBall imaging (Tuch et al., 2002).

Towards an accurate diffusion direction representation

As mentioned previously, we know from anatomical considerations that the spinal white matter contains longitudinal ascending and descending tracts, but also crossing fibres, e.g., collaterals of descending tracts, commissural fibres and afferent fibres. Results from the

present study showed that major nerve tracts were discernible via the tensor model. However, one might wonder how the diffusion profile would appear if it weren't restricted in one principal direction. Furthermore, results in the injured spinal cord clearly showed axonal disruption at the site of complete lesion. However, more subtle loss of axonal continuity in partial lesions was more difficult to assess in a robust way. Additionally, white matter plasticity associated with subtle changes in axonal network (sprouting) might require another model than that of the tensor.

In the last five years, other methods have been developed allowing several preferred diffusion directions represented by an orientation distribution function (ODF) (Descoteaux et al., 2006; Tuch et al., 2003). One purpose of such models is to combine high-angular resolution diffusion imaging (HARDI) with processing methods allowing representation of the diffusion anisotropy at each voxel on a high resolved discrete sphere. Such highly angular resolved acquisitions allow a better description of underlying fibres as demonstrated in the *ex vivo* monkey brain using high spatial and angular resolution (Schmahmann et al., 2007).

The present article provides an incentive to use the ODF to represent the diffusion process in the injured spinal cord for two reasons. First, white matter organisation at the spinal level implies multiple sites of crossing fibres. Second, the plasticity process following injury might induce a reorganisation of white matter pathways. Such subtle reorganisation, involving a limited number of axons, might be invisible to the principal eigenvectors usually represented in DTI. Also, the ODF might better depict sprouting of dorsal roots which will be more or less at 90 degrees relative to major spinal pathways. The use of the ODF to describe the diffusion process in the spinal cord will be part of our future work.

Conclusion

High spatial and angular resolution acquisition in the *in vivo* cat spinal cord allowed consistent tractography using the tensor model, without visible distortion. Nevertheless, more subtle reorganisation of axons might require better description of the diffusion process by means of an orientation distribution function, thus requiring high angular acquisition. In conclusion, it appears feasible to identify various anatomical tracts coursing through different quadrants and thus assess the continuity of specific spinal tracts after spinal cord injury. It is hoped that such studies, especially when performed longitudinally, will allow a better correlation between locomotor recovery and spinal cord integrity.

Acknowledgement

We thank H. Leblond, J. Provencher, G. Barrière and A. Frigon for the cat preparations, G. Barrière for providing histological sections, C. Gauthier for the illustration, J. Doyon for providing support from the UNF, C. Hurst for assistance with MRI acquisitions, S. Ardekani for providing the code for correcting geometric distortions and C. Gauthier for her revision of the

manuscript. This work was supported by the Canada Research Chair on the Spinal Cord provided by the Canadian Institute of Health Research (CIHR) to S. Rossignol and for a studentship to J. Cohen-Adad and by the Multisdisciplinary Team on Locomotor Rehabilitation (Regenerative Medicine and Nanomedicine, CIHR) for scan time.

5. Article #2: Detection of multiple pathways in the spinal cord using q-ball imaging

J. Cohen-Adad[1,3], M. Descoteaux[2], S. Rossignol[3], R.D. Hoge[4], R. Deriche[2], H. Benali[1]

[1]*INSERM U678, Université Pierre et Marie Curie (Paris VI), CHU Pitié-Salpêtrière, Paris, France*
[2]*Odyssée Project Team, INRIA/ENPC/ENS, INRIA Sophia Antipolis, France*
[3]*GRSNC, Faculty of Medicine, Université de Montréal, Montreal, QC, Canada*
[4]*Unité de Neuroimagerie Fonctionnelle, CRIUGM, Université de Montréal*

Published in NeuroImage. Received 15 February 2008; revised 3 April 2008; accepted 14 April 2008; Available online 30 April 2008

Preface

In the previous article we showed that DTI can retrieve major longitudinal pathways, *i.e.*, axon bundles oriented in the rostro-caudal direction. However, other types of fibres not oriented longitudinally are also present in some parts of the cord. The purpose of this article was to use QBI to show the benefits of model-free approaches in the characterization of complex white and grey matter pathways in the spinal cord. This work has been published in NeuroImage (Cohen-Adad et al., 2008f). It has also been published as a short article in conference proceedings (Cohen-Adad et al., 2008g) and in abstract forms (Cohen-Adad et al., 2008c; Cohen-Adad et al., 2008e). My contribution to this article was to prepare the *ex vivo* spinal cord phantom, to acquire HARDI data, to process the data and to write the article. Co-authors of this article and their individual contribution are listed hereafter:

Maxime Descoteaux has developed and implemented the method to estimate and to visualise ODF based on HARDI data.

Serge Rossignol is my co-supervisor and has been involved in actively reviewing the manuscript as well as in providing useful comments on neurophysiology.

Richard D. Hoge has provided useful comments on MRI acquisitions.

Rachid Deriche is the supervisor of Maxime Descoteaux and provided useful insights about the methods.

Habib Benali is my co-supervisor and has been involved in providing useful comments on data processing.

Abstract

Magnetic resonance diffusion tensor imaging (DTI) has been extensively applied to the spinal cord for depicting its architecture and for assessing its integrity following spinal lesions. However, DTI is limited in representing complex white matter architecture, notably in the presence of crossing fibres. Recently, q-ball imaging (QBI) has been proposed as a new method for recovering complex white matter architecture. We applied this technique to both *ex vivo* and *in vivo* spinal cords of cats using a 3T scanner. For the purpose of comparison, gradients have been applied in 55 and 100 encoding directions and b-values varied from 800 to 3000 s/mm^2. As a result, QBI was able to retrieve crossing fibre information, where the DTI approach was constrained in a unique diffusion direction. To our knowledge, this is the first study demonstrating the benefits of QBI for detecting the presence of longitudinal, commissural and dorso-ventral fibres in the spinal cord. It is a first step towards *in vivo* characterization of the healthy and injured human spinal cord using high angular resolution diffusion imaging and QBI.

Keywords: Diffusion tensor imaging, high angular resolution diffusion imaging, q-ball, spinal cord, white matter

Introduction

Diffusion tensor imaging (DTI) is a method derived from magnetic resonance imaging (MRI) used for mapping white matter structure (Basser et al., 1994). It has been recently applied to the spinal cord and has demonstrated its benefits for assessing white matter integrity following injury (Agosta et al., 2007a; Budde et al., 2007; Cohen-Adad et al., 2008b; DeBoy et al., 2007; Deo et al., 2006; Ducreux et al., 2007; Fujiyoshi et al., 2007; Kim et al., 2007a; Lammertse et al., 2007; Nevo et al., 2001; Ohgiya et al., 2007a; Plank et al., 2007; Ries et al., 2000; Schwartz et al., 2005d; Shen et al., 2007; Thurnher and Bammer, 2006a; Valsasina et al., 2005; Vargas et al., 2008). Also, it has been shown that DTI can retrieve major longitudinal pathways, *i.e.*, axon bundles oriented in the rostro-caudal direction (Bilgen et al., 2005; Ciccarelli et al., 2007; Cohen-Adad et al., 2008b; Ellingson et al., 2007b; Fenyes and Narayana, 1999; Gullapalli et al., 2006; Maier, 2007; Wheeler-Kingshott et al., 2002). However, other types of fibres not oriented longitudinally are also present in some parts of the cord. These are for instance commissural fibres coursing in the medio-lateral direction, and dorso-ventral fibres that may originate from dorsal root afferents or terminal fibres of descending tracts. Since the diffusion tensor can only account for a single principal diffusion direction, these pathways might not be visible using DTI (Hagmann et al., 2006). Furthermore, after lesions or in the presence of tumours or cysts tracts can be displaced so that they are no longer following a longitudinal direction.

To overcome this issue, model-free approaches have been proposed to measure the microscopic diffusion without constraining its representation. These methods are known as q-space imaging (Callaghan et al., 1988) or diffusion spectrum imaging (Wedeen et al., 2005) and have already demonstrated benefits for imaging the brain (Schmahmann et al., 2007) and the spinal cord (Assaf et al., 2000). However, long acquisition time is required for adequate sampling of q-space to retrieve the three-dimensional diffusion profile. To reduce acquisition times, a similar method has been proposed where sampling of q-space is restricted to a single sphere in many directions. This method is known as high angular resolution diffusion imaging (HARDI). A popular HARDI reconstruction method is q-ball imaging (QBI), which allows the retrieval of crossing fibres information with shorter acquisition time (Campbell et al., 2005; Tuch, 2004).

In the present study, we applied this technique in both *in vivo* and *ex vivo* feline spinal cord. We show that QBI can recover longitudinal pathways as DTI does, but can also recover medio-lateral and dorso-ventral directions which are consistent with the known architecture of the spinal cord.

Material and methods

Ex vivo acquisition

The experiments were conducted in accordance with the Ethics Committee of the University of Montreal. One cat was sacrificed with an overdose of barbiturate (Somnotol). A laminectomy was performed at the lumbar level followed by the dissection of the dura matter. Dorsal and ventral roots were sectioned. The cord corresponding to lumbar segments 3 to 7 was extracted and put in saline solution (0.9 %). Thirty minutes after extraction, the cord was placed into a gelatine solution (6 %). It was imaged five hours later. We chose not to fix the cord because this chemical process induces a significant decrease of transverse relaxation time in the white matter (Carvlin et al., 1989; Pfefferbaum et al., 2004). Based on previous tests performed on fixed samples, we have concluded that constraints on our diffusion sequence parameters prevented us from reaching a echo time (TE) small enough to obtain sufficient signal in the white matter.

Datasets were acquired on a Siemens Trio system (3T) using an 8-channel spine array coil allowing parallel imaging. RF transmission was performed using the body coil integrated into the magnet bore. Anatomical scans were conducted using proton-density (PD) weighting as these provide good contrast between white and grey matter. Parameters were: Turbo Spin-Echo sequence (turbo factor of 13), matrix = 320×320, voxel size = 0.25×0.25×3 mm^3, TR = 3500 ms, TE = 11 ms, flip angle = 120°. PD scans were used to generate regions of interest (ROIs – see section on data processing).

Diffusion-weighted (DW) scans were acquired with a single-shot spin echo EPI pulse sequence. Parallel acquisition using GRAPPA (GeneRalized Autocalibrating Partially Parallel Acquisition) was used with an acceleration factor of 4 to limit the extent of susceptibility artifacts induced by the gelatine-air interface and by ferromagnetic micro-particles contained in the gelatine. To limit the effect of eddy-current distortions, the sequence included a twice refocusing pulse (Reese et al., 2003). Parameters were: matrix = 120×120, voxel size = 1×1×3 mm^3, TR = 4000 ms, TE = 96 ms, flip angle = 90°, three repetitions, b-value = 0 and 1500 s/mm^2, 100 directions using a polyhedron scheme (Madi et al., 2005). To evaluate the impact of different b-values, three additional datasets were acquired using a circularly polarised transmit-receive wrist coil to get higher signal-to-noise ratio (SNR). No parallel imaging was used for these scans. Parameters were: matrix = 128×128, voxel size = 0.65×0.65×3 mm^3, TR = 4700 ms, TE = 152 ms, flip angle = 90°, three repetitions, b-value = 1000, 2000 and 3000 s/mm^2, 100 directions.

In vivo acquisition

One healthy cat was used for the *in vivo* study. It was anaesthetized in the scanner (isoflurane 2 % through an endotracheal tube) and breathed freely. The cat was positioned feet-first-supine over an 8-channel phased-array coil, as done in (Cohen-Adad et al., 2008b). The centre was aligned on the fourth lumbar vertebral (L4) level. The cat was well propped up in the coil using bags to avoid any motion during the acquisition.

Anatomical PD-weighted scans were conducted with the following parameters: Turbo Spin-Echo sequence (turbo factor of 7), axial orientation, matrix = 512×512, voxel size = 0.35×0.35×3 mm^3, 20 slices, TR = 2000 ms, TE = 14 ms, flip angle = 150°.

DW data were acquired using the same single-shot spin echo EPI sequence as for *ex vivo* acquisitions. Parameters were: matrix = 128×128, voxel size = 1.1×1.1×1.1 mm^3, 15 slices, TR = 9500 ms, TE = 109 ms, flip angle = 90°, b-value = 0 and 800 s/mm^2. We performed two acquisitions to compare QBI at various sampling schemes. In the first acquisition, DW gradients have been applied in 28 directions (6 b_0 repetitions, 4 repetitions, 22 minutes scan). In the second acquisition, DW gradients have been applied in 55 directions (3 b_0 repetitions, 4 repetitions, 38 minutes scan). Although cardiac-gated acquisition has been suggested for reducing ghosting artifacts (Summers et al., 2006), the relatively high cardiac frequency in cats (~ 2 Hz) compared to that in humans (~ 1 Hz), the irregularity of cardiac frequency due to the anaesthetic state, and the high TR and number of slices made it difficult to apply this technique within a reasonable scan time for anaesthetised animals.

Q-ball estimation

QBI, originally proposed in (Tuch, 2004), reconstructs the diffusion orientation distribution function (ODF) directly from the raw high angular resolution diffusion imaging (HARDI) measurements on a single sphere using the Funk-Radon transform (FRT). This FRT

can be solved analytically, efficiently and robustly with the spherical harmonic (SH) basis (Anderson, 2005; Descoteaux et al., 2007a; Hess et al., 2006). The key idea is to express the HARDI signal as a SH series of order L and to solve the FRT using the Funk-Hecke theorem. The final ODF reconstruction, Ψ, in direction (θ,φ) is

$$\Psi(\theta,\phi)=\sum_{k=0}^{L}\sum_{m=-k}^{k}2\pi P_k(0)c_k^m Y_k^m(\theta,\phi) \tag{5.1}$$

where Y_k^m denote SH of order k and degree m, c_k^m are the SH coefficients describing the input HARDI signal and P_k is a Legendre polynomial of order k. Note that it is also possible to impose a Laplace-Beltrami regularization criterion while estimating the SH coefficients c_k^m, as done in (Descoteaux et al., 2006). Here, we used a regularization parameter of 0.006 and estimation order L = 4 to get robust fibre detection (Descoteaux et al., 2006). From the reconstructed ODF, we computed the generalized fractional anisotropy (GFA) (Tuch, 2004), which is a HARDI anisotropy measure similar to the popular DTI fractional anisotropy (FA) (Pierpaoli and Basser, 1996). As an extension of the FA, the GFA is defined as the standard deviation divided by the root mean square of the ODF. Hence, it is also a measurement of the anisotropy but it is generalized throughout more than three eigenvalues. Thus we have

$$\begin{aligned} GFA &= \sqrt{\frac{n\sum_{i=1}^{n}\left(\Psi(u_i)-\langle\Psi\rangle\right)^2}{(n-1)\sum_{i=1}^{n}\Psi(u_i)^2}} \\ &= \sqrt{1-\frac{\left(c_0^0\right)^2}{\sum_{k=0}^{L}\sum_{m=-k}^{k}\left(c_k^m\right)^2}} \end{aligned} \tag{5.2}$$

where

$$\langle\Psi\rangle=\left(\frac{1}{n}\right)\sum_{i=1}^{n}\Psi(u_i) \tag{5.3}$$

is the mean of the ODF. The diffusion ODF (dODF) is a blurred version of the "true" fibre ODF (fODF). Because of this blurring effect, the extracted maxima of the dODF are often used for fibre analysis. An alternative is to use spherical deconvolution methods that provide a direct estimate of the fODF. Several algorithms have recently appeared in the literature to estimate this fODF (Jian and Vemuri, 2007; Tournier et al., 2007). These techniques have better angular resolution than QBI and produce sharper fODF profiles than the q-ball dODF (Descoteaux et al., 2007b; Tournier et al., 2004). Thus, small fibre compartments with small volume fractions are sometimes visible with the fODF and not with the dODF. In the present study, the fODF was estimated using the method proposed in (Descoteaux, 2008; Descoteaux et al., 2007b). Please note that in this paper, "ODF" will always refer to the fibre ODF for clarity purpose.

Data processing

Images were first averaged to their diffusion directions and were two times interpolated. Series acquired without parallel imaging were corrected for susceptibility-induced distortions using the method described in (Ardekani and Sinha, 2005). Diffusion tensors (DTs) and ODFs were estimated with the Odyssée Toolbox publicly available with BrainVISA (http://brainvisa.info/), using methods proposed in (Descoteaux et al., 2007a; Descoteaux et al., 2007b). Based on anatomical scans, a manual segmentation was performed to delineate white matter from grey matter over 10 axial slices for *ex vivo* and *in vivo* series, as shown in Figure 5.1. For each series, two masks were then created. FA and GFA were computed respectively from DTs and ODFs, and were averaged within each created mask.

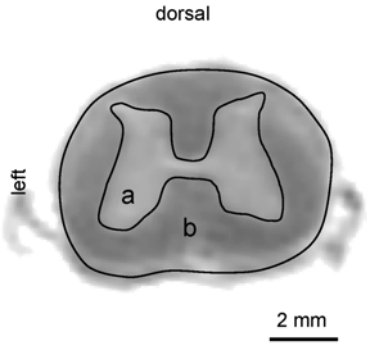

Figure 5.1. Axial PD image showing segmented white and grey matter
Axial slice (L5 spinal level) of the *ex vivo* PD scan showing both ROIs in the grey (**a**) and in the white matter (**b**). These ROIs are used for FA and GFA quantifications.

Results

Detection of multiple pathways

After processing the data and extracting ODF maxima, a major diffusion direction was almost exclusively detected in the white matter along the rostro-caudal axis. This result was expected since major ascending and descending fibres follow this orientation. As an example, Figure 5.2b illustrates the diffusion properties in the ventral white matter. More interestingly, other directions were observed within the spinal cord grey matter, as described hereafter. A medio-lateral direction was obtained in a region including the central canal and might correspond to commissural fibres (Figure 5.2c). These axons, linking both sides of the spinal cord grey matter, notably originate from grey matter interneurons and cross to the opposite side through the anterior commissure. Note that this lateral direction has already been identified in previous studies through the use of the diffusion tensor (Mamata et al., 2006; Schwartz et al., 2005d). A third direction dorso-ventrally oriented was observed and might correspond to fibres

coursing from the dorsal to the ventral horn (Figure 5.2d). These axons arise from the projection of dorsal roots (sensory afferents) at several spinal levels. Some of them project on motoneurons located in the ventral horn directly or through various synaptic pathways. There could also be terminal fibres of descending tracts that reach different spinal laminae within the grey matter.

To appreciate the evolution of reconstructed ODF across slices, extracted maxima are provided in Figure 5.3. For each slice, we delineated white and grey matter and counted the number of detected peaks. We expected mostly one peak in the white matter region, and 2 to 3 peaks in the grey matter region, given the presence of collateral and dorso-ventral fibres. Results are provided in Figure 5.4. As expected, a large majority of voxels in the white matter were subject to a unique diffusion direction, in a very consistent fashion across slices. In the grey matter however, we expected the number of peaks to vary across slices since sensory afferents project at specific rostro-caudal levels only. However, it was hard to relate the anatomical spinal level with the actual peak count for two reasons. First, projections of sensory afferents are spread throughout a certain rostro-caudal extent, thus making it hard to assess the consistency of level-dependent dorso-ventral diffusion direction. Second, slice thickness was 3 mm, which certainly induced a non negligible partial volume effect of the detected diffusion directions.

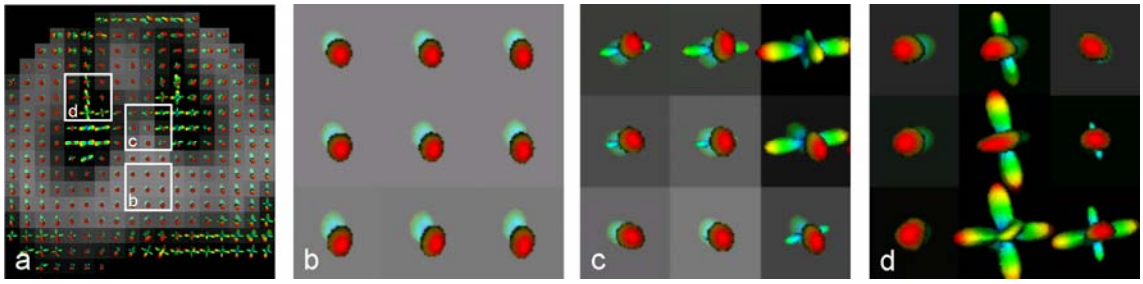

Figure 5.2. Mapping of q-ball ODF in the spinal cord

a: Results of QBI in the spinal cord. ODFs were overlaid on an axial GFA map (top is dorsal, left is left). Zoomed panels show ODFs in the ventral white matter (**b**), in the central canal (**c**) and in the right grey matter posterior horn (**d**). ODF colour code goes from red to blue for maximal to minimal values on the sphere, respectively. Also, the radius of the ODF is proportional to its value on the sphere.

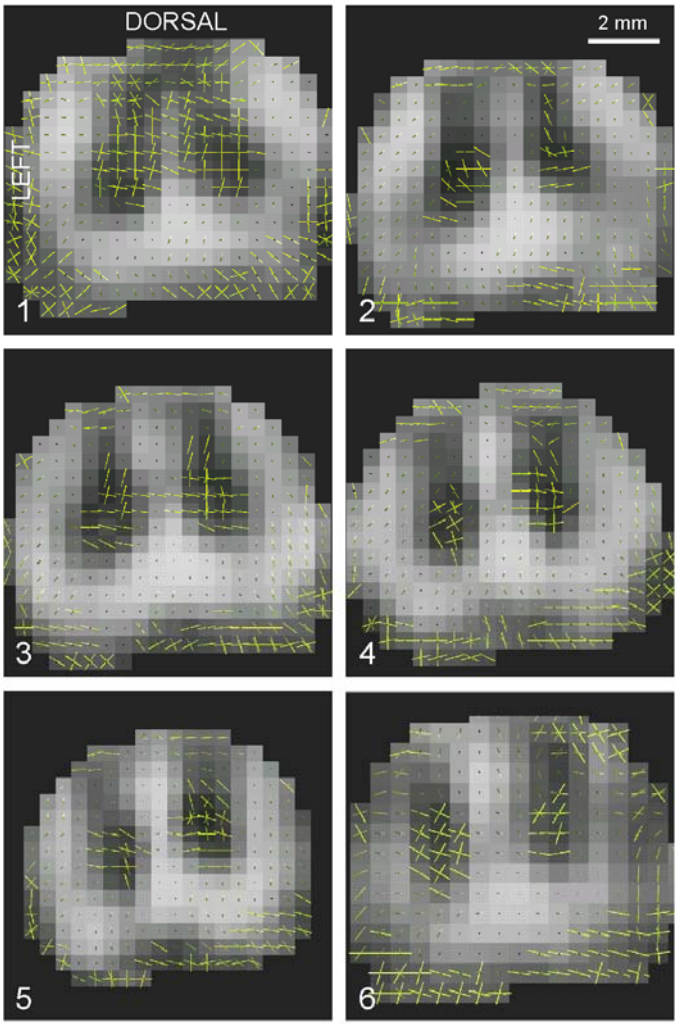

Figure 5.3. Evolution of diffusion maxima across slices

Comparison of extracted maxima along the cord. Each axial slice is 3 mm thick, covering a rostro-caudal region 18 mm long, centred at L5. Slices are numbered from 1 to 6, the most rostral slice being 1.

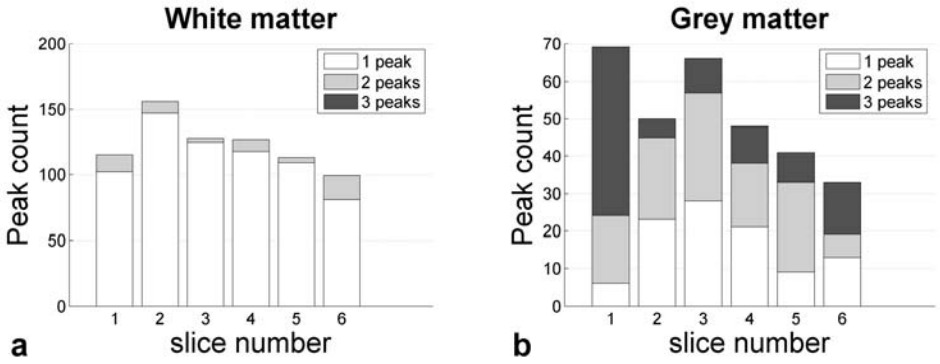

Figure 5.4. Number of diffusion directions in spinal cord white and grey matter

Peaks count in the white (**a**) and grey matter (**b**) of extracted maxima in every slice showed in Figure 5.3. Counting was based on a manual segmentation of the white and grey matter.

Comparison between DTI and QBI

To evaluate the benefits of QBI over DTI, we compared both approaches by selecting a region including the three major directions that were observed previously, *i.e.*, longitudinal, lateral and dorso-ventral. As expected, tensors yielded a very anisotropic profile in the white matter, pointing in the longitudinal direction (Figure 5.5c bottom-right). Quantifications of the first eigenvector's components confirmed that observation (Vz in Figure 5.5b). Similarly, ODFs presented one unique direction (Figure 5.5d bottom-right).

However, in the grey matter central canal the disk shape of tensors suggests two first eigenvalues of the same order (yellow ellipsoids in Figure 5.5c top-right). Quantification of the tensors' first eigenvector components indeed showed an increase of water diffusion in the lateral direction (Vx in Figure 5.5b). Using QBI, one can clearly distinguish these two major diffusion directions (Figure 5.5d top-right). When looking at a region more lateral than the central canal, tensors tend to become spherical, which indicates an apparent loss of FA with no clear principal diffusion direction. This region of the grey matter is known to be the site of intermingled fibres coursing in various directions. However, longitudinal and lateral pathways are still present. It resulted in first eigenvectors having components in the three directions (Figure 5.5b). This intravoxel heterogeneity was better described by ODFs which pointed in the longitudinal, lateral and antero-posterior directions (Figure 5.5d top-left).

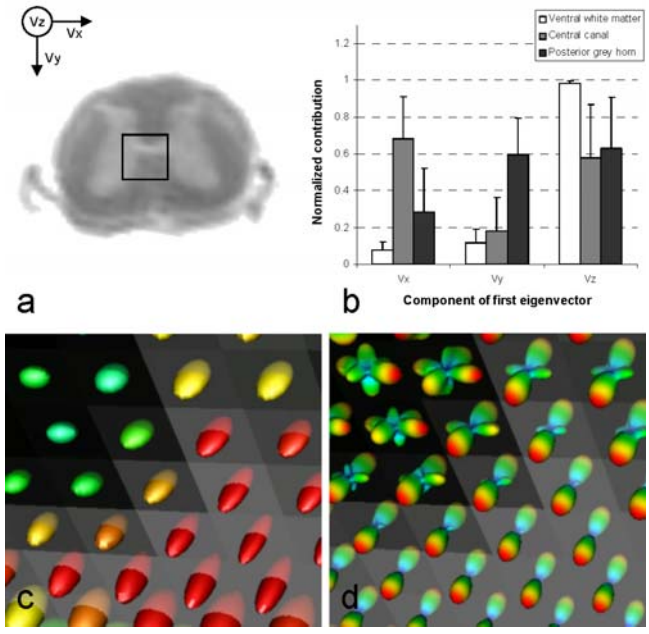

Figure 5.5. Comparison of DTI and QBI

a: Axial anatomical MRI with a selected region including the white matter, the central canal and partially the dorsal and ventral horn. **b**: Components of diffusion tensors first eigenvector in three different regions of the cord. Overlay of DTs (**c**) and ODFs (**d**) for the selected region of interest over a GFA axial slice. DT colour code goes from red to green for maximum anisotropy to minimum anisotropy, respectively. QBI shows benefits over DTI for retrieving regions that are prone to crossing fibres.

In vivo spinal cord

In vivo datasets were of high enough quality to delineate white and grey matter – in the case of PD images – and to apply the fibre ODF reconstruction method – in the case of EPI-based DW images. SNR was estimated as the mean signal in the cord divided by the standard deviation of the background noise. For PD images, SNR was 93.13 *ex vivo* and 71.28 *in vivo*. For EPI (b=0) images, SNR was 116.15 *ex vivo* and 83.01 *in vivo*.

As in *ex vivo* data, detection of multiple directions was possible from the *in vivo* cat. Figure 5.6 shows q-ball ODFs estimated from the acquisition made at 55 directions. The coronal view clearly shows a principal direction along the rostro-caudal axis in the spinal cord white matter, and a lateral direction in the grey matter (Figure 5.6b). When looking at axial views, ODF shapes look very similar to those observed from the *ex vivo* acquisition (Figure 5.6c-f), although diffusion profiles are less sharp due to the lower b-value. Medio-lateral as well as antero-posterior directions were observed, corresponding to commissural and sensory afferents, respectively. Note that we chose to illustrate regions centred at L5 since this is where the spinal cord is the largest (~10 mm lateral, ~7 mm antero-posterior), thus yielding a relatively clear delineation between white and grey matter at that spatial resolution.

For comparison purposes, we also provide FA and GFA quantifications for both *ex vivo* and *in vivo* datasets (see Table 5.1.). Although cats and acquisition parameters were different (b-value, number of gradient encoding directions, TR/TE, bandwidth, etc.), FA values in the white matter were significantly higher in the *in vivo* than that in the *ex vivo* sample (P<0.005), which is consistent to what was already reported in the rat spinal cord (Madi et al., 2005). More interestingly, if we use the empiric relationship linking *in vivo* and *ex vivo* FA, as observed by Madi *et al.* and defined as

$$FA_{\text{in vivo}} = 1.214 \times FA_{\text{ex vivo}} \tag{5.4}$$

the *in vivo* estimated values were in very close agreement to the actual *in vivo* measurements for both the FA and GFA.

	White matter		**Grey matter**	
	FA	GFA	FA	GFA
ex vivo	0.33 ± 0.20	0.61 ± 0.35	0.14 ± 0.09	0.05 ± 0.08
in vivo	0.42 ± 0.14	0.75 ± 0.49	0.10 ± 0.04	0.07 ± 0.07
*in vivo**	0.40 ± 0.24	0.74 ± 0.42	0.17 ± 0.11	0.06 ± 0.10

Table 5.1. FA and GFA quantifications

Comparison of anisotropy measurements between ex vivo and in vivo data (first two lines). Values are given as mean ± standard deviation within a tissue-dependent mask. The mask was centred at L5 for both datasets, and contained 24 axial slices corresponding to about 2 cm in the rostro-caudal direction. The third line of the array corresponds to the in vivo value estimated empirically (Madi et al., 2005).

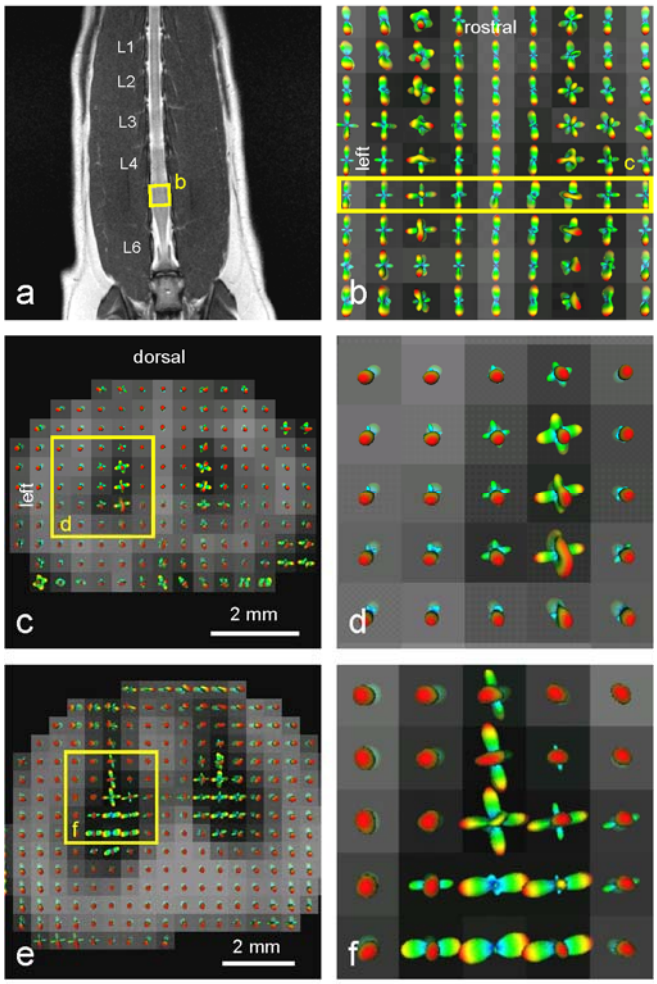

Figure 5.6. QBI results from in vivo data

Results of QBI from an *in vivo* cat. **a**: Coronal view of the anatomical image showing lumbar levels L1 to L7. **b**: Coronal view of the GFA map centred at L5, with an overlay of ODFs. The central and vertical light-grey line corresponds to the white matter. Within that region ODFs show one principal diffusion direction oriented along the rostro-caudal axis. Both lateral vertical dark-grey paths correspond to the grey matter. Within that region ODFs show an additional diffusion direction oriented right-left. **c**: Axial view of the GFA map centred at L5, with an overlay of ODFs. **d**: Zoomed panel from picture c showing the left grey matter. **e**: Axial view of the GFA map derived from the *ex vivo* acquisition, with an overlay of ODFs. The axial slice is centred at L5 with the same orientation as previously (top-left is dorsal-left). **f**: Zoomed panel from the *ex vivo* slice showing the left grey matter. Note that the scale is slightly different due to the in-plane resolution which was different *in vivo* and *ex vivo* (both were 2× interpolated).

Impact of b-value

The choice of b-value is related to the attenuation of moving protons in each of the diffusion weighting directions. Small b-values produce high signal but low angular resolution. On the contrary, large b-values provide better angular resolution but MRI signal recorded from moving protons is more attenuated, yielding lower signal. The b-value should then be carefully set given the q-space sampling. In the *ex vivo* study, we did three acquisitions at 100 directions using b-values of 1000, 2000 and 3000 s/mm^2. Results showed that with such a high sampling rate, low b-values yield maxima in the dorso-ventral direction, which might be incorrect when observing the central canal region (Figure 5.7b). Indeed, no fibres are known to course in the antero-posterior direction at that precise location. On the contrary, higher b-values tend to decrease the number of maxima in the area of commissural fibres (Figure 5.7d). Note that inconsistent maxima could be due to noisy ODF reconstruction.

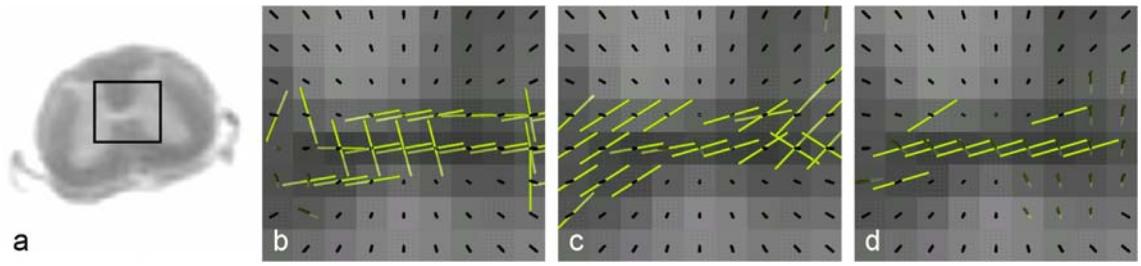

Figure 5.7. Impact of b-value on ODF estimation

Impact of b-value on ODF estimation. **a**: Axial anatomical MRI with a selected region centred on the central canal (top is dorsal). Comparison of ODF maxima for b-values of 1000 (**b**), 2000 (**c**) and 3000 s/mm^2 (**d**). Maxima are overlaid on a GFA map estimated from data at 3000 s/mm^2. Maxima were extracted using a finite difference on the ODF mesh, considering values superior to 0.5.

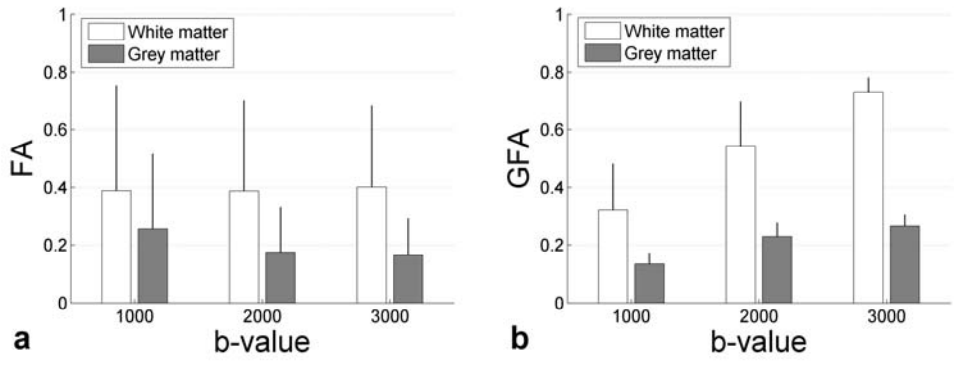

Figure 5.8. GFA quantifications at various b-values

Fractional anisotropy (**a**) and generalized fractional anisotropy (**b**) quantification in the white and grey matter at various b-values (given in s/mm^2). Bars and error-bars indicate the mean and standard deviation, respectively. Masks used for quantifying those metrics in the white and the grey matter were the same across b-values, enabling consistent comparison.

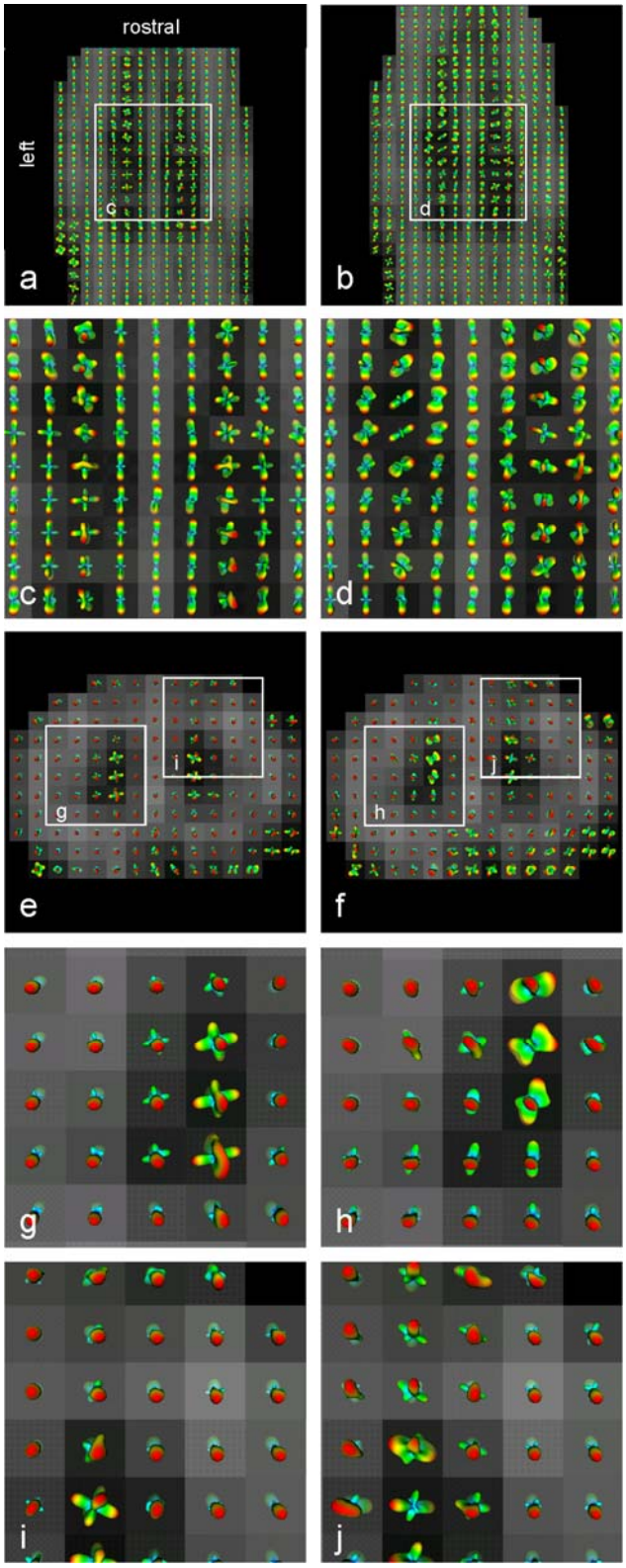

Figure 5.9. Impact of q-space sampling

Impact of diffusion direction sampling. ODFs were computed from *in vivo* data acquired at 55 (left column) and 28 (right column) directions. Both columns show GFA maps computed from the 55 directions dataset (the purpose here is to compare ODFs and not GFA measurements). **a,b**: Coronal slice centred at L5, half cutting the spinal cord. **c,d**: zoomed window centred on the central canal. **e,f**: axial slice (top is dorsal). **g,h**: zoomed window centred on the grey matter left ventral horn. **i,j**: zoomed window centred on the dorsal right region, where afferent dorsal roots project into the spinal cord grey matter.

Quantifications of anisotropy at various b-values yielded interesting results (see Figure 5.8). In the white matter, which is a highly anisotropic region having mostly a unique diffusion direction, FA did not significantly vary across b-values in the white matter. Only the standard deviation decreased when b-value increased, indicating a better specificity of the measured anisotropy. However, GFA increased with b-value which confirmed previous observations, *i.e.*, higher b-values tend to decrease the number of maxima, thus increasing the specificity as well. Similarly, quantifications in grey matter showed an increase of GFA with b-value. These results raise the question of how to report GFA measurement, since the latter strongly varies with the choice of b-value, as investigated for the FA (Melhem et al., 2000).

Impact of diffusion direction sampling

To appreciate the impact of diffusion direction sampling on QBI, *in vivo* data were acquired at 28 and 55 directions using a polyhedron sampling scheme (Madi et al., 2005). Knowing that increasing the number of direction impacts the SNR, we compared both data at equivalent scan time, as done in (Jones, 2004; Landman et al., 2007; Ni et al., 2006). We used 4 repetitions for data acquired at 28 directions and 2 repetitions for data acquired at 55 directions. ODFs were estimated at order $L = 4$ using the same regularization criterion (see section Q-ball estimation). ODFs for both datasets are shown in Figure 5.9. On the coronal view, both sampling schemes yielded principal diffusion directions along the rostro-caudal axis in the white matter. However, medio-lateral directions were better depicted at 55 directions (Figure 5.9c-d). Looking at axial views, the detection of medio-lateral as well as dorso-ventral directions was again better at 55 directions (Figure 5.9g-j).

Discussion

Benefits of QBI for the spinal cord

As demonstrated in this study, QBI can retrieve crossing fibre information in the spinal cord, whereas the DTI approach is constrained by its single diffusion direction. Although the second eigenvector might be used to account for crossing fibres in the brain (Wiegell et al., 2000) and in the spinal cord (Mamata et al., 2006), there is a restriction imposed by the tensor itself. When the primary direction is defined by the principal eigenvector, the second eigenvector is limited in degrees of freedom since its direction is necessarily on the plane orthogonal to the longitudinal fibres. In the presence of non orthogonal fibres, the usual way of decomposing the tensor becomes less efficient (Alexander et al., 2001). Moreover, when a voxel contains more than one diffusion direction, one can not rely on the first eigenvector's orientation anymore since the latter results from a linear combination of major diffusion directions. Knowing that spinal cord architecture is not only oriented rostro-caudal and that today's MRI acquisition provides a spatial resolution on the order of the millimetre, HARDI reconstruction schemes such as QBI aim at representing this subtle intravoxel heterogeneity.

Validation

A few words should however be said about the validation of this technique. There have been attempts to validate QBI in non-biological phantom preparations (Perrin et al., 2005). However, in biological tissue the validation step is complex as it involves tract tracing (Lin et al., 2003; Schmahmann et al., 2007). The focus of the present study was to propose a methodology to acquire *ex vivo* and *in vivo* HARDI data in the spinal cord, and to estimate ODFs with robust algorithms. We showed that some extracted maxima were very consistent with the known anatomy of the spinal cord. In future study, the validation aspect will be investigated more deeply.

Impact of voxel shape

In vivo acquisitions were performed using isotropic voxel of 1.1 mm^3. As mentioned in (Cohen-Adad et al., 2008b), this was done to limit any bias in the determination of major diffusion directions. However, *ex vivo* acquisitions were performed using a ratio between in plane resolution and slice thickness of 1:3 and 1:4.6. This heterogeneity had certainly induced a relative increase of the diffusion-weighted SNR in the Z direction, which was aligned with the longitudinal direction of the cord. Such a choice of voxel shape resulted from a compromise between the axial resolution and the SNR which had to be high enough to yield consistent ODF reconstruction. Since the present study aimed at depicting the axial heterogeneity in terms of diffusion directions, we chose to image at very high in plane resolution (up to 650×650 μm^2) thus imposing an anisotropic voxel shape. We are conscious that the ODF reconstruction was biased in terms of absolute directionality (*i.e.*, longitudinal versus transverse diffusion profile), however in plane components of the ODF were still informative for detecting collaterals and dorso-ventral pathways. Moreover, ODF profiles derived from *ex vivo* and *in vivo* datasets looked very similar and showed consistent collaterals in all cases, *i.e.*, ratio between in plane resolution and slice thickness of 1:1, 1:3 and 1:4.6. In the future, we however recommend the use of an isotropic voxel shape when the aim is to explore the anatomical structure of the white matter without bias.

Strategy for optimal b-value and q-space sampling

Looking at the comparison of three different b-values, results showed more extracted maxima for lower b-values. However, some maxima were not consistent with the known architecture of the spinal cord's axonal pathways. Although partial volume effect might explain the presence of false positives, another argument should be considered. As supported by (Ronen et al., 2005), the results presented here suggest that low b-values increase the sensitivity for retrieving diffusion directions but reduce their specificity.

Regarding the optimal number of directions to apply for q-space sampling, results obtained in the *in vivo* study suggest a real benefit of data acquired in 55 directions versus 28 directions. In DTI, there is an ongoing debate whether increasing the number of directions over

a certain threshold yields significant benefits for modelling diffusion (Hosey et al., 2005; Jones, 2004; Lee et al., 2006; Ni et al., 2006). In the case of model-free approaches, HARDI data are of clear interest, since a much higher number of degrees of freedom is permitted for estimating the ODF (Perrin et al., 2005; Poupon et al., 2007). However the trade-off is the acquisition duration. Further studies are required for optimizing these sensitive parameters.

Local HARDI reconstruction

The study of local HARDI reconstruction methods is currently an active field of research (Alexander, 2005; Descoteaux, 2008). We have shown the benefits of QBI and the usefulness of the diffusion ODF (dODF) and fibre ODF (fODF) reconstruction. It is important to note that there are other techniques using spherical deconvolution and multiple fibre models that also aim at reconstructing the fODF (Descoteaux, 2008; Jian and Vemuri, 2007). More complicated methods are available that aim at reducing the numerical instabilities and errors that are known to occur in the spherical deconvolution process. Each of these techniques have different underlying assumptions but seem to produce very similar fODF profiles (Descoteaux, 2008). More involved comparisons are needed to decide what reconstruction is more appropriate for what application.

Perspectives

The present study has been performed in cats. Although subject positioning, coil arrangement and also motion patterns might be somehow different, HARDI acquisition are theoretically feasible in the spinal cord of other mammals, including humans. Moreover, the proof of concept showing that the QBI method is able to depict non-longitudinal fibres naturally applies to other mammals. Also note that the use of a higher magnetic field could improve greatly the sensitivity of detecting collateral fibres, as demonstrated in the human brain (Mukherjee et al., 2008).

From a neurophysiological perspective, the next step is to evaluate the method in cats with spinal cord injury, using the added value of tractography. It will aim at understanding white matter reorganization after lesion and possibly after various treatments or training methods have been applied to regain locomotion (Rossignol, 2006b). Indeed, there may be regeneration of damaged axons or collateral sprouting of axons in spared descending/ascending pathways or primary afferents (Kerschensteiner, 2007). These new growths can project through different spinal paths as they are forming new circuits and adopt unpredicted trajectories as they by-pass the scar tissue (Bareyre et al., 2004; Fouad and Pearson, 2004). Such subtle reorganisation, involving a limited number of axons, might be invisible to the principal eigenvectors usually represented in DTI. The present study thus provides an incentive to use both HARDI and QBI to represent the diffusion process in the healthy and injured spinal cord.

Acknowledgement

We thank H. Leblond and J. Provencher for the cat preparation, J. Doyon for providing support from the UNF, C. Hurst for assistance with MRI acquisitions, and C. Gauthier for her revision of the manuscript. We also thank the reviewers for their precious comments. This work was supported by the Canada Research Chair on the Spinal Cord provided by the Canadian Institute of Health Research (CIHR) to S. Rossignol and by the Multisdisciplinary Team on Locomotor Rehabilitation (Regenerative Medicine and Nanomedicine, CIHR). J. Cohen-Adad has a fellowship from the Fondation pour la Recherche Médicale (FRM, France) and from the Groupe de Recherche sur le Système Nerveux Central (GRSNC, Université de Montréal).

6. Article #3: Investigations on spinal cord fMRI of cats under ketamine

J. Cohen-Adad[1,2], R.D. Hoge[3,4,6], H. Leblond[1,4], G. Xie[1], G. Beaudoin[7], A.W. Song[8], G. Krueger[9], J. Doyon[3,4,5], H. Benali[2,3], S. Rossignol[1,4]

[1]*GRSNC, Faculty of Medicine, Université de Montréal, Montreal, QC, Canada*
[2]*INSERM U678, Université Pierre et Marie Curie (Paris VI), CHU Pitié-Salpêtrière, Paris, France*
[3]*Unité de Neuroimagerie Fonctionnelle, CRIUGM, Université de Montréal*
[4]*Multidisciplinary Team in Locomotor Rehabilitation (CIHR), Canada*
[5]*Departement of Psychology, Université de Montréal, Montreal, QC, Canada*
[6]*Institute of Biomedical Engineering, Université de Montréal, Montreal, QC, Canada*
[7]*Department of Radiology, Centre Hospitalier de l'Université de Montréal (CHUM), Montreal, QC, Canada*
[8]*Brain Imaging and Analysis Center, Duke University, Durham, NC, USA*
[9]*Siemens Medical Solutions, Erlangen, Germany*

Published in NeuroImage. Received 23 June 2008; revised 5 August 2008; accepted 15 September 2008; Available online

Preface

Given the relatively poor number of people succeeded in reporting activations in the spinal cord using BOLD fMRI, given the controversies and the fact that very few groups detected neuronal activity using the SEEP effect and given the large consensus about the low reproducibility and robustness of spinal cord fMRI, the purpose of this article was to investigate the reproducibility of BOLD responses in the spinal cord of anaesthetized animals. This work has been submitted to NeuroImage (Cohen-Adad et al., 2009a). It has also been published in abstract forms (Cohen-Adad et al., 2006a; Cohen-Adad et al., 2006b). My contribution to this article was to develop the methodology, to acquire the data, to process the data and to write the article. Co-authors of this article and their individual contribution are listed hereafter:

Richard D. Hoge has been involved in actively reviewing the manuscript as well as in providing useful comments on MRI acquisitions.

Hugues Leblond has been involved in the cats' implantation, anaesthesia and positioning in MRI.

Guoming Xie has been involved in the cats' anaesthesia and monitoring.

Gilles Beaudoin has been involved in the early stage of experiments by providing useful comments on MRI acquisitions.

Allen W. Song has been involved in the early stage of experiments by providing useful comments on MRI acquisitions.

Gunnar Krueger has been involved in the early stage of experiments by providing useful comments on MRI acquisitions.

Julien Doyon has been involved in actively reviewing the manuscript.

Habib Benali is my co-supervisor and has been involved in providing useful comments on data processing.

Serge Rossignol is my co-supervisor and has been involved in actively reviewing the manuscript as well as in providing useful comments on neurophysiology.

Abstract

Functional magnetic resonance imaging (fMRI) of the spinal cord has been the subject of intense research for the last ten years. An important motivation for this technique is its ability to detect non-invasively neuronal activity in the spinal cord related to sensorimotor functions in various conditions such as after spinal cord lesions. Although promising results of spinal cord fMRI have arisen from previous studies, the poor reproducibility of activations and their characteristics remain a major drawback. In the present study we investigated the reproducibility of BOLD fMRI in the spinal cord of cats (N=9) by repeating the same stimulation protocol over a long period (~2 hours). Cats were anaesthetized with ketamine, and spinal cord activity was induced by electrical stimulation of cutaneous nerves of the hind limbs. As a result, task-related signals were detected in most cats with relatively good spatial specificity. However, percent signal change varied between cats and between sessions in the same cat. This variability was notably attributed to the moderate intensity of the stimulus producing a haemodynamic response of low amplitude, variation in end-tidal CO_2 during the session, low signal-to-noise ratio (SNR) in spinal fMRI time series and animal-specific vascular anatomy. Original contributions of the present study are: (i) first spinal fMRI experiment in ketamine-anaesthetized animals, (ii) extensive study of intra- and inter-subject variability of activation, (iii) characterisation of static and temporal SNR in the spinal cord and (iv) investigation on the impact of CO_2 end-tidal level on the amplitude of BOLD signal.

Keywords: fMRI, spinal cord, cat, bold, reproducibility, noise, CO2

Introduction

Functional magnetic resonance imaging (fMRI) allows non-invasive detection of neuronal activity. It has been applied to the spinal cord of animals and humans for the last ten years (Lammertse et al., 2007; Stroman, 2005). Such a technological development is of interest in a clinical perspective, notably for determining actual sensorimotor changes in the spinal cord following an injury (Kornelsen and Mackey, 2007). Moreover, given the spinal cord changes occurring with time after a lesion, fMRI would allow longitudinal studies in animals with spinal injuries and could help to detect underlying plastic physiological processes leading for instance to locomotor recovery (Frigon and Rossignol, 2006; Rossignol, 2006a).

Previous studies have shown that fMRI can detect motor (Backes et al., 2001; Giulietti et al., 2008; Govers et al., 2007; Komisaruk et al., 2002; Kornelsen and Stroman, 2004, 2007; Madi et al., 2001; Maieron et al., 2007b; Ng et al., 2006; Ng et al., 2008; Stroman and Ryner, 2001; Yoshizawa et al., 1996) and sensory (Brooks et al., 2008; Endo et al., 2008; Lawrence et al., 2004; Lawrence et al., 2008b; Li et al., 2005; Lilja et al., 2006; Majcher et al., 2006; Malisza and Stroman, 2002; Moffitt et al., 2005; Porszasz et al., 1997; Stroman et al., 2004; Stroman et al., 2005a; Zhao et al., 2008) activation in the spinal cord. Although most published studies have used a new type of contrast based on signal enhancement by extravascular protons (SEEP) (Stroman et al., 2003b), few studies succeeded in reporting activations in the spinal cord based on blood oxygenation level dependent (BOLD) (Backes et al., 2001; Brooks et al., 2008; Endo et al., 2008; Giove et al., 2004; Giulietti et al., 2008; Govers et al., 2007; Lilja et al., 2006; Madi et al., 2001; Maieron et al., 2007b; Stroman et al., 1999; Yoshizawa et al., 1996; Zhao et al., 2008). The poor reproducibility of the activation patterns and their characteristics – in terms of amplitude and location of BOLD signal – have been invoked as significant concerns by several authors (Backes et al., 2001; Brooks et al., 2008; Giove et al., 2004; Govers et al., 2007; Zhao et al., 2008). In spite of these difficulties, we believe it is worth understanding why detecting the BOLD effect is so challenging in the spinal cord, given that this technique has been successfully used by neuroscientists in other regions of the central nervous system for the last 18 years. Moreover, we think it is important for the community to be able to conduct comparative fMRI studies between the brain and the spinal cord using a similar contrast. The main difficulties in spinal fMRI arise from the small size of the spinal cord, the presence of large movements due to cardiac pulsation and respiration (Brooks et al., 2008; Figley and Stroman, 2007) and magnetic field inhomogeneities around inter-vertebral disks, which induce significant susceptibility artifacts (Cohen-Adad et al., 2007d).

In the present study, we investigated the reproducibility of BOLD fMRI in the spinal cord by repeatedly performing the same stimulation protocol during long sessions of acquisition (~2 hours). We used a ketamine-anaesthetized cat preparation (N=9) and low-level electrical stimulation of hind limbs cutaneous nerves. Image quality was quantitatively assessed using signal-to-noise ratio (SNR) and temporal SNR indices, as done in recent brain fMRI studies (Bellgowan et al., 2006; Bodurka et al., 2007; Triantafyllou et al., 2005). We also investigated

the impact of end-tidal CO_2 level over amplitude of BOLD signal. Results of this fMRI study showed focal activation with good spatial specificity. The relatively low intra- and inter-subject reproducibility was partially attributed to the low stimulus intensity, noise characteristics and end-tidal CO_2 variations. Parts of these results have already been published in abstract form (Cohen-Adad et al., 2006b).

Material and methods

Animal preparation and stimulation protocol

Experiments were conducted in accordance with the Ethics Committee of the Université de Montréal. To investigate the inter-subject reproducibility of fMRI results, acquisitions were conducted in nine cats. To induce electrical stimulations in the hind limbs, five cats were chronically implanted with *in situ* polymer cuff electrodes around either the superficial peroneal nerve innervating the dorsum of the foot, or the tibial nerve innervating the plantar surface of the foot. The four other cats were implanted with subcutaneous electrodes on the dorsal aspect of the hind feet. All cats were first anaesthetized with isoflurane (2%) in a mixture of 95% O_2 and 5% CO_2, through an intratracheal tube. Anaesthetic was then switched to ketamine (10 $mg.kg^{-1}.h^{-1}$ intravenous). The stimulation threshold was estimated after positioning the cat in the scanner to avoid any electrode displacement. By varying the stimulation intensity, we evaluated the threshold current needed to evoke a twitch. This value was then used as a reference stimulus (threshold) for each cat. Thresholds were 0.15 ± 0.09 mA for nerve stimulation and 3.19 ± 1.8 mA for subcutaneous stimulation (mean values across cats). During fMRI experiments, stimuli were sent at a frequency of 0.5 Hz and consisted of 50-100 ms trains of 1 ms pulses. The frequency of pulses within train was 100-300 Hz. To increase the sensitivity of detecting BOLD signal without eliciting noxious responses, stimulation intensity was set to twice the threshold. For three cats, the intensity of the stimulation varied from one to five times the threshold to study the impact of increasing the stimulation strength on BOLD amplitude. Following stimulus threshold evaluation, cats were paralyzed with pancuronium (0.2 $mg.kg^{-1}.h^{-1}$ as the initial dose and 0.1 $mg.kg^{-1}.h^{-1}$ for maintenance) and ventilated mechanically (Magellan-2200 Model 1, Oceanic Medicial Products, USA). End tidal CO_2 was continuously monitored using a Datex apparatus (Datex Normocap 200, Denver, USA).

MRI acquisition

All MRI data were acquired on a Siemens Trio system (3T). Cats were positioned feet-first-supine as described in (Cohen-Adad et al., 2008b). In four cats, we used the 8-channel spine array coil. In five other cats, we used a single-channel human knee coil. The choice of coil was dictated by the size and degree of immobilization in a given cat. Although the sensitivity profiles of both antennas are very different, images produced using these two different coils were similar in terms of SNR and homogeneity, as were measured in the lumbar spinal cord region. Each fMRI run was 10 minutes long and consisted of a block-design, alternating

between 60 s of rest and 60 s stimulation. To investigate the intra-cat reproducibility, runs were repeated between eight and eleven times, depending on each cat's tolerance of the anaesthetic over time. This resulted in a scan session duration of just under three hours, including cat positioning, stimulation threshold estimation, localizer, anatomical and functional scans.

Anatomical scans were conducted using a 3D MPRAGE sequence with the following parameters: sagittal orientation, 112 slices, TR = 1800 ms, TE = 3.53 ms, nominal inversion time = 900 ms, flip angle = 9°, matrix = 256×256, voxel size = 0.75×0.75×0.75 mm^3, 2 averages, bandwidth = 240 Hz/pixel. Functional scans were conducted using a 4-shot gradient echo planar imaging (GE-EPI) sequence. Parameters were: sagittal orientation, 9 slices centred over the spinal canal and covering vertebral levels L1 to L7, phase-encoding anteroposterior, TR = 500 ms (time per image was 2 s), TE = 20-30 ms, flip angle = 45°, matrix = 96×96, voxel size = 2×2×2 mm^3, bandwidth = 1630 Hz/pixel. No parallel imaging was used for these scans. We chose to image using isotropic voxels to limit partial volume effects along the rostro-caudal axis and to investigate the point spread function of BOLD signal in the spinal cord. Given the relationship between vertebral and spinal levels (see Figure 6.1a), activation was expected primarily at vertebral level L4 and L5.

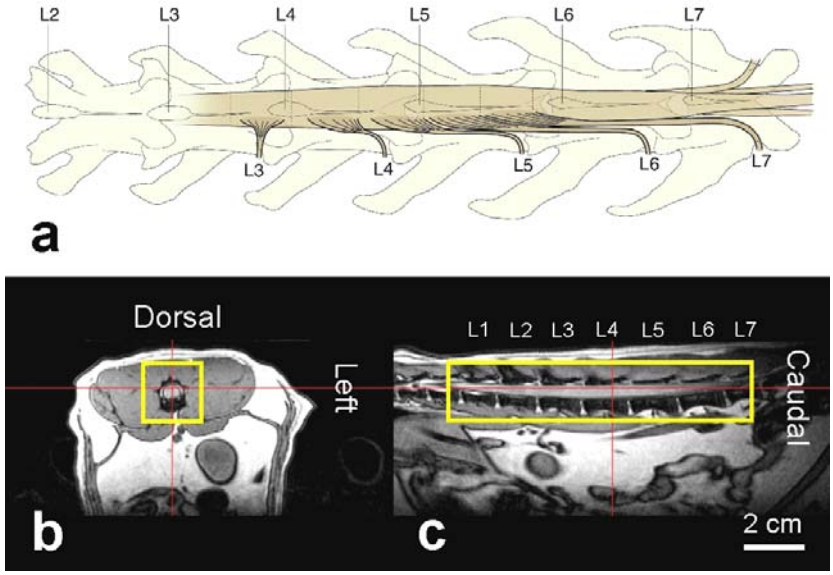

Figure 6.1. Mask used for the GLM

a: Correspondence between vertebral and spinal levels in the cat. This drawing illustrates how the spinal roots enter the vertebral canal and the levels at which they project. Labels at the bottom point to the roots as they enter or exit the vertebral canal through the intervertebral foramina whereas the labels on the top point to the mid spinous processes of each vertebra. Note that the projections of roots can be 1-2 segments rostral to the entry zone in the vertebral canal. **b,c**: Typical mask used for statistical analysis. The mask is overlaid in the axial and sagittal views and includes the spinal cord from levels L1 to L7, the cerebrospinal fluid, the vertebral column and adjacent muscles.

Data analysis

Image quality

Previous studies have shown that static SNR and temporal SNR have a significant impact on the sensitivity to detect BOLD activations (Bellgowan et al., 2006; Bodurka et al., 2007; Parrish et al., 2000; Triantafyllou et al., 2005). Static SNR (SNR_0) is associated with system and thermal noise intrinsic to MR signal, and is defined as a ratio of the average signal in the region of interest over background standard deviation. It thus represents the SNR of individual images. On the other hand, temporal SNR (tSNR) includes the time dimension. It is defined as a ratio of the average voxel time course signal over time course standard deviation (Krueger and Glover, 2001). It includes fluctuations of blood flow and volume, which depend on basal metabolism, cardiac and respiratory variations. In this study, we quantified both SNR_0 (corrected for Rayleigh distribution) and tSNR to evaluate the ability to detect BOLD signal in the spinal cord. We also computed the ratio of physiological noise variance σ_p to thermal noise variance σ_0 based on the following relationship

$$\frac{\sigma_p}{\sigma_0} = \sqrt{\left(\frac{SNR_0}{tSNR}\right)^2 - 1} \tag{6.1}$$

Computed measurements were compared with those reported in the literature (Triantafyllou et al., 2005), after adjusting for flip angle and voxel size. We think it is important to compare SNR in various conditions since BOLD effect is proportional to the baseline signal. Hence, showing differences in the brain versus in the spinal cord would help to understand the difficulties in finding significant activation in spinal cord fMRI.

Additionally, susceptibility artefacts were evaluated on the basis of distortions produced in raw EPI. We qualitatively assessed the shape of the cord on sagittal slices for each run and each session, as done in (Voss et al., 2006).

General linear model

Slice timing was first performed on fMRI time series to correct for the time shift between slices. Then, an appropriate rigid-body realignment was conducted by estimating the transformation matrix based on specific voxels (Cohen-Adad et al., 2007g; Stroman et al., 2004). These voxels were selected over the spine but not in regions prone to strong physiological motion, such as the kidneys and the air-abdomen interface. Then, each slice was spatially smoothed by convolving it with a 2-D Gaussian kernel (FWHM = 4 mm). A general linear model (GLM) approach was conducted using the SPM package (Friston et al., 1994a). The regressor of interest was built by convolving the block design matrix with the default canonical haemodynamic response function from SPM. We used a high-pass filter with cut-off at 128 s and a 1st order autoregressive model to account for autocorrelations mostly induced by cardiac fluctuations. To evaluate the false positive rate, we included in the analysis voxels not

only located within the spinal cord, but also those contained in the surrounding fat, cerebrospinal fluid (CSF), spine and muscles. A typical mask is shown in Figure 6.1b,c. Data from different runs were combined for each cat using a fixed-effect analysis.

ROI analysis within the spinal cord

We evaluated whether the spinal cord showed a spatially consistent pattern of activation. Based on the anatomical volume, regions of interest (ROI) were selected to include the whole lumbar spinal cord. After drawing ROIs in all the cats, each one was divided into seven sections corresponding to each vertebral level, *i.e.,* from L1 to L7. Then, T-scores based on fixed-effect analysis were averaged within each ROI. Following this procedure, we tested for differences between vertebral levels. For that purpose, Student's T-tests were conducted by comparing averaged activations between each adjacent pairs of vertebral levels (Kim and Cohen, 1998).

ROI analysis within focal activation

To quantify the variability of BOLD signal over time, an individual ROI was obtained for each cat by thresholding T-maps obtained from the fixed-effect analysis. Knowing that the resulting activations were expected to vary significantly among cats (Giove et al., 2004), this threshold was defined individually for each cat. Using that procedure, we adjusted the threshold to get about 30 voxels per activation cluster (*P* varied between 0.005 and 0.0005 depending on the cat). In the next step, the mean and standard deviation of percent signal change was quantified within each specific ROI for all runs. This enabled to study the evolution of functional activation across time.

Measurements of end-tidal CO_2

Since fMRI signals reflect changes in blood oxygenation, blood flow and blood volume, this relative measurement is highly sensitive to the basal vascular state (Stefanovic et al., 2006). There are many factors that impact the basal state, such as anaesthetics, respiration rate or blood pressure (Sicard et al., 2003). To address possible effects related to blood gas level, end-tidal CO_2 was recorded for each run and each session. The tube directed to the mechanical ventilator was split, and the second extremity was connected to an acquisition system which converted gas pressure into digital values (Datex Normocap 200, Denver, USA). A home-made program written in MATLAB® (R14, The Mathworks) detected CO_2 peak levels and averaged them for each run. Mean CO_2 levels were then compared to the mean percent signal change using a least square-based linear regression. A Fisher F-test was performed to test the linear relationship between these two parameters.

Results

Detection of task-related signal in the spinal cord

Focal activations were detected in seven out of nine cats at the L4-L5 vertebral level. This corresponds to the region to which the stimulated nerves project. T-maps for these cats are shown in Figure 6.2. In some cases, task-related signal was recorded within the aorta (Figure 6.2b, encircled in white). This false-positive signal could be due either to a change of blood flow at this specific region, or motion induced by non-skeletal muscles.

Assuming that BOLD signal mostly arises from local field potentials generated at the post-synaptic level (Logothetis et al., 2001), activations were expected to occur mainly at the L4 and L5 levels (see Figure 6.1). To evaluate the spatial specificity, T-scores were averaged within ROIs specific to the lumbar spinal cord, from L1 to L7. For most cats, mean T-scores within the spinal cord were highest at levels L4 and L5 (see Figure 6.3). This result demonstrated that the pattern of activation was consistent with the stimulated superficial peroneal and tibial nerves.

To extrapolate this quantitative measurement to the group level, we used results from the statistical test, measuring the difference between the mean level of activation of two adjacent vertebral levels. The method was similar to what was done in (Govers et al., 2007). We attributed a score corresponding to a certain level of significance: 1, 2 and 3 stood respectively for P=0.05, P=0.01, and P=0.005, while a null score stood for no significant difference between the mean activation of two adjacent vertebral levels. At the group level (N=9), the highest scores where obtained for pairs L6-L5 and L4-L3, suggesting that L4 and L5 where the most activated regions in the spinal cord (Table 6.1).

Despite the relatively good specificity along the cord, there was a poor inter-cat reproducibility of the activation location in the axial plane. In the anteroposterior direction, activated clusters were sometimes dorsal (Figure 6.2b,d), medial (Figure 6.2c,e,g) or ventral (Figure 6.2a,f). Also, lateralization was hard to assess since most activated clusters were located in the medial portion of the cord. Out of nine cats, only three showed a clear activation pattern ipsilateral to the stimulated nerves (Figure 6.2a,f,d). Furthermore, activated clusters were sometimes located slightly outside the spinal cord (Figure 6.2d,f).

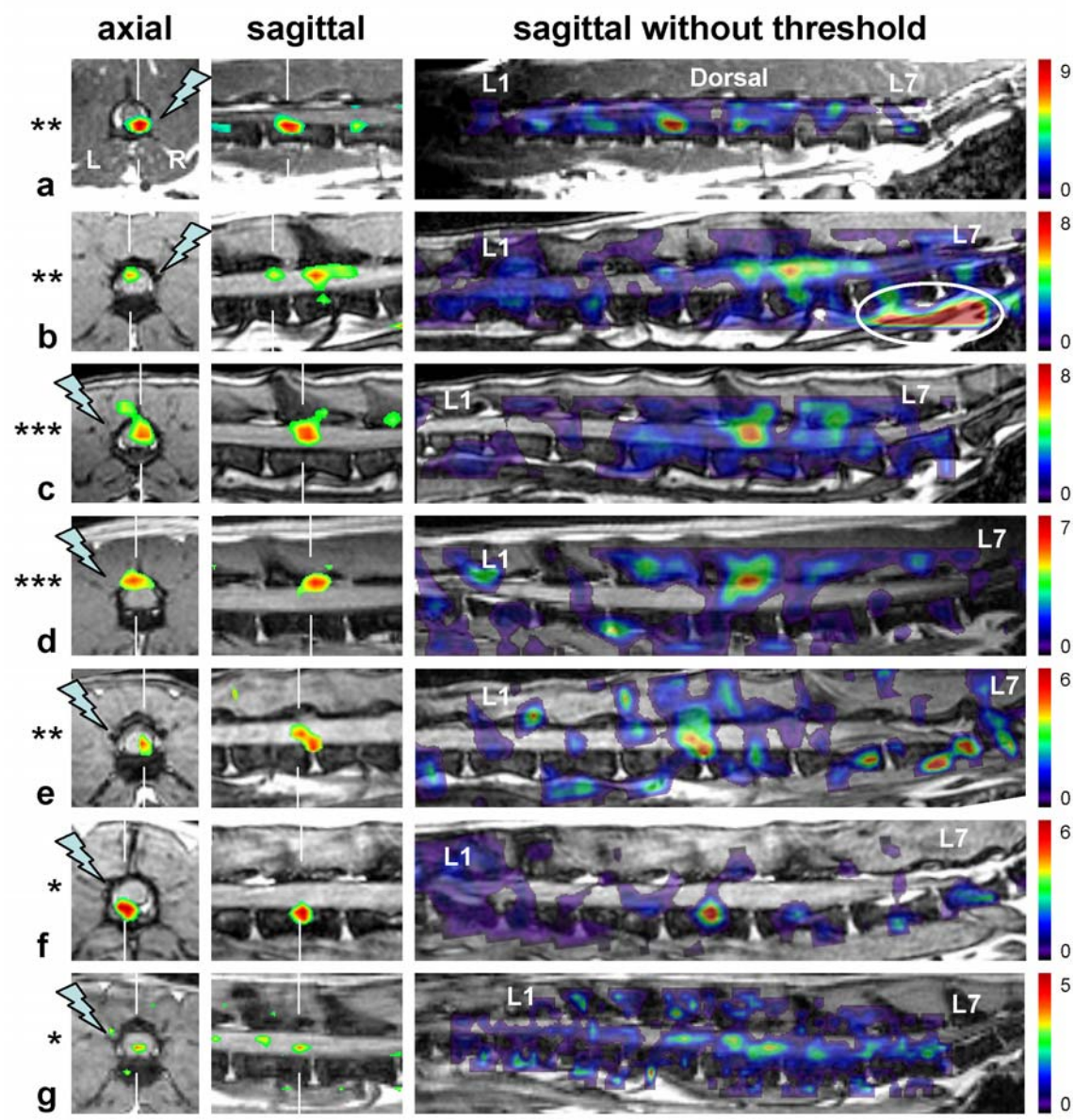

Figure 6.2. Fixed-effect results in seven cats

Axial (left column), sagittal (middle and right column) views of anatomical volumes are displayed, with an overlay of activation maps. Sagittal and axial slices are centred over the activation peak, and their location is represented as vertical white bars over the axial and sagittal view, respectively. T-score is indicated on the right, and the colour scaling is kept constant between columns. To appreciate the specificity of activation, T-maps with no positive threshold are provided. In maps where a threshold was applied, the cut-off is indicated on the left (*: $P<0.01$; **: $P<0.001$; ***: $P<0.0001$, not corrected). The laterality of electrical stimulation is indicated in the axial view. The presence of task-related signal at the level of the aorta is encircled in panel b.

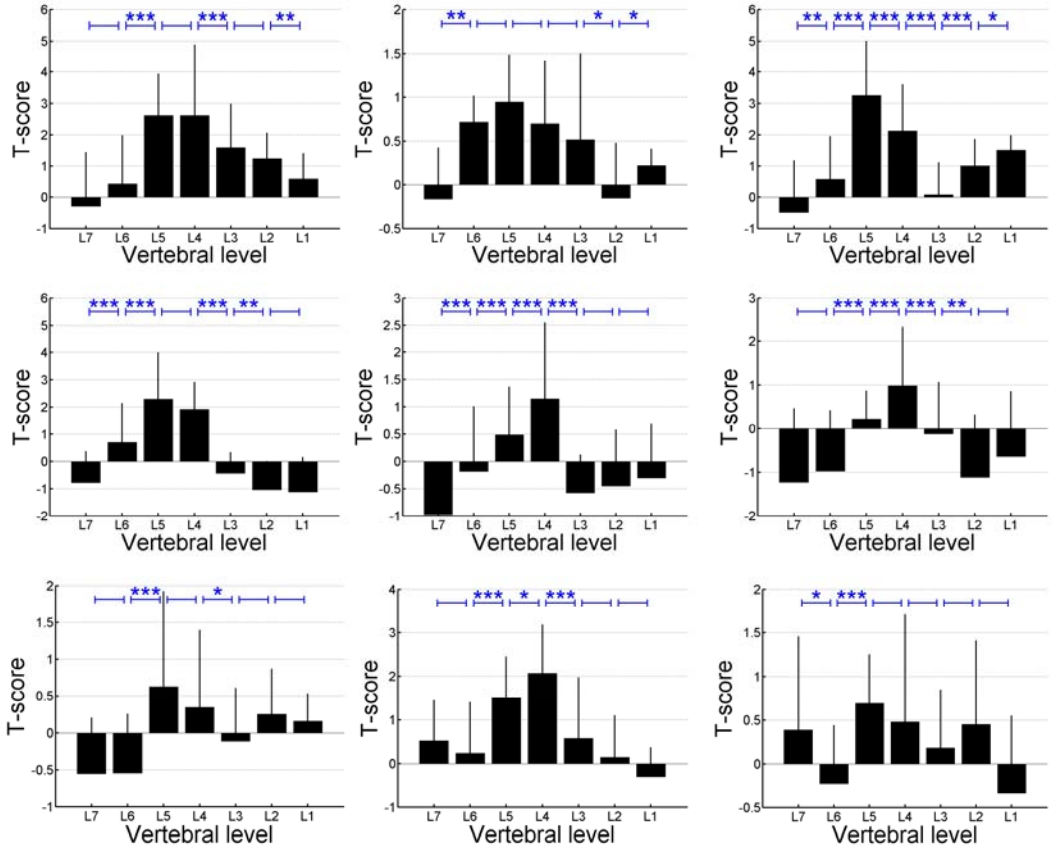

Figure 6.3. Quantification of T-scores along the spinal cord of the nine cats

Student's T-tests have been performed to compare averaged activation between each adjacent pairs of vertebral levels (***: P<0.005 ; **: P<0.01 *: P<0.05).

	L7-L6	L6-L5	L5-L4	L4-L3	L3-L2	L2-L1
cat #1	0	3	0	3	0	2
cat #2	2	0	0	0	1	1
cat #3	2	3	3	3	3	1
cat #4	3	3	0	3	2	0
cat #5	3	3	3	3	0	0
cat #6	0	3	3	3	2	0
cat #7	0	3	0	1	0	0
cat #8	0	3	1	3	0	0
cat #9	1	3	0	0	0	0
sum	**11**	**24**	**10**	**19**	**8**	**4**

Table 6.1. Weighting table of activation between adjacent vertebras

Weighting table of activation differences between vertebral pairs, as computed from Figure 6.3. Each value corresponds to a certain level of significance: 1,2 and 3 stand respectively for P=0.05, P=0.01, and P=0.005, similarly to what has been done in (Govers et al., 2007). Null values stand for no significant difference between two vertebral levels. The last row displays a sum of the table, showing where most differences have been observed for all cats.

Variability within cat

To study the variability of BOLD responses within cats, we plotted the percent signal change for every run performed on four cats (Figure 6.4). Mean percent change was 0.9 ± 0.1 %. For most cats, responses were very different from run to run, without any slow slope that could be explained by system drifts (Smith et al., 1999) or by physiological habituation to the stimuli (Bandettini et al., 1997; Liu et al., 2002). To appreciate the spatial distribution of responses across runs, Figure 6.5 shows T-maps overlaid on anatomical volume for one cat. Similar variability was observed in other cats. Task-related intensity was extremely variable over time. However, the spatial location of activated clusters remained constant for each individual cat, yielding fixed-effect maps with robust activated clusters and relatively good spatial specificity.

To check for any BOLD signal dependence on nerve stimulation intensity, two cats were scanned at variable stimulation intensity, from one to five times the threshold. Figure 6.6 shows a clear correlation between signal change and stimulation intensity. We tested this correlation using a simple linear regression between percent signal change and stimulation intensity. Results of linear regression implied a significant relationship for both cats (P<0.005).

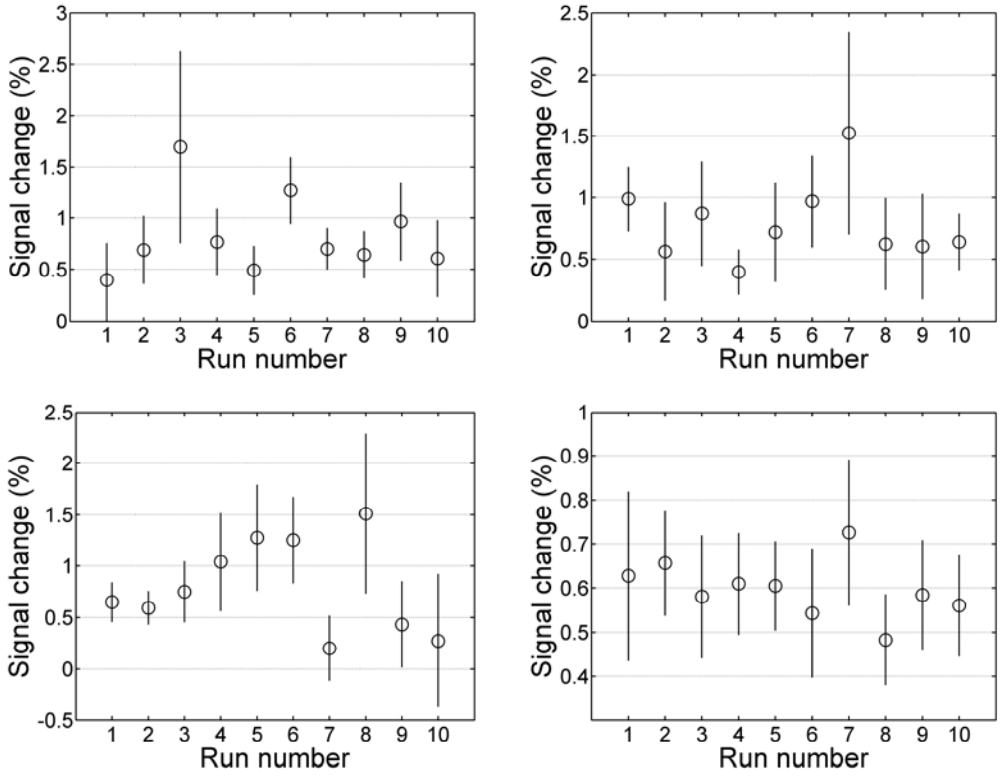

Figure 6.4. Quantification of responses across runs for four cats

Percent signal changes are plotted as mean and standard deviation. These values were computed in each cat-specific ROI, which were designed based on fixed-effect results. This figure illustrates the intra-cat variability of responses with time.

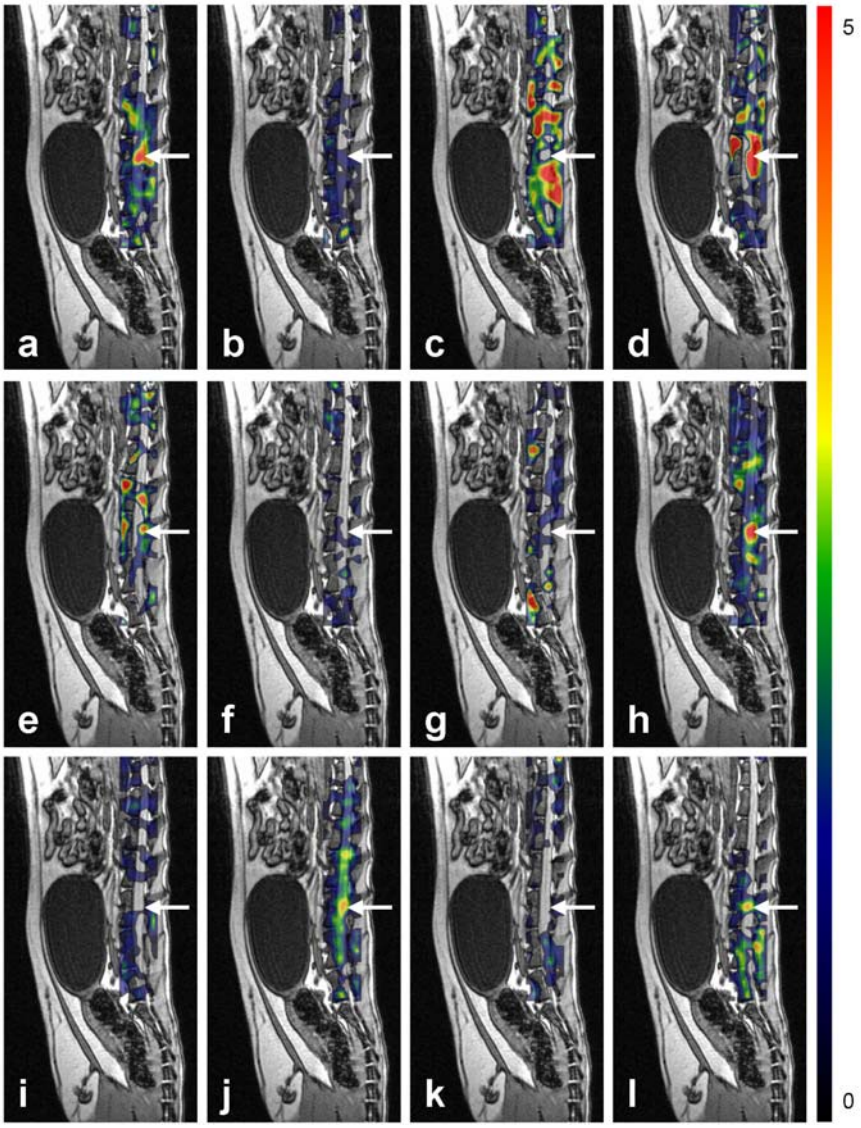

Figure 6.5. T-map across runs selected from one cat

a: Result of the fixed-effect analysis with an activated cluster located at L5 (arrow). **b-l:** T-maps derived from eleven runs conducted on that cat, displayed in chronological order (from left to right and then top to bottom). Note that the anatomical volume on which the T-maps are overlaid is the same in all panels.

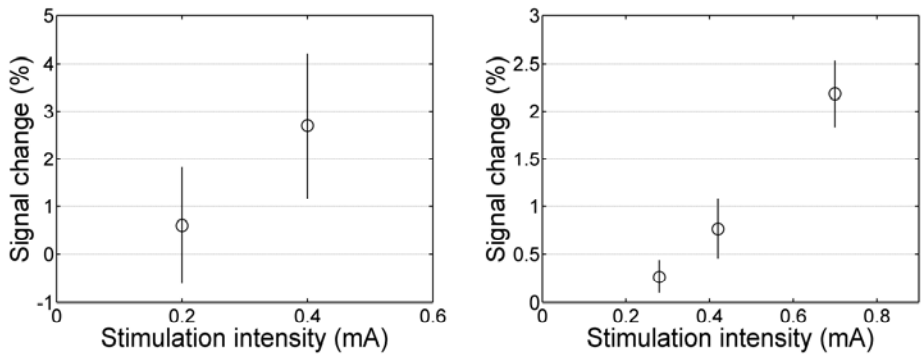

Figure 6.6. Percent signal change in function of stimulation intensity in two cats

For each stimulus condition, signal change has been averaged across four runs and standard deviation has been reported on the graph. This figure suggests that BOLD response increases with amplitude of stimuli.

Noise characteristics

Previous studies have shown that SNR characteristics have a significant impact on the sensitivity to detect BOLD activations (Bellgowan et al., 2006; Bodurka et al., 2007; Parrish et al., 2000; Triantafyllou et al., 2005). This section provides an extensive investigation of noise measurements in the spinal cord. Figure 6.7 shows a typical raw EPI used in our fMRI study. The spinal cord is covered by three to four sagittal slices as shown in Figure 6.7d-f and exhibits a moderate signal as detailed hereafter.

Figure 6.8 provides a comparison of noise maps from one cat and from a typical brain fMRI study in human. Acquisition parameters for the human brain were similar to the ones we used in the cat (same MRI system, TR= 2000 ms, TE = 30 ms, flip angle = 90°, voxel size = 2×2×2 mm3, bandwidth = 2055 Hz/pixel). On both SNR maps, one can observe a higher signal for the brain, which could be partly explained by lower physiological fluctuations, a longer TR (since no multi-shot EPI was used for the brain dataset) and a higher flip angle.

Quantification of SNR0, tSNR and $\sigma p/\sigma 0$ in the spinal cord are reported in Table 6.2. Mean values were SNR0 = 30.2 ± 4.5, tSNR = 25.4 ± 7.7 and $\sigma p/\sigma 0$ = 1.00 ± 0.61. These results were compared with values obtained in the brain at 3T (Triantafyllou et al., 2005). For a meaningful comparison, we adjusted reported measurements for the flip angle and voxel size used in our study. We proceeded as follows: based on Triantafyllou et al. measurements, SNR0 and tSNR given as a function of flip angle were extrapolated using a 2nd order polynomial trend. SNR0 as a function of voxel size was extrapolated using a linear trend, and tSNR using a logarithmic trend. After these adjustments, values reported by Triantafyllou et al. at 3T were SNR0 = 45.3, tSNR = 39.4 and $\sigma p/\sigma 0$ = 0.57. The difference between those values and the ones we obtained in the cat could be attributed to the much higher physiological noise level in spinal cord (Brooks et al., 2008) as well as to differences in acquisition parameters (bandwidth, segmentation of data acquisition, multi-channel RX, TE and TR). Although direct comparison was not possible, these values are still informative in terms of SNR roughly to be expected.

To investigate the impact of SNR on amplitude of the BOLD response, we performed a linear regression between estimated betas and noise parameters. After regression, a Fisher F-test was performed to test the significance of the inferred relationship. Results are provided in Table 6.3. Out of seven cats, a significant relationship was obtained in four cats for SNR0 and tSNR parameters, and in two cats for the $\sigma p/\sigma 0$ parameter.

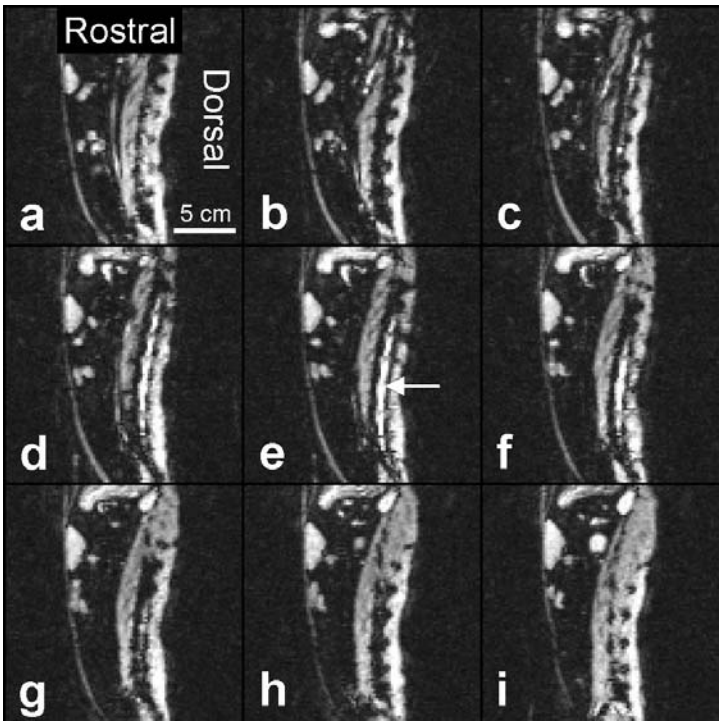

Figure 6.7. Typical raw EPI obtained in one cat
Sagittal slices are running from right (a) to left (i). The spinal cord is indicated with a white arrow. Distortions were greatly reduced by the use of multi-shot acquisition (phase-encoding direction was A-P).

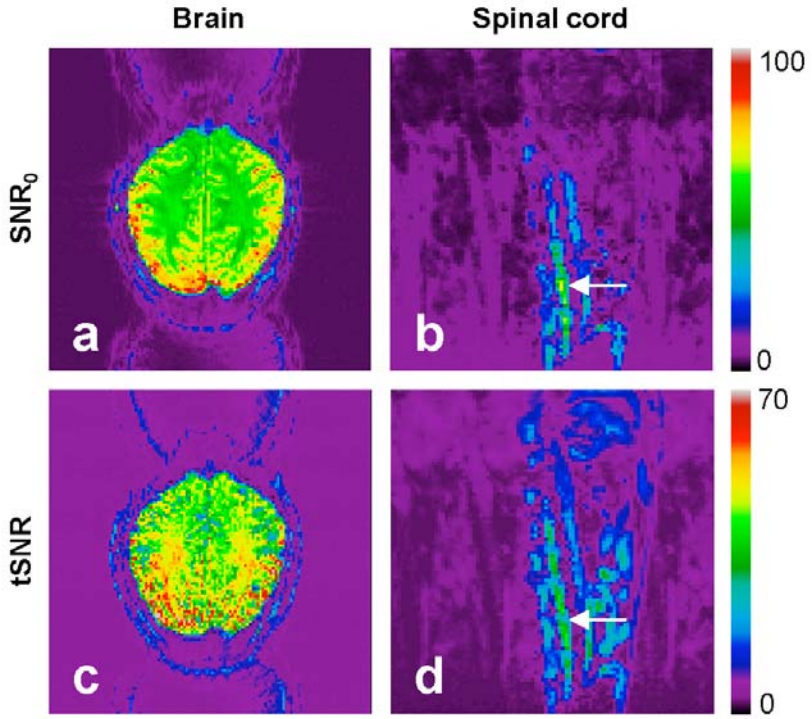

Figure 6.8. Temporal and static SNR in the brain and spinal cord
Comparison of SNR0 (top panels) and tSNR (bottom panels) in the brain (a,c) and spinal cord (b,d). The spinal cord (sagittal view) is indicated with an arrow.

	SNR_0	**tSNR**	**σ_p/σ_0**
cat #1	26.2 ± 1.2	18.8 ± 3.0	0.98 ± 0.30
cat #2	28.4 ± 2.3	27.5 ± 1.9	0.42 ± 0.30
cat #3	30.5 ± 0.8	39.4 ± 3.2	-
cat #4	30.2 ± 8.9	20.26 ± 9.8	1.66 ± 0.98
cat #5	41.5 ± 17.8	21.8 ± 1.0	1.72 ± 0.8
cat #6	27.8 ± 2.1	25.4 ± 9.8	0.39 ± 0.23
cat #7	29.7 ± 1.6	27.9 ± 7.7	0.81 ± 0.30
cat #8	27.3 ± 2.4	14.2 ± 2.1	1.66 ± 0.17
cat #9	30.5 ± 2.5	33.1 ± 3.6	0.34 ± 0.20
mean	**30.2 ± 4.5**	**25.4 ± 7.7**	**1.00 ± 0.61**

Table 6.2. Quantification of static and temporal SNR in the spinal cord

Quantification of SNR_0, tSNR and σ_p/σ_0 measurements in the spinal cord. For each cat and each run, SNR_0 (corrected for Rayleigh distribution) has been estimated based on one raw data prior to any pre-processing. A mask including the whole lumbar cord has been used. TSNR has been computed as the mean signal within the cord – using the same mask as previously – divided by the residuals' standard deviation obtained after computing the GLM. SNR_0 and tSNR values were then averaged within each session. In this table, we indicate the result of that average ± standard deviation. The physiological over thermal noise ratio σ_p/σ_0 was computed based on Equation (6.1). The '-' sign indicates non-defined values, *i.e.*, when SNR_0 was inferior to tSNR.

	SNR_o	tSNR	σ_p/σ_0
cat #1	7.7*	5.6*	12.2*
cat #3	11.9*	13.3*	-
cat #4	3.6	2.1	3.3
cat #5	4.9	6.4*	4.3
cat #6	7.8*	2.7	0.6
cat #7	4.4	4.3	0.6
cat #8	22.1**	21.4**	21.2**

Table 6.3. F-score results of linear regression between betas and noise parameters

Betas were averaged within the activated regions for every cat, except for those which did not show clear activation pattern (cats #2 and #9). Non-defined values of σ_p/σ_0 were removed from the regression analysis (*i.e.*, when SNR_0 was inferior to tSNR). Note that for cat #3, all σ_p/σ_0 were undefined, which explains the '-' sign. Significant relationship is indicated as *: $P<0.05$; **: $P<0.005$.

BOLD dependence on CO_2 level

In this study, we evaluated the impact of CO_2 on BOLD amplitude to test whether the variability we observed could be partly explained by this parameter. Figure 6.9 shows plots of percent signal change and CO_2 levels over time, in four cats for which the stimulation protocol remained constant. No obvious relationship could be seen on these graphs, except for the third one which shows a slight negative-correlation between signal change and CO_2 levels. Given that no BOLD response was obtained in runs #7, #9 and #10 for the third dataset (Figure 6.9c), we eliminated these outlier runs and found a significant linear relationship (F=41, P<0.0005) as shown in Figure 6.10. The regression coefficient was negative, indicating that BOLD response was decreasing when CO_2 level was increasing, as would be expected (Hoge et al., 1999a; Sicard and Duong, 2005). This result suggests that BOLD responses might have been partly dependent on basal CO_2. In the following paragraph we will investigate one reason that could explain the absence of BOLD response in three runs.

The most plausible hypothesis was that the cat may have experienced strong motion during these runs. Although the cat was paralyzed, its visceral system – not affected by pancuronium – may have undergone transient activity. We therefore quantified cat motion during each run by examining transformation matrices given by the rigid-body realignment. We checked whether mean translation and mean rotation were less than one voxel and one degree, respectively. We observed that no translation was larger than the quarter of one voxel and no rotation was larger than 0.01° (see Figure 6.11). In particular, no abnormal motion or discontinuity was observed during runs #7, #9 and #10. We thus conclude that cat motion could not explain the lower BOLD signal observed in those specific runs.

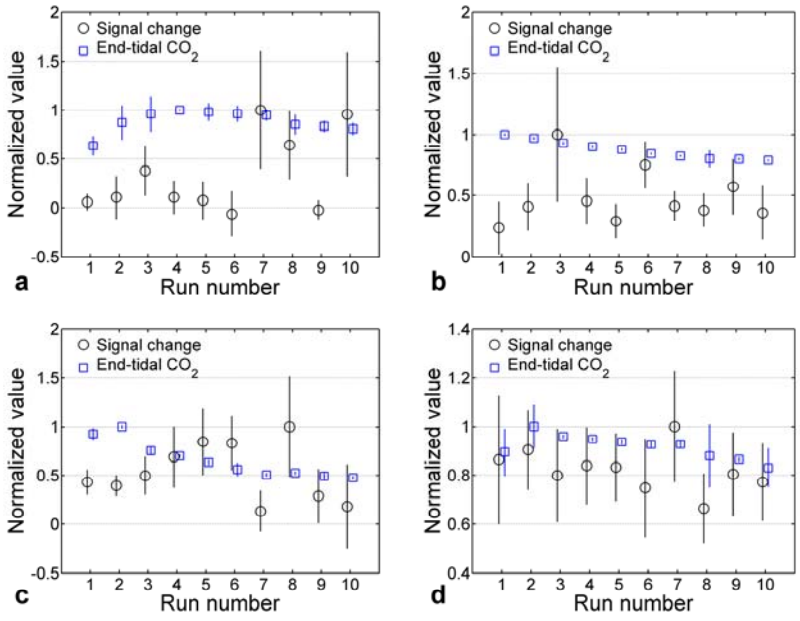

Figure 6.9. Quantification of percent signal change and CO_2 across time
Signal change (circles) and end-tidal CO_2 (squares) in four cats. Negative-correlation is noticeable in one cat (**c**).

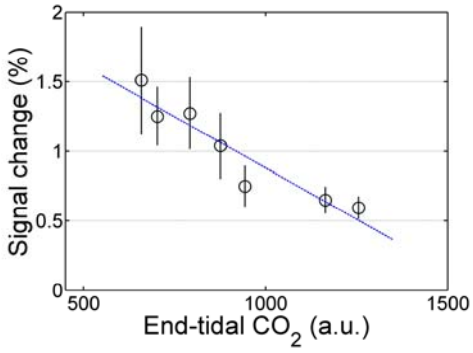

Figure 6.10. Percent signal change in function of CO_2 level

Plot of percent signal change in function of CO_2 level for the cat corresponding to Figure 6.9c. For each CO_2 value, signal change has been averaged within an ROI (located over the spinal cord and derived from the T-map) and standard deviation has been reported on the graph. Result of linear regression between percent signal change and CO_2 level is plotted in blue dashed line, suggesting a negative-correlation between BOLD amplitude and O_2 saturation.

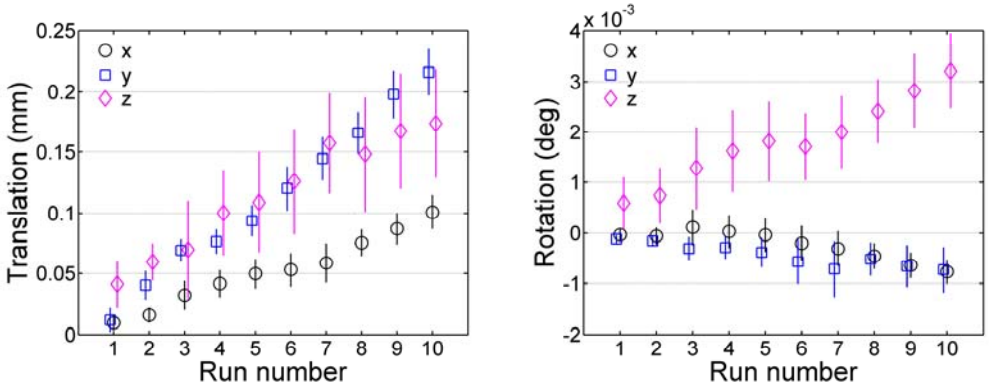

Figure 6.11. Rigid-body registration parameters

Translation (left) and rotation (right) transformation parameters for the cat corresponding to Figure 6.9c.

Discussion

Task-related signal was detected in most cats with relatively good spatial specificity. However, its amplitude significantly varied between cats and between runs in the same cat. In the present study, we investigated whether this variability might be explained by different levels of noise, by the use of low stimulation amplitudes or by CO_2 variations. In the following discussion we introduce physical, physiological and analytical considerations based on the literature, and propose future directions.

Acquisition parameters and image quality

Unlike many previous studies (Backes et al., 2001; Endo et al., 2008; Govers et al., 2007; Kornelsen and Stroman, 2004; Lilja et al., 2006; Madi et al., 2001; Maieron et al., 2007b; Moffitt et al., 2005; Ng et al., 2008; Stroman and Ryner, 2001; Yoshizawa et al., 1996; Zhao et

al., 2008), we chose to image in the sagittal plane using isotropic voxels (2×2×2 mm^3). This approach offered the benefits of extensive spinal coverage using only a few slices (Stroman et al., 2005a). Moreover, since BOLD fMRI relies on the haemodynamic effects – and *a fortiori* venous effects since we employed the GRE technique – we aimed at increasing the rostro-caudal resolution to better depict the location of activated clusters. Due to the limited SNR however, one disadvantage of having isotropic voxels is the difficulty of reaching high spatial resolution in the spinal cord cross-section, which might be of interest for precisely assessing the lateralization of the activation as done in (Lilja et al., 2006; Maieron et al., 2007b; Yoshizawa et al., 1996).

Another original contribution of the present study is the quantitative comparison of both static and temporal SNR in the spinal cord versus in the brain. The relatively low SNR that was measured in the spinal cord could partly explain the difficulty of measuring a clear activation, as suggested by others (Bellgowan et al., 2006; Bodurka et al., 2007; Parrish et al., 2000; Triantafyllou et al., 2005). The noise characterisation presented here could serve as reference for future fMRI studies in the spinal cord.

Lateralization of the activation

Results showed a focal activated cluster in the cord at vertebral L4-L5 for most cats. Moreover, no or little activation was present outside this region (at the threshold values used), suggesting a low false positive rate. Although encouraging, this finding must be qualified by noting the absence of a robust lateralization of the activation. However, neuronal activity was also expected in the contralateral side of the cord due to the activation of interneurons and motoneurons through various crossed spinal pathways (Jankowska, 1992). Also, peroneal stimulations probably activated the spinothalamic system and the dorsal column system. Nevertheless activation was expected to be prominent on the ventral ipsilateral side, which was not always the case. Although consistent ipsilateral activation has already been reported (Brooks et al., 2008; Maieron et al., 2007b; Stroman and Ryner, 2001), its poor reproducibility has also been noted (Backes et al., 2001; Giove et al., 2004; Govers et al., 2007; Yoshizawa et al., 1996).

A first hypothesis for these difficulties in discriminating lateralization is that partial volume effect might induce an activation detected either medially or in the contralateral side of the cord. Nonetheless, contralateral activations were recorded much further from the medial axis, without any activation in the ipsilateral side. A second hypothesis is that susceptibility artefacts, which are prominent in spinal cord imaging, might induce image distortion thus biasing the delineation of ipsi- from contralateral side. However in this study, phase-encoding was set in the anteroposterior direction which prevented this type of lateralization discrimination error. Moreover, the use of multi-shot EPI drastically reduced susceptibility-related distortions. A third hypothesis is the detection of BOLD signal in larger veins adjacent to the spinal cord. This hypothesis seems to be the most plausible and is discussed below.

Spatial specificity

Some cats showed activations slightly outside the spinal cord. This unexpected spatial location has already been observed in previous spinal cord fMRI studies (Backes et al., 2001; Govers et al., 2007; Zhao et al., 2008). The most plausible explanation has to do with venous effects particularly present in GE EPI. Indeed, previous studies have shown that BOLD signal may arise predominantly from large venules and veins (Duong et al., 2003; Mandeville and Marota, 1999; Zhao et al., 2004), with a wider point spread function relative to spin echo (SE) sequences (Parkes et al., 2005). Hence, activation signal could even be detected several millimetres from the activation site (Malonek and Grinvald, 1996; Ogawa et al., 1998; Turner, 2002). Furthermore, in contrast to the brain, the spinal cord grey matter is surrounded by white matter. The latter is directly in contact with large draining veins carrying deoxygenated blood along the axis of the cord, where the highest amplitude BOLD signals would be expected due to the large size of the vessels. This interpretation is also supported by others (Backes et al., 2001; Govers et al., 2007; Zhao et al., 2008). The geometry of the vasculature could also be responsible for activation at the edges of the cord. As demonstrated in (Menon, 2002), activation-related hyperoxygenation induces both T_2 and T_2* effects within large veins oriented in a coherent way. On the contrary, randomly-oriented capillaries will only produce a magnitude change, yielding less T_2*-weighting MRI signal change. In the spinal cord vasculature, surface veins surrounding the cord as well as some radial venules have the potential to induce a significant signal phase change. In addition to this, the variability in activation location between cats could be explained by slight differences in the vascular architecture, such as the large number of anastomoses in the venous system of the spinal cord (Govers et al., 2007).

Perspectives for improving spatial specificity of spinal cord fMRI could include blood flow measurements (Smirnakis et al., 2007), SE sequences (Hulvershorn et al., 2005; Parkes et al., 2005; Zhao et al., 2006b), SEEP contrast (Stroman et al., 2005b), contrast agents such as monocrystalline iron oxide nanoparticles (MION) (Goense et al., 2007), measurement of anisotropic diffusion coefficients (Roberts et al., 2007; Song et al., 2002b), or analytical approaches aiming to model and remove the venous contribution (Menon, 2002; Nencka and Rowe, 2007).

Intensity of stimulation

In most cats, stimulation intensity was less than 3 times the activation threshold. Thus, only A-fibres (Aα, Aβ) giving rise to non-noxious stimuli were activated. On the contrary, C-fibres and Aδ fibers which are known to give rise to noxious stimuli, were probably not activated at this electrical intensity. Previous studies have reported a drastic improvement of reproducibility and sensitivity of activation when inducing noxious versus non-noxious stimuli in rats (Lawrence et al., 2008a; Lilja et al., 2006; Zhao et al., 2008). Although more activation might have been detected if cats had been stimulated at higher intensity, the objective here was

to investigate the limit of BOLD sensitivity in the spinal cord. Indeed, one long term motivation of this study was the detection of the motoneuronal and interneuronal activity underlying plastic processes in the spinal cord following spinal cord injury, for instance in models of locomotor-trained animals (Rossignol, 2006a).

Modelling the haemodynamic response

The low sensitivity could also be explained in terms of the physiological models employed in the analysis. First, physiological-related noise is particularly prominent in the spinal cord due to the surrounding vasculature and CSF, thus yielding lower sensitivity for detecting signals of interest using the general linear framework without accurate physiological modelling (Brooks et al., 2008). Second, since the haemodynamic response function (HRF) observed in the brain has been found to vary widely in terms of temporal shape and peaking location (Aguirre et al., 1998; Biswal et al., 2003; Hoge et al., 1999c), the question is raised whether the HRF form used in our study was appropriate for modelling haemodynamic activity in the spinal cord. Moreover, the present study was performed on anaesthetized animals, in which the HRF might be different from that in awake humans (Fukuda et al., 2005; Sicard et al., 2003). However, we used a block-design protocol with interval of one minute between transitions, which would be expected to reduce the impact of the specific HRF form on the overall response model. To assess the validity of our assumed HRF, we performed spatial independent component analysis (ICA) on the majority of our data. This method allows recovery of spatio-temporal signals without requiring any assumptions about the form of the response (McKeown et al., 1998; Perlbarg et al., 2007). Results of ICA showed components with a temporal time course highly correlated with the stimulation paradigm (data not shown). Moreover, no apparent phase shift was observed between extracted components and the stimulation paradigm convolved with the HRF we used. Further studies involving event-related designs in anaesthetized animals will be needed for temporally characterizing the HRF. One solution that might be particularly suitable for low SNR data is to locate temporally the HRF peak by shifting the data towards the design matrix (Cohen-Adad et al., 2007e).

CO_2 basal state and BOLD signal

Focal BOLD signal was detected in the expected region for most cats. However, its amplitude and spatial location varied significantly. Additionally to the low stimulus intensity used in the present study, we believe other factors are responsible for the fluctuation of BOLD signal over time: the anaesthetic state (Fukuda et al., 2005; Sicard et al., 2003) and the O_2 saturation of basal blood flow (Hoge et al., 1999b). Although we maintained a constant dose of anaesthetic during each session, our results suggest that variations in O_2 saturation might have had an impact on the amplitude of BOLD responses. Future studies aiming to isolate specific factors are required.

Conclusion

BOLD fMRI showed task-related activation in the spinal cord of seven cats. To our knowledge, this is the first study investigating BOLD signal in the spinal cord of ketamine-anaesthetized animals, as well as providing correlations between percent signal change and parameters that are known to impact the BOLD signal.

Spinal fMRI has demonstrated its ability to detect differences in spinal cord activity following injury (Endo et al., 2008; Kornelsen and Stroman, 2007). Although clinical applications of this technique have been recently proposed, results obtained up to now dictate cautious use of spinal fMRI data (Kornelsen and Mackey, 2007). Indeed, the high inter-subject variability in BOLD amplitude would be a challenge in any comparison of control and spinal cord injured patients. We believe that at this time it is important to pursue more detailed investigations to gain better confidence in BOLD signal in the spinal cord.

Acknowledgement

We thank J. Provencher for the preparation of cats, C. Hurst and A. Cyr for assistance with MRI acquisitions and C. Gauthier for her revision of the manuscript. We also thank the reviewers for their precious comments. This work was supported by the Canada Research Chair on the Spinal Cord provided by the Canadian Institute of Health Research (CIHR) to S. Rossignol and by the Multisdisciplinary Team on Locomotor Rehabilitation (Regenerative Medicine and Nanomedicine, CIHR). J. Cohen-Adad has a fellowship from the Fondation pour la Recherche Médicale (FRM, France) and from the Groupe de Recherche sur le Système Nerveux Central (GRSNC, Université de Montréal).

7. Discussion

Summary of results

The initial motivation in the DW-MRI project was to assess whether tractography can identify various pathways in the *in vivo* spinal cord. The first article provides results of diffusion tensor maps, as well as extracted fibre bundles showing anatomical tracts in various sub-divisions of the cord such as the dorsal and ventral columns as well as lateral tracts. There was good coherence in the longitudinal orientation of principal eigenvectors, without visible distortion in the phase encoding direction. Anatomical localisation of nerve roots entering on either side of the cord was also feasible. The relatively high spatial resolution that was used yielded sufficient SNR to reconstruct the tensor or ODF while limiting partial volume effect that hampered anisotropic measurements notably at the CSF-white matter interface. Another significant achievement was the use of a relatively large FOV (about 14 cm). This enabled consistent tractography throughout several levels of the cat spinal cord (from T12 to L7 vertebral bodies). Tractography with large FOV is a first step towards accurate identification of specific spinal tracts, because the ability to really identify tracts depends on the inclusion of a start and end point. For instance, tracking fibres from supraspinal to lumbar regions such as the reticulospinal of rubrospinal tracts would require seed points in the nucleus of origin, *i.e.*, in the mesencephalon. This article also demonstrates the feasibility to detect and to localize SCI in the *in vivo* cat. FA was significantly decreased at the site of the injury, suggesting a loss of white matter tissue. Note that we also observed a decrease in mean diffusivity and first eigenvalue (data not showed). The interpretation of FA decrease needs further investigations since partial volume effect as well as the presence of scar tissue, oedema, haemorrhage, glial scar, myelinated state and residual axons play a significant role in the measurement of a diffusion signal (Beaulieu and Allen, 1994; Schwartz et al., 2005d). This notably implies that presented results cannot support the detection of Wallerian degeneration via DW-MRI.

Conclusions of the first article pointed out the limits of the diffusion tensor given the presence of crossing fibres in the spinal cord. Therefore, we suggested investigating model-free approaches such as QBI. This has been achieved in the second article. We acquired HARDI data in both *in vivo* and *ex vivo* cat spinal cord and showed that QBI is able to detect the presence of longitudinal, commissural and dorso-ventral fibres. The second article therefore provides an incentive to use both HARDI and QBI to represent the diffusion process in the healthy and injured spinal cord of mammals.

The third article investigated the reproducibility of BOLD responses in anaesthetized cats. Spinal cord activity was induced by electrical stimulation of cutaneous nerves of hind limbs. As a result, stimulus-related signals were detected in most cats with relatively good spatial specificity. However, percent signal change varied between cats and between sessions in

the same cat. This article presents the first spinal fMRI experiment in ketamine-anaesthetized animals. It also provides an extensive study of intra- and inter-subject variability of activation, the characterisation of SNR_0 and tSNR in the spinal cord and investigations on the impact of CO_2 end-tidal level on the amplitude of the BOLD response.

Other contributions

Apart from the three presented articles, other articles are included as supplementary contribution to this thesis (see Appendix B, C and D). Article #4 is a short article presented at a conference (Cohen-Adad et al., 2007g). In this article we demonstrated that automatic algorithms that aim at correcting motion during fMRI data acquisition may introduce spurious effect in human spinal cord time series. This was notably attributed to the particular spatiotemporal characteristics of physiological noise. This finding strongly influenced – and improved – the pre-processing step of the methodology that has been used in the third article presented in this thesis (spinal cord fMRI in cats).

Article #5 on which I'm the second author has been accepted for publication in the *Magnetic Resonance Imaging* journal (Piché et al., 2008). Based on the above-mentioned findings about motion correction algorithms and the fact that cardiac-related signal is prominent in spinal datasets, we investigated the spatiotemporal distribution of cardiac signal in the human cervical spinal cord. Interestingly, we observed invariants in the spatial location of cardiac signal. This finding opens the door to ICA-based methods for removing physiological variance from spinal fMRI time series based on spatial priors (Perlbarg et al., 2007).

Article #6 arose from investigations on the GLM that were done early in this thesis (Cohen-Adad et al., 2007e). Those investigations notably aimed to apply the GLM – widely used in fMRI – on diffuse optical imaging (DOI) data. Apart from this goal I also proposed a method which enables to detect the presence of a task-related activation in low SNR optical imaging data. This so-called 'shift method' is based on pattern recognition of multiple GLM analyses, done by shifting the data relative to the design matrix. This technique is modality-independent and can also be applied to fMRI.

Limitations

Although the main objectives of this thesis have been addressed, significant limitations have also arisen. In this section we will discuss some of these limitations.

Results presented in QBI qualitatively assessed the feasibility to detect non-longitudinal fibres in the spinal cord. However, extensive validation using histological staining needs to be conducted in order to confirm that observation (Choe et al., 2008; Herrera et al., 2008). Moreover, proper interpretation of water diffusion in the healthy and injured spinal cord is a difficult issue. Although DTI provides quantitative measurements such as the FA, the mean

diffusivity and eigenvalues, those measurements depend on a large number of physical and biological parameters including voxel size and shape (Basser et al., 2000; Oouchi et al., 2007), b-value (Mattiello et al., 1997), q-space sampling (Hasan et al., 2001; Jones, 2004; Landman et al., 2007; Madi et al., 2005; Ni et al., 2006; Papadakis et al., 1999; Peng and Arfanakis, 2007), noise characteristics (Anderson, 2001; Jones, 2004; Skare et al., 2000), Eddy-currents (Mangin et al., 2002; Reese et al., 2003), partial volume effects (Alexander et al., 2001; Smith et al., 2008), spinal cord motion (Figley and Stroman, 2007; Kharbanda et al., 2006; Summers et al., 2006), axonal density (Jespersen et al., 2007) and size (Ong et al., 2008), myelin sheath (Concha et al., 2006; Nair et al., 2005; Song et al., 2005), oedema (Sen and Basser, 2005) and glial scar (Schwartz et al., 2005d). Hence, modelling the diffusion signal will be more than required for accurate estimate of axon and myelin integrity (Assaf and Basser, 2005; Beaulieu, 2002; Jespersen et al., 2007; Roth et al., 2008; Sen and Basser, 2005). Nevertheless, even combining high resolution and accurate quantitative diffusion metrics, one might still wonder if DW-MRI as currently implemented would allow for the identification of sprouting fibres (Fouad and Tse, 2008; Goldstein et al., 1997; Kerschensteiner, 2007). Recent results demonstrating plasticity in the brain suggest that this might indeed be feasible (Ramu et al., 2008). In future work, it could be worth examining this phenomenon in *ex vivo* samples to get even higher resolution without being hampered by physiological and susceptibility effects. The validity of transposing *in vivo* from *ex vivo* results has already been investigated in mice (Kim et al., 2007b), in cats (Pattany et al., 1997), as well as in humans (Maier and Mamata, 2005).

Spinal fMRI has demonstrated its ability for detecting differences in spinal cord activity following injury (Endo et al., 2008; Kornelsen and Stroman, 2007). Although clinical applications of this technique have been recently proposed, results obtained up to now dictate cautious use of spinal fMRI data. Indeed, the high inter-subject variability in BOLD amplitude would be a challenge in any comparison of control and spinal cord injured patients. We believe that at this time it is important to pursue more detailed investigations to gain better confidence in BOLD responses in the spinal cord. These investigations should focus on acquisition, analytical and biological aspects to better understand low level processes underlying the measured MRI signal.

Ongoing work

Longitudinal DW-MRI study in cats

Thanks to an accepted project that is being funded by the Christopher and Dana Reeve Foundation (USA) we are currently conducting a longitudinal study in cats . The principal aim of the study is to use DW-MRI to assess the continuity of spinal pathways in a cat model of partial SCI (unilateral hemisection) and to correlate the integrity of certain pathways with locomotor recovery on a treadmill. The protocol involves four imaging sessions: (i) on an intact cat ; (ii) within one week of a partial spinal lesion done at T11 (unilateral hemisection) ; (iii) at the end of the locomotor training period ; (iv) after complete spinal section at T13. The data for

all imaging sessions will be processed to study the continuity of spinal fibre tracts coursing through the dorsal columns, the dorso-lateral column, the ventro-lateral column and the ventral columns on both sides. We will evaluate changes that may occur in these pathways as a function of time and recovery of function.

In comparison to the methodology that has been used in the presented thesis, some improvement will be brought. The limitation of slice thickness in sagittal acquisition is an issue for evaluating the extent of hemisection. Therefore, we are currently acquiring two sets of 2 mm slice thickness data (respiratory-gated, 30 minutes of acquisition each). Those two datasets are shifted through-plane by 1 mm to enable the use of super-resolution reconstruction methods that have been proposed in previous studies (Carmi et al., 2006; Greenspan et al., 2002; Peled and Yeshurun, 2001). Additional development will also be conducted for inferring other QBI metrics than the GFA for better characterizing the injured white matter tissue (Cohen-Adad et al., 2009b). This development is being done in collaboration with Dr. Maxime Descoteaux (Neurospin / CEA, Saclay, France).

Transposing the DW-MRI method in humans

We are currently developing DW-MRI of the cervical, thoracic and lumbar spinal cord in humans using the method developed in the presented work. Short articles presented at conferences demonstrated the proof-of-concept for imaging the human cervical cord (Cohen-Adad et al., 2008d; Cohen-Adad et al., 2008i). Those acquisitions yielded good image quality (*e.g.*, susceptibility effects, SNR, motion) and reproducibility across healthy subjects (N=5). Reproducibility is crucial when conducting clinical studies that involve scanning a certain number of subjects, having potentially different age, different cord size and shape and more or less ability to stay still in the scanner.

Hypercapnia study in humans

Given numerous challenges of fMRI in the spinal cord (Giove et al., 2004), it is worth investigating the sensitivity and specificity of BOLD activation maps during controlled stimuli. Hypercapnia is characterized by an elevated state of end-tidal CO_2. It induces global increases in blood flow throughout the central nervous system (Hoge et al., 1999a). This makes it highly suitable for use as a positive control stimulus for assessing the sensitivity of BOLD fMRI under different conditions. Similarly to a previous breath-hold study (Maieron et al., 2007a), we are conducting a study in which a moderate degree of hypercapnia (5 mmHg) is being induced in a block-design fashion. We use a computer-controlled system that allows targeting of specific end-tidal CO_2 values. This study will help to characterize the sensitivity of the BOLD response in the human spinal cord. Preliminary results have been presented at a conference (Cohen-Adad et al., 2008h; Gauthier et al., 2009). The detailed methodology for data acquisition is provided in Appendix A.

Distortion correction

Regarding susceptibility artifacts in EPI, I am currently investigating what would be the best approach for correcting distortions in the spinal cord (Cohen-Adad et al., 2009c ; Lundell and Cohen-Adad, 2009). This project is made in collaboration with Henrik Lundell (DRCMR / Panum Institute, Copenhagen, Denmark). Additionally to the three approaches described in the Methodology section (*i.e.*, the field-map, the reversed gradient and the co-registration methods), we are testing another method which corrects for phase errors based on acquisition of the point spread function (Zaitsev et al., 2004).

Slice-by-slice realignment for spinal time series

Contrary to the brain, rigid motion (*i.e.*, translation and rotation) is often different from slice to slice in spinal cord time series notably due to some non-linear geometric deformation of the spinal cord across time (*e.g.*, modification of the neck curvature). Therefore standard 3-D realignment methods are not optimal for spinal cord time series. For this purpose I am currently developing an algorithm that performs slice-by-slice registration based on correlation cost function (Cohen-Adad et al., 2009d). This method will be particularly suitable for axial time series due to the large amount of A-P motion (*e.g.*, CSF flow and subject swallowing). When the development will be finished I will validate it with existing realignment methods (Bannister, 2003; Oakes et al., 2005).

Future directions

Data acquisition and field strength

Since spinal DW-MRI and fMRI acquisitions share similar difficulties when performed in EPI, novel techniques that aim at reducing susceptibility artifacts apply for both modalities. The most straightforward approach for doing EPI of the spinal cord probably involves FOV reduction in the phase encoding direction. Also, combining multi-shot and parallel imaging would further reduce susceptibility effects. For the latter technique to work optimally, future developments should aim at designing array coils having multiple channels, as suggested by (Wiggins et al., 2006). To summarize, combining (i) EPI technique, (ii) reduced FOV with outer volume suppression or spectral excitation pulse, (iii) multi-shot acquisition with navigator echoes correction, (iv) parallel imaging and (v) optimized coil design would certainly lead to a significant improvement of both DW-MRI and fMRI of the spinal cord.

Improving data acquisition towards susceptibility effects would certainly benefit the use of higher field MRI (>3T). At higher field strength, spatial resolution and contrast-to-noise ratio (CNR) could be further improved. This has a significant impact on the quality of diagnosis, as demonstrated in 7T scanners for the detection of early multiple sclerosis lesions (Ciccarelli et al., 2007; Neema et al., 2007; Pagani et al., 2007). Also, high field MRI scanners have the

potential to depict tissue morphology with greater details (Duyn et al., 2007; Fischl and Wald, 2007; Mukherjee et al., 2008).

DW-MRI of the spinal cord

Although application of spinal DW-MRI already demonstrated significant supply to clinical parameters in lesions (Peles et al., 2004; Shanmuganathan et al., 2008), tumours (Ducreux et al., 2006), cord compression (Aota et al., 2008; Facon et al., 2005), arteriovenous malformation (Ozanne et al., 2007), ischemia (Thurnher and Bammer, 2006b), multiple sclerosis (Agosta et al., 2007a; Ciccarelli et al., 2007; Ohgiya et al., 2007b; Valsasina et al., 2005) and amyotrophic lateral sclerosis (Blain et al., 2007; Ciccarelli et al., 2006; Karlsborg et al., 2004 ; Thivard et al., 2007), studies would certainly benefit from further investigations on the origin of the diffusion signal in various pathological conditions such as haemorrhage, scar tissue, Wallerian degeneration, or on the origin of plastic processes such as axonal sprouting. Better interpretation of the diffusion signal would certainly open the door to a large number of clinical trials that aim to investigate therapeutic approaches for treating spinal cord pathologies. In clinical routine, DW-MRI would also be used together with other approaches such as evoked potentials and clinical evaluations to further improve diagnosis as well as prognosis. This new tool might indeed help the early prediction of a potential functional outcome after spinal injuries.

FMRI of the spinal cord

As mentioned previously, the poor sensitivity and reproducibility fMRI in the spinal cord highlights the importance to better understand low-level physical and physiological processes giving rise to the MR signal of interest as well as to improve technical and analytical developments. These studies could focus on: the characterization of oxidative metabolism in spinal motoneurons (Cannon and Gelderd, 1983) ; the characterization of neurovascular coupling at the spinal level which might be somehow different than that in the brain, since vascular reactivity was reported to be more brisk in the cord (Nix et al., 1976) ; investigating the influence of anaesthetics on neuronal and vascular response (Martin et al., 2006; Sicard et al., 2003) ; linking the recruitment of activated fibres (in case of motor or sensory stimuli) with the number of activated neurons ; modelling the link between vascular response and MRI signal (Buxton et al., 2004) ; optimising the use of pulse sequences, *e.g.*, using multi-echo techniques to increase the sensitivity of activation detection (Chen et al., 2003; Posse et al., 1999) ; designing dedicated coils for improved sensitivity (Bodurka et al., 2008) ; optimizing the processing of spinal fMRI data given the relative importance of physiological-related noise in spinal fMRI time series (Brooks et al., 2008; Stroman, 2006) and investigating non-haemodynamic based techniques (Jasanoff, 2007; Stroman et al., 2005b).

Perspectives for improving spatial specificity of spinal cord fMRI could include blood flow measurements (Smirnakis et al., 2007), SE sequences (Hulvershorn et al., 2005; Parkes et al., 2005; Zhao et al., 2006b), BOLD-FSE sequences (Poser and Norris, 2007), signal

enhancement by extravascular proton density (SEEP) contrast (Stroman et al., 2005b), contrast agents such as monocrystalline iron oxide nanoparticles (MION) (Goense et al., 2007), measurement of anisotropic diffusion coefficients (Roberts et al., 2007; Song et al., 2002b), or analytical approaches aiming at modelling and removing the venous contribution (Menon, 2002; Nencka and Rowe, 2007). Also, using the initial dip as a temporal index would narrow the BOLD PSF since transient deoxyhemoglobin increase arises from the capillary bed only (Malonek et al., 1997). However, the poor sensitivity of initial dip detection would be problematic in spinal cord imaging.

It should also be mentioned that other imaging modalities (*e.g.*, DW-MRI, transcranial magnetic stimulation, positron emission tomography, etc.) could add useful information to be used for validation of spinal cord fMRI (Harel and Strittmatter, 2008).

8. General conclusion

The main purpose of this thesis was to develop a framework allowing acquisition and processing of DW-MRI and fMRI data in the spinal cord of cats and humans. Although this objective has been successfully fulfilled a large number of open questions remain. Among them, some are related to the applicative part of this thesis: spinal cord injury. One crucial role of MRI is to non-invasively assess the anatomical and functional integrity of the spinal cord in individuals after trauma. Results obtained up to now demonstrate that MRI has the potential to detect abnormalities using classical and diffusion-weighted sequences. However, accurate quantification of axonal density, degree of demyelination or presence of axonal sprouting still remains hypothetical in clinical routine. This clearly motivates further technical and methodological development in the near-future. Being able to develop a reliable neuroimaging tool for confirming clinical parameters would enable to monitor the effect of various rehabilitation strategies. This would certainly bring hope to a large number of people suffering from trauma and neurodegenerative diseases such as spinal cord injury, tumours, multiple sclerosis and amyotrophic lateral sclerosis. Similarly to DW-MRI although with even more reserves, spinal cord fMRI is still at a developmental step and no clear consensus has arisen for its reliability. Therefore it appears wise to further push fundamental investigations to better understand low-level processes coupling neuronal activity with MRI signal rather than encouraging clinical trials.

To conclude however on a more optimistic mood, the trust in the clinical potential of MRI that is growing in the politico-economical sphere (Cowley et al., 1994) will certainly motivate a large amount of grey matter to achieve the methodological developments that are required to fulfil the original purpose of what MRI can do – rather than focusing on what MRI cannot do.

A. Guideline for imaging the spinal cord of cats and humans

DW-MRI of the cat thoraco-lumbar spinal cord

This guideline is directed at people aiming to image the thoraco-lumbar spinal cord of healthy and spinal cord injured cats. All sequences were parameterized on the Siemens TIM Trio (Syngo VB15) at the Unité de Neuroimagerie Fonctionnelle (Université de Montréal, Montreal, Canada) and are saved in the directory 'JCA' under the folder 'Diff'. The imaging protocol is the following:

- Reversed gradient scans (5 min)
- DW scans (2×30 min)
- FSE sagittal scan (11 min)
- FSE axial scan (15 min)
- T_1-weighted scan (9.5 min, facultative)

Coils

Use the spine coil + the large body matrix. Position the body matrix as close as possible from the thoracic spinal region, to maximize the sensitivity in this region. Plug the large body matrix in one of the feet plug so that the coil cable do not overlap the coil (see Figure A.1). For all scans, the RF transmission will be done via the body coil, and RF recording will be done via elements SP6, SP7, BO1 and BO2.

Physiological monitoring

Respiratory gating will be done for all scans. Put the Siemens respiratory belt at the lumbar level. Fold it in two so that it gets thicker plus it will be more sensitive to the cat chest motion. Wait 10 seconds without touching anything (dynamic adjustment). Look at the MRI monitor, and check whether the probe is sensitive to the cat respiration. Note that the probe should remain stable during ~2 hours.

Cat positioning

Position the cat lateral left feet-first. Dispose the cat so the vertebral level T12 is right between the SP6 and SP7 elements (those number can be seen laterally to the MRI table). Make

sure that the T12 vertebral level is also centred in the R-L direction (relative to the table). Put a marker (vitamin) on the right side of the cat. Make sure the cat fore and hind limbs will not be present in the sagittal FOV (T8-L4). Put the isocentre over T12. An illustration of the cat arrangement in the MRI is provided in Figure A.1.

Localizer

Do a quick localizer from the template 'localizer_quick'. Adjust the slices so that sagittal slices are aligned along with the cord. Also, remember to rotate axial slices along with the spinous process. Then, do a higher resolution localizer 'localizer_long'.

Reversed gradient scans

Take the sequence template called 'ep2d_diff_cat_DTI'. Use the same parameters as for DW scans (see Table A.1.), except that there will be no diffusion-weighting, phase encoding direction will be rotated by 180° (in the 'routine' card) and the number of measurements will be 20 (to get sufficient SNR). Those scans will serve for subsequent distortion correction (Voss et al., 2006).

Step 1: Position the FOV adequately to align the spinal cord with sagittal slices (see Figure A.2). Make sure physiological gating is activated (using respiration triggering). Do some acquisition with one averaging and check the quality of images. We should at least see the cord from T7 to L3 (see Figure A.3a). Step 2: Do an acquisition with twenty averaging. The image should then look like in Figure A.3b. Step 3: Do the same acquisition as in step 2 with phase encoding at 0° (again twenty averaging). Distortions should follow a slightly different pattern as shown in Figure A.3c.

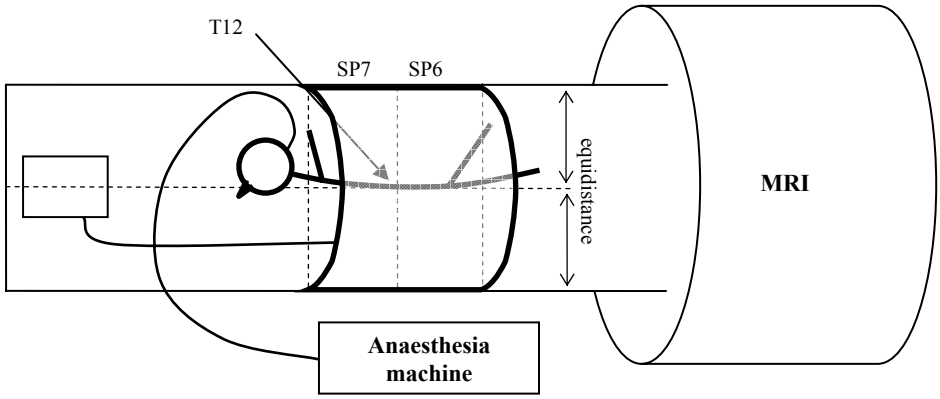

Figure A.1. Cat positioning for DW scans

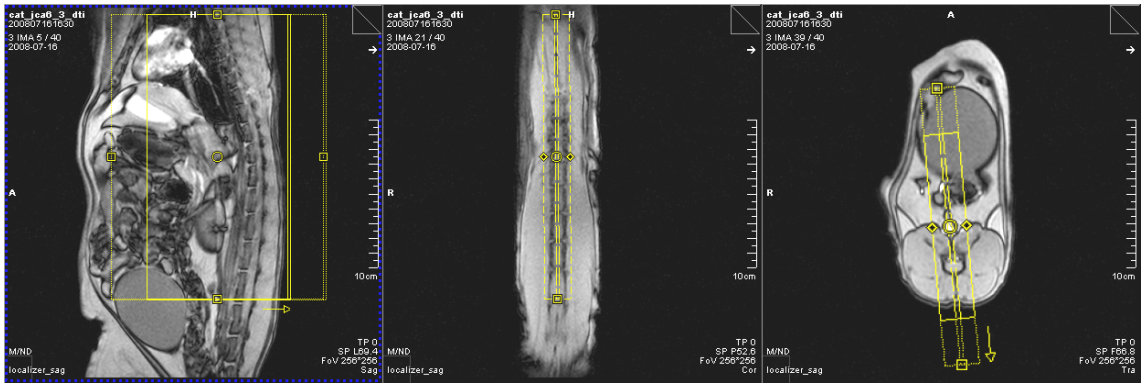

Figure A.2. Slice positioning for DW in cat
Sagittal (left), coronal (middle) and axial (right) localizer images with FOV in yellow for slice positioning in the cat.

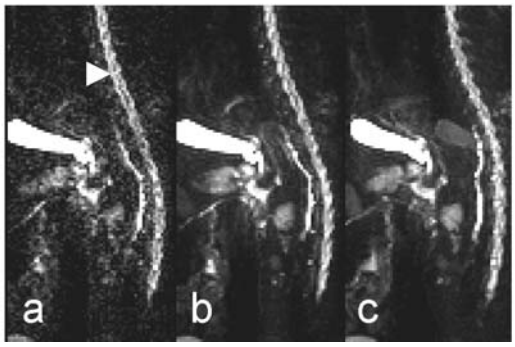

Figure A.3 Typical T_2-weighted SE-EPI in cat
Sagittal T_2-weighted SE-EPI of the cat thoraco-lumbar spinal cord acquired with one shot (a), 20 averaging (b) and 20 averaging with phase encoding rotated by 180° (c). The spinal cord is indicated with the white arrow in a. The difference in distortion pattern is clearly visible between b and c. This difference serves as a basis to correct distortions using the reverse gradients method.

DW acquisition

Use the last acquisition that was performed (step 3 on the reversed gradient scans). Put the number of averaging to seven, and add the diffusion-weighted sequence (card 'Diff'). There should be 64 directions with a b-value of 1000 s/mm^2. This acquisition lengths about 30 min.

Super-resolution acquisition

An additional set of reversed-gradient and DW data will be acquired. For the following scans, the FOV will be shifted through-plane by 1 mm to enable the use of super-resolution reconstruction methods as done in (Carmi et al., 2006; Greenspan et al., 2002; Peled and Yeshurun, 2001). Load the reversed-gradient scan that was done at step 2. To shift the FOV through plane, do the followings. Click on the '...' button right to the 'Position' field (routine tab). Then, select position mode as 'Offcenter-Shift', then add 1 mm to the 'shift' field. Make sure the cord is still completely included in slices. Do the acquisition. Then, rotate the phase encoding direction back to 0°. Do the acquisition. Based on the latter scan, acquire DW dataset

as described in the previous section (add the DW sequence, adjust the number of averaging, etc.). Typical image is shown in Figure A.4b.

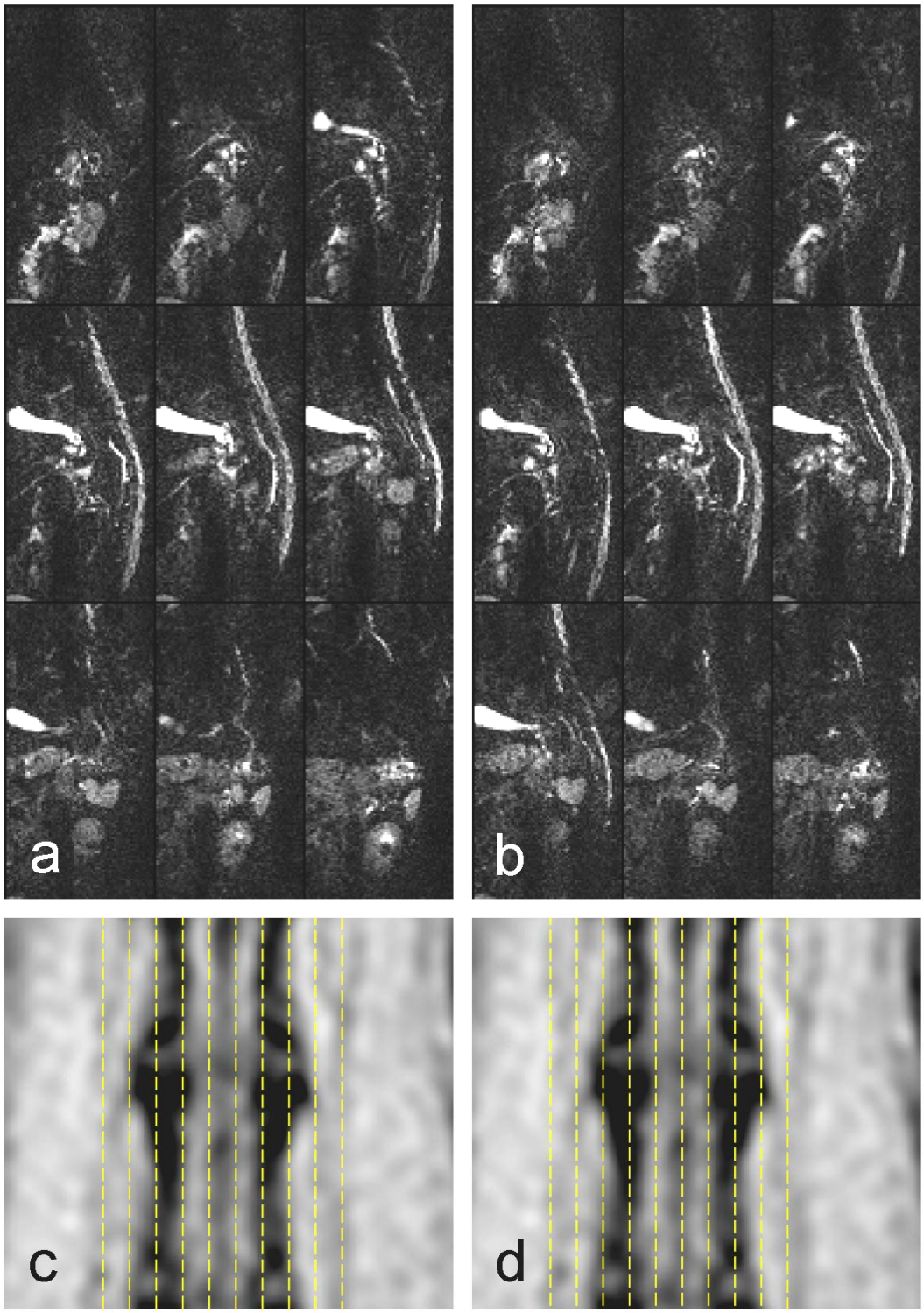

Figure A.4.Principle of super-resolution MRI
Mosaic sagittal T_2-weighted SE-EPI of the cat thoraco-lumbar spinal cord acquired without (a) and with FOV shifted by 1 mm through plane (b). Coronal anatomical images showing slice prescription without (c) and with shift (d).

FSE sagittal acquisition

Position slices as in the previous section (click on the sequence and do 'copy parameters – copy slices').

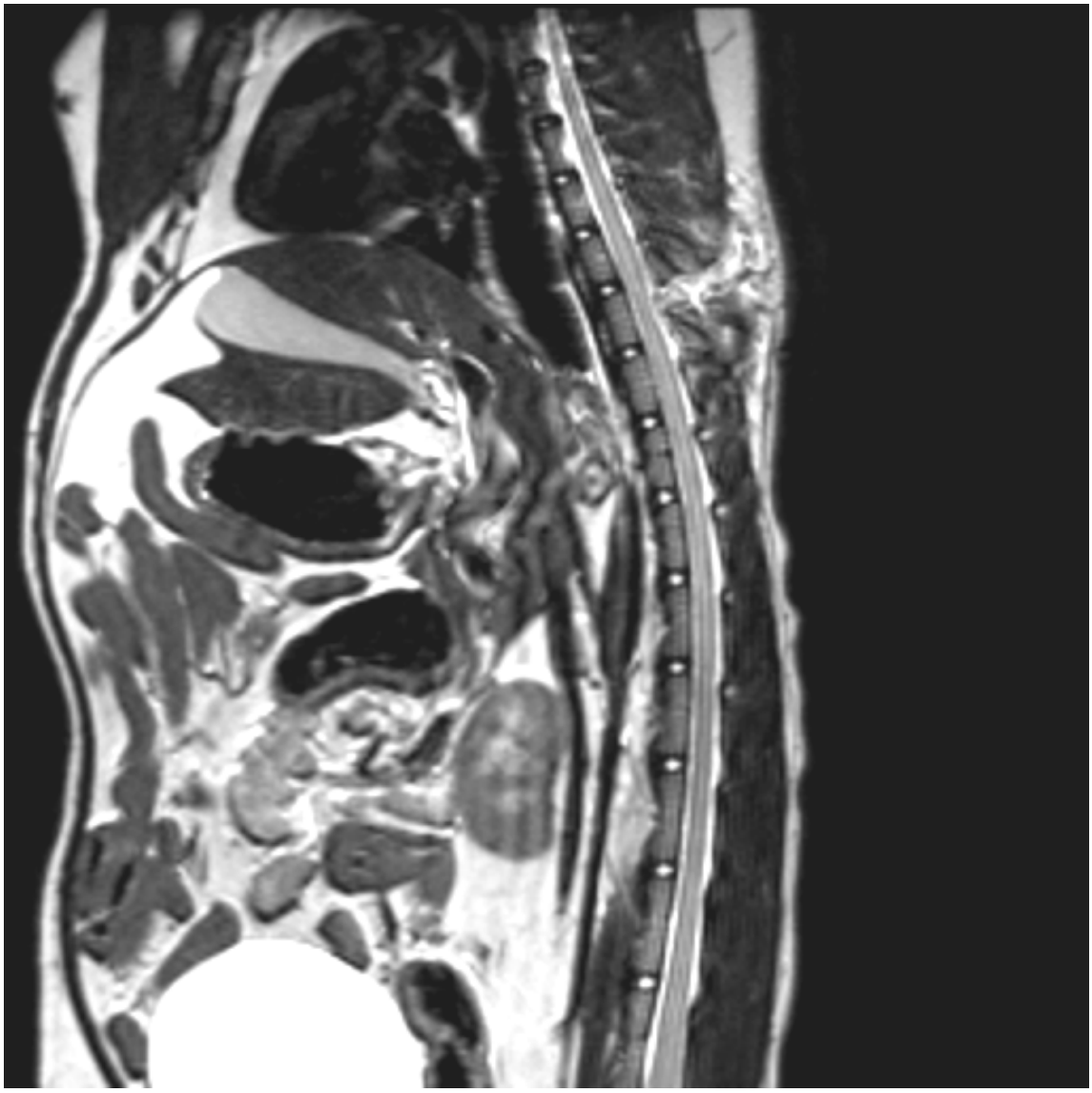

Figure A.5. Typical sagittal FSE image in cat

FSE axial acquisition

Position slices as in the previous section (click on the sequence and do ‘copy parameters – copy slices’)..

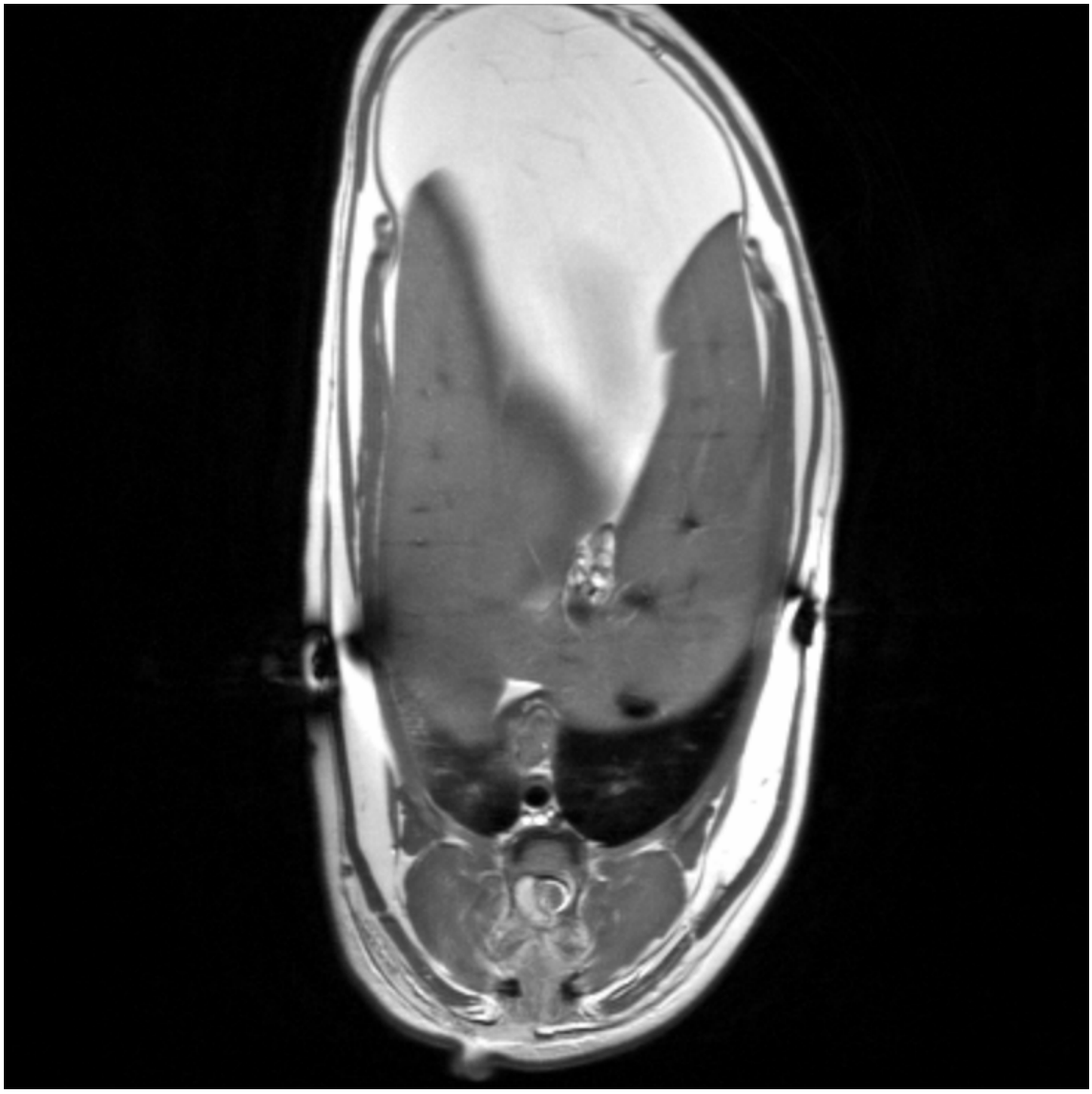

Figure A.6. Typical axial FSE in a cat with left hemilesion

T_1-weighted acquisition

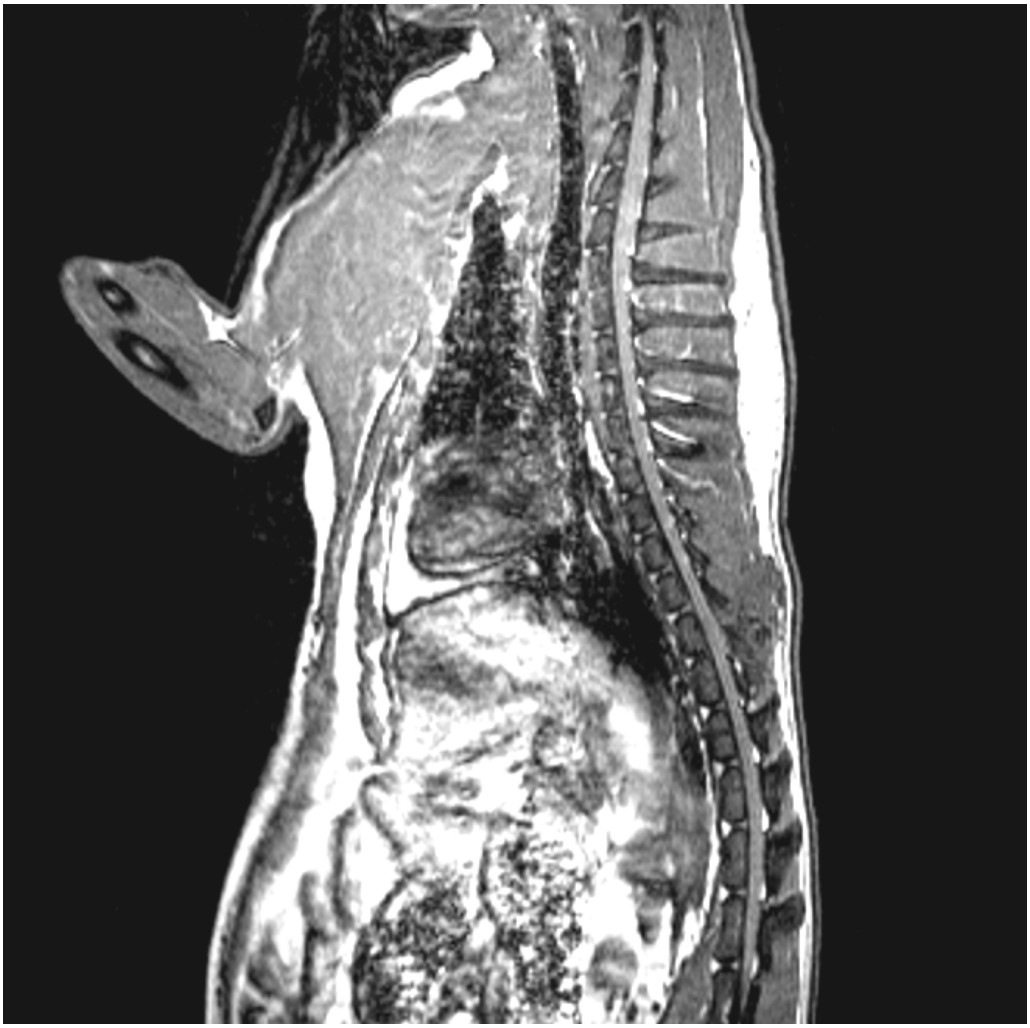

Figure A.7. Typical T_1-weighted image in cat

FMRI of the human cervical spinal cord and brain

Purpose: imaging both the cervical spinal cord and the brain of healthy subjects to investigate the vascular response to hypercapnia. The imaging protocol is as follows:

- Reversed gradient scans (1 min)
- Functional scans with hypercapnia (9 min)
- Functional scans with motor task (squeezing ball, 9 min)
- Resting state scans acquired as control (9 min)
- Susceptibility weighted imaging (SWI) scan (7.1 min)
- Anatomical scan (9.5 min)

Coils

Use the neurovascular coil (12 channels) with the neck coil (only the posterior part). The combination of coil elements have been optimized through sensitivity tests on a water phantom as illustrated in Figure A.8.

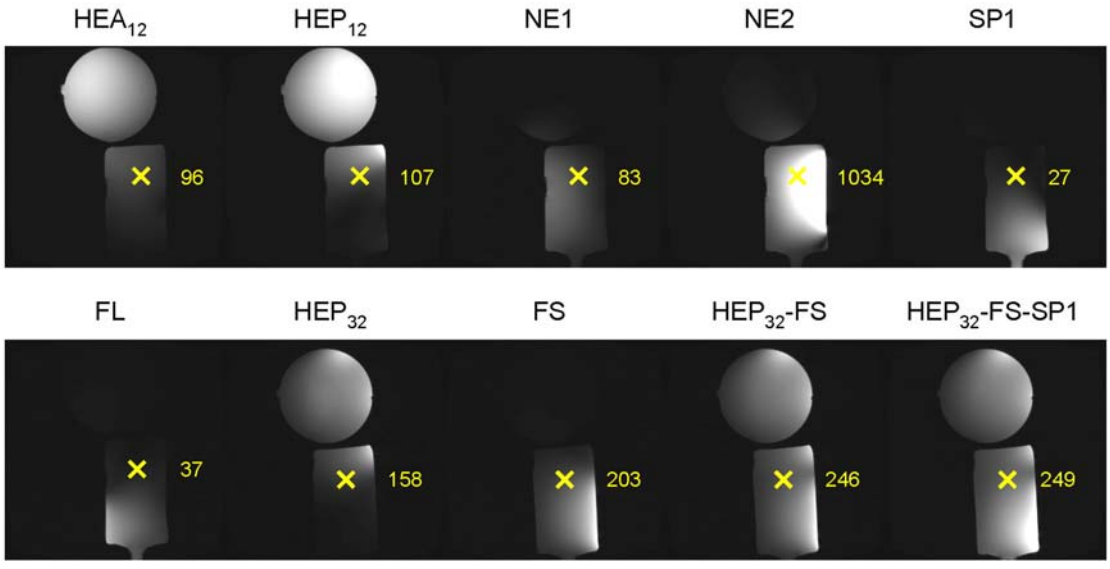

Figure A.8. Coil sensitivity mapping on a water phantom
Water phantom consisted of a sphere and a large bottle to mimic the head and spinal morphology. Both phantom had the same concentration. Abreviations stand for HEA_{12}: Head coil anterior 12 channels, HEP_{12}: Head coil posterior 12 channels, NE1-2: Neck coil 1-2, SP1: Spine coil first 1 (most rostral), FL: Large flex coil, HEP_{32}: Head coil 32 channels, FS: Small flex coil. The yellow cross is located at a region roughly corresponding to C4. Intensity values are reported for each coil combination.

Physiological recordings

Physiological monitoring during fMRI scans are performed using a Biopac system (MP150, Goleta, CA, USA). Place a pulse oxymeter probe in the subject's right index and connect it to the Biopac to record both cardiac pulsation and MRI triggering (100 Hz sampling rate). Place a respiratory bellow around the subject's thoracic cage and connect it to the Biopac system. Use a third channel to record MRI triggering for subsequent synchronization. Those external recordings will be used for modelling fMRI time series via the RETROICOR method (Glover et al., 2000).

Subject positioning

This part is excessively important for axial acquisition. Position the subject head-first supine, with a 1 cm thick pillow over the neurovascular coil. Use no pillow over the neck coil to limit the natural cervical cord lordosis at around C3-C4 (*i.e.*, excessive cord curvature in the A-P direction). Ask the subject to be as straight as possible and to slightly tile his head to limit lordosis. The cord should be straightened in the R-C direction. Also ask him not to swallow during data acquisition.

Functional acquisition

After localizer scan, the crucial step is to adequately position the slices. This adjustment will serve for functional and structural scans. Slices should be positioned axial, roughly perpendicular to the cervical cord – this is the reason why a straight cord is desirable. Adjust the gap to get one slice centred in the vertebral body and one slice centred at the intervertebral disk. Typical slice positioning is shown in Figure A.9. Exhaustive parameters are provided hereafter. Typical image is shown in Figure A.10.

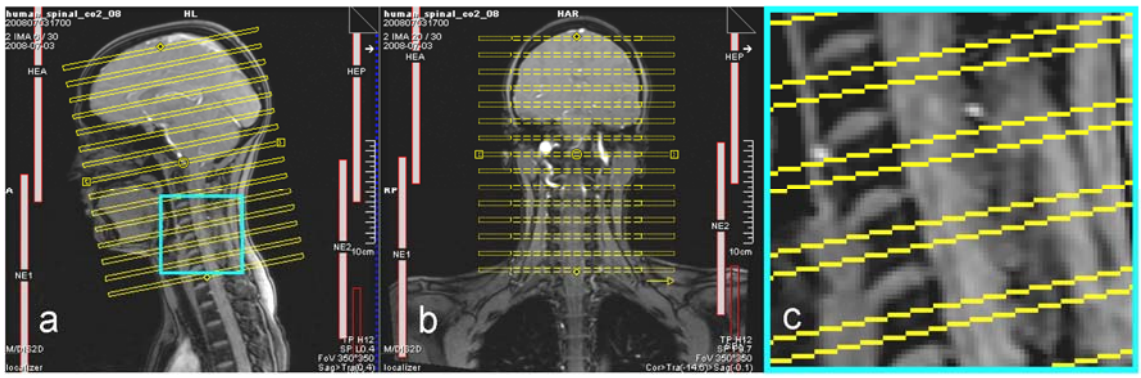

Figure A.9. Slice positioning for fMRI acquisition in human
Sagittal (a) and coronal (b) localizer with slice positioning. Zoomed panel of sagittal view is provided (c). Positioning consists in orienting slices in the plane orthogonal to the spinal cord, adjusting the gap to have all slices centred in vertebral bodies. This is achieved to limit susceptibility artifact.

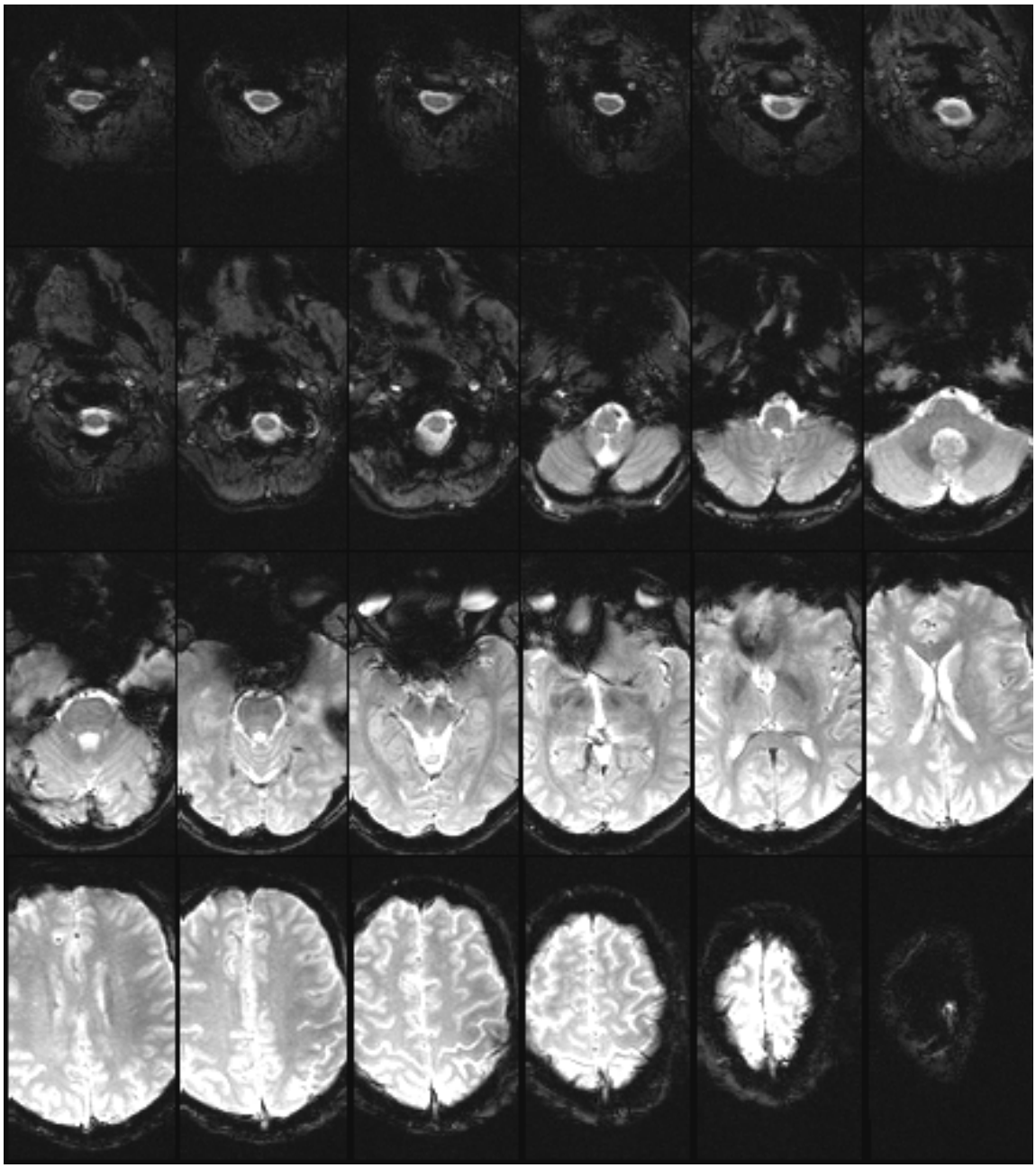

Figure A.10. Typical T_2-weighted GE-EPI in human
Axial mosaic images running from the spinal cord (top left) to the brain (bottom right). In some slices it is possible to delineate grey from white matter in the spinal cord.

Reversed gradient acquisition

Use the same parameters as for functional scans, except that phase encoding direction should be rotated by 180° (in the 'routine' card), and the number of measurements should be 20 to get sufficient SNR. Those scans will be used for subsequent distortion correction (Voss et al., 2006). During pre-processing step, fMRI time series should be co-registered to this image.

T_1-weighted acquisition

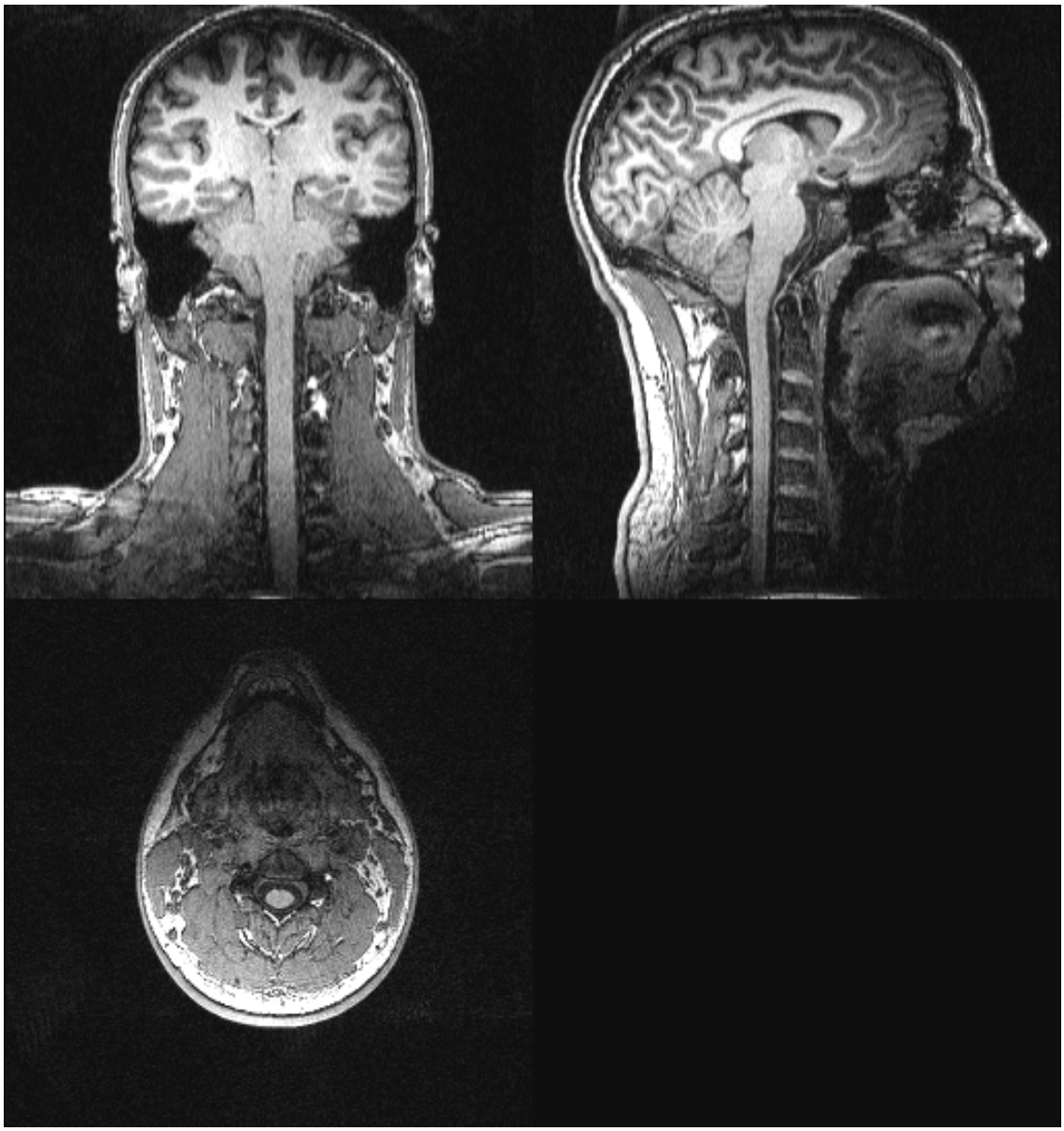

Figure A.11. Typical T_1-weighted image in human
Coronal (top left), sagittal (top right) and axial (bottom left) images of a human brain and spinal cord. Axial view is centred at C3 vertebral body.

Susceptibility weighted images (SWI) acquisition

This type of sequence provides a mapping of large veins – this will be of interest for correlating spatial distribution of activations with localisation of venous network. Typical image is shown in Figure A.12.

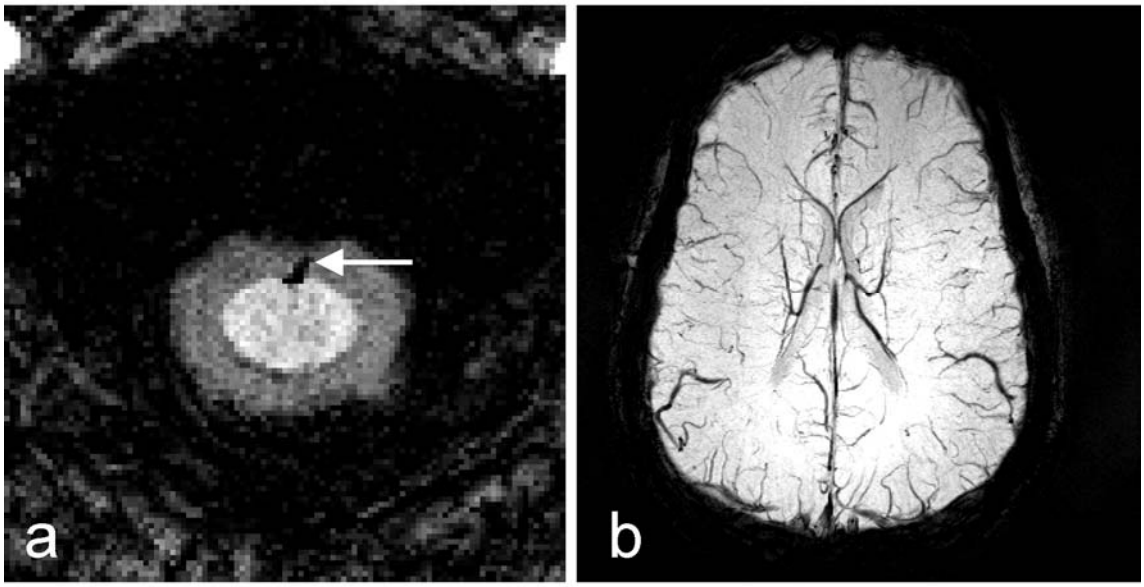

Figure A.12. Typical SWI in human
Axial maps of maximum intensity projection (MIP) from the C3 spinal cord (a) and from the brain (b). This type of sequence allowed to detect a large vein at the ventral aspect of the spinal cord (white arrow). The scaling has been modified between both pictures to enlarge the spinal cord.

B. Article #4: Impact of realignment on spinal functional MRI time series

J. Cohen-Adad[1,2], M. Piché[1], P. Rainville[1], H. Benali[2], S. Rossignol[1]

[1]*GRSNC, Faculty of Medicine, Université de Montréal, Montreal, QC, Canada*
[2]*INSERM U678, Université Pierre et Marie Curie (Paris VI), CHU Pitié-Salpêtrière, Paris, France*

Published in Proceedings of the 29th IEEE EMBS conference. Received 2 April 2007; accepted 7 June 2007.

Abstract

Functional magnetic resonance imaging (fMRI) of the spinal cord produces dataset that are particularly noisy because of cardiac-related motions. Realignment methods allowing subject motion correction might be sensitive to such noisy dataset. By realigning and quantifying cardiac variance on spinal dataset, we showed that such procedures decrease cardiac noise within the volumes. This has a direct and positive impact on functional imaging when estimating the T-score by means of the general linear model.

Keywords: Realignment, functional MRI, fMRI, spinal cord, cardiac noise, general linear model, GLM.

Introduction

Functional magnetic resonance imaging (fMRI) allows for the detection of task-related neuronal activity through acquisition of successive MRI volumes. Analysis of functional MRI series mostly relies on a voxel-by-voxel comparison of signals with and without performing a task (e.g., motor task, visual stimuli). Given the duration of the data acquisition subjects might move in the scanner and the location of every voxel might vary between scans. To correct for these motion artifacts, a preprocessing of fMRI time series is usually applied for realignment. It consists in an inter-scan rigid-body co-registration based on voxel intensities matching. Investigations in brain time series already showed the benefits of this preprocessing step (Friston et al., 1996), (Woods et al., 1998) as well as its limitations (Freire and Mangin, 2001), (Grootoonk et al., 2000), (Liao et al., 2005). However, no investigation has been performed to apply this method to spinal cord time series.

Spinal cord fMRI time series are particularly prone to physiological noise (Giove et al., 2004). Although that noise also arises from respiratory and Mayer-waves phenomena (Julien, 2006), cardiac fluctuations are the main cause of physiological noise in spinal fMRI (Brooks et al., 2004). Artifacts related to cardiac activity come from cerebrospinal fluid (CSF) pulsation and from the main vessels surrounding the spinal cord. Since cardiac noise mostly contributes to variance in spinal data, one could expect different outcomes of realignment procedure when performed in spinal versus brain fMRI time series. Indeed, realignment estimation is based on a majority of voxels that have the same rigid motion. Since cardiac phenomenon is widespread in spinal imaging and thus induces in-phase variation of a large number of voxels, estimation of the motion correction matrix might include these variations. In other words, the transformation matrix computed for correcting only subject motion within the scanner might also include cardiac fluctuations. Thus, applying the transformation for each whole volume, we would expect changes in the cardiac signal distribution throughout the volume including the region of interest (ROI), *i.e.*, the spinal cord. A similar phenomenon has already been observed in the brain when realignment introduced spurious activation signal within the preprocessed dataset (Freire and Mangin, 2001).

When the ROI contains cardiac noise, difficulties may arise when performing a linear regression assuming general linear model (GLM) hypotheses. Widely used in the neuroscience community, the GLM is implemented in freely available software such as SPM (Friston et al., 1994a) or FSL (Smith et al., 2004). The basic idea is to test a condition compared to a baseline, assuming the null hypothesis. The physiological counterpart of that condition is a neuronal activity which induces a local change in the hemodynamic steady state. The expected effect is a local change in the MRI signal, known as blood oxygenation level dependent (BOLD). When a GLM inference is performed on every voxel of MRI time series, one condition for a valid statistic is that residuals should be independent and identically normally distributed (i.i.d.). If cardiac signal is not modeled by drift regressors when performing the inference, residuals will not follow the i.i.d. assumption any more. When temporal autocorrelations are present in residuals the estimated variance is biased, consequently inducing false T-score and altering the activation detection sensitivity (Lund et al., 2006), (Dagli et al., 1999). In this paper, we investigated how cardiac signal is modified throughout the fMRI series when performing realignment procedure on cervical spinal cord data. The direct outcome of this work is a better understanding of the impact of realignment procedure on spinal fMRI.

Methods

Subjects

Four healthy volunteers from the laboratory of one of the investigators (PR) participated in the study as part of developmental tests to assess the feasibility of spinal fMRI. All subjects were familiar with the MRI acquisition procedure.

Acquisition

Acquisition was performed on a 1.5T Siemens Avanto MR scanner. For each subject, four runs were acquired. One run consisted of 6 minutes acquisition (single shot spin echo EPI, sagittal orientation, TR/TE = 250/40 ms, FA = 45°, matrix = 64×64, FOV = 120 mm, slice thickness = 2 mm, gap = 0.4 mm). TR was set to 250 ms in order to avoid any aliasing effect arising from cardiac signal, knowing that cardiac frequency in human is generally lower than 1.5 Hz (Frank et al., 2001). In order to meet the same conditions as for standard BOLD-fMRI acquisition, a motor task (fist clenching) consisting of 6 blocks of 30 s was performed. No task-related activated voxels were expected due to the low TR used in this study. Again, the aim of the study was not to detect any task-related activity but to quantify cardiac variance along the cervical cord.

Cardiac signal was recorded by means of a Biopac System (MP150) combined to a plethysmograph (Nonin 8600FO) attached to each subject's left index finger. Sampling frequency was set to 1000 Hz but signal was then sub-sampled at 4 Hz in order to match MRI acquisition frequency.

Realignment

The rigid-body transformation matrix was estimated using SPM-realign (Friston et al., 1996). Parameters were set to default, *i.e.*, quality of realignment of 1, FWHM of the Gaussian smoothing kernel of 5 mm, first volume set as reference for the registration, 2 degree B-spline interpolation. For each run, all volumes were realigned to the first volume. No mask was applied for this procedure in order to assess the effect of the cardiac signal contained in the whole volume.

Analysis

Let's call $V_{i,j}$ the raw volumes, with i = [1…16] denoting the run number and j = [1…500] denoting the volume number[10]. For all $V_{i,j}$ the realignment matrix was estimated and applied, giving the volumes $Vr_{i,j}$. Each $V_{i,j}$ was then compared with $Vr_{i,j}$ with the following method. Knowing the cardiac signal during the scan session for each run, we designed a band-pass filter F_i based on the cardiac spectrum. $V_{i,j}$ and $Vr_{i,j}$ were filtered in order to retrieve most of the cardiac variance. Filtered data $Vf_{i,j}$ and $Vrf_{i,j}$ were then averaged over j in order to quantify cardiac contribution in every run. A subject-specific mask M_i containing the spinal cord was used to assess the impact of the realignment procedure on the spinal cord region. A diagram of the whole procedure is shown in Figure B.1. A more detailed description of the method is provided in the following paragraphs.

[10] Although we mostly acquired 1500 volumes per run we performed the analysis on 500 volumes because two runs were not acquired completely. We verified the consistency of the results in some runs using the whole dataset.

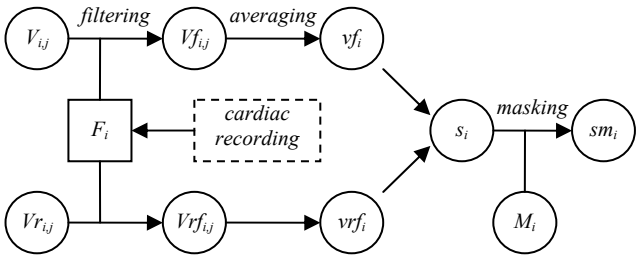

Figure B.1. Diagram of the analysis method for run *i* and volume *j*.

Design of filter

A fast Fourier transformation was performed on each cardiac recording re-sampled at 4 Hz. Based on the power spectrum, a band-pass Butterworth filter F_i was designed with an *ad hoc* spectral window of 0.3 Hz to account for intra-recording cardiac frequency variations, as done in (Thomas et al., 2002). That window was centered on the mode of each cardiac recording. $V_{i,j}$ and $Vr_{i,j}$ were then filtered in the time dimension with F_i, giving $Vf_{i,j}$ and $Vrf_{i,j}$. Since the Nyquist frequency was two times superior to the cardiac spectrum, there was no aliasing of the cardiac signal. Each voxel of Vf_i and Vrf_i thus showed time courses containing most of the cardiac variance.

Design of mask

A volume V_i defined as the mean of $V_{i,j}$ over j was generated for each run. Based on this mean volume, a mask M_i containing the desired ROI was generated. The ROI consisted of the spinal cord as well as the CSF. The generation of the mask was based on the following automatic procedure. The volume was first normalized by the mean, then a Gaussian filter was applied to smooth the volume (FWHM = 11 mm^3). The volume was then made binary using a threshold based on the intensity histogram. Isolated voxels were eliminated using mathematical morphology (opening with a 5-voxels disk). The output was multiplied by a rough mask containing the ROI to eliminate isolated non-wanted structures. All masks were examined by an expert after the automatic procedure. For each run, we thus disposed of a mask showing the spinal cord with surrounding CSF.

Estimation of cardiac variance

Mean of $Vf_{i,j}$ and $Vrf_{i,j}$ over j were estimated in order to retrieve the mean variance of the cardiac signal contained in the raw and realigned series, giving vf_i and vrf_i. For each run, we thus computed a topography of the cardiac variance. Each vrf_i was divided by vf_i to get rid of inter-subject variability towards a different variance extent, giving s_i. The ratio s_i thus quantified the impact of realignment procedure on the presence of cardiac variance. By masking s_i with M_i (denoted sm_i) we performed statistics over the cervical spinal cord.

Results

Realignment procedure did have a significant impact on the cardiac variance distribution in spinal fMRI time series as detailed below.

Estimation of transformation matrix

The matrix transformation usually describes a rigid-body transformation accounting for intra-scan subject motion. Our hypothesis was that since cardiac signal is widely present in spinal fMRI time series, estimation of the matrix would include cardiac signal. We did observe such a phenomenon for all runs and all subjects. Some translation and rotation parameters were correlated with the cardiac recording as illustrated in Figure B.2.

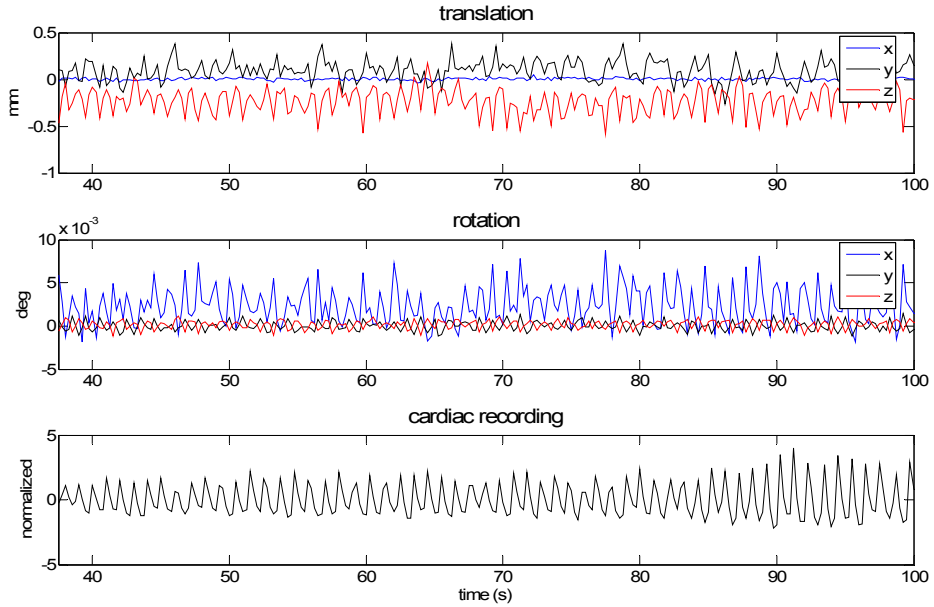

Figure B.2. Comparison of transformation matrix and cardiac signal
Parameters of the transformation matrix (top and middle) and cardiac recording (bottom) for subject 1 run 2. Some translation and rotation parameters are highly correlated with cardiac signal, e.g., the 'z translation' parameter had a Pearson-correlation score of 0.47 (n=500, $p<0.01$).

Quantification of cardiac variance

The proposed method allowed us to quantify the cardiac variance within a ROI. Here the ROI was defined as the cervical spinal cord with surrounding voxels including the CSF. Quantification of cardiac variance showed a reduced cardiac signal for realigned series versus raw series. Table B.1 gives a quantification of the cardiac variance before and after realignment for all subjects. To illustrate the impact realignment had on the data, Figure B.3 shows a topography of the cardiac variance before and after realignment.

	s	sm
subject 1	0.71 ± 0.02	0.74 ± 0.04
subject 2	0.24 ± 0.15	0.58 ± 0.05
subject 3	0.22 ± 0.15	0.49 ± 0.10
subject 4	0.24 ± 0.20	0.64 ± 0.05
all subjects	**0.36 ± 0.08**	**0.61 ± 0.03**

Table B.1. Ratio of cardiac variance before and after realignment
This table is computed for the whole volumes (*s*) and for the mask containing the spinal cord and CSF (*sm*). For each subject, results are averaged across four runs. There was a mean diminution of the cardiac variance of about 39% within the ROI. Note that the standard deviation in 'all subjects' refers to the variation between runs.

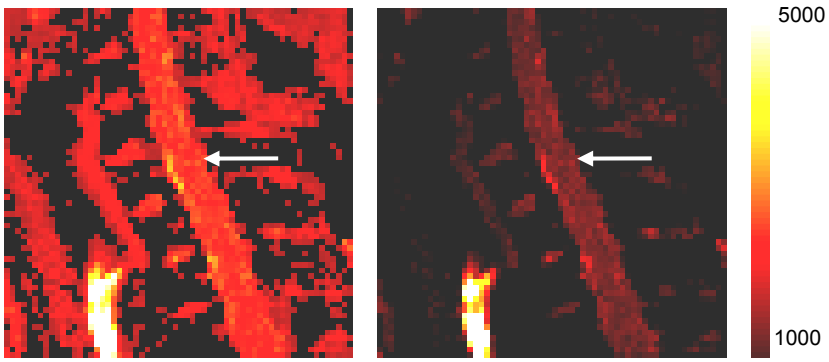

Figure B.3. Effect of realignment on cardiac signal distribution map
Sagittal topography of the cardiac variance before (left) and after (right) realignment for subject 1 run 2. White arrows show the spinal cord. The bottom left structure with high cardiac variance is an artery. The color code represents MRI intensity values (same scale for both pictures).

Discussion

Let us now consider far this work can be applied to classical spinal fMRI studies and the implication of such a noise decrease on statistical inference.

Realignment algorithms

Motion correction methods are based on either different cost functions such as image difference (Friston et al., 1996), image ratio uniformity (Woods et al., 1998), correlation (Collins et al., 1995a) and mutual information (Maes et al., 1999), or other approaches like ICA-based motion correction (Liao et al., 2005).

The present study examined the impact of realignment procedure using one of the most common algorithms (Friston et al., 1996), which may be more sensitive to outliers as pointed

out by Freire *et al.* (Freire and Mangin, 2001). Nevertheless, this work focuses on cardiac-induced bias and not activation-induced bias. In the latter case, the realignment procedure is critical because it may create false positive activation. In our case, we showed that using realignment method with spinal data may also serve to improve the quality of spinal datasets since it reduced the cardiac variance on the ROI.

Although many studies already compared motion correction packages, they were all concerned towards brain datasets (Morgan et al., 2001), (Oakes et al., 2005). Further work has to be done in order to better characterize the impact of other realignment methods by considering both spurious activation and physiological variance redistribution on cardiac-noisy fMRI dataset.

Impact of GLM analysis on spinal fMRI data

One major problem when analyzing fMRI data using the GLM is the assumption made regarding the Gaussian characteristic of residuals. Let us denote by Y the measured data (e.g., the time course of an MRI voxel), by X a time series describing the response to an experimental paradigm (e.g., the paradigm convoluted to the hemodynamic response function), by β the amplitude of that response, by D a matrix modeling the structured background signal with contribution λ, and by e the residuals. The signal Y can be modeled as follows

$$Y = \beta \cdot X + \lambda \cdot D + e \tag{B.1}$$

In this model, one assumes that e is i.i.d.. Given the following inference, one can compute a T-score defined as the estimated β divided by its standard deviation. If e were not i.i.d., the variance of the estimator would be underestimated, thus leading to a biased T-score.

In the case of spinal fMRI, cardiac signal contributes significantly to the voxels contained within the spinal cord. Thus, when modeling Y with the GLM, one has to take cardiac signal into account otherwise residuals e would include cardiac fluctuations leading to colored residuals, *i.e.*, there would be temporal autocorrelations within residuals leading to a biased T-score. In some cases, it is possible to model cardiac signal, e.g., when there is no aliasing of the cardiac signal, typically with TR < 400 ms which is quite rare. In case of aliasing, more complex approaches have to be considered to model physiological noise (Lund et al., 2006).

In this study we showed that the realignment procedure decreases the variance of the cardiac signal. We could thus expect a change in the estimation of the T-score when performing the GLM on classical spinal fMRI studies. Although the realignment procedure seemed to improve sensitivity for detecting activated areas, additional studies on simulation and real data are needed in order to further quantify the benefits of the realignment procedure on spinal fMRI time series.

Limitation of the study

The present study did not account for other orientation planes (*i.e.*, coronal and axial) or other field of view sizes. These parameters have a direct impact on the number of voxels prone to cardiac noise, thus leading to the extraction of more or less of the cardiac signal in the computed realignment matrix. Nevertheless, since cardiac signal is the main signal source in spinal fMRI data, we would expect realignment procedure to have similar effects with other acquisition parameters. Also, some spinal acquisitions might be sensitive to ghosting artifacts, *i.e.*, spreading of a moving structure in the phase encoding direction. More studies would be required to evaluate the effect of physiologically-induced ghosting artifacts on the realignment procedure.

Another key aspect may occur when dataset contain BOLD activation. Since we saw that cardiac-induced motion correction may alter voxel integrity by slightly smoothing them, it might be the case that very localized BOLD signal would be spread, thus reducing the variance of the activation signal by extending its energy on adjacent voxels. This might then reduce both sensitivity and precision for activation detection.

Conclusion

The realignment procedure applied on cervical spinal fMRI datasets reduced the contribution of cardiac activity. Decrease of cardiac signal has a direct and positive impact on the variance estimation when performing the GLM, thus leading to a less biased T-score and an improved sensitivity.

Acknowledgment

We thank G. Beaudoin and the staff of the CHUM Notre-Dame for their support in data acquisition and C. Gauthier for her revision of the manuscript.

C. Article #5: Characterization of cardiac-related noise in fMRI of the cervical spinal cord

M. Piché[1,2], J. Cohen-Adad[1,2,3], M. Khosh Nejad[1,2], V. Perlbarg[3], G. Xie[1,2], G. Beaudoin[4], H. Benali[3,6], P. Rainville[2,5,6]

[1]Department of Physiology and
[2]Groupe de recherche sur le système nerveux central (GRSNC), University of Montreal, Montreal, QC, Canada H3T 1J4
[3]INSERM U678, University Pierre et Marie Curie, Faculty of medicine, Pitié-Salpêtrière, Paris, F-75013 France.
[4]Department of Radiology, CHUM - Notre-Dame Hospital, Montreal, QC, Canada. H2L 4M1
[5]Department of Stomatology, University of Montreal, Montreal, QC, Canada H3T 1J4
[6]Centre de recherche en neuropsychologie et cognition (CERNEC) and Centre de recherche de l'Institut universitaire de gériatrie de Montréal (CRIUGM)

Published in Magnetic Resonance Imaging. Received 20 February 2008; revised 25 June 2008; accepted 30 July 2008. Available online 17 September 2008.

Abstract

In the past 15 years, fMRI studies have largely contributed to our understanding of brain function. At the spinal cord level however, fMRI encounters major technical challenges with cardiac noise being considered a major source of noise. The present study relied on T2*-weighted echo-planar images of the cervical cord (C3 to T1-T2) acquired at 4Hz and combined with plethysmographic recordings to characterize the spatio-temporal properties of cardiac-induced signal changes. Frequency-based analyses examining signal change at the cardiac frequency confirmed mean fluctuations of about 10% in the spinal cord and surrounding CSF, with maximal responses reaching up to 66% in some voxels. A spatial independent component analysis (sICA) revealed that cardiac noise is a significant source of variance in spinal fMRI with several components showing a response coherent with the cardiac frequency spectrum. The time-course of the main cardiac components approximated a sinusoidal function tightly coupled to the cardiac systole with at least one component showing a comparable temporal profile across runs and subjects. Both the frequency-domain analysis and the sICA demonstrated cardiac noise distributed irregularly along the full rostro-caudal extent of the segments scanned with peaks concentrated in the ventral part of the lateral slices in all scans and subjects, consistent with the major channels of CSF-flow. These results demonstrate how cardiac-induced changes are a

significant source of noise likely to affect the detection of spinal BOLD responses. This underscores the importance of developing and validating strategies to control for physiological noise in spinal fMRI studies. Promising strategies are outlined.

Keyword: spinal cord, BOLD, fMRI, cardiac, physiological noise, cervical, human, method.

Introduction

The development of functional magnetic resonance imaging (fMRI) methods has been outstanding but significant sources of noise strongly limit their application to study spinal cord activity. Spinal cord activation has been reported with BOLD fMRI in humans (Backes et al., 2001; Govers et al., 2007; Komisaruk et al., 2002; Madi et al., 2001; Maieron et al., 2007b; Stracke et al., 2005; Stroman et al., 1999; Stroman and Ryner, 2001; Yoshizawa et al., 1996), but no standard protocol has been established and the intra and inter-subject reliability dramatically needs to be improved (Giove et al., 2004). The relatively poor reliability of the effects reported in most of the available studies could be explained, at least in part, by a poor control of physiological noise. A few spinal fMRI studies were designed to control for cardiac noise artefacts (Backes et al., 2001; Stroman, 2006). However, these methods need to be improved and significant advances require a better characterization of physiological noise.

There are at least two ways by which cardiac activity may affect fMRI signal at the spinal level. The first one involves direct effect induced by the dilation of arteries following the systole. Cerebral fMRI signal has been found to vary considerably across the cardiac cycle, especially along the major brain vessels (Dagli et al., 1999). At the cervical level, the arterial inflow comes from branches of the vertebral arteries to one anterior spinal artery and two posterior spinal arteries which run along the rostro-caudal axis of the ventral and dorsal cord, respectively. Pulsatile activity within those vessels may induce cardiac-related signal change that may contaminate fMRI signal within the ventral and dorsal horn of the spinal cord.

The second possible source of cardiac noise in fMRI signal is indirect, through the movement of the CSF. A transient increase in intracranial pressure is observed following the systole leading to a rostro-caudal displacement of CSF from the intracranial subarachnoid space into the subarachnoid space of the spinal cord (Alperin et al., 1996; Du Boulay, 1966; O'connell, 1943; Schroth and Klose, 1992). During the diastole, the CSF flows back in the caudo-rostral direction (Henry-Feugeas et al., 1993). This flux and reflux of CSF flows at approximately 3 cm/s but can reach a velocity as high as 7 cm/s at the cervical cord level (Henry-Feugeas et al., 1993; Watabe et al., 1999). This CSF flow is further organised spatially along four channels of the spinal subarachnoid space: one ventral, one dorsal and two lateral (left and right) channels (Henry-Feugeas et al., 1993). An MRI study using a cine-phase-contrast pulse sequence demonstrated that CSF flow is not continuous from the upper cervical to the thoracic level and is not uniform in the different channels (Henry-Feugeas et al., 2000).

More specifically, the velocity is lower in the narrow dorsal CSF channel, and the dorsal and ventral channels are interrupted in part by the curvature of the spine (cervical lordosis). This leads to a flow from the anterior and posterior channels into the lateral channels, from the midcervical level to the thoracic level. Thus, the cervical CSF pulsation is spatially heterogeneous and varies according to the location within the spinal canal. This CSF flow is likely to produce significant changes in fMRI signal that must be characterized before an adequate correction method can be developed and applied effectively.

Previous studies have looked at cardiac-induced signal change in brain fMRI (Dagli et al., 1999; Hu et al., 1995) but, as in the vast majority of fMRI studies, the fMRI acquisition rate was much lower than the heart rate, therefore aliasing the fundamental frequency of the cardiac cycle. A retrospective gating method has been applied to estimate and remove the signal change induced by the cardiac cycle; however, although this method may prove to be effective in some circumstances, it does not allow for a precise characterization of the cardiac noise and it may partly remove variance in the signal of interest because of aliasing. Another strategy is to increase the sampling rate of fMRI images to avoid aliasing. Images can then be filtered temporally to estimate the variance within the bandwidth of cardiac frequency and generate a spatial map of the related signal change. In the present study we first applied such an approach to fMRI at the spinal level, allowing quantification of the cardiac fluctuations.

A second analysis strategy based on independent component analysis (ICA) can be used to identify cardiac components in spinal fMRI data. ICA allows for the extraction of a phenomenon from a mixture of signals (Comon, 1994) and is a validated approach to identify and characterize physiological noise in brain-related physiological data in EEG recordings (Srivastava et al., 2005). Spatial ICA (sICA) has been applied to identify and correct for structured noise in brain fMRI data (Perlbarg et al., 2007). This method may contribute to the characterization of cardiac noise from spinal fMRI data.

The primary goal of this study was to quantify the cardiac-related signal change in spinal fMRI and describe its spatio-temporal characteristics. In a first analysis, a filtering procedure was used to isolate cardiac variance in the images and quantify the signal change. In the second analysis, the most important cardiac components in the spinal fMRI time series were identified by sICA and characterized in relation to the cardiac systole. Using both methods, we provide spatial maps of the cardiac-related signal change.

Methods

Spinal imaging

A total of 15 fMRI scans were performed in four healthy volunteers familiar with the MRI acquisition procedure as part of developmental tests to assess the feasibility of spinal fMRI. Images were acquired on a 1.5T Siemens Avanto MR scanner. All subjects performed 4

scanning runs (390s each) except one in whom the last scan was discontinued due to technical problems. Subjects were positioned to limit head movement and reduce neck lordosis and were requested not to move. A sagittal localizer was first acquired to determine the area to cover in the functional scans and a coronal localizer was acquired to allow slice positioning within the spinal cord. The subject's neck was carefully positioned and repositioned if necessary after the localizers. The second of three sagittal slices was centered on the mid-sagittal plane of the spinal cord and the two lateral slices covered the lateral aspects of the spinal cord including dorsal and ventral horn regions (thickness = 2 mm; gap = 0.4 mm). Slices were positioned to cover the vertebral body of C3 to T1-T2 (Figure C.1). FMRI data were acquired using a gradient-echo EPI sequence with a TE = 40 ms, a matrix of 64×64, and a Field of View = 120 mm (in plane resolution = 1.9 mm). A short TR of 250 ms was used to sample the signal changes across the cardiac cycle adequately. The flip angle was adjusted accordingly to 45°. Gradient spoiling, consisting in 2 diffusion gradients in opposite phase, was used to suppress spin-memory effects (steady-state free precession) due to the short-TR acquisition and potentially affected by cardiac activity. Although the present study was not designed to detect spinal activity, a motor task consisting in 6 blocks of 30s of isometric fist clenching was performed. This insured that the assessment of cardiac-related noise was performed in conditions similar to those normally tested in BOLD-activation studies. Ad-hoc analysis of task-related activation based on the general linear model (SPM2) and correcting for multiple comparisons using an appropriate statistical criterion (e.g. Bonferroni correction based on random field theory) did not yield significant effects.

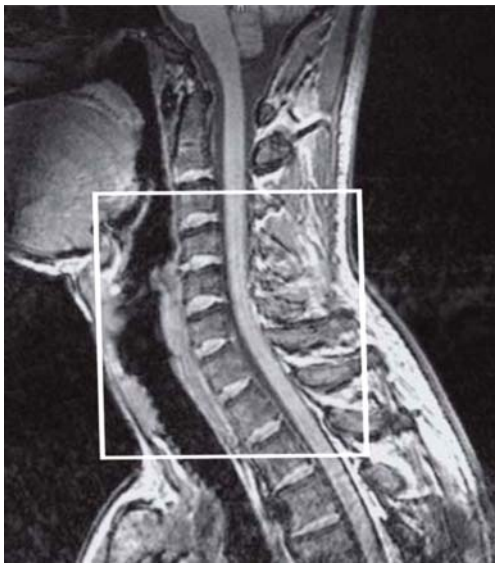

Figure C.1. Field of view for sagittal acquisition in human
Anatomical image in the sagittal plane showing the field of view of fMRI time series acquisitions.

Physiological monitoring

Heart rate was monitored continuously using a plethysmograph (Nonin model 8600FO) with the sensor attached to the subject's left index finger. During the functional scans, a TTL pulse for each fMRI volume and the continuous plethysmographic data were sampled at 1000 Hz and recorded on a MP150 system (Biopac Systems, Goleta, CA 93117). This allowed us to determine precisely the acquisition time of each volume relative to the cardiac systole (*i.e.* post-systole delay).

Data analysis

Data analysis is outlined as follow. FMRI data analysis was done in parallel using two separate procedures as described in Figure C.2. Mosaic DICOM files were saved into Analyze format. In the first procedure, masks for each run were generated to include the spinal cord and CSF. Next, the images were filtered to extract, quantify and localize variance in the range of cardiac frequency. In the second procedure, sICA was applied to extract 30 independent components from unmasked data. Linear regression between the power spectra of independent components and that of the corresponding plethysmographic recordings allowed selecting sICA components showing time course coherent with cardiac activity. Spatial maps of those cardiac components were generated. The temporal relationship between the time course of the cardiac components and the plethysmographic recording was further examined by plotting the signal change against the post-systole delay of each volume acquisition. Details on each of these analysis steps are described in the following subsections.

Subject motion and slice timing

Motion and slice-timing correction are part of standard fMRI analysis. However, the impact of cardiac noise is expected to be widespread, inducing variation in a large number of voxels, so the estimation of the motion-correction matrix might include these variations. Moreover, realignment has been shown to affect the integrity of the data (Freire and Mangin, 2001) and may affect the estimate of cardiac-related signal changes (Cohen-Adad et al., 2007g). In the present data set, motion was less than 1 mm and 0.2 degree along the three axes in all runs (rigid-body transformation; SPM realign). Since the aim of the present study was to characterize the cardiac-related signal, realignment was not applied to preserve the integrity of the signal as much as possible.

The maximum inter-slice time interval was only 160 ms (between the first and third slice acquired). No slice-timing correction was applied as variations occurring within the acquisition of a volume would not hinder our ability to characterize the magnitude and location of cardiac-related noise. This also preserves the integrity of the data from the interpolation process artefacts inherent to slice-timing correction (Calhoun et al., 2000). It may introduce a phase shift in the spatio-temporal pattern of cardiac-related signal fluctuations between slices. However, sICA is designed to capture effects that are spatially distributed (including between

slices). Moreover, this would represent a rostro-caudal shift (between outermost slices) of 5 mm at the most for a CSF velocity of 3cm/s (Henry-Feugeas et al., 1993; Watabe et al., 1999).

Design of masks

A mask containing the spinal cord and the surrounding cerebrospinal fluid (CSF) was created using the mean functional image of each run. The design of the mask was based on the following automatic procedure: the volume was normalized then smoothed using a Gaussian filter (FWHM = 11 mm). Next, the smoothed volume was made binary using a threshold according to the intensity histogram. Mathematical morphology was used to eliminate isolated voxels (opening with a 5-voxels disk). The created mask was then multiplied by a coarse mask containing the spinal cord and surrounding CSF to eliminate unwanted structures, such as large arteries, in which cardiac variance was present. The output masks were examined and validated by an expert after the automatic procedure. A separate mask of the spinal cord with surrounding CSF was created for each run.

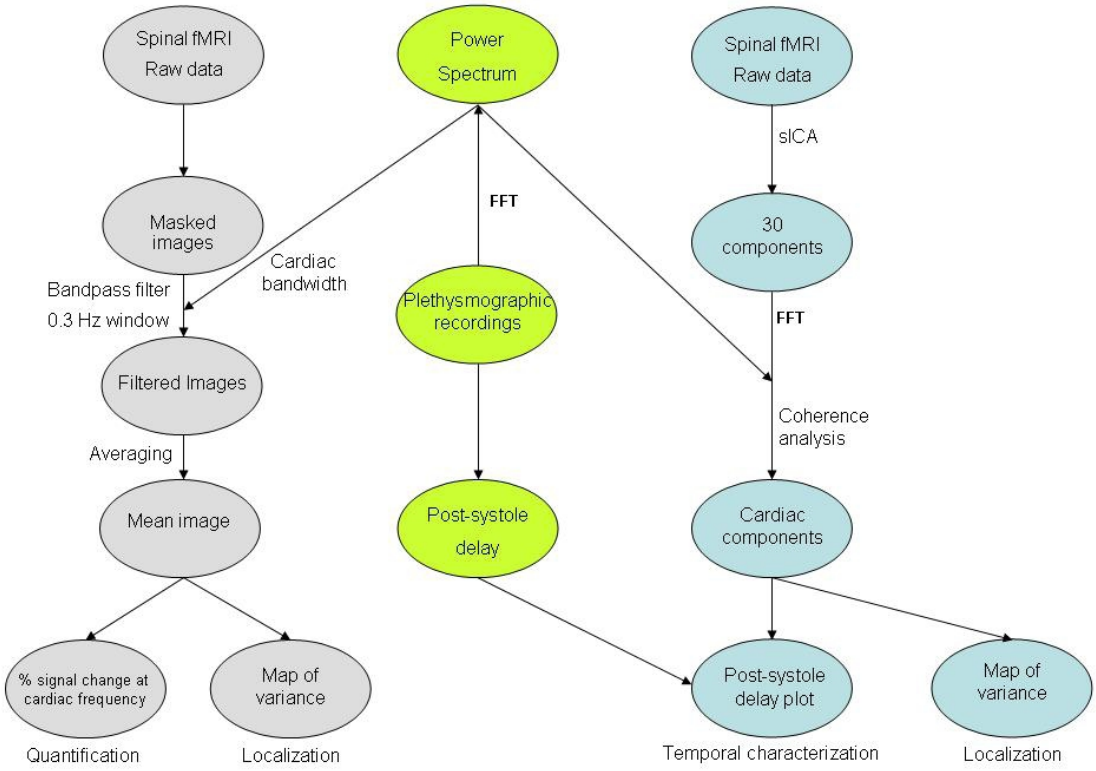

Figure C.2. Flowchart of data processing

Data processing. Two procedures were used to quantify the cardiac-related signal change in spinal fMRI and to describe its spatio-temporal characteristics. On the left, raw images are band pass filtered based on the target cardiac frequency band determined by the power spectrum of the plethysmographic recordings. The resulting mean image allows quantification and localization of the noise at cardiac frequencies. On the right, sICA is applied to extract the first 30 independent components from the raw data. The cardiac components are determined by a coherence analysis between the power spectra of the plethysmographic recordings and the components. The resulting cardiac components allow for temporal characterization and localization of the cardiac noise.

Cardiac data processing and fMRI data filtering

A fast Fourier transformation was performed on each plethysmographic recording, resampled from 1000Hz to 4 Hz to have a sampling identical to fMRI time-series (TR of 250 ms = 4 Hz). Based on the power spectrum of the plethysmographic recording, a band pass Butterworth filter was designed as follows: (i) the frequency centre of the filter was set to the observed modal frequency and (ii) an *ad hoc* spectral window of 0.3 Hz was used to account for intra-recording cardiac frequency variations (Thomas et al., 2002). We verified that most of the cardiac spectrum was contained within that window. A constant spectral window was used in order to avoid biased intra-subject quantification of standard deviation after filtering the fMRI series.

Quantification and localization of cardiac variance

A baseline was defined for each run as the mean of all voxels intensity within the mask. All fMRI series were then filtered in the time domain with the run-specific Butterworth filter described above to extract variance within the observed cardiac frequency band. The magnitude of signal change in the range of cardiac frequency was quantified (%) in relation to the mean signal in the unfiltered fMRI time-series. Since Nyquist frequency was more than twice the maximum of the cardiac spectrum, there was no aliasing of the fundamental frequency of the cardiac signal. The standard deviation of every time course was estimated and normalized to the baseline (Dagli et al., 1999). Thus, a voxel-by-voxel analysis of the standard deviation of MRI signal within the range of cardiac frequency was performed for each run and spatial maps of percent signal-change were generated.

Spatial ICA decomposition and selection of cardiac-related components

In a subsequent analysis (Figure C.2; right panel), each scan was analysed separately with a spatial ICA decomposition (sICA © 2006 Inserm U678 V. Perlbarg) to isolate the independent components from the raw fMRI data (McKeown et al., 1998). It was assumed that most of the cardiac variance would be captured within the first 30 components. Using a fast Fourier transformation, the power spectrum of each component was extracted and compared with the power spectrum of concurrent plethysmographic recordings using a linear regression analysis. This frequency–domain coherence analysis allows for the identification of putative cardiac components independent from potential phase-shifts between the cardiac systole and the time courses of the sICA components. For each scan, correlation coefficients reached statistical significance for at least one component (Pearson-r ; $p < 0.05$, adjusted using the Bonferroni-correction based on the number of components tested). The spatial structure of these cardiac components was then examined.

Temporal characterization in relation to the cardiac systole

To further characterize the signal change of putative cardiac components in relation to the cardiac activity, the normalized signal of each identified component was plotted against the post-systole delay, as determined by the cardiac and image acquisition recordings. Based on combined ECG and plethysmographic recordings obtained outside of the scanner, the cardiac systole was estimated to occur about 400 ms before the finger pulse. This interval was used to approximate the true post-systole delay. This analysis provided (1) a confirmation that the coherence analysis correctly identified signal-change time-locked to the cardiac systole and (2) a description of the temporal characteristics of cardiac noise. It also allowed for a comparison of cardiac noise with patterns of CSF flow velocity described in previous studies (Henry-Feugeas et al., 1993; Watabe et al., 1999).

Results

Heart rate activity was calculated from the plethysmographic recording obtained in all scans. The mean heart rate across all runs and subjects was 63.6 ± 5.4 bpm. The mean standard deviation (intra-run variance) for all runs and subjects was 6.4 ± 2.5 bpm.

Quantification of signal change at the cardiac frequency

The first question addressed concerned the magnitude of the cardiac-related signal change. The quantification was done on the temporally filtered images (bandwidth of 0.3 Hz centered on the modal frequency). The value of signal intensity for the voxels included in the mask (see methods) was calculated and the results for each of the three slices are presented separately for each scanning run in Table C.1. Considering the mean voxel value, the signal change was similar across slices, runs and subjects (around 10%). However, based on peak values (the maximum variation in a voxel), some voxels presented very large signal change. For instance, a peak of 66% was found in subject 1, run 2 (see Table C.1, peak_s3). Interestingly, the most extreme variations are found in the two outermost slices. Indeed, the maximum signal change in the middle slice did not exceed 20% whereas the outermost slices presented variations between 22% and 66%. This distribution is illustrated in the spatial maps of standard deviation (Figure C.3,Figure C.4,Figure C.5).

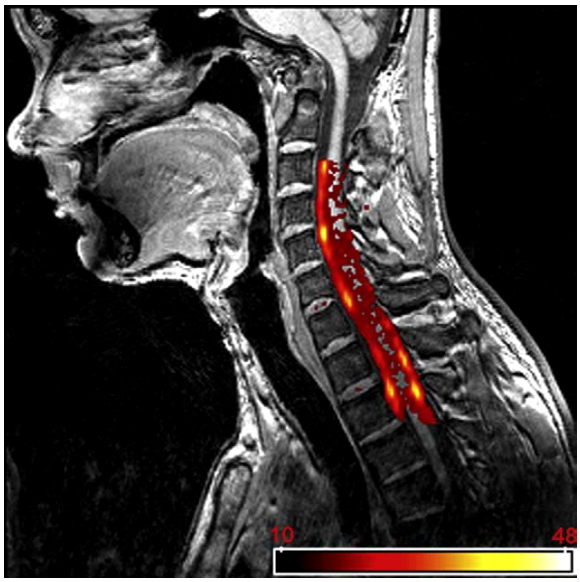

Figure C.3. Cardiac mapping in the cervical spinal cord

Signal change within the cardiac frequency range overlaid on the T1 anatomical image in one subject. The color scale indicates the percent signal change relative to the mean value of all voxels included in the mask (see methods). The highest peaks are found in the CSF but note that decreasing the threshold also shows signal changes within the spinal cord.

subj	run	mean_s1	mean_s2	mean_s3	peak_s1	peak_s2	peak_s3	sd_s1	sd_s2	sd_s3
1	**1**	10.8	10.7	10.3	36.5	15.8	61.7	4.9	5.1	5.4
	2	11.2	11.2	10.8	41.9	15.6	66.2	5.8	6.0	6.3
	3	11.1	11.2	10.7	39.5	16.4	58.1	5.6	5.8	6.1
	4	10.9	10.9	10.5	37.6	13.6	47.2	5.2	5.4	5.7
mean		**11.0**	**11.0**	**10.6**	**38.9**	**15.4**	**58.3**	**5.4**	**5.6**	**5.9**
2	**1**	11.0	10.8	10.3	33.9	12.5	49.3	4.5	4.9	5.1
	2	10.4	10.5	9.9	48.0	13.2	48.4	5.7	6.0	6.1
	3	10.2	10.3	9.8	38.6	11.7	47.8	5.0	5.3	5.4
	4	11.4	11.6	10.8	47.1	13.0	52.4	5.3	5.6	5.9
mean		**10.7**	**10.8**	**10.2**	**41.9**	**12.6**	**49.5**	**5.1**	**5.4**	**5.6**
3	**1**	10.7	10.5	10.4	24.2	15.1	25.9	2.8	3.2	3.3
	2	10.2	10.1	10.0	22.4	14.1	21.5	2.4	2.8	2.9
	3	10.8	10.5	10.4	25.8	14.2	24.2	2.8	3.4	3.5
	4	10.6	10.4	10.3	24.9	13.2	25.3	2.7	3.2	3.4
Mean		**10.6**	**10.4**	**10.3**	**24.3**	**14.1**	**24.2**	**2.7**	**3.1**	**3.3**
4	**1**	10.5	10.8	10.1	30.4	19.6	31.4	3.5	3.6	4.2
	2	9.5	9.7	8.9	24.3	17.9	22.1	2.4	2.6	3.7
	3	9.9	10.1	9.5	23.6	19.6	21.1	2.5	2.7	3.8
Mean		**10.0**	**10.2**	**9.5**	**26.1**	**19.0**	**24.9**	**2.8**	**3.0**	**3.9**

Table C.1. Quantification of cardiac variance

Mean, maximum (peak) and standard deviation (sd) of the percent signal variation within the range of cardiac frequency in each of the three slices (s1-s3) and for each subject (subj 1-4) and run (1-4).

Localization of signal change at cardiac frequencies

The filtered signal in one slice for one typical functional run was overlaid on an anatomical image and is presented in Figure C.3. The peak variations are found at the interface between the CSF and the spinal cord, with maxima reaching as high as 48% signal change in this representative example. Importantly, this effect was not limited to isolated voxels but rather extended to groups of voxels along the rostro-caudal axis. To better illustrate the effect, the three slices for all runs in one subject are presented in Figure C.4. The prominent characteristic is the larger signal variations at the anterior CSF/spinal cord interface, especially in the two outermost slices.

Intra- and inter-session reliability

To examine the reliability of the effect described above, intra- and inter-session comparisons are illustrated. The intra-session comparison across runs is shown for one subject in Figure C.4. Note that similar results were obtained in all subjects. The four runs acquired in that subject clearly show that the signal change at cardiac frequency is very stable both in terms of localization and magnitude. The peaks are located at the same position and the pattern across slices is preserved. The range of mean and peak signal change is also comparable across runs (see Table C.1).

To evaluate the inter-session reliability of the signal change within the range of cardiac frequency, one run from each subject is shown in Figure C.5. Some inter-individual differences were expected but the comparison of the four subjects indicates that the spatial distribution of the most affected voxels and their range of signal change was relatively comparable (see Table C.1 for quantitative results). Larger effects were found again on the rostro-caudal axis along the CSF/spinal cord border. For all subjects, the anterior CSF/spinal cord interface in the two outermost slices was more affected by the extreme signal variations, confirming the results from one subject presented in Figure C.4. Subject 4 displayed the most pronounced cervical lordosis and presented additional peak signal variations in the dorsal CSF/spinal cord interface and in the mid-saggital slice. This subject also displayed the largest peak signal change in the middle slice compared to the other subjects, and the smallest differences across slices (see Table C.1). This suggests a relatively more important spreading of cardiac noise that might be associated with the sharper lordosis.

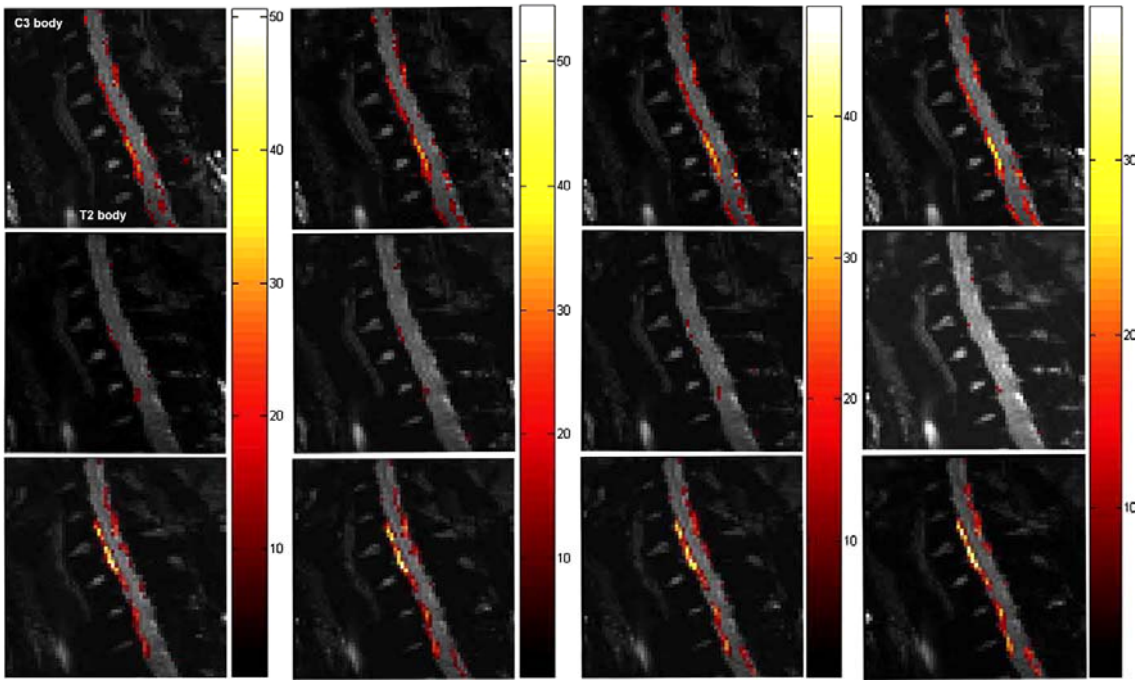

Figure C.4. Intra-subject variability of cardiac contribution to fMRI signal

Illustration of the cardiac-induced signal change in one subject. Columns represent each of the four runs with the vertical colour scale indicating the percent signal change (relative to the mean value of all voxels included in the mask). Each column is composed of three images representing the three slices of the volume from left (top) to right (bottom). The maps of percent signal-change are overlaid on the mean functional images. Vertebral bodies are easily identified in the images (see C3 and T1 bodies in the upper right image).

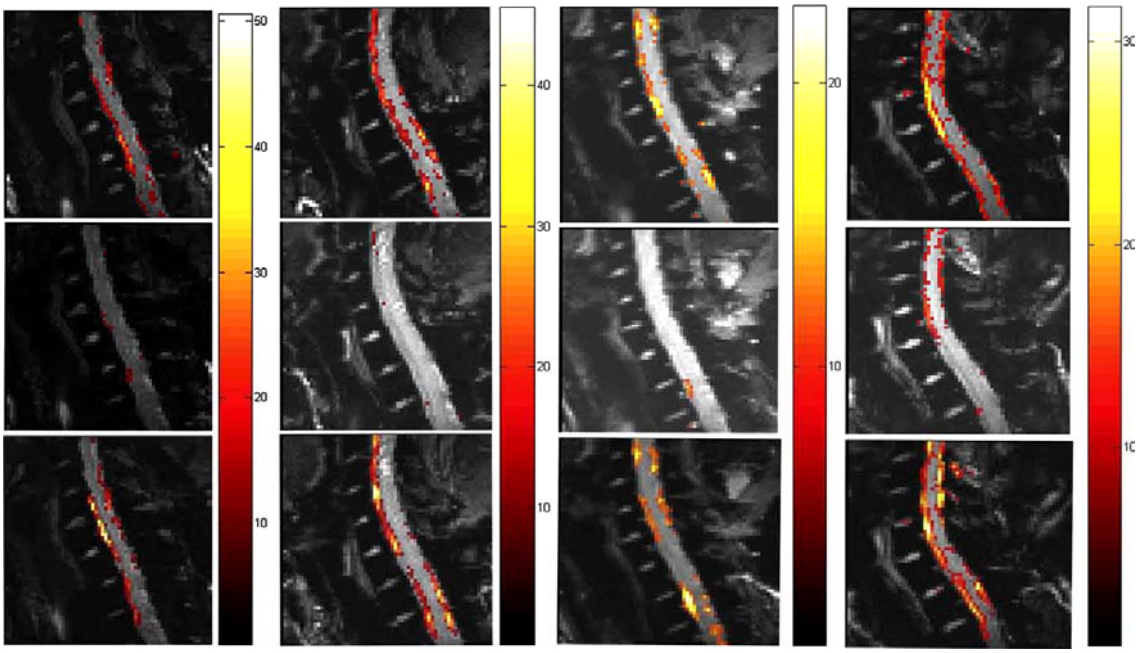

Figure C.5. Inter-subject variability of cardiac contribution

Comparison of the cardiac-induced signal changes in four subjects for one run. Columns represent each of the four subjects with a vertical scale indicating the percent signal change (relative to the mean value of all voxels included in the mask). Each column is composed of three images representing the three slices of the volume from left (top) to right (bottom). The maps of percent signal-change are overlaid on the mean functional images.

Spatial ICA decomposition and identification of cardiac components

In the second analytical approach (see left panel in Figure C.2), the first 30 independent components (ranked by eigenvalues) were extracted from each volumetric time-series using sICA. The mean variance explained by these first 30 components across all runs and subjects was 17.8 ± 1.5 % of the total variance. Individual component over the 30th explained less than 0.25% of the total variance. Among the selected components, one to four cardiac components were identified based on the significant coherence with the cardiac frequency spectrum extracted from the plethysmographic recordings. The mean variance explained by the selected cardiac components within a run was 4.0 ± 1.2 % of the total variance. In all runs, all significant cardiac components were found within the first 7 sICA components (ranked by eigenvalue). The first cardiac component was always found within the first three sICA components and in 11/15 cases the first two sICA components were related to cardiac activity. This confirmed that at least part of the cardiac noise has a stable spatio-temporal structure that can be captured by sICA.

A spatial map of z-scores assessing the contribution of each voxel to the time course of each independent component was used to localize cardiac noise. One representative example is presented in

Figure C.6. Overall, the spatial distribution of the cardiac noise was highly consistent with the results from the frequency-based analysis. Here again, the anterior CSF/spinal cord border in the two outermost slices was more affected by the extreme signal variations. To look at temporal characteristics of the cardiac components, the normalized signal of the cardiac components was plotted against the post-systole delay for each volume acquisition. An example of this plot for one cardiac component is shown at the bottom right of

Figure C.6. Each point represents a volume with the associated signal value of the corresponding component plotted against the post-systole delay. For that component, there was a clear sinusoidal pattern describing the signal change time-locked to the cardiac systole.

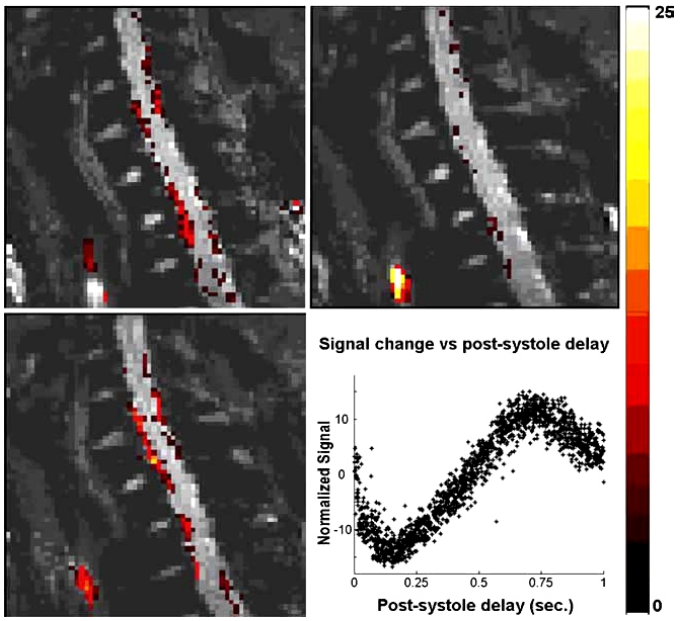

Figure C.6. Variance map of an ICA component related to post-systolic phase
Spatial map of variance for one sICA component displaying a cardiac-coherent power spectrum. The left and middle slices are presented at the top left and right, respectively, and the right slice at the bottom left. The graph represents the time course of the normalized signal for that component plotted against the post-systole delay. Each point in the graph corresponds to one time point (each run = 390s * 4Hz = 1560 data points).

Pattern of signal change relative to the cardiac systole

All cardiac components identified from the output of sICA by the coherence analysis were examined in the time-domain. The normalized signal for each cardiac component was plotted against the post-systole delay. To allow for an intra- and inter-session comparison, the results are presented together for all runs in Figure C.7. The plot of each component was fitted with a 10th degree polynomial in order to provide an accurate summary of each time-course with minimal constraints.

In addition to showing a clear temporal relation with the cardiac cycle, all significant components are spatially distributed along the rostro-caudal axis at the CSF/spinal cord border (as shown in the representative example in

Figure C.6). There is also a remarkable stability in the spatio-temporal profile of several cardiac components identified across runs within the same subject (Figure C.7). For example in subject 1, two cardiac components with a very similar temporal profile were found across the 4 runs. For all subjects, at least one component could be readily identified that followed the same temporal pattern across all runs. One cardiac component also displayed a very similar temporal profile across subjects and runs (see red lines in Figure C.7) except for subject 3 runs 1-2. The signal change for that component has its minimum and maximum around 200 ms and 700 ms post-systole, respectively.

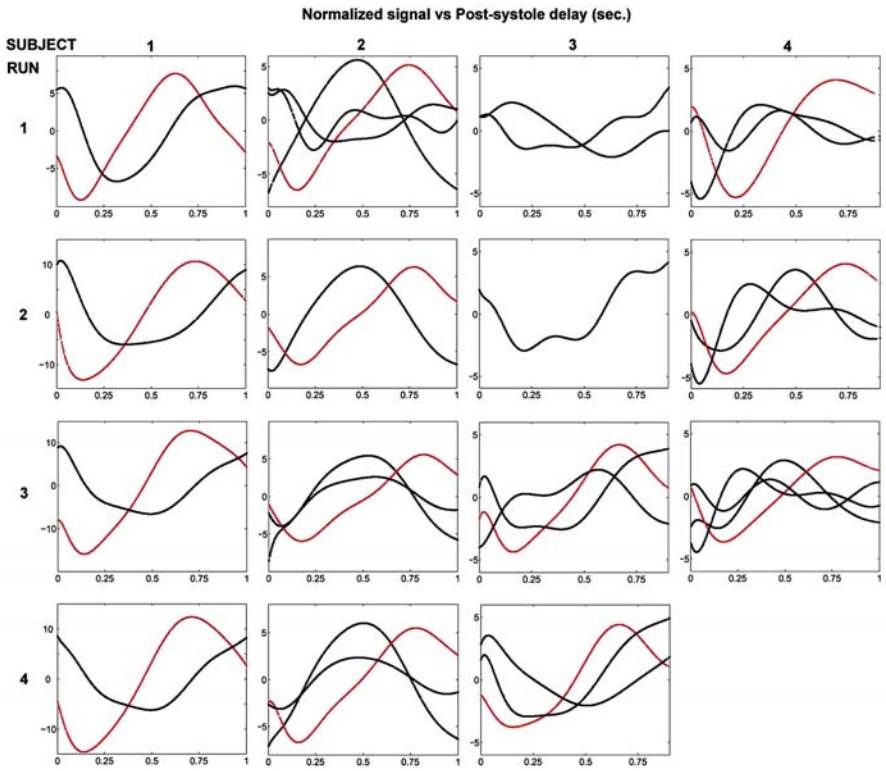

Figure C.7. Independent component related to cardiac cycle

Cardiac-induced signal change in relation to the post-systole delay for all runs. In all runs, the cardiac-related effect was decomposed into several independent components coherent with the cardiac power spectrum and demonstrating

responses time-locked to the cardiac systole. One component displaying a consistent temporal pattern (red line) was found in most runs. Also note the variable phase-shift of the different components within runs.

Discussion

Cardiac-related noise is widely recognized in spinal fMRI (Brooks et al., 2008; Giove et al., 2004; Stroman, 2005, 2006). However, until recently (Brooks et al., 2008), there was no study in which a method was used to appropriately isolate and remove cardiac noise from the functional data. In the current study, a spatio-temporal characterization of cardiac noise in cervical spinal fMRI is provided. Results indicate that functional images of the cervical spinal cord are significantly affected by very large signal variations time-locked to the cardiac systole. Those variations are very consistent across runs and, to a certain degree, across subjects. The characteristics of the signal fluctuations are compatible with mechanisms involving pulsating CSF flow induced by cyclic changes in intra-cranial pressure produced by cardiovascular activity.

Quantification of cardiac-induced signal change

It was previously suggested that cardiac noise contributes to deterioration of the signal in spinal fMRI (Brooks et al., 2008; Giove et al., 2004) but no study had yet characterized its magnitude. In the present study, a band pass filter was applied to the fMRI time series to estimate the magnitude of the signal changes occurring at cardiac frequencies. The results confirmed the hypothesis that cardiac noise is very significant in cervical spinal fMRI with signal changes of 10.4% in average and up to 66% in some voxels. As a comparison, cardiac-induced noise is thought to induce signal changes in the order of 1-8% along the major brain vessels in cerebral fMRI (Dagli et al., 1999). Considering that the BOLD changes due to neuronal activity are expected to be considerably smaller (Giove et al., 2004), it appears indispensable to control for cardiac noise to avoid deterioration of spinal signal and improve the detection of valid functional activations.

Source and localization of cardiac effects

The two potential sources of cardiac-related noise postulated are the systole-induced pulsation in spinal arteries and CSF pulsation in the subarachnoid space. According to the spatial distribution of the cardiac-related effects observed, a CSF-pulsation effect appears more likely. Indeed, the middle slice of our acquisitions included the ventral fissure of the spinal cord where the anterior spinal artery lies and where cardiac-related effects were weakest relative to the two lateral slices. This result contrasts with the effect reported in brain fMRI where cardiac noise appears to be concentrated along major brain vessels (Dagli et al., 1999). This difference may reflect the smaller diameter of spinal compared to brain arteries. Cardiac noise in spinal fMRI may therefore be largely secondary to CSF flow induced by variations in intracerebral pressure due to cerebral arterial inflow.

The CSF flow in the spinal subarachnoid space induced by cardiac-related changes has been characterized in studies using flow-sensitive MRI sequences (Friese et al., 2004; Henry-Feugeas et al., 2000; Henry-Feugeas et al., 1993; Schroth and Klose, 1992), and is the most plausible source of signal variation in the present study. The most extreme variations are found in the two outermost slices of the volume, at the ventral aspect of the CSF/spinal cord interface. This is highly consistent with the ventro-lateral inflow of CSF due to anatomical interruptions of the subarachnoid space (Henry-Feugeas et al., 1993), as described in the introduction. Assuming that increasing CSF velocities induce a greater artefact in the MRI signal, these differences are also compatible with the earlier description of CSF flow velocity in the different channels of the spinal subarachnoid space.

Additional sources of structured noise might also contribute to the present results. Future studies should include additional lateral slices that are not expected to contain CSF flow in order to confirm the proposed interpretation and rule out some other forms of structured field disturbance. Furthermore, a recent study by Figley and Stroman (2007) suggests that cardiac-related noise might involve motion of the spinal cord, primarily in the ventral-dorsal direction. However, this motion is likely to be secondary to CSF flow within the spinal canal and such motion would be expected to affect signal at the CSF-cord interface in all three sagittal slices acquired in the present study. In contrast, we observed cardiac-related signal fluctuations primarily in the two lateral slices and much less in the mid-sagittal plane so our results likely reflect more than cord motion. In any case, Figley and Stroman (2007) and the present results demonstrate the usefulness of principal component analysis and sICA to characterize physiological noise in spinal fMRI data (also see Brooks et al., 2008).

Temporal pattern of cardiac effects

One of the cardiac component common to most runs (red lines in Figure C.7) displayed a temporal profile highly compatible with cardiac-induced CSF pulsation. Indeed, signal changes peaked around 200 ms and 700 ms, consistent with previous studies on CSF-velocity changes (Friese et al., 2004; Henry-Feugeas et al., 2000; Henry-Feugeas et al., 1993). Importantly, more than one cardiac component was found in most runs. Those multiple components varied in phase relative to the cardiac systole and were distributed along the rostro-caudal axis of the spinal cord. This further suggests a broad spatio-temporal distribution of cardiac noise. Several sICA components were out of phase by a delay approximating, or larger than, the TR (250ms) as shown in Figure C.7. Those separate components are unlikely to reflect a single cardiac-related wave of signal change captured at different time points in different slices, depending on a systematic shift potentially introduced by the slice-time delay (160ms between slice 1 and 3). This illustrates the complexity of the cardiac noise and the potential difficulties in the attempts of modelling it a priori in spinal fMRI analyses.

Intra- and inter-session reliability

The reliability of the cardiac-related signal fluctuations identified with the temporally filtered images was assessed by qualitatively comparing the results across runs and subjects. Based on anatomical landmarks visible on the images (disks and vertebral bodies), there is a remarkable stability across runs in the same subject (see Figure C.4 and Table C.1). The peaks were generally in the same segment and the magnitude of the signal change was similar. This within-subject stability has an important impact on future developments of spinal fMRI. This suggests that cardiac noise correction in long-TR data may be based on cardiac-related information derived from separate scanning runs TR (see below).

As for inter-individual reliability, differences were expected in the signal magnitude and distribution. For instance, anatomical interruption of the subarachnoid space and the differences in the dynamic of CSF flow is likely to vary across subjects (Henry-Feugeas et al., 2000; Henry-Feugeas et al., 1993; Watabe et al., 1999). Nevertheless, as shown in Figure C.5, the spatial pattern is relatively similar across the four subjects. These comparisons confirm that the cardiac-related noise identified is present in all subjects at the CSF/spinal cord interface.

The reliability of the cardiac-related signal fluctuations was also evaluated based on the cardiac components identified using sICA. A plot of the signal change relative to the post-systole delay showed that for each subject, there was a stable component across runs (Figure C.7). This has an important implication for the correction of the cardiac noise: the identification of subject-specific spatial patterns of cardiac noise with a single short TR acquisition should be valid for a fMRI acquisition session involving several scans. Interestingly, at least one component was present for most of the runs across all subjects, suggesting a common phenomenon. These results further demonstrate the reliability of sICA in extracting cardiac variance from spinal fMRI time-series.

Limitations of the study

The present study was designed to characterize the cardiac noise in spinal fMRI and the proposed methodology relied on two general approaches that have some limitations. The quantification of the systole-related signal changes was based on filtered images. Although most cardiac variance was preserved within the window of 0.3 Hz, the analysis might have underestimated the importance of signal changes. On the other hand, the bandwidth selected for the filter might include phenomenon other than cardiac in origin. This would bring an overestimation of the signal changes. Nevertheless, the spatial distribution of the variance argues for a cardiac source involving CSF pulsation. In any case, while the quantification procedure might include some error, results clearly confirmed that the relative magnitude of cardiac noise is significant relative to the magnitude of signal changes typically associated with BOLD-related effects.

Another factor not addressed in the present study is the additional contribution of other sources of physiological noise. Although the present study did not address the potential artefacts created by respiratory movements, their impact on spinal fMRI have to be considered. Apart from gross movement and susceptibility artefacts created by the expansion of the thorax, respiration may also affect the CSF flow and contribute to physiological noise (Friese et al., 2004; Schroth and Klose, 1992). Further research is needed to characterize respiratory-related noise and validate a method to control for it in spinal fMRI. The methodology proposed in the present study could be applied to this question by simply adding a concurrent monitoring of respiratory activity.

Another limitation of the present study is related to the acquisition parameters. The short-TR acquisition used here is well suited for cardiac noise characterization but is not optimally sensitive to T2* effects and BOLD signal changes due to neuronal activity; i.e the lower flip angle used in short-TR acquisition considerably reduces signal (Huettel et al., 2004). On the other hand, long-TR acquisitions typically used to detect BOLD effects do not allow for an unequivocal identification and removal of cardiac noise because of aliasing the cardiac frequency. At long TR, aliasing of the cardiac frequency may contaminate task-related signal changes and introduce a confounding factor that could contribute to false positive activations. In that respect, short-TR acquisition can provide a compelling account of cardiac signal changes as demonstrated in the present study. An important consideration for short-TR acquisitions however is the disturbance of the steady-state free processing. This phenomenon can occur in gradient-echo EPI acquisitions when TR<T2 (especially in the CSF) and causes voxel-wise temporal variation or additional noise (Zhao et al., 2000). The present study did not address the characterization of that potential source of noise. However, that additional source of noise was suppressed by the gradient-spoiling used here, as described in the methods. Further research may provide additional characterization of SSFP disturbances by comparing acquisitions with or without gradient spoiling in spinal fMRI.

Conclusion

There is yet no consensus on a strategy to control physiological noise in spinal fMRI. The present results demonstrate that the large cardiac-related signal-change in spinal fMRI is characterized by complex spatio-temporal patterns which were stable across runs and relatively comparable across subjects. Linear modelling of the cardiac noise (Stroman, 2006) may be a difficult task in view of the observed nonlinear effects. In contrast, ICA-based methods similar to the second analytical approach used here, have recently provided encouraging results (Brooks et al., 2008). This research further emphasize the importance of developing and validating more efficient strategies to control for cardiac, and other, sources of physiological noise.

Acknowledgment

We thank Boualem Mensour and Jean Gauthier for their help in data analysis in the early phase of this project and Serge Rossignol and Rick Hoge for their comments on the manuscript. This research is funded by an operating grant from the Canadian Institutes of Health Research (CIHR) awarded to Pierre Rainville. Mathieu Piché has received support from the CIHR, the Quebec Chiropractic Research Foundation, and the Research Team in Disability Prevention of the "Fonds de la recherche en santé du Québec (FRSQ)". Julien Cohen-Adad, Guoming Xie and Mina Kosh Nedjad are supported by fellowships from the "Groupe de recherche sur le système nerveux central" (GRSNC) of the Université de Montréal.

D. Article #6: Activation detection in diffuse optical imaging by means of the general linear model

J. Cohen-Adad[1,4,5], S. Chapuisat[2,4,5], J. Doyon[4,5], S. Rossignol[1], J.-M. Lina[3,4,5], H. Benali[4,5], F. Lesage[2,4,5]

[1]*Groupe de Recherche sur le Système Nerveux Central, Department of Physiology, Faculty of Medicine, Université de Montréal, Montréal, Québec, Canada*
[2]*Département de génie électrique and Institut de génie biomédical, École Polytechnique de Montréal, C.P. 6079, Succursale Centre-ville, Montréal, Québec, Canada H3C 3A7*
[3]*Département de génie électrique, École de technologie supérieure, 1100, rue Notre-Dame Ouest, Montréal, Québec, Canada H3C 1K3*
[4]*Unité de Neuroimagerie Fonctionnelle, Centre de recherche de l'Institut Universitaire de Gériatrie de Montréal, Montréal, Québec, Canada*
[5]*INSERM U678, Université Paris VI, CHU Pitié-Salpêtrière, Paris, France*

Published in Medical Image Analysis. Received 27 September 2006; revised 2 June 2007; accepted 4 June 2007; available online 22 June 2007.

Abstract

Due to its non-invasive nature and low cost, diffuse optical imaging (DOI) is becoming a commonly used technique to assess functional activation in the brain. When imaging with DOI, two major issues arise in the data analysis: (i) the separation of noise of physiological origin and the recovery of the functional response; (ii) the tomographic image reconstruction problem. This paper focuses on the first issue. Although the general linear model (GLM) has been extensively used in functional magnetic resonance imaging (fMRI), DOI has mostly relied on filtering and averaging of raw data to recover brain functional activation. This is mainly due to the high temporal resolution of DOI which implies a new design of the drift basis modelling physiology. In this paper, we provide (i) a filtering method based on cosine functions that is more adapted than standard averaging techniques for DOI specifically; (ii) a new mode-locking technique to recover small signals and locate them temporally with high precision (shift method). Results on real data show the capability of the shift method to retrieve HbR and HbO_2 peak locations.

Keywords: Diffuse optical imaging, DOI, General linear model, GLM, Activation detection.

Introduction

Over the last few years diffuse optical imaging (DOI) has seen significant efforts directed towards the development of new methods to study functional activation through measurement of the hemodynamic properties of the brain (Baird et al., 2002; Cannestra et al., 2003; Gratton et al., 2003; Kato et al., 2002). The interest in DOI stems from its innocuity and the fact that the dominant chromophores are oxyhemoglobin (HbO2) and deoxyhemoglobin (HbR) providing functional information along with less dominant absorption from lipids and water (Jobsis, 1977; Yodh and Chance, 1995). Separate studies in functional magnetic resonance imaging (fMRI) have legitimated the technique by correlating brain neurophysiology to behavioral tasks and confirmed the correlation between BOLD and the HbR/HbO2 signals measured in DOI (Huppert et al., 2006). Advantages of DOI are the low cost, recent availability of commercial instruments and access to a wider population due to the ease with which acquisitions can be made. Mostly used to locate activated regions in the brain in topography, recent progress has shown that by using different source and detector locations, tomographic studies can be done over large tissue volume. However, difficulties in accuracy arise because of the highly diffusive nature of the tissues, the attenuation of light as it propagates in the medium and the heterogeneities from the different tissues. It is thought that up to 3 cm of tissue depth can be accessed by DOI (Boas et al., 2004).

When applied to brain function, two challenges have to be faced when performing DOI data analysis: (i) separation of the stimulus related brain function from the background physiology and the noise; (ii) reconstruction of tomographic images with good accuracy. To some extent, progress has been achieved on both fronts: in the latter, use of more sophisticated systems (frequency domain or time domain). Fantini et al. (1999) have allowed a better estimation of absorption and diffusion coefficients, an essential input to the imaging problem. Another, non-conflicting, approach has been to use anatomical MRI data as a prior to the reconstruction problem (Bamett et al., 2003; Boas et al., 2004). All these progresses in tomography are good but, in essence, the former problem is also under very active scrutiny: as the technique evolves, new and more accurate methods to analyze the optical data are emerging.

One of these can be taken as the starting point for this paper: in Huppert et al. (2006), the authors did an extensive comparison of the different temporal responses of fMRI BOLD, ASL and DOI data. Recording were done simultaneously and provided a good framework for comparison. Using event-related finger tapping tasks, the authors were able to establish a close temporal correlation between the fMRI BOLD signal and the HbR signal in DOI. A similar correlation was also uncovered between the ASL sequences measuring blood flow and HbO2 signal in DOI. These correlations open the door to the use of the general linear model (GLM) in optical imaging.

These correlations can naturally also be used to get a better understanding of the origin of the BOLD signal. The relationship between the neuronal activity and the fMRI signal is complex and still under investigation (Bandettini and Ungerleider, 2001). A convenient way to

deal with this issue is to model the brain as a black box linear system characterized by its transfer function, also called hemodynamic response function (HRF). Knowledge of the HRF is hypothesized to give insight into the brain processes generating the observed BOLD signals from any input stimuli. The so-called ‘‘canonical’’ HRF has been defined as the theoretical signal that fMRI would detect in response to a single, very short stimulus of unit intensity (Friston et al., 1994b). The model, whose key assumptions are the stationarity and linearity of the underlying physiology, fairly well accounts for the properties of the real system, as long as the inter-stimulus interval does not decrease beyond about 2 s. Below this value, non-linearities may appear. This has notably been shown for visual stimuli (Dale and Buckner, 1997). Although the problem of HRF estimation has been explored, this general definition offers a possibility that has not been explored extensively in optical imaging: the use of a canonical hemodynamic response function and the construction of an associated GLM should also apply to the analysis of optical data. This technique has been used for years in fMRI studies and should, for optical studies, open the door for a general framework to study multi-event protocols of the HRF itself.

Historically, analysis of DOI data in response to cognitive tasks has been mainly done using block protocols and ensemble averages. Although these methods recover activated regions, they are not appealing to scientists doing cognitive studies, who are usually interested in imaging more than one condition under an event-related type task. Event-related activation detection has been used in fMRI studies for many years, but methods to perform the same in DOI in a robust and well understood approach are still under investigation (Huppert et al., 2006; Jasdzewski et al., 2003; Schroeter et al., 2006).

Typically, DOI data analysis goes through a series of steps to recover activation. In particular, it is known that instrument noise as well as noise of physiological origin hampers the analysis. Physiology interferes with the data through changes in the systemic cardiovascular system and cerebral auto-regulation. Attempts at modelling these changes are done through complex models (Lu et al., 2003; Mukkamala and Cohen, 2001) and short-term variability is difficult to infer. Thus, a typical DOI data analysis starts with the denoising of the raw signal. Filtering methods can be simple: a band-pass filter in the Fourier domain, or a more accurate filtering of physiological data through separate recordings of heartbeat, respiration, etc. This, in turn, may affect both block and event-related protocols: as the frequency support of the physiology overlaps with that of the protocol, one is not only filtering but also removing information originating from the protocol. Other modelling approaches for reducing the noise variance have been explored in DOI through the state space model (Diamond et al., 2006; Prince et al., 2003), or using principal component analysis (Zhang et al., 2005b). Nevertheless, filtering procedures using a Bayesian-based GLM have not been explored in DOI yet.

An undiscussed issue is the fact that 0.1 Hz fluctuations also appear in the HRF frequency spectrum and may have a significant contribution to the signal, as already observed in DOI (Tachtsidis et al., 2004). These so-called Mayer waves are still not fully understood (Julien, 2006). They may originate either from an endogenous oscillator located within the

sympathetic nervous system (Pagani et al., 1997; Preiss and Polosa, 1974), or from a mechanical oscillator induced by the cardiac baroreflex loop (Chapuis et al., 2004; Vielle, 2005). Differentiation of these oscillations from the HRF can be done by averaging over different subjects or trying to de-synchronize the protocol with the base frequency of the physiological signals. Finally, if one is not only interested in the hemodynamic response but also wants to study the physiology, classical filtering methods make it difficult since they may discard the data.

To summarize, the common use of the GLM in DOI suffers from the high temporal resolution of that modality in two different aspects: (i) Noise modelling drift functions are distributed over a wider spectrum in DOI versus fMRI. Hence, we propose a method that bypasses the ad hoc filtering of raw data by designing an appropriate set of functions for the physiological and instrumental noise. Doing so, we developed a method of activation detection that takes into account this set of drift parameters and opens the door for denser event related protocols. (ii) Since HbR and HbO2 have a different timing (Huppert et al., 2006), it seems unappropriate to use the paradigm convoluted with a single canonical HRF as a regressor. DOI deserves a method which allows precise detection of both HbO2 and HbR peaks. We thus present a method whose concept is to shift the raw data towards the projection basis and to perform a GLM estimation at each shift step. We refer to this scanning procedure as the shift method. Furthermore, acquiring additional rest measurements, we show that it is possible to assess the presence of activation in a relative way. In that sense, the shift method allows better activation detection for low signal-to-noise ratio (SNR) data.

Methods

The general linear model (GLM) has been mainly used in fMRI data analysis (Worsley and Friston, 1995) and significant progress has been made in understanding the limitations and advantages of this model (Lange et al., 1999). In DOI, the GLM has be used only recently, mostly in the context of the evaluation of the hemodynamic response function. In this section, we review the model and describe an approach previously used in the context of fMRI for activation detection (as opposed to estimation). As we will see in the following sections, one of the key aspect of the method is the design of the drift functions. The distinction between fMRI and DOI will be the number of drift functions one needs to add in order to stabilize the technique.

Hemodynamic and optical modelling

Let us set the notations and definitions to be used in the following. In this work, we are not interested in tomography but rather in detecting the hemodynamic response (as opposed to recovering, but more on that later). Modelling of light propagation is typically done with the use of the diffusion approximation

$$-\nabla(D\nabla\Phi(r,t)) + \mu_a\Phi(r,t) + \frac{1}{v}\frac{\partial\Phi(r,t)}{\partial t} = S(r,t) \tag{D.1}$$

where $\mu_a(r)$ and $D(r)$ are the absorption and diffusion coefficients, respectively, and v the speed of light in the medium. The photon fluence $U(r, t)$, measured in response to a light source $S(r, t)$, can be used to recover the distribution of $\mu_a(r)$ and $D(r)$ in the three dimensional volume being probed, the so-called solution to the inverse problem. In practice, however, it is difficult to solve for these coefficients and form an accurate image. In particular, if one only has access to continuous wave (CW) measurements, the problem is ill posed and even with a time domain or frequency domain instrument, the heterogeneity of the absorption and diffusion distribution in the brain create to accuracy issues.

In practice, it has not been such an issue because, by looking at the data in topography, *i.e.*, by observing the response at the different source–detector pair locations, one can infer regions of interest where a change in hemodynamic occurred. Moreover, we are typically interested in the changes in absorption occurring in time, since they are the ones related to physiology. In order to do this, the non-linear nature of the inverse problem is often linearized by the use of a perturbation technique, either the Born or the Rytov model (Arridge, 1999). In both cases, each voxel in the reconstructed volume contributes to the changes in measured intensity in an additive manner, *e.g.*, for a given source–detector pair situated at r_s and r_d, respectively, we have under the Rytov approximation and the assumption that scattering is not modified in a given task

$$\ln\left(\frac{\Phi(t,\lambda)}{\Phi_0(t,\lambda)}\right) \propto \int_V d^3r\, G(|\, r_s - r\,|, \mu_a^0, D^0)\delta\mu_a(r)G(|\, r - r_d\,|, \mu_a^0, D^0) \tag{D.2}$$

where $G(r, \mu_a^0, D^0)$ is the complete linearized Green's function solution of (1) with $S(r, t)$ taken to be a point source and $\Phi_0(t,k)$ is the measured fluence without activation. Up to a sign, the previous expression defines the optical density

$$\Delta OD(t,\lambda) = -\ln\left(\frac{\Phi(t,\lambda)}{\Phi_0(t,\lambda)}\right) \tag{D.3}$$

Any changes in hemodynamics map to variations in local optical absorption, $\mu_a(r) = \mu_a^0 + \delta\mu_a(r)$, defined in a discrete space (voxels). If one, or many, of these voxels have in their temporal behaviour a component corresponding to the hemodynamic response, then it will sum up in the final signal and the optical density will have a trace of the hemodynamic response. The main point here is that this trace is additive and, within the perturbative model, we are justified in separating the response from the background physiology additively. In our approach (shown below), we used the Beer–Lambert law to perform topography keeping in mind that the signals can be additively deconvolved.

This trace depends on local chromophore concentration and, assuming we want to differentiate between HbR and HbO2, we use two specific wavelengths (λ_1 and λ_2) that contrast

the two absorbers. Then, the optical densities at each wavelength are a weighted mixture of the variation in chromophores concentration and we can write

$$\begin{bmatrix} C_{HbO_2}(t) \\ C_{HbR}(t) \end{bmatrix} = \begin{bmatrix} \varepsilon_{HbO_2}^{\lambda_1} & \varepsilon_{HbR}^{\lambda_1} \\ \varepsilon_{HbO_2}^{\lambda_2} & \varepsilon_{HbR}^{\lambda_2} \end{bmatrix}^{-1} \begin{bmatrix} \Delta OD(t,\lambda_1) \\ \Delta OD(t,\lambda_2) \end{bmatrix} \tag{D.4}$$

where ε stands for the extinction coefficient of HbR and HbO2 at the two wavelengths λ_1 and λ_2. Obviously, the deeper the absorbers carrying the hemodynamic response are located, the weaker the corresponding fluctuations in optical densities are generated. But the techniques presented here will still be able to extract the response from the physiological signal, up to the detectability limit. In this linear framework, the separation of the HRF from the background can be done out of the measurements prior to performing the three dimensional imaging and the two problems are decoupled. This will be our working hypothesis. However, it is not clear this holds true in the non-linear case where interferences in the signal can be non-additively originating from physiological noise that might have a distinct spatial distribution.

The general linear model

The Bayesian framework

As explained previously, time series can be considered as the sum of an HRF convoluted with a given protocol. Let us denote by X a time series describing the experimental paradigm (when only one type of stimuli is present, X is a vector) and by C the chromophore concentration[11] for a given source–detector pair, this signal can be modelled as follows:

$$C = X_h\beta + B\theta + e \tag{D.5}$$

In this model, X_h represents one or many regressors related to the expected hemodynamic response. It is computed through the convolution of the protocol X with the canonical HRF. β is a vector describing the intensity of the response to each stimulus condition, as declined in X: this is the quantity of interest to be estimated. B is a matrix that models the structured background signal, *i.e.*, a set of drift functions with contribution h and e is the residual term having null mean and variance σ^2.

The purpose here is to estimate the responses $\beta = (\beta_1, \cdots, \beta_{n_s})$ to the n_s conditions in the stimuli. As mentioned previously, the typical approach is to filter the data, but this filtering can lead to information loss, in particular when X_h has support over the filtered bands. Here, the approach is to model the drift functions and then to make estimations in the subspace orthogonal to these drifts. Using an orthogonal subspace is, in a sense, an improved filtering

[11] Here, we assume that concentrations are recovered by taking the signal at two or more wavelengths and using the Beer–Lambert law. The full imaging problem in 3D will not be addressed here although extensions are obvious as mentioned before.

method since we can remove drifts correlating with the protocol, thereby making sure that we minimize the overlap between the filter and the expected response.

Let us suppose the instrumental and physiological drift functions are described by the polynomial basis functions:

$$B_a \in \left\{1, t, t^2, \cdots, t^n\right\} \tag{D.6}$$

together with a set of periodic basis functions

$$B_b \in \left\{\cos(\frac{\pi k t}{T}), k = 1, 2, \cdots m-1\right\} \tag{D.7}$$

The vector θ in Equation (D.5) has m + n components. Our choice of $B = [B_a B_b]$ is motivated by observations done on the data (instrumental drift functions are mostly polynomial whereas physiological functions tend to be periodic). Once this projection basis is chosen, estimation can be done through a Bayesian approach, as developed in (Marrelec et al., 2003). For data compatible with the model, we have the following posterior distribution on the model parameters:

$$p(\beta, \theta, \sigma^2 \mid C) = \frac{p(\beta, \theta, \sigma^2)\, p(C \mid \beta, \theta, \sigma^2)}{p(C)} \tag{D.8}$$

The denominator can be eliminated, since it only acts as a normalization factor. Moreover, assuming the drifts and the noise are independent, we write the prior density function as follows:

$$p(\beta, \theta, \sigma^2) = p(\beta) \cdot p(\theta) \cdot p(\sigma^2) \tag{D.9}$$

In absence of any prior information that may define some densities in this expression, we consider non-informative priors to be[12]:

$$\begin{aligned} &p(\beta) \propto const \\ &p(\theta) \propto const \\ &p(\sigma^2) \propto (\sigma^2)^{-1} \end{aligned} \tag{D.10}$$

Moreover, assuming residual gaussian noise, we can write the posterior probability density function as

$$p(\beta, \theta, \sigma^2 \mid C) \propto (\sigma^2)^{-L/2-1} \exp\left[-\frac{1}{2\sigma^2} \| C - X_h \beta - B\theta \|^2\right] \tag{D.11}$$

[12] This can be questioned in the case of $p(\theta)$, one could have distinct stimuli having a correlation, or, when considering the HRF and its derivative, the prior could be limited by heuristics.

where L stands for the number of samples. Our main concern relates to the estimation of the vector β and thus, we must integrate over the drift parameters θ to generate the desired marginal posterior probability density of β

$$\begin{aligned} p(\beta,\sigma^2 \mid C) &= \int p(\beta,\theta,\sigma^2 \mid C)d\theta \\ &= \frac{(2\pi\sigma^2)^{n_d/2}}{\sqrt{\det(B^tB)}} \times \exp\left[-\frac{1}{2\sigma^2}\left[(C-X_h\beta)^t J(C-X_h\beta)\right]\right] \end{aligned} \tag{D.12}$$

with n_d being the total number of drift functions considered in the projection basis. Here, $J = I - B(B^tB)^{-1}B^t$ satisfies $J^2 = J$ and $JB = 0$. As expected, J is the projector on the subspace orthogonal to the drift matrix. It thus removes the drifts from the data. Given that β is Student-t distributed, we can estimate it by simple integration, leading to

$$\begin{aligned} \hat{\beta} &= E[\beta \mid C] \\ &= [X_h{}^t JX_h]^{-1} X_h{}^t JC \end{aligned} \tag{D.13}$$

The variance of the estimator is given by

$$\begin{aligned} \hat{v}_\beta &= \frac{1}{d}(\widehat{\beta^2} - \hat{\beta}^2) \\ &= \frac{1}{d}([C^tJC - \hat{\beta}^t X_h{}^t JX_h\hat{\beta}][X_h^tJX_h]^{-1}) \\ &= \frac{1}{d}(C^tJJ_XJC[X_h^tJX_h]^{-1}) \end{aligned} \tag{D.14}$$

where $J_X = I - X_h(X_h^tJX_h)^{-1}X_h^t$ and d stands for the degree of freedom defined as $d = L - (n_s + 1) - (n_d + 1)$.

Now, let us consider the statistical inference on the estimation. By doing this linear regression, one estimates the value $\hat{\beta}$ for which the error on the estimation is minimum in the least square sense, *i.e.*, for which the variance of e is minimum in Equation (D.5). Since β is Student-t distributed, we can define the null hypothesis as $\hat{\beta} = 0$ (*i.e.*, no variation in chromophore concentration) and then test the null-hypothesis towards the parametric distribution of β. Our objective is to reject that hypothesis in order to detect a significant variation of $\hat{\beta}$ related to the regressor of interest (*e.g.*, the task). The null hypothesis is rejected when

$$\frac{|\hat{\beta}|}{\sqrt{\hat{v}_\beta \times d}} > t_{threshold} \tag{D.15}$$

Considering the k^{th} regressor in the design matrix X and denoting by ξ_k the k^{th} term in the diagonal of $X_h^tJX_h$, the estimated variance of β_k can be written

$$\hat{v}_{\beta_k} = \frac{1}{d} \times \frac{C^t J J_X J C}{\xi_k} \tag{D.16}$$

Leading to the t-value of $\hat{\beta}_k$ with *d* degrees of freedom

$$t_d = \pm \sqrt{\widehat{\beta_k}^2 \xi_k [C^t J J_X J C]^{-1}} \tag{D.17}$$

Since $JB = 0$, this is an unbiased estimator of β. We observe that overlap between the design matrix X and the drift matrix B manifests itself through the product $J_X J$ in the variance of the estimator. We can thus ask the following question: what is the consequence of the choice of drift matrix on the estimation? This aspect is discussed in the following section.

Design of B

The previous estimator depends on the form of the operator *J* that filters the raw data *C*. This operator characterizes our ability to handle carefully the background drifts. Clearly, *JC* should increase the signal-to-noise ratio by filtering out undesirable contributions of the drifts as much as possible without removing the hemodynamic response we are looking for, if any. Therefore, we must have $JX_h \simeq 0$, *i.e.*, $B^t X_h \simeq 0$. This requires the drift matrix *B* and the stimuli response X_h to be non-correlated. In section 'Modelling of drift components subspace' we will use this condition in order to optimize the design of *B*.

Shift method

When estimating with the GLM, one assumes that: (i) the data projected on the nuisance regressors do not contain the variance of interest and (ii) residuals have a gaussian distribution, such that the regression hypothesis is fulfilled. In DOI, we still have little knowledge of the noise. Furthermore, the SNR is relatively low. Hence, since the estimator is biased by the choice of drifts and the residual noise it is difficult to assess the presence of neuronal activity when estimating a single β per optical pair. What is usually done to get around this problem is to perform many acquisitions and use statistics to gain greater confidence in the data. However, this indirect method limits our ability to perform single trial detection for small signals. Here, we propose an original method that helps assessing the presence of a task-related signal. Instead of estimating a single value of β, let us add one acquired rest periods before and after the task and exploit this feature. One can then shift the raw data in time and, if there is no noise, a distinctive pattern should emerge that correlates with the amount of overlap we have with the actual activation sites (see Figure D.1). As we move the task-related signal away from the protocol, the estimation should be different from that observed in synchrony with the protocol: $|\beta|$ should decrease. In case of a block design paradigm, we should observe a wave train that is periodic with the paradigm period, *i.e.*, the estimated $|\beta|$ should be higher when the paradigm is in phase with the activity. One thus disposes of several β values that can be compared to each other. The originality of that method is the relative consideration of the estimation.

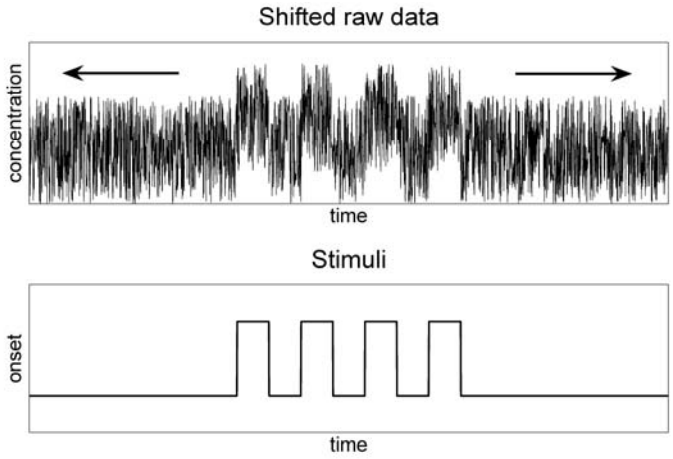

Figure D.1. Principle of the shift method
Raw data truncated and shifted in time (top), paradigm of stimuli (bottom). For each shift step, one estimation is performed. The correlation between actual activity and the paradigm is then reflected on the pattern of estimations.

Data acquisition

In order to shift raw data in time, one must truncate them on both edges, *i.e.*, the bigger the shift range is, the more the data will be truncated. For instance, let us consider a 6000 samples dataset containing 2000 samples of paradigm and 2000×2 samples of rest at both edges. In order to symmetrically shift the whole paradigm over the paradigm regressor, one must truncate the data and use only a 2000 samples window. If shifts are performed only in one direction, the acquisition structure could be like 2000 samples rest + 2000 samples paradigm, or 2000 samples paradigm + 2000 samples rest, which requires less acquisition time. In the following, we will show that this technique is indeed very powerful to assess the presence or absence of signal.

Adjusting the method with simulated data

We performed a series of simulations to quantify the ability of the Bayesian estimation proposed above to recover hemodynamic data. In order to generate realistic simulated data, we first acquired DOI data where the subject was asked to rest, so that the signal recorded only contained instrumental noise, as well as noise of physiological origin. Then we added a fictive paradigm consisting of sequences 'rest-activation-rest', each lasting four minutes. The activation section consisted of periodic stimuli lasting 7 seconds, interleaved with 7 second rest periods. We chose that paradigm to match the paradigm used on real data (see Figure D.2).

The baseline DOI data was acquired using a CW NIR commercially available (Techen CW5). The optical probe was positioned over the right motor cortex of three human subjects (3 young males). The subjects were asked to rest for twelve minutes in the dark and to breathe normally. Optical data were acquired for 4 source positions and 8 detector positions. The instrument modulates the data, so it was further demodulated and downsampled to 10 Hz. No

further filtering was done and the photon fluence data was then converted to optical density via Equation . The photon fluence Φ_0 was measured during the first 2 seconds of the acquisition.

To that noisy baseline, we added fictive activation on given optical source-detector pairs. The activation consisted of a 7 seconds block, convoluted with a 'canonical' response similar to that used in fMRI studies (Friston et al., 1994b). The justification for using the canonical response can be found in (Huppert et al., 2006).

Modelling of drift components subspace

The motivation for a good drift components subspace modelling is to minimize the variance of the activation signal to be taken from the drifts and at the same time, maximize the variance of the noisy information to be projected on that subspace. The problem of detrending has already been well documented through fMRI data. One way of modelling that subspace consists of modelling drifts by a set of basis functions such as polynomial functions (Worsley et al., 2002) or discrete cosine transform (DCT) functions (Friston et al., 2000). fMRI noise has also been proposed to match an 1/f-model (Zarahn et al., 1997). Nevertheless, DOI noise has never been modelled towards a GLM approach. This motivated us for using a DCT functions basis which is polyvalent.

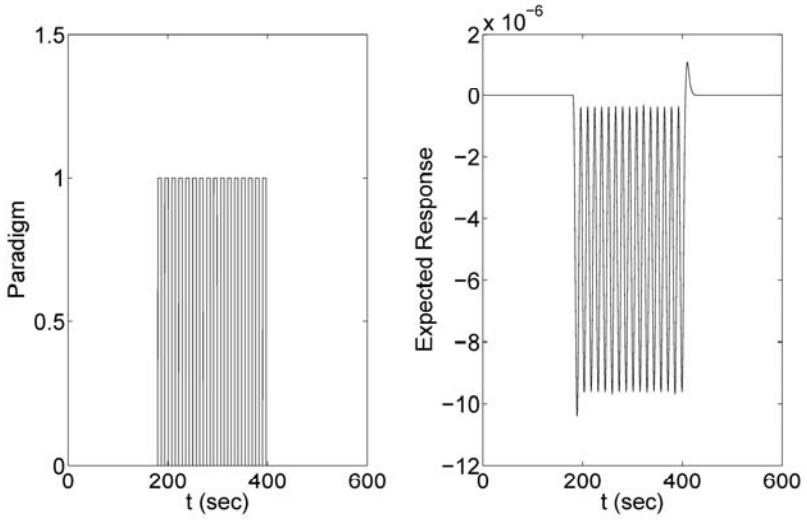

Figure D.2. Paradigm and modelled response to a series of stimuli
From the left: (1) periodic stimulus (7 s task, 7 s rest), (2) convolution with the canonical HRF (for HbR, *i.e.*, negative contribution).

Filtering the subspace

We wish to model correctly the various instrumental and physiological signals, and in such a way that this modelling is sufficiently sparse not to cover the hemodynamic response. As seen in Section 'Design of *B*', one method for studying this intersection of functional spaces is to look at the correlations between the periodic drifts and the protocol convoluted with the canonical HRF.

Correlation results are shown on Figure D.3. The computation shows a strong correlation between the protocol and the stimulus at a frequency corresponding to the activation frequency which is expected since the protocol simulated has a periodic nature. Thus, we expect that the estimation will become less accurate as we go over this frequency, since a degeneracy will emerge and the projected subspace in which we perform the estimation becomes small.

Another approach relies on adapted subspace drifts based on the orthogonalization between the various time series and the protocol (Ardekani et al., 1999; Bagarinao et al., 2003). Although interesting because it provides a drift basis independent from the paradigm, we chose not to rely on such a method for several reasons: (i) Orthogonalization procedures (e.g., using Gram–Schmidt algorithm) distort DCT functions. Since DOI noise is not well characterised yet, having a weighting coefficient for each DCT function allows one to retrieve physiological signals and reconstruct them using a small basis of DCT functions. This could be of interest for simulation purpose. (ii) Combining orthogonalization methods with the shift method we used (see Section 'Shift method') would have introduced a bias in the estimation pattern. Indeed, since the shape of the paradigm is reflected within all drift regressors when orthogonalization is performed, the estimation would have been distributed within first drifts in an uncontrolled manner according to the applied shift.

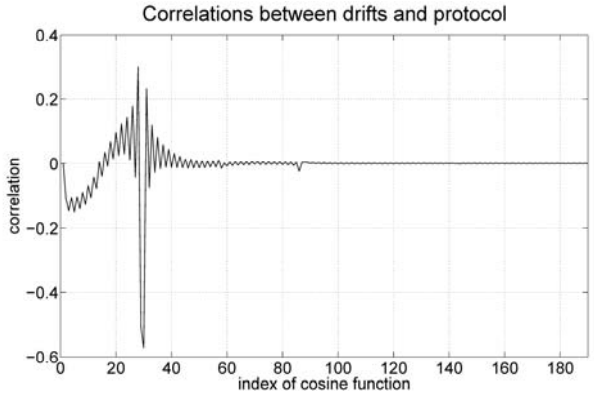

Figure D.3. Correlations between drifts and protocol
Correlation between the same stimuli protocol and periodic drifts. The frequency associated with the index is $f=(n-1)/2T$ where T is the acquisition length (200 seconds here). We thus observe a strong correlation, appearing between the protocol and the 30th cosine drift which oscillates at 0.075 Hz. Rest data were acquired (2000 samples) and added to a block protocol convoluted with the canonical HRF multiplied by a scalar. β_{real} was set to $5\times10^{-6-}$ which corresponds to an SNR of -19.6 dB.

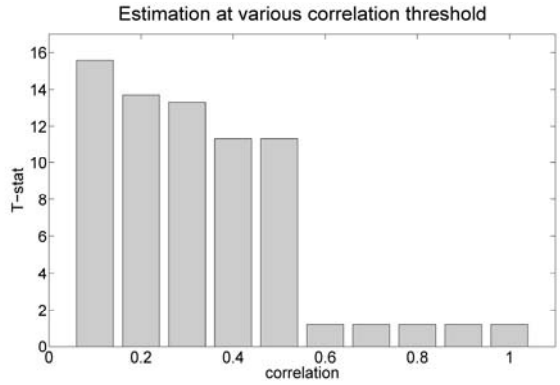

Figure D.4. Computed T-score in function of correlation threshold
The impact of the correlation threshold on the T-score. Estimations of β were performed on the same simulated data as in Figure D.3 with a set of 100 DCT functions as input.

Therefore, we propose a filtering method where drift functions that have a strong correlation with the protocol are removed. The correlation threshold above which drifts are discarded can be arbitrarily fixed. We usually use correlation values from 0.1 to 0.2. In doing so we minimize the cross-correlation of the protocol with the drift functions and construct a filter adapted to a given protocol. For example, Figure D.4 shows a comparison of estimations performed at various correlation thresholds for the same data as in Figure D.3. In the 0.1 correlation threshold case, 16 cosines have been discarded. We clearly see the improvement in the statistical inference when correlated drifts are discarded.

Number of components

Another important parameter when designing the drift basis is its size. Indeed, having non-modelled drift components increases the variance of e in Equation (D.5). On the contrary, having too many basis functions increases the variance repartition over a huge number of regressors. This diminishes the accuracy of the estimation (Meyer, 2003). Nevertheless, using a great number of drift functions increases the estimation robustness towards the number of components, *i.e.*, after a certain threshold, the estimated β remains unchanged as we increase the number of drift functions (see Figure D.5). It should be noted, however, that this threshold depends on the number of acquisition samples. As an example, we limited the number of cosine functions to 100 for a 2000 samples acquisition which may seem large but is reasonable for optical data. In contrast, for fMRI, the number of samples is generally lower than in DOI, meaning that the number of parameters aiming at modelling a system is thus statistically lower in fMRI than in DOI.

What also differs in DOI versus fMRI is that the sampling rate is much higher in the former modality. DOI sampling rate can reach up to 100 Hz. Knowing that most of physiological signal occurs at up to 2 Hz for human, the high Nyquist frequency in DOI enables observation of all physiological phenomena without aliasing. In order to model these variations, one has to use high frequencies in the drift subspace of projection.

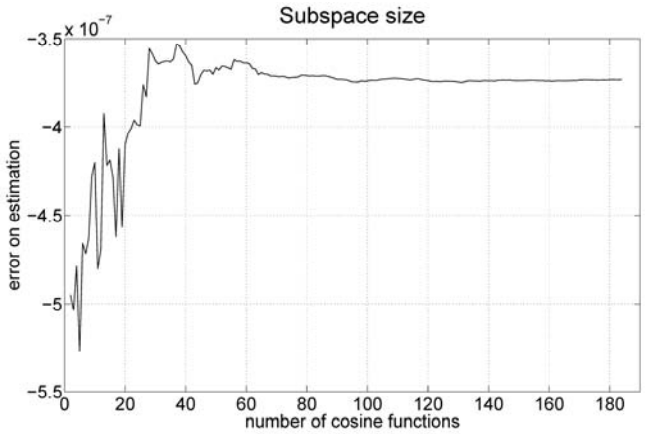

Figure D.5. Error on β estimation as a function of basis size
The impact of the number of cosine functions on the estimation error. Errors in β estimation were performed on the same simulated data as in Figure D.3 for a number of DCT functions varying from 2 to 200. Error is defined as $|\beta_{estimated} - \beta_{real}|$.

Detectable signal

With a better understanding of how to include drift functions and how many are necessary, we can perform experiments that will help us quantify the sensitivity of the Bayesian approach. In this set of experiments, we add to a single source–detector pair different level of activation in the corresponding optical density channel. These levels of activation are computed by convoluting the protocol with the canonical HRF, as shown previously. The added signals where simulated to have a dynamic range that is lower than the overall signal as shown in Figure D.6 and in line or lower than what is observed in a typical finger tapping optical acquisition.

From this data, we can directly apply the shift method discussed above and evaluate its performance. In Section 'Shift method' we proposed a new technique to assess the presence or absence of response. From the data in Figure D.7 we observe that the Bayesian method, without any filtering, can recover hemodynamic response from simulated data in a clear manner. It should be noted that in this set of experiments, the estimation of the variance on the estimation remains somewhat constant, while the estimated parameter β is lowered. We observe that for the estimation done for the case $\beta_{real} = 5.0 \times 10^{-6}$ showed in Figure D.7, we get a clear pattern, whilst for $\beta_{real} = 1.0 \times 10^{-6}$, no such pattern emerges. This result shows that even with a low SNR, we are able to recover the presence of a task related signal by distinguishing that pattern. Furthermore, we can also precisely locate in time the shift value for which $|\beta|$ is maximum, which can be of interest when having no prior on the peaking time of the chromophore concentration.

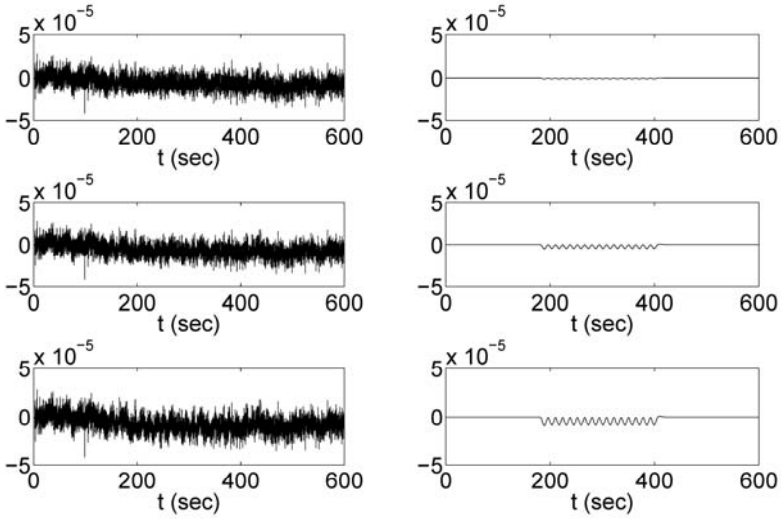

Figure D.6. Detectability in function of effect size

Signals from the simulations, left is the raw signal with added hemodynamics, right are the different responses added for the different values of $\beta_{real} \in [1\times10^{-6}, 5\times10^{-6}, 9\times10^{-6}]$ showed on the same scale.

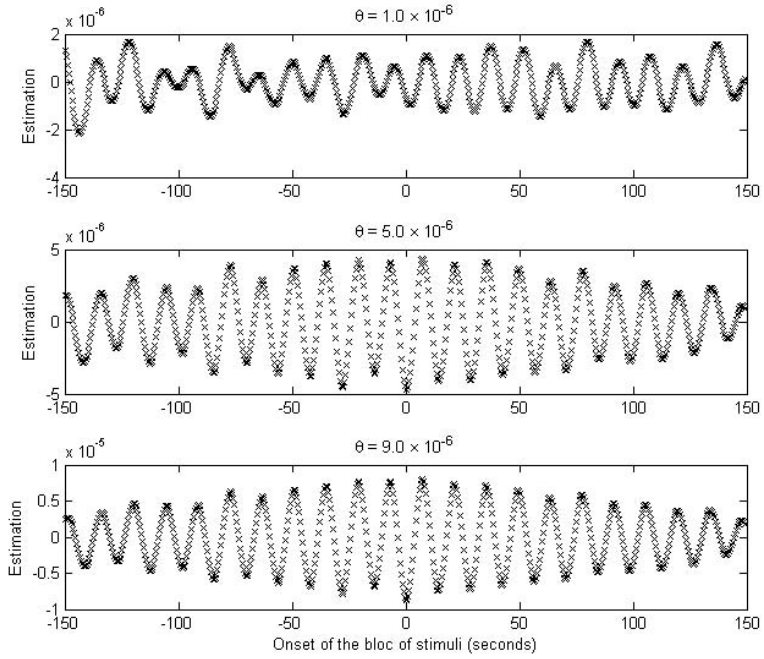

Figure D.7. Shift method on simulated data

This graph shows recovered estimates of β at different values of the raw data shift. As expected the maximum value for $|\beta|$ occurs at the point of zero shift. For the three graphs, we see an oscillating pattern showing the alternating overlap of the data over the paradigm. The period of these oscillations is the period of the block design. Also for the last graph we see a decreasing value of $|\beta_{extremum}|$ following an increase of the shift value. This was also expected since each shift period (*i.e.*, 14 s here) corresponds to a loss of the variance of the raw data projected on one block of activation.

Results

The task protocol was as follows: the same three subjects were asked to rest for the first 4 min, then they were asked to perform a simple left hand movement task (during 7 s at 2 Hz) every 14 s during 3.5 min, then follows a second rest period of 4 min. The instruction was presented 2 s before the first stimulus. Stimuli were indicated by a changing colour square on a screen. The activation was expected to occur on the right motor cortex. The processing method has been described in Section 'The general linear model'. The GLM was applied with a drift projection basis made up of a constant and a set of 100 DCT functions. According to Section 'Modelling of drift components subspace', filtering threshold was set to $r < 0.15$ which discarded three DCT functions from the drifts basis. Note that all figures shown hereafter were generated from a single subject. We found a significant inter subject variability which prevented us from doing averaging, as found in (Huppert et al., 2006). However, the goal of the present study was to demonstrate the benefits of the proposed activation detection method in single subjects.

Task-related signal detected

We performed a series of estimations for each of the 14 source–detector pairs using the shift method described in Section 'Shift method'. For the shifted data that matched most closely the real task regressor, we expected to find the greatest $|\beta|$ values motor-related areas of the cortex, as the task performed was a motor task. This area was mostly covered by pairs number 4, 9 and 5 (see Figure D.8).

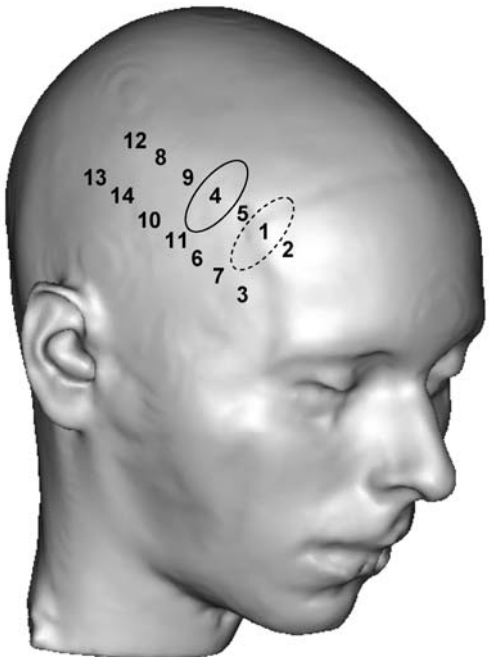

Figure D.8. Localization of source–detector pairs over the head
Solid and dashed ellipses indicate, respectively, the location of motor and premotor areas.

Oscillating pattern

We first looked at estimations on HbR concentration and results did confirm the hypothesis towards a minimum value of β for HbR concentration. We present a series of estimations for a 0.1 s-shift of the data for pair 4, which showed the most significant activity (see Figure D.9). The oscillation pattern observed is similar to the one found on simulated data (see Figure D.7). On the one hand, β is minimum for an almost null shift, which confirms that HbR concentration was minimum while the subject was performing the task. On the other hand, when the overlap is null (*i.e.*, when shift value is $7 \pm n \times 14$ seconds, with $n \subset \mathbb{Z}$) the actual activity and the theoretical stimuli are in phase opposition. In that case estimation of β gives an opposite sign. The periodic nature of the in-phase and the opposite phase reflects the period of the stimulus protocol. We indeed observe that on Figure D.9, where the curve oscillates at a period of 14 s corresponding to the period of the task. This result gives a good overview of the relation between the applied shift and the estimated β. It is also an indicator for the robustness of the chosen detection method since estimated β are null at non-activity temporal sites, *i.e.*, when the actual activity half overlaps the protocol.

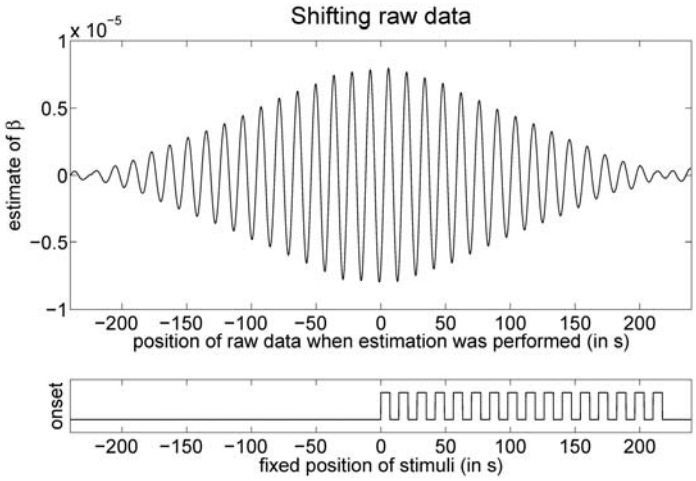

Figure D.9. Shift method applied to real data

Top panel shows 4800 estimations on HbR concentration for pair number 4, performed by temporally shifting the raw data towards the block of stimuli and other regressors. The bottom panel shows the stimuli centred at 0. Estimation was based on a set of 97 DCT functions which covered a spectral range up to 0.067 Hz.

HbO2 concentration

When looking at these results, we notice that extremum β values are all obtained for an almost null shift value, which is consistent with our expectations. We are now interested in analyzing more precisely the shift values for which β reaches the extremum. Applying again the shift method, we also confirmed the presence of a task-related activity towards HbO2 concentration. We had several hypotheses: (i) HbO2 concentration should increase along with

activity; (ii) HbO2 maximum concentration value should be reached before the minimum value of HbR concentration, as HbO2 stands for a pre-capillary phenomenon. Thus its variation should be detected around 500 ms before the HbR peak; and (iii) the HbO2 absolute signal should be stronger than that of HbR. So we performed series of shifted-estimation for HbO2 concentration at high resolution time shift. The recovered results validate all of our hypotheses (see Figure D.10).

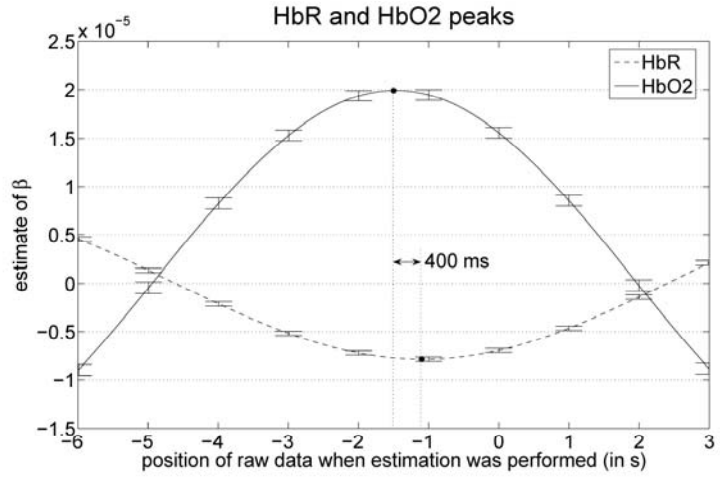

Figure D.10. HbR and HbO2 peaking time

Peak locations for HbR and HbO2 concentration on pair number 4 for the same estimation parameters as in Figure D.9. Hypothesis are validated as: (i) we clearly observe a negative and positive peak for HbR and HbO2, respectively; (ii) the HbO2 peak occurs 400 ms before the HbR peak; and (iii) HbO2 absolute intensity is higher than the HbR one (1.93×10^{-5} versus 0.79×10^{-5}). N.B. Standard deviations are only displayed every second for clarity purposes.

Spatial coherence

These results have also been observed in all other pairs having a significant estimation of β ($P < 0.00005$). The previously described oscillating pattern has mainly been observed on pairs 4, 5 and 9, *i.e.*, where the motor area was best covered. Given that all pairs may not be temporally synchronized (*i.e.*, it is possible to have a given region where the hemodynamics come earlier than another), we used the following method to estimate the activation. Considering one specific pair, since several estimations have been performed (at different shifts), we disposed of a set of β values oscillating with the applied shift. The actual β values we considered to quantify activation were the minimum value for HbR and the maximum value for HbO2 in the oscillation pattern. Using this method for selecting β, Figure D.11 provides a spatial mapping of estimated β, where one can clearly see the spatial coherence between the activated region of the cortex and the pair localization.

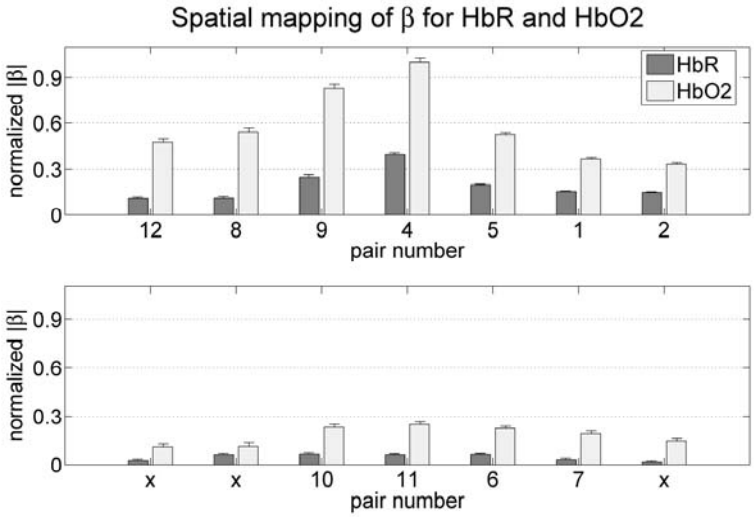

Figure D.11. Spatial mapping of estimated β for each pair

Values were all normalized towards the maximum value of β (as well as for standard deviations). Data related to HbR concentration are represented as absolute value. Top and bottom panels, respectively, represent superior and inferior pairs. For precise localization, one can refer to Figure D.8. Pairs numbered as ''x'' were non-significant for HbR ($P < 0.00005$).

High resolution time shift

One of the main advantages of DOI over fMRI is its higher time resolution. We also took advantage of this aspect by performing series of shift estimations with a 100 ms shift step, which corresponds to the sampling period. By identifying precisely the shift value at which HbR and HbO2 concentrations were, respectively, minimum and maximum, we observed that this value is not 0 as expected, but rather less. For instance, in pair number 4 we observe a minimum of HbR and a maximum of HbO2 concentrations, respectively, at -1.1 s and -1.5 s relative to the protocol onset (see Figure D.10). It means that the overall activity is not overlapped by the protocol, but is located before the protocol. Note that the protocol has been convolved with the canonical HRF (as done in Section 'Shift method'). Hence, every time delay is given relative to the peaking time of the canonical HRF which is 5 s. Therefore, another HRF peaking time would lead to other values of temporal shift that give the maximum activation in the premotor cortex. In future works, a temporal normalization relative to the HRF peaking time might be of interest.

We have one hypothesis for such a shifted activity: the subject might have been active before each stimulus. We believe that the repetitiveness of the task generated an anticipation reflected by a cognitive activity in the responsible areas of the cortex. That hypothesis is based on observations of such phenomena in motor (Zang et al., 2003) and premotor areas (Praamstra et al., 2006). Note that one corollary of that hypothesis lies in the fact that with respect to one specific task, the canonical HRF used for estimating β may vary along the cortex, as reported in (Aguirre et al., 1998; Biswal et al., 2003).

To validate this hypothesis, we used two different methods: (i) for each pair, a shift value corresponding to the extremum β was related to the spatial localization of that pair along the cortex, in order to assess a higher shift value in premotor versus motor area; (ii) event-related acquisition was performed on two subjects. In that case, we expected no time shift as the subjects could not have anticipated the stimuli.

Both results did confirm this hypothesis (see Figure D.12). On the first experiment, we observed a complete linearity of the shift value towards pairs localization along the frontal lobe: shift value decreased in the antero-posterior direction. On the event-related acquisition, we observed almost no shift value on all significant pairs. Given the observation above and the capabilities of optical imaging, we hope to come back to this issue in more detail in subsequent work.

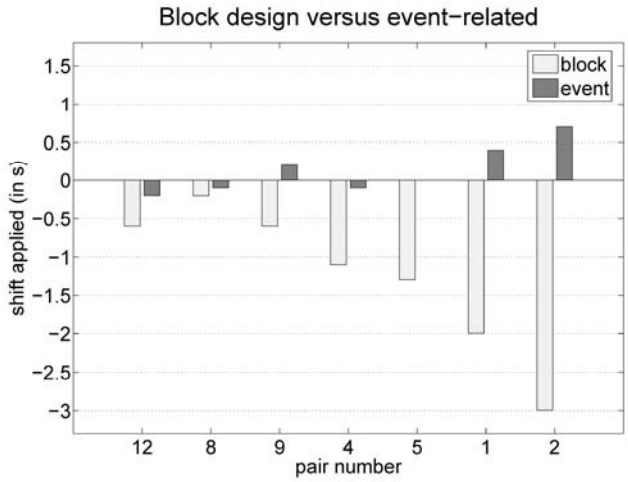

Figure D.12. Spatial mapping of temporal delay in haemodynamic response
Spatial mapping of estimated shift values for which estimated β on HbR were extremum. Only superior pairs are displayed (see Figure D.8). One can clearly observe an increasing value of the shift in the rostral direction for the block design. These values are maximum on pairs number 1 and 2 which covered the premotor area. Furthermore event-related design did show an almost null shift value for all considered pairs.

Towards hemodynamic response estimation

The general linear model presented above is aimed at signal detection and can be seen as a simpler form or dimensionally reduced version of a similar model used for HRF estimation. Estimation techniques in the literature are mainly aimed at recovering the whole form of the HRF and are thereby trying to estimate many parameters: one for each point of the HRF to be determined with weak priors (Marrelec et al., 2003).

In this section, we propose a different approach to HRF estimation. We introduced strong priors based on the following observations: (i) typically the HRF is smooth; and (ii) changes observed in its form are mainly a time shift and potentially a change in the spread of the response.

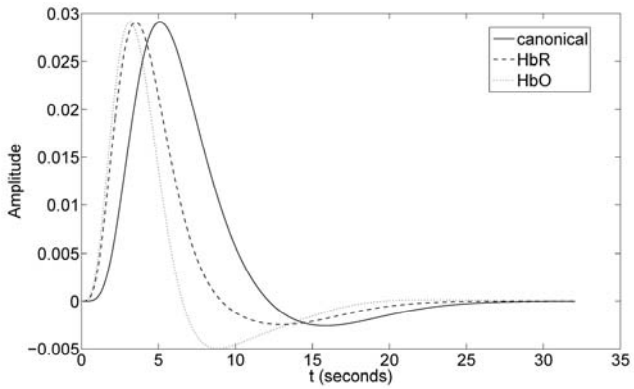

Figure D.13. Estimation of the HRF time shift on block data
Observe that the technique does recover very well the peak time value and is consistent with the shifted protocol estimations done before.

With these observations in mind, and the canonical HRF, $h_c(t)$, it should be possible to approximate the real estimated HRF, $h(t)$, by a parametric model. First we note that the following expansion:

$$h(t) = h_c(t) + a_1 h_{c'}(t) + \cdots + a_n h_c^{(n)} + o(h_c^{(n+1)}) \tag{D.18}$$

when truncated to the first two terms is just a Taylor expansion and it describes a time-shifted canonical HRF by $\Delta t = a_1$. Thus, by expanding the design matrix to include the first derivative of the canonical response, we can model time shifts. Let us use the same data presented above to estimate the HRF time shift by using the method presented here. The estimation procedure is the same as usual: we construct a design matrix consisting of the canonical HRF and its first derivative. Then, a correlation of each drift function is computed with the design matrix. If the correlation exceeds a given threshold, the given drift is eliminated from the list. Once this is done, parameters a_0, a_1 and the HRF are estimated. Since the time shifted estimations of the canonical HRF provide at least an estimate of where the estimated HRF should peak, we performed a parametric HRF estimation on the same block data. Results are presented in Figure D.13. As expected, we observed a shift towards earlier times. Peak positions found are: Canonical: 5.1 s, HbR: 3.6 s, HbO2: 3.1 s, leading to a 500 ms difference between HbO2 and HbR peaks (compared to 400 ms with the time shift method) and an overall lag of -1.5 s with the canonical response which is comparable to the previous estimation.

Further deformations can also be modelled such as scaling of the function. Let us review the canonical form used for detection (here, we use the form built in SPM):

$$h_c(t; s, p_i) = G_{pdf}(t, p_1 / s, dt / s) - G_{pdf}(t, p_2 / s, dt / s) / p_3 \tag{D.19}$$

$$G_{pdf}(t, h, l) = \frac{l^h t^{h-1} e^{-lt}}{\Gamma(h)} \tag{D.20}$$

where s is a scale parameter and p_i are parameters chosen to model a specific response. For example, p_1, p_2 model the delay of the response and undershoot, respectively, whereas p_3 characterizes the strength of the dip. A small variation in scale induces changes in the HRF as follows:

$$\delta h_c(t) = \frac{\partial h_c(t; s, p_i)}{\partial s} \tag{D.21}$$

The extended model above can be used to develop a hybrid method to estimate the HRF that is better conditioned by using a design matrix of the form

$$Xh_c \rightarrow X(h_c, h_{c'}, \delta h_c) \tag{D.22}$$

and estimating the parameters a_i. This procedure leads to an estimated HRF of the form

$$h(t) = h_c(t) + a_1 h_{c'}(t) + a_2 \delta h_c(t) \tag{D.23}$$

This parametric expression of the new canonical HRF introduces more components in the design matrix H_h and can allow the recovery of the whole HRF by estimating fewer parameters (a_i) than the regular sampling of the HRF itself (Marrelec et al., 2003; Marrelec et al., 2004). Obviously the procedure proposed here can be extended by including further parameters modelling the whole HRF better but the tradeoff is the loss of the dimensional reduction, the sole advantage of this approach.

Discussion

Analyses of DOI data, aiming at detecting brain activated regions, have been conducted using the general linear model (GLM) and an original detection method: the shift method. The GLM we proposed makes use of basic but relevant a priori information concerning the physiological process underlying the response. It proved to be reliable and robust regarding the actual SNR level and physiological structure, as well as the stimulus sequence.

Physiological structure and filtering

In optical imaging conventional analysis methods of hemoglobin concentration go through a series of steps to recover activation. It starts with the denoising of the raw data by using a simple band-pass filter, [0.01–0.05 Hz], in the Fourier domain. The argument used is that the HRF has support over that frequency band. This may affect information originating from the protocol, when the support of the physiological signal spectrum overlaps that of the protocol. As we have seen in the previous section, one key aspect of the proposed general linear model is the use of a large set of drift functions (DCT) modelling physiological signals. Then, the drift functions having a large correlation ($0.15 < r < 1.0$) with the protocol are discarded leading to a better estimation of the activation parameters.

Model estimation

The maximum a posteriori (MAP) estimators introduced in the proposed Bayesian framework were shown to be essentially insensitive to the true noise structure (Marrelec et al., 2003). This can be interpreted as follows. Two models were set: one for the HRF and one for the noise. The latter was based on the sole hypothesis that the noise has given (yet unknown) mean and variance, and the Gaussian structure imposed itself as the least biased under this hypothesis. From there, two situations can happen. If the model including a large set of drift functions is sufficiently well defined to retrieve the HRF (*i.e.*, the prior information on parameters and the data are sufficient to lead to correct inference), then the noise structure is mostly irrelevant to the estimation. In this case, introduction of more refined information, for example temporal correlation, would only slightly improve the estimation. On the contrary, if the model for the HRF and drift functions is badly specified, then any additional information will greatly improve the results.

Shift method

This scanning method provides at least four valuable pieces of information: first, it can provide the temporal peak location of the HRF convoluted with the stimuli. The high temporal resolution of DOI leads to a good precision on that peak value (on the order of 100 ms here, but DOI could have a time resolution of up to 10 ms). Although the problem of peak detection has already been explored by introducing other regressors such as first and second derivatives of the canonical HRF, this method uses no prior for the peaking value of the HRF. Indeed, introducing HRF derivatives requires assurance that the peak value is relatively close to the actual one (which peaks at ~5 s). The proposed shift method allows a large range of HRF peak values to be explored and thus uses a prior only on its shape. This could notably be of interest to investigate animal hemodynamic models. Second, it can serve as an assessment of the relative presence of activity in the raw data. Indeed, each shift the estimation gives an absolute value of β associated with a T-statistic. One can then compare them to obtain a relative variation of β expressing the amount 'real activity' that has been detected. Third, as a validation tool for the estimator since we expected a proportional increase of the β towards the amount of overlap between the actual activity and the stimuli. Fourth, when used on data containing rest periods before and/or after the task paradigm, the shift method becomes a tool for comparing rest periods in order to study learning and retention of timed motor sequences (Doyon and Benali, 2005). Indeed, by acquiring long rest periods before and after the motor task, one can analyze the pattern provided after the shifting method (see Figure D.9). In the case of a remanent activity that pattern should not show a symmetrical distribution. Furthermore, the shift method does not depend on the modality and could also be applied to EEG–MEG data since their temporal resolution is on the order of DOI. Finally, it could be applied to fMRI for activation detection when the peaking location of the HRF is unknown (e.g., animal preparation, subject under anaesthesia).

Limitation of the filtering method

Using a white noise in the model is contradictory with the idea of removing some drifts but not those correlated with the paradigm, and leads to biased T-stats. Hence, one should carefully consider the validity of the estimated T-score when the aim of the study is to quantify the amount of activation. However, T-scores are still valuable when compared to each other, as done in the present study with the shift method. Indeed, when a T-score is estimated at various shift steps and then displayed on a graph, the relative comparison of T-scores still provides valuable information such as the global peaks of the graph indicating the temporal location of the maximum activation. Moreover, drift functions that partly match the protocol are not introduced into the projection basis. They thus colour the noise and also bias the estimation. The goal of the T-stat graph is to show consistency between the increase of the Tstat at a given correlation threshold and the estimation error. The simulation data showed this coherence (see Section 'Modelling of drift components subspace'). Furthermore, the choice of a Bayesian method for the inference was made in order to limit the bias related to the presence of temporal autocorrelations in the residuals. As shown on simulated data where several type of noise (notably coloured noise) were used in order to verify the consistency of the estimation of the variance, the Bayesian method provides better variance estimation (Marrelec et al., 2003).

Limitation of the shift method

We presented the shift method using rest data before and after the task period. This is a significant constraint when doing experiments with long task period. Nevertheless, the shift method can also be used without such rest period. For instance, one can only apply a few shifts (e.g., along 20 samples) to localize the temporal peak for which $|\beta|$ is maximum. This is of particular interest in DOI since the sampling frequency of that modality is significantly higher than the frequency spectrum of physiological signals.

Another point to be discussed is the prior made on the shape of the HbR and HbO2 signals. Indeed, the regressor of interest was the same for both chromophore concentrations. The shape of HbR concentration variation corresponds quite well to the shape of the HRF, since BOLD signal is correlated to a change in HbR concentration. Nevertheless, HbO2 concentration variation is not well characterized yet. In order to maximize the sensitivity of the activation detection, we thus need a better parametric description of HbO2 signal through more event-related experiments. The HRF estimation model we proposed could help designing a proper HRF for HbO2 concentration acting on the scaling of the curve.

Also, the proposed time shift method has only been presented for approximately periodic stimuli. In the case of event-related protocols, one could ask whether the shift method would be still valid. This aspect is interesting and deserves more experiments. On the event-related acquisition, one will not be able to find the 'oscillating pattern' described in this paper. Nevertheless, one should still be able to localize extremum values of β in time when the 'real activity' perfectly overlaps the regressor of interest. Thus the use of the shift method would be

reduced only to 20–30 shifts. Furthermore, acquiring additional rest data, one would be able to compare β estimated within rest period versus protocol period.

HRF estimation

Estimation of the HRF in more detail is a relatively recent concern. In fMRI HRFs have been increasingly suspected to vary from region to region, task to task, and subject to subject (Aguirre et al., 1998). Age and disease are also more and more believed to have a significant influence on the BOLD response (D'Esposito et al., 1999). Furthermore, knowledge about the response function is a key issue to a better understanding of the underlying dynamics of brain activation and the relationship between brain areas (Biswal et al., 2003; Miezin et al., 2000). In DOI data, precise and robust estimation of the HRF is a challenging issue and the subject of ongoing research. We hope to come back to this issue.

Conclusion

In this paper, we have investigated in detail how the GLM performs when used with DOI data. Our initial goal was, as in fMRI, to obtain a general framework by which block and event-related protocols can be analysed. Outcomes of the work are: (i) a filtering method based on DCT functions; (ii) a scanning method to recover small signals and locate them temporally with high precision (shift method); and (iii) a dimensionally reduced method to estimate the hemodynamic response function with a shape prior. A by product of this work has been a better understanding of the differences between the use of the GLM in fMRI and optical imaging.

Although the use of the GLM is not innovative in itself, the particularities of its usage in DOI and the shift method are, we believe, new. It should be noted that the use of DCT functions for physiological modelling can be extended by means of physiological recordings (respiration, heart-beat, and blood-pressure). These measurements can then be included as regressors in the model without difficulty as investigated for fMRI in (Lund et al., 2006).

The work presented here has left open problems to be investigated in future work, namely: the proposed method for parametric estimation of the HRF is interesting due to its dimensional reduction but should be compared with more established methods. The observed anticipation/preparation of the subject in the periodic task seems to indicate that this issue can be approached by means of DOI with some benefits due to its time precision. Moreover, the shift method has been based on a heuristic evaluation of the resulting graph (*i.e.*, the identification of the wave-train). When moving towards protocols having a less periodic structure, these identifications will need to become more quantitative. Thus, a numerical technique should be developed for pattern identification.

Acknowledgments

We thank Guillaume Marrelec for providing the first version of the GLM software including the Bayesian framework. We also sincerely thank the referees for their precious comments, and Claudine Gauthier for proofreading the manuscript. Julien Cohen-Adad is supported by the Institut National de la Santé et de la Recherche Médicale and by Canada Research Chair on the spinal Cord to Serge Rossignol provided by the Canadian Institute of Health Research.

Bibliography

Abel, K.M., Allin, M.P., Kucharska-Pietura, K., Andrew, C., Williams, S., David, A.S., Phillips, M.L., 2003. Ketamine and fMRI BOLD signal: distinguishing between effects mediated by change in blood flow versus change in cognitive state. Hum Brain Mapp 18, 135-145.

Agosta, F., Absinta, M., Sormani, M.P., Ghezzi, A., Bertolotto, A., Montanari, E., Comi, G., Filippi, M., 2007a. In vivo assessment of cervical cord damage in MS patients: a longitudinal diffusion tensor MRI study. Brain 130, 2211-2219.

Agosta, F., Valsasina, P., Caputo, D., Rocca, M.A., Filippi, M., 2007b. Tactile-associated fMRI recruitment of the cervical cord in healthy subjects. Hum Brain Mapp (in press).

Agosta, F., Valsasina, P., Caputo, D., Stroman, P.W., Filippi, M., 2008. Tactile-associated recruitment of the cervical cord is altered in patients with multiple sclerosis. Neuroimage 39, 1542-1548.

Aguirre, G.K., Zarahn, E., D'Esposito, M., 1998. The variability of human, BOLD hemodynamic responses. Neuroimage 8, 360-369.

Alexander, A.L., Hasan, K.M., Lazar, M., Tsuruda, J.S., Parker, D.L., 2001. Analysis of partial volume effects in diffusion-tensor MRI. Magn Reson Med 45, 770-780.

Alexander, A.L., Lee, J.E., Wu, Y.C., Field, A.S., 2006. Comparison of diffusion tensor imaging measurements at 3.0 T versus 1.5 T with and without parallel imaging. Neuroimaging Clin N Am 16, 299-309, xi.

Alexander, D.C., 2005. Multiple-fiber reconstruction algorithms for diffusion MRI. Ann N Y Acad Sci 1064, 113-133.

Alperin, N., Vikingstad, E.M., Gomez-Anson, B., Levin, D.N., 1996. Hemodynamically independent analysis of cerebrospinal fluid and brain motion observed with dynamic phase contrast MRI. Magn Reson Med 35, 741-754.

Anderson, A.W., 2001. Theoretical analysis of the effects of noise on diffusion tensor imaging. Magn Reson Med 46, 1174-1188.

Anderson, A.W., 2005. Measurement of fiber orientation distributions using high angular resolution diffusion imaging. Magn Reson Med 54, 1194-1206.

Anderson, K.D., Gunawan, A., Steward, O., 2007. Spinal pathways involved in the control of forelimb motor function in rats. Exp Neurol 206, 318-331.

Andersson, J.L., Hutton, C., Ashburner, J., Turner, R., Friston, K., 2001. Modeling geometric deformations in EPI time series. Neuroimage 13, 903-919.

Andersson, J.L., Skare, S., Ashburner, J., 2003. How to correct susceptibility distortions in spin-echo echo-planar images: application to diffusion tensor imaging. Neuroimage 20, 870-888.

Antognini, J.F., Barter, L., Carstens, E., 2005. Overview movement as an index of anesthetic depth in humans and experimental animals. Comp Med 55, 413-418.

Aota, Y., Niwa, T., Uesugi, M., Yamashita, T., Inoue, T., Saito, T., 2008. The correlation of diffusion-weighted magnetic resonance imaging in cervical compression myelopathy with neurologic and radiologic severity. Spine 33, 814-820.

Ardekani, B.A., Kershaw, J., Kashikura, K., Kanno, I., 1999. Activation detection in functional MRI using subspace modeling and maximum likelihood estimation. IEEE Trans Med Imaging 18, 101-114.

Ardekani, S., Selva, L., Sayre, J., Sinha, U., 2006. Quantitative metrics for evaluating parallel acquisition techniques in diffusion tensor imaging at 3 Tesla. Invest Radiol 41, 806-814.

Ardekani, S., Sinha, U., 2004. Quantitative assessment of parallel acquisition techniques in diffusion tensor imaging at 3.0 Tesla. In: 26th International Conference of the IEEE Engineering in Medicine and Biology Society (EMBS), San Francisco, USA, 2, 1072-1075.

Ardekani, S., Sinha, U., 2005. Geometric distortion correction of high-resolution 3 T diffusion tensor brain images. Magn Reson Med 54, 1163-1171.

Arridge, S.R., 1999. Optical tomography in medical imaging. Inverse Problems 15, R41-R93.

Arsigny, V., Fillard, P., Pennec, X., Ayache, N., 2006. Log-Euclidean metrics for fast and simple calculus on diffusion tensors. Magn Reson Med 56, 411-421.

Assaf, Y., Basser, P.J., 2005. Composite hindered and restricted model of diffusion (CHARMED) MR imaging of the human brain. Neuroimage 27, 48-58.

Assaf, Y., Blumenfeld-Katzir, T., Yovel, Y., Basser, P.J., 2008. AxCaliber: a method for measuring axon diameter distribution from diffusion MRI. Magn Reson Med 59, 1347-1354.

Assaf, Y., Cohen, Y., 2000. Assignment of the water slow-diffusing component in the central nervous system using q-space diffusion MRS: implications for fiber tract imaging. Magn Reson Med 43, 191-199.

Assaf, Y., Kafri, M., Shinar, H., Chapman, J., Korczyn, A.D., Navon, G., Cohen, Y., 2002. Changes in axonal morphology in experimental autoimmune neuritis as studied by high b-value q-space (1)H and (2)H DQF diffusion magnetic resonance spectroscopy. Magn Reson Med 48, 71-81.

Assaf, Y., Mayk, A., Cohen, Y., 2000. Displacement imaging of spinal cord using q-space diffusion-weighted MRI. Magn Reson Med 44, 713-722.

Assaf, Y., Mayk, A., Eliash, S., Speiser, Z., Cohen, Y., 2003. Hypertension and neuronal degeneration in excised rat spinal cord studied by high-b value q-space diffusion magnetic resonance imaging. Exp Neurol 184, 726-736.

Backes, W.H., Mess, W.H., Wilmink, J.T., 2001. Functional MR imaging of the cervical spinal cord by use of median nerve stimulation and fist clenching. AJNR Am J Neuroradiol 22, 1854-1859.

Bagarinao, E., Matsuo, K., Nakai, T., Sato, S., 2003. Estimation of general linear model coefficients for real-time application. Neuroimage 19, 422-429.

Baird, A.A., Kagan, J., Gaudette, T., Walz, K.A., Hershlag, N., Boas, D.A., 2002. Frontal lobe activation during object permanence: data from near-infrared spectroscopy. Neuroimage 16, 1120-1125.

Bamett, A.H., Culver, J.P., Sorensen, A.G., Dale, A., Boas, D.A., 2003. Robust inference of baseline optical properties of the human head with three-dimensional segmentation from magnetic resonance imaging. Appl Opt 42, 3095-3108.

Bammer, R., Augustin, M., Prokesch, R.W., Stollberger, R., Fazekas, F., 2002. Diffusion-weighted imaging of the spinal cord: interleaved echo-planar imaging is superior to fast spin-echo. J Magn Reson Imaging 15, 364-373.

Bammer, R., Fazekas, F., 2003. Diffusion imaging of the human spinal cord and the vertebral column. Top Magn Reson Imaging 14, 461-476.

Bammer, R., Herneth, A.M., Maier, S.E., Butts, K., Prokesch, R.W., Do, H.M., Atlas, S.W., Moseley, M.E., 2003. Line scan diffusion imaging of the spine. AJNR Am J Neuroradiol 24, 5-12.

Bammer, R., Stollberger, R., Augustin, M., Simbrunner, J., Offenbacher, H., Kooijman, H., Ropele, S., Kapeller, P., Wach, P., Ebner, F., Fazekas, F., 1999. Diffusion-weighted imaging with navigated interleaved echo-planar imaging and a conventional gradient system. Radiology 211, 799-806.

Bandettini, P.A., Kwong, K.K., Davis, T.L., Tootell, R.B., Wong, E.C., Fox, P.T., Belliveau, J.W., Weisskoff, R.M., Rosen, B.R., 1997. Characterization of cerebral blood oxygenation and flow changes during prolonged brain activation. Hum Brain Mapp 5, 93-109.

Bandettini, P.A., Ungerleider, L.G., 2001. From neuron to BOLD: new connections. Nat Neurosci 4, 864-866.

Bannister, P.R., 2003. Motion Correction for Functional Magnetic Resonance Images. PhD Thesis, University of Oxford.

Bar-Shir, A., Duncan, I., Cohen, Y., 2008. q-Space MRI and DTI of excised myelin deficient rat brains. In: 16th Annual Meeting of the International Society for Magnetic Resonance in Medicine (ISMRM), Toronto, Canada, 2105.

Barbeau, H., Rossignol, S., 1987. Recovery of locomotion after chronic spinalization in the adult cat. Brain Res 412, 84-95.

Bareyre, F.M., Kerschensteiner, M., Raineteau, O., Mettenleiter, T.C., Weinmann, O., Schwab, M.E., 2004. The injured spinal cord spontaneously forms a new intraspinal circuit in adult rats. Nat Neurosci 7, 269-277.

Barrière, G., Cohen-Adad, J., Benali, H., Rossignol, S., 2008. Locomotor recovery after spinal lesions in the cat using behavioral and imaging techniques. In: Spinal Cord : Function, Repair and Rehabilitation after Injury, Montreal, Canada.

Barriere, G., Leblond, H., Provencher, J., Rossignol, S., 2008. Prominent role of the spinal central pattern generator in the recovery of locomotion after partial spinal cord injuries. J Neurosci 28, 3976-3987.

Basser, P.J., Mattiello, J., LeBihan, D., 1994. Estimation of the effective self-diffusion tensor from the NMR spin echo. J Magn Reson 103, 247-254.

Basser, P.J., Pajevic, S., Pierpaoli, C., Duda, J., Aldroubi, A., 2000. In vivo fiber tractography using DT-MRI data. Magn Reson Med 44, 625-632.

Basso, D.M., Beattie, M.S., Bresnahan, J.C., 1995. A sensitive and reliable locomotor rating scale for open field testing in rats. J Neurotrauma 12, 1-21.

Beaulieu, C., 2002. The basis of anisotropic water diffusion in the nervous system - a technical review. NMR Biomed 15, 435-455.

Beaulieu, C., Allen, P.S., 1994. Determinants of anisotropic water diffusion in nerves. Magn Reson Med 31, 394-400.

Becerra, J.L., Puckett, W.R., Hiester, E.D., Quencer, R.M., Marcillo, A.E., Post, M.J., Bunge, R.P., 1995. MR-pathologic comparisons of wallerian degeneration in spinal cord injury. AJNR Am J Neuroradiol 16, 125-133.

Behrens, T.E., Woolrich, M.W., Jenkinson, M., Johansen-Berg, H., Nunes, R.G., Clare, S., Matthews, P.M., Brady, J.M., Smith, S.M., 2003. Characterization and propagation of uncertainty in diffusion-weighted MR imaging. Magn Reson Med 50, 1077-1088.

Beirowski, B., Adalbert, R., Wagner, D., Grumme, D.S., Addicks, K., Ribchester, R.R., Coleman, M.P., 2005. The progressive nature of Wallerian degeneration in wild-type and slow Wallerian degeneration (WldS) nerves. BMC Neurosci 6, 6.

Bell, A.J., Sejnowski, T.J., 1995. An information-maximization approach to blind separation and blind deconvolution. Neural Comput 7, 1129-1159.

Bellgowan, P.S., Bandettini, P.A., van Gelderen, P., Martin, A., Bodurka, J., 2006. Improved BOLD detection in the medial temporal region using parallel imaging and voxel volume reduction. Neuroimage 29, 1244-1251.

Benner, T., van der Kouwe, A., Sorensen, A., Wang, R., Wiggins, G., Yates, D., Wedeen, V., 2008. Fiber Tracking of Cervical Spinal Cord and Nerves. In: Proceedings 16th Scientific Meeting, International Society for Magnetic Resonance in Medicine, 846.

Berens, S.A., 2006. Use of MRI to study excitotoxic spinal cord injury. Ph.D. Thesis, University of Florida.

Bernstein, M., King, K., Zhou, X., 2004. Handbook of MRI Pulse Sequences. Elsevier Academic Press.

Bilgen, M., 2006. Imaging corticospinal tract connectivity in injured rat spinal cord using manganese-enhanced MRI. BMC Med Imaging 6, 15.

Bilgen, M., Al-Hafez, B., Berman, N.E., Festoff, B.W., 2005. Magnetic resonance imaging of mouse spinal cord. Magn Reson Med 54, 1226-1231.

Bilgen, M., Elshafiey, I., Narayana, P.A., 2001. In vivo magnetic resonance microscopy of rat spinal cord at 7 T using implantable RF coils. Magn Reson Med 46, 1250-1253.

Bilgen, M., Peng, W., Al-Hafez, B., Dancause, N., He, Y.Y., Cheney, P.D., 2006. Electrical stimulation of cortex improves corticospinal tract tracing in rat spinal cord using manganese-enhanced MRI. J Neurosci Methods 156, 17-22.

Biswal, B.B., Pathak, A.P., Ulmer, J.L., Hudetz, A.G., 2003. Decoupling of the hemodynamic and activation-induced delays in functional magnetic resonance imaging. J Comput Assist Tomogr 27, 219-225.

Biton, I.E., Duncan, I.D., Cohen, Y., 2006. High b-value q-space diffusion MRI in myelin-deficient rat spinal cords. Magn Reson Imaging 24, 161-166.

Biton, I.E., Duncan, I.D., Cohen, Y., 2007. q-Space diffusion of myelin-deficient spinal cords. Magn Reson Med 58, 993-1000.

Blain, C.R., Williams, V.C., Johnston, C., Stanton, B.R., Ganesalingam, J., Jarosz, J.M., Jones, D.K., Barker, G.J., Williams, S.C., Leigh, N.P., Simmons, A., 2007. A longitudinal study of diffusion tensor MRI in ALS. Amyotroph Lateral Scler, 1-8.

Boas, D.A., Dale, A.M., Franceschini, M.A., 2004. Diffuse optical imaging of brain activation: approaches to optimizing image sensitivity, resolution, and accuracy. Neuroimage 23 Suppl 1.

Boccara, G., Mann, C., Pouzeratte, Y., Bellavoir, A., Rouvier, A., Colson, P., 1998. Improved postoperative analgesia with isoflurane than with propofol anaesthesia. Can J Anaesth 45, 839-842.

Bodurka, J., Ledden, P., Bandettini, P., 2008. SENSE Optimized Sixteen Element Receive Array for Cervical Spinal Cord Imaging at 3T. In: 16th Annual Meeting of the International Society for Magnetic Resonance in Medicine (ISMRM), Toronto, Canada, 1078.

Bodurka, J., Ye, F., Petridou, N., Murphy, K., Bandettini, P.A., 2007. Mapping the MRI voxel volume in which thermal noise matches physiological noise--implications for fMRI. Neuroimage 34, 542-549.

Bouwman, C.J., Wilmink, J.T., Mess, W.H., Backes, W.H., 2008. Spinal cord functional MRI at 3 T: Gradient echo echo-planar imaging versus turbo spin echo. Neuroimage (in press).

Brevard, M.E., Duong, T.Q., King, J.A., Ferris, C.F., 2003. Changes in MRI signal intensity during hypercapnic challenge under conscious and anesthetized conditions. Magn Reson Imaging 21, 995-1001.

Brooks, J., Robson, M., Schweinhardt, P., Wise, R., Tracey, I., 2004. Functional magnetic resonance imaging (fMRI) of the spinal cord : a methodological study. In: American Pain Society Abstracts, 667.

Brooks, J.C., Beckmann, C.F., Miller, K.L., Wise, R.G., Porro, C.A., Tracey, I., Jenkinson, M., 2008. Physiological noise modelling for spinal functional magnetic resonance imaging studies. Neuroimage 39, 680-692.

Brosch, J.R., Talavage, T.M., Ulmer, J.L., Nyenhuis, J.A., 2002. Simulation of human respiration in fMRI with a mechanical model. IEEE Trans Biomed Eng 49, 700-707.

Budde, M.D., Kim, J.H., Liang, H.F., Schmidt, R.E., Russell, J.H., Cross, A.H., Song, S.K., 2007. Toward accurate diagnosis of white matter pathology using diffusion tensor imaging. Magn Reson Med 57, 688-695.

Buxton, R.B., Uludag, K., Dubowitz, D.J., Liu, T.T., 2004. Modeling the hemodynamic response to brain activation. Neuroimage 23 Suppl 1, S220-233.

Cai, J., Sheng, K., Sheehan, J.P., Benedict, S.H., Larner, J.M., Read, P.W., 2007. Evaluation of thoracic spinal cord motion using dynamic MRI. Radiother Oncol 84, 279-282.

Calhoun, V., Golay, X., Pearlson, G., 2000. Improved fMRI slice timing correction: interpolation errors and wrap around effects. In: 9th Annual Meeting of the International Society for Magnetic Resonance in Medicine (ISMRM), Denver.

Calhoun, V.D., Adali, T., Pearlson, G.D., Pekar, J.J., 2001. Spatial and temporal independent component analysis of functional MRI data containing a pair of task-related waveforms. Hum Brain Mapp 13, 43-53.

Callaghan, P.T., Eccles, C.D., Xia, Y., 1988. NMR microscopy of dynamic displacements: k-space and q-space imaging. J Phys E Sci Instrum 21, 820-822.

Campbell, J.S., Siddiqi, K., Rymar, V.V., Sadikot, A.F., Pike, G.B., 2005. Flow-based fiber tracking with diffusion tensor and q-ball data: validation and comparison to principal diffusion direction techniques. Neuroimage 27, 725-736.

Cannestra, A.F., Wartenburger, I., Obrig, H., Villringer, A., Toga, A.W., 2003. Functional assessment of Broca's area using near infrared spectroscopy in humans. Neuroreport 14, 1961-1965.

Cannon, M.S., Gelderd, J.B., 1983. Spinal cord vasculature of the rat: a histochemical study of the metabolism of arteries and arterioles. Stroke 14, 611-616.

Carmi, E., Liu, S., Alon, N., Fiat, A., Fiat, D., 2006. Resolution enhancement in MRI. Magn Reson Imaging 24, 133-154.

Carvlin, M.J., Asato, R., Hackney, D.B., Kassab, E., Joseph, P.M., 1989. High-resolution MR of the spinal cord in humans and rats. AJNR Am J Neuroradiol 10, 13-17.

Cercignani, M., Horsfield, M.A., Agosta, F., Filippi, M., 2003. Sensitivity-encoded diffusion tensor MR imaging of the cervical cord. AJNR Am J Neuroradiol 24, 1254-1256.

Chang, H., Fitzpatrick, J.M., 1992. A technique for accurate magnetic resonance imaging in the presence of field inhomogeneities. IEEE Trans Med Imaging 11, 319-329.

Chapuis, B., Vidal-Petiot, E., Oréa, V., Barrès, C., Julien, C., 2004. Linear modelling analysis of baroreflex control of arterial pressure variability in rats. J Physiol 559, 639-649.

Chen, N.K., Egorova, S., Guttmann, C.R., Panych, L.P., 2003. Functional MRI with variable echo time acquisition. Neuroimage 20, 2062-2070.

Chenevert, T.L., Brunberg, J.A., Pipe, J.G., 1990. Anisotropic diffusion in human white matter: demonstration with MR techniques in vivo. Radiology 177, 401-405.

Chin, C.L., Wehrli, F.W., Fan, Y., Hwang, S.N., Schwartz, E.D., Nissanov, J., Hackney, D.B., 2004. Assessment of axonal fiber tract architecture in excised rat spinal cord by localized NMR q-space imaging: simulations and experimental studies. Magn Reson Med 52, 733-740.

Choe, A., Hong, X., Colvin, D., Stepniewska, I., Ding, z., Anderson, A., 2008. Quantitative Comparison of Fiber Properties from DTI, HARDI and Light Microscopy. In: 16th Annual Meeting of the International Society for Magnetic Resonance in Medicine (ISMRM), Toronto, Canada, 565.

Ciccarelli, O., Behrens, T.E., Altmann, D.R., Orrell, R.W., Howard, R.S., Johansen-Berg, H., Miller, D.H., Matthews, P.M., Thompson, A.J., 2006. Probabilistic diffusion tractography: a potential tool to assess the rate of disease progression in amyotrophic lateral sclerosis. Brain 129, 1859-1871.

Ciccarelli, O., Parker, G.J., Toosy, A.T., Wheeler-Kingshott, C.A., Barker, G.J., Boulby, P.A., Miller, D.H., Thompson, A.J., 2003. From diffusion tractography to quantitative white matter tract measures: a reproducibility study. Neuroimage 18, 348-359.

Ciccarelli, O., Wheeler-Kingshott, C.A., McLean, M.A., Cercignani, M., Wimpey, K., Miller, D.H., Thompson, A.J., 2007. Spinal cord spectroscopy and diffusion-based tractography to assess acute disability in multiple sclerosis. Brain 130, 2220-2231.

Clark, C.A., Barker, G.J., Tofts, P.S., 2000. Improved reduction of motion artifacts in diffusion imaging using navigator echoes and velocity compensation. J Magn Reson 142, 358-363.

Clark, C.A., Werring, D.J., 2002. Diffusion tensor imaging in spinal cord: methods and applications - a review. NMR Biomed 15, 578-586.

Cohen-Adad, J., 2008. Diffusion Tensor Imaging and Tractography of the spinal cord in animals and humans. In: Spinal Cord : Function, Repair and Rehabilitation after Injury, Montreal, Canada.

Cohen-Adad, J., Benali, H., Barrière, G., Leblond, H., Hoge, R.D., Rossignol, S., 2008a. Development of clinical diffusion tensor MRI of the spinal cord in a context of spinal cord injury. IRBM 29, 255-260.

Cohen-Adad, J., Benali, H., Hoge, R.D., Leblond, H., Barrière, G., Doyon, J., Rossignol, S., 2007a. Spinal cord in vivo diffusion tensor imaging of healthy human and spinalized cats. In: 13th Annual Meeting of the Organization for Human Brain Mapping (HBM), Chicago, USA, S887.

Cohen-Adad, J., Benali, H., Hoge, R.D., Rossignol, S., 2007b. In vivo assessment of spinal cord integrity by diffusion tensor imaging. In: Society for Neuroscience, San Diego, USA, 37, 77.10.

Cohen-Adad, J., Benali, H., Hoge, R.D., Rossignol, S., 2007c. In vivo diffusion tensor imaging of the spinal cord. In: Canadian Physiological Society, Mont Ste-Anne, Quebec, Canada.

Cohen-Adad, J., Benali, H., Hoge, R.D., Rossignol, S., 2008b. In vivo DTI of the healthy and injured cat spinal cord at high spatial and angular resolution. Neuroimage 40, 685-697.

Cohen-Adad, J., Benali, H., Rossignol, S., 2006a. A functional MRI methodology to map the neuronal activity in the spinal cord of cats. In: 28th International Symposium of the Groupe de recherche sur le système nerveux central et le Centre de recherche en sciences neurologiques: "Computational Neuroscience", Montreal, Canada.

Cohen-Adad, J., Benali, H., Rossignol, S., 2007d. Methodology for MR diffusion tensor imaging of the cat spinal cord. In: 29th International Conference of the IEEE Engineering in Medicine and Biology Society (EMBS), Lyon, France, 1, 323-326.

Cohen-Adad, J., Chapuisat, S., Doyon, J., Rossignol, S., Lina, J.M., Benali, H., Lesage, F., 2007e. Activation detection in diffuse optical imaging by means of the general linear model. Med Image Anal 11, 616-629.

Cohen-Adad, J., Descoteaux, M., Barrière, G., Hoge, R.D., Deriche, R., Benali, H., Rossignol, S., 2008c. Characterization of the healthy and injured spinal cord using q-ball imaging. In: Pathogenesis and Mechanisms of White Matter Injury, Krakow, Poland.

Cohen-Adad, J., Descoteaux, M., Barrière, G., Hoge, R.D., Deriche, R., Benali, H., Rossignol, S., 2008d. Characterization of the healthy and injured spinal cord using q-ball imaging. In: 8th international congress of the IRME, Paris, France.

Cohen-Adad, J., Descoteaux, M., Deriche, R., Rossignol, S., Hoge, R.D., Benali, H., 2008e. Q-ball imaging of the spinal cord. In: 16th Annual Meeting of the International Society for Magnetic Resonance in Medicine (ISMRM), Toronto, Canada, 569.

Cohen-Adad, J., Descoteaux, M., Rossignol, S., Hoge, R.D., Deriche, R., Benali, H., 2008f. Detection of multiple pathways in the spinal cord using q-ball imaging. Neuroimage 42, 739-749.

Cohen-Adad, J., Descoteaux, M., Rossignol, S., Hoge, R.D., Deriche, R., Benali, H., 2008g. Detection of multiple pathways in the spinal cord white matter using q-ball imaging. In: 5th IEEE International Symposium on Biomedical Imaging (ISBI), Paris, France, 1380.

Cohen-Adad, J., Gauthier, C., Rossignol, S., Benali, H., Hoge, R.D., 2008h. BOLD signal responses to controlled hypercapnia in human spinal cord. In: 16th Annual Meeting of the International Society for Magnetic Resonance in Medicine (ISMRM), Toronto, Canada, 3403.

Cohen-Adad, J., Hoge, R.D., Benali, H., Rossignol, S., 2007f. In vivo diffusion MRI of the cat spinal cord following injury. In: Symposium on Motor Systems, San Diego, USA.

Cohen-Adad, J., Hoge, R.D., Leblond, H., Xie, G., Beaudoin, G., Song, A., Krueger, G., Doyon, J., Benali, H., Rossignol, S., 2009a. Investigations in functional MRI of the spinal cord of cats. Neuroimage 44, 328-339.

Cohen-Adad, J., Leblond, H., Ghosh, A., Descoteaux, M., Deriche, R., Benali, H., Rossignol, S., 2009b. Evaluation of q-ball metrics for assessing the integrity of the injured spinal cord. In: 17th Annual Meeting of the International Society for Magnetic Resonance in Medicine (ISMRM), Honolulu, Hawaii.

Cohen-Adad, J., Lundell, H., Rossignol, S., 2009c. Distortion correction in spinal cord DTI: What's the best approach? In: 17th Annual Meeting of the International Society for Magnetic Resonance in Medicine (ISMRM), Honolulu, Hawaii.

Cohen-Adad, J., Perlbarg, V., Doyon, J., Hoge, R.D., Beaudoin, G., Song, A., Leblond, H., Provencher, J., Rossignol, S., Benali, H., 2006b. Methodology to study functional MRI of the cat lumbar spinal cord. In: 12th Annual Meeting of the Organization for Human Brain Mapping (HBM), Florence, Italy, S2851.

Cohen-Adad, J., Piche, M., Rainville, P., Benali, H., Rossignol, S., 2007g. Impact of realignment on spinal functional MRI time series. In: 29th International Conference of the IEEE Engineering in Medicine and Biology Society (EMBS), Lyon, France, 1, 2126-2129.

Cohen-Adad, J., Rossignol, S., Benali, H., Hoge, R.D., 2008i. In vivo assessment of axonal disruption using diffusion magnetic resonance imaging. In: 31st Canadian Medical and Biological Engineering Conference, Montreal, Canada, (in press).

Cohen-Adad, J., Rossignol, S., Hoge, R.D., 2009d. Slice-by-slice motion correction in spinal cord fMRI: SliceCorr. In: 17th Annual Meeting of the International Society for Magnetic Resonance in Medicine (ISMRM), Honolulu, Hawaii.

Cohen, M.A., Taylor, J.A., 2002. Short-term cardiovascular oscillations in man: measuring and modelling the physiologies. J Physiol 542, 669-683.

Cohen, Y., Assaf, Y., 2002. High b-value q-space analyzed diffusion-weighted MRS and MRI in neuronal tissues - a technical review. NMR Biomed 15, 516-542.

Collins, D.L., Evans, A., Holmes, C.J., Peters, T.M., 1995a. Automatic 3D segmentation of neuro-anatomical structures from MRI. In: Information Processing in Medical Imaging (IPMI), Ile de Berder, France, 139-152.

Collins, J.G., Kendig, J.J., Mason, P., 1995b. Anesthetic actions within the spinal cord: contributions to the state of general anesthesia. Trends Neurosci 18, 549-553.

Comon, P., 1994. Independent component analysis, a new concept? Signal processing 36, 287-314.

Concha, L., Gross, D.W., Wheatley, B.M., Beaulieu, C., 2006. Diffusion tensor imaging of time-dependent axonal and myelin degradation after corpus callosotomy in epilepsy patients. Neuroimage 32, 1090-1099.

Conturo, T.E., Lori, N.F., Cull, T.S., Akbudak, E., Snyder, A.Z., Shimony, J.S., McKinstry, R.C., Burton, H., Raichle, M.E., 1999. Tracking neuronal fiber pathways in the living human brain. Proc Natl Acad Sci U S A 96, 10422-10427.

Cowley, L.T., Isaacs, H.L., Young, S.W., Raffin, T.A., 1994. Magnetic resonance imaging marketing and investment. Tensions between the forces of business and the practice of medicine. Chest 105, 920-928.

Cusack, R., Brett, M., Osswald, K., 2003. An evaluation of the use of magnetic field maps to undistort echo-planar images. Neuroimage 18, 127-142.

D'Arceuil, H.E., Westmoreland, S., de Crespigny, A.J., 2007. An approach to high resolution diffusion tensor imaging in fixed primate brain. Neuroimage 35, 553-565.

D'Esposito, M., Zarahn, E., Aguirre, G.K., Rypma, B., 1999. The effect of normal aging on the coupling of neural activity to the bold hemodynamic response. Neuroimage 10, 6-14.

Dagli, M.S., Ingeholm, J.E., Haxby, J.V., 1999. Localization of cardiac-induced signal change in fMRI. Neuroimage 9, 407-415.

Dale, A., Buckner, R., 1997. Selective averaging of rapidly presented individual trials using fMRI. Human Brain Mapping 5, 329-340.

Darquie, A., Poline, J.B., Poupon, C., Saint-Jalmes, H., Le Bihan, D., 2001. Transient decrease in water diffusion observed in human occipital cortex during visual stimulation. Proc Natl Acad Sci U S A 98, 9391-9395.

de Crespigny, A.J., Marks, M.P., Enzmann, D.R., Moseley, M.E., 1995. Navigated diffusion imaging of normal and ischemic human brain. Magn Reson Med 33, 720-728.

De Jong, R.H., Robles, R., Corbin, R.W., Nace, R.A., 1968. Effect of inhalation anesthetics on monosynaptic and plysynpatic transmission in the spinal cord. J Pharmacol Exp Ther 162, 326-330.

DeBoy, C.A., Zhang, J., Dike, S., Shats, I., Jones, M., Reich, D.S., Mori, S., Nguyen, T., Rothstein, B., Miller, R.H., Griffin, J.T., Kerr, D.A., Calabresi, P.A., 2007. High resolution diffusion tensor imaging of axonal damage in focal inflammatory and demyelinating lesions in rat spinal cord. Brain 130, 2199-2210.

Deng, J., Omary, R.A., Larson, A.C., 2008. Multishot diffusion-weighted SPLICE PROPELLER MRI of the abdomen. Magn Reson Med 59, 947-953.

Deo, A.A., Grill, R.J., Hasan, K.M., Narayana, P.A., 2006. In vivo serial diffusion tensor imaging of experimental spinal cord injury. J Neurosci Res 83, 801-810.

Descoteaux, M., 2008. High Angular Resolution Diffusion MRI: from Local Estimation to Segmentation and Tractography. PhD Thesis, University Nice-Sophia Antipolis.

Descoteaux, M., Angelino, E., Fitzgibbons, S., Deriche, R., 2006. Apparent diffusion coefficients from high angular resolution diffusion imaging: estimation and applications. Magn Reson Med 56, 395-410.

Descoteaux, M., Angelino, E., Fitzgibbons, S., Deriche, R., 2007a. Regularized, fast, and robust analytical Q-ball imaging. Magn Reson Med 58, 497-510.

Descoteaux, M., Deriche, R., Anwander, A., 2007b. Deterministic and Probabilistic Q-Ball Tractography: from Diffusion to Sharp Fiber Distributions. INRIA Research Report 6273.

Diamond, S.G., Huppert, T.J., Kolehmainen, V., Franceschini, M.A., Kaipio, J.P., Arridge, S.R., Boas, D.A., 2006. Dynamic physiological modeling for functional diffuse optical tomography. Neuroimage 30, 88-101.

Dietrich, O., Herlihy, A., Dannels, W.R., Fiebach, J., Heiland, S., Hajnal, J.V., Sartor, K., 2001. Diffusion-weighted imaging of the spine using radial k-space trajectories. Magma 12, 23-31.

Douek, P., Turner, R., Pekar, J., Patronas, N., Le Bihan, D., 1991. MR color mapping of myelin fiber orientation. J Comput Assist Tomogr 15, 923-929.

Doyon, J., Benali, H., 2005. Reorganization and plasticity in the adult brain during learning of motor skills. Curr Opin Neurobiol 15, 161-167.

Du Boulay, G., O'Connell, J., Currie, J., Bostick, T., Verity, P., 1972. Further investigations on pulsatile movements in the cerebrospinal fluid pathways. Acta Radiol Diagn (Stockh) 13, 496-523.

Du Boulay, G.H., 1966. Pulsatile movements in the CSF pathways. Br J Radiol 39, 255-262.

Ducreux, D., Fillard, P., Facon, D., Ozanne, A., Lepeintre, J.F., Renoux, J., Tadie, M., Lasjaunias, P., 2007. Diffusion tensor magnetic resonance imaging and fiber tracking in spinal cord lesions: current and future indications. Neuroimaging Clin N Am 17, 137-147.

Ducreux, D., Lepeintre, J.F., Fillard, P., Loureiro, C., Tadie, M., Lasjaunias, P., 2006. MR diffusion tensor imaging and fiber tracking in 5 spinal cord astrocytomas. AJNR Am J Neuroradiol 27, 214-216.

Duong, T.Q., Yacoub, E., Adriany, G., Hu, X., Ugurbil, K., Kim, S.G., 2003. Microvascular BOLD contribution at 4 and 7 T in the human brain: gradient-echo and spin-echo fMRI with suppression of blood effects. Magn Reson Med 49, 1019-1027.

Duyn, J.H., van Gelderen, P., Li, T.Q., de Zwart, J.A., Koretsky, A.P., Fukunaga, M., 2007. High-field MRI of brain cortical substructure based on signal phase. Proc Natl Acad Sci U S A 104, 11796-11801.

Dyrby, T.B., Sogaard, L.V., Parker, G.J., Alexander, D.C., Lind, N.M., Baare, W.F., Hay-Schmidt, A., Eriksen, N., Pakkenberg, B., Paulson, O.B., Jelsing, J., 2007. Validation of in vitro probabilistic tractography. Neuroimage 37, 1267-1277.

Ellingson, B.M., Ulmer, J.L., Kurpad, S.N., Schmit, B.D., 2008a. Diffusion Tensor MR Imaging in Chronic Spinal Cord Injury. AJNR Am J Neuroradiol.

Ellingson, B.M., Ulmer, J.L., Schmit, B.D., 2007a. Gray and white matter delineation in the human spinal cord using diffusion tensor imaging and fuzzy logic. Acad Radiol 14, 847-858.

Ellingson, B.M., Ulmer, J.L., Schmit, B.D., 2007b. Optimal diffusion tensor indices for imaging the human spinal cord. Biomed Sci Instrum 43, 128-133.

Ellingson, B.M., Ulmer, J.L., Schmit, B.D., 2008b. Morphology and morphometry of human chronic spinal cord injury using diffusion tensor imaging and fuzzy logic. Ann Biomed Eng 36, 224-236.

Elshafiey, I., Bilgen, M., He, R., Narayana, P.A., 2002. In vivo diffusion tensor imaging of rat spinal cord at 7 T. Magn Reson Imaging 20, 243-247.

Endo, T., Spenger, C., Westman, E., Tominaga, T., Olson, L., 2008. Reorganization of sensory processing below the level of spinal cord injury as revealed by fMRI. Exp Neurol 209, 155-160.

Evers, A.S., Crowder, C.M., 2001. General anesthetics. In: Hardman JG, L.L. (Ed.), The pharmacological basis of therapeutics. McGraw-Hill, New York, p. 340.

Facon, D., Ozanne, A., Fillard, P., Lepeintre, J.F., Tournoux-Facon, C., Ducreux, D., 2005. MR diffusion tensor imaging and fiber tracking in spinal cord compression. AJNR Am J Neuroradiol 26, 1587-1594.

Feinberg, D.A., Oshio, K., 1994. Phase errors in multi-shot echo planar imaging. Magn Reson Med 32, 535-539.

Fenyes, D.A., Narayana, P.A., 1999. In vivo diffusion characteristics of rat spinal cord. Magn Reson Imaging 17, 717-722.

Figley, C., Stroman, P., 2008. Physiological noise reduction in spinal fMRI from a single-stage, motion-compensating GLM approach. In: 16th Annual Meeting of the International Society for Magnetic Resonance in Medicine (ISMRM), Toronto, Canada, 2474.

Figley, C.R., Stroman, P.W., 2007. Investigation of human cervical and upper thoracic spinal cord motion: implications for imaging spinal cord structure and function. Magn Reson Med 58, 185-189.

Figley, C.R., Yau, D., Stroman, P.W., 2008. Attenuation of Lower-Thoracic, Lumbar, and Sacral Spinal Cord Motion: Implications for Imaging Human Spinal Cord Structure and Function. AJNR Am J Neuroradiol.

Fillard, P., Arsigny, V., Pennec, X., Ayache, N., 2006. Clinical DT-MRI estimation, smoothing and fiber tracking with Log-Euclidean metrics. In: 3rd IEEE International Symposium on Biomedical Imaging (ISBI), 786-789.

Finsterbusch, J., Frahm, J., 1999. Diffusion-weighted single-shot line scan imaging of the human brain. Magn Reson Med 42, 772-778.

Finsterbusch, J., Frahm, J., 2000. Diffusion tensor mapping of the human brain using single-shot line scan imaging. J Magn Reson Imaging 12, 388-394.

Fischl, B., Wald, L.L., 2007. Phase maps reveal cortical architecture. Proc Natl Acad Sci U S A 104, 11513-11514.

Fletcher, T.F., Malkmus, S.A., 1999. Spinal anatomy of experimental animals. In: Yaksh, T.L. (Ed.), Spinal drug delivery. Elsevier Science.

Ford, J.C., Hackney, D.B., Joseph, P.M., Phelan, M., Alsop, D.C., Tabor, S.L., Hand, C.M., Markowitz, R.S., Black, P., 1994. A method for in vivo high resolution MRI of rat spinal cord injury. Magn Reson Med 31, 218-223.

Fouad, K., Pearson, K., 2004. Restoring walking after spinal cord injury. Prog Neurobiol 73, 107-126.

Fouad, K., Tse, A., 2008. Adaptive changes in the injured spinal cord and their role in promoting functional recovery. Neurol Res 30, 17-27.

Fox, P.T., Raichle, M.E., Mintun, M.A., Dence, C., 1988. Nonoxidative glucose consumption during focal physiologic neural activity. Science 241, 462-464.

Fraidakis, M., Klason, T., Cheng, H., Olson, L., Spenger, C., 1998. High-resolution MRI of intact and transected rat spinal cord. Exp Neurol 153, 299-312.

Frank, L., Buxton, R., Wong, E., 2001. Estimation of respiration-induced noise fluctuations from undersampled multislice fMRI data. Magnetic Resonance in Medicine 45, 635-644.

Freire, L., Mangin, 2001. Motion Correction Algorithms May Create Spurious Brain Activations in the Absence of Subject Motion. Neuroimage 14, 709-722.

Friese, S., Hamhaber, U., Erb, M., Kueker, W., Klose, U., 2004. The influence of pulse and respiration on spinal cerebrospinal fluid pulsation. Invest Radiol 39, 120-130.

Frigon, A., Rossignol, S., 2006. Functional plasticity following spinal cord lesions. Prog Brain Res 157, 231-260.

Friston, K.J., Ashburner, J., Frith, C.D., Poline, J.B., Heather, J.D., Frackowiak, R.S.J., 1995. Spatial registration and normalization of images. Human Brain Mapping 3, 165-189.

Friston, K.J., Holmes, A.P., Worsley, K.J., Poline, J.B., Frith, C.D., Frackowiak, R.S.J., 1994a. Statistical parametric maps in functional imaging: A general linear approach. Human Brain Mapping 2, 189-210.

Friston, K.J., Jezzard, P., Turner, R., 1994b. Analysis of functional MRI time-series. Human Brain Mapping 1, 153-171.

Friston, K.J., Josephs, O., Zarahn, E., Holmes, A.P., Rouquette, S., Poline, J., 2000. To smooth or not to smooth? Bias and efficiency in fMRI time-series analysis. Neuroimage 12, 196-208.

Friston, K.J., Williams, S., Howard, R., Frackowiak, R.S., Turner, R., 1996. Movement-related effects in fMRI time-series. Magn Reson Med 35, 346-355.

Fujiyoshi, K., Yamada, M., Nakamura, M., Yamane, J., Katoh, H., Kitamura, K., Kawai, K., Okada, S., Momoshima, S., Toyama, Y., Okano, H., 2007. In vivo tracing of neural tracts in the intact and injured spinal cord of marmosets by diffusion tensor tractography. J Neurosci 27, 11991-11998.

Fukuda, M., Rajagopalan, U.M., Homma, R., Matsumoto, M., Nishizaki, M., Tanifuji, M., 2005. Localization of activity-dependent changes in blood volume to submillimeter-scale functional domains in cat visual cortex. Cereb Cortex 15, 823-833.

Gauthier, C., Cohen-Adad, J., Brooks, J., Rossignol, S., Hoge, R.D., 2009. Investigation of venous effects in spinal cord fMRI using hypercapnia. In: 17th Annual Meeting of the International Society for Magnetic Resonance in Medicine (ISMRM), Honolulu, Hawaii, (submitted).

Giove, F., Garreffa, G., Giulietti, G., Mangia, S., Colonnese, C., Maraviglia, B., 2004. Issues about the fMRI of the human spinal cord. Magn Reson Imaging 22, 1505-1516.

Giulietti, G., Giove, F., Garreffa, G., Colonnese, C., Mangia, S., Maraviglia, B., 2008. Characterization of the functional response in the human spinal cord: Impulse-response function and linearity. Neuroimage 42, 626-634.

Gjedde, A., Kuwabara, H., Hakim, A.M., 1990. Reduction of functional capillary density in human brain after stroke. J Cereb Blood Flow Metab 10, 317-326.

Glover, G.H., Li, T.Q., Ress, D., 2000. Image-based method for retrospective correction of physiological motion effects in fMRI: RETROICOR. Magn Reson Med 44, 162-167.

Goense, J.B., Zappe, A.C., Logothetis, N.K., 2007. High-resolution fMRI of macaque V1. Magn Reson Imaging 25, 740-747.

Golabchi, F., Hoge, W., Mamata, H., Maier, S., Brooks, D., 2004. Techniques for automatic spinal cord histology characterization for validation of diffusion tensor imaging. In: 26th International Conference of the IEEE Engineering in Medicine and Biology Society (EMBS), San Francisco, USA, 3, 1640-1643.

Goldstein, B., Little, J.W., Harris, R.M., 1997. Axonal sprouting following incomplete spinal cord injury: an experimental model. J Spinal Cord Med 20, 200-206.

Govers, N., Beghin, J., Van Goethem, J.W., Michiels, J., van den Hauwe, L., Vandervliet, E., Parizel, P.M., 2007. Functional MRI of the cervical spinal cord on 1.5 T with fingertapping: to what extent is it feasible? Neuroradiology 49, 73-81.

Gratton, G., Fabiani, M., Elbert, T., Rockstroh, B., 2003. Seeing right through you: applications of optical imaging to the study of the human brain. Psychophysiology 40, 487-491.

Greenspan, H., Oz, G., Kiryati, N., Peled, S., 2002. MRI inter-slice reconstruction using super-resolution. Magn Reson Imaging 20, 437-446.

Grootoonk, S., Hutton, C., Ashburner, J., Howseman, A.M., Josephs, O., Rees, G., Friston, K.J., Turner, R., 2000. Characterization and correction of interpolation effects in the realignment of fMRI time series. Neuroimage 11, 49-57.

Gudbjartsson, H., Maier, S.E., Mulkern, R.V., Morocz, I.A., Patz, S., Jolesz, F.A., 1996. Line scan diffusion imaging. Magn Reson Med 36, 509-519.

Gulani, V., Iwamoto, G.A., Jiang, H., Shimony, J.S., Webb, A.G., Lauterbur, P.C., 1997. A multiple echo pulse sequence for diffusion tensor imaging and its application in excised rat spinal cords. Magn Reson Med 38, 868-873.

Gulani, V., Webb, A.G., Duncan, I.D., Lauterbur, P.C., 2001. Apparent diffusion tensor measurements in myelin-deficient rat spinal cords. Magn Reson Med 45, 191-195.

Guleria, S., Gupta, R.K., Saksena, S., Chandra, A., Srivastava, R.N., Husain, M., Rathore, R., Narayana, P.A., 2008. Retrograde Wallerian degeneration of cranial corticospinal tracts in cervical spinal cord injury patients using diffusion tensor imaging. J Neurosci Res 86, 2271-2280.

Gullapalli, J., Krejza, J., Schwartz, E.D., 2006. In vivo DTI evaluation of white matter tracts in rat spinal cord. J Magn Reson Imaging 24, 231-234.

Gustafson, K.J., Moffitt, M.A., Wang, X., Sun, J., Snyder, S., Grill, W.M., 2006. Topography of spinal neurons active during hindlimb withdrawal reflexes in the decerebrate cat. Neuroscience 141, 1983-1994.

Hagmann, P., Jonasson, L., Maeder, P., Thiran, J.P., Wedeen, V.J., Meuli, R., 2006. Understanding diffusion MR imaging techniques: from scalar diffusion-weighted imaging to diffusion tensor imaging and beyond. Radiographics 26 Suppl 1, S205-223.

Hammond, K.E., Lupo, J.M., Xu, D., Metcalf, M., Kelley, D.A., Pelletier, D., Chang, S.M., Mukherjee, P., Vigneron, D.B., Nelson, S.J., 2008. Development of a robust method for generating 7.0 T multichannel phase images of the brain with application to normal volunteers and patients with neurological diseases. Neuroimage 39, 1682-1692.

Harel, N.Y., Strittmatter, S.M., 2008. Functional MRI and other non-invasive imaging technologies: providing visual biomarkers for spinal cord structure and function after injury. Exp Neurol 211, 324-328.

Hasan, K.M., Parker, D.L., Alexander, A.L., 2001. Comparison of gradient encoding schemes for diffusion-tensor MRI. J Magn Reson Imaging 13, 769-780.

Heeger, D.J., Ress, D., 2002. What does fMRI tell us about neuronal activity? Nat Rev Neurosci 3, 142-151.

Heidemann, R.M., Ozsarlak, O., Parizel, P.M., Michiels, J., Kiefer, B., Jellus, V., Müller, M., Breuer, F., Blaimer, M., Griswold, M.A., Jakob, P.M., 2003. A brief review of parallel magnetic resonance imaging. Eur Radiol 13, 2323-2337.

Hennig, J., Nauerth, A., Friedburg, H., 1986. RARE imaging: a fast imaging method for clinical MR. Magn Reson Med 3, 823-833.

Henry-Feugeas, M.C., Idy-Peretti, I., Baledent, O., Poncelet-Didon, A., Zannoli, G., Bittoun, J., Schouman-Claeys, E., 2000. Origin of subarachnoid cerebrospinal fluid pulsations: a phase-contrast MR analysis. Magn Reson Imaging 18, 387-395.

Henry-Feugeas, M.C., Idy-Peretti, I., Blanchet, B., Hassine, D., Zannoli, G., Schouman-Claeys, E., 1993. Temporal and spatial assessment of normal cerebrospinal fluid dynamics with MR imaging. Magn Reson Imaging 11, 1107-1118.

Herrera, J.J., Chacko, T., Narayana, P.A., 2008. Histological correlation of diffusion tensor imaging metrics in experimental spinal cord injury. J Neurosci Res 86, 443-447.

Hess, C.P., Mukherjee, P., Han, E.T., Xu, D., Vigneron, D.B., 2006. Q-ball reconstruction of multimodal fiber orientations using the spherical harmonic basis. Magn Reson Med 56, 104-117.

Hoge, R.D., Atkinson, J., Gill, B., Crelier, G.R., Marrett, S., Pike, G.B., 1999a. Investigation of BOLD signal dependence on cerebral blood flow and oxygen consumption: the deoxyhemoglobin dilution model. Magn Reson Med 42, 849-863.

Hoge, R.D., Atkinson, J., Gill, B., Crelier, G.R., Marrett, S., Pike, G.B., 1999b. Linear coupling between cerebral blood flow and oxygen consumption in activated human cortex. Proc Natl Acad Sci U S A 96, 9403-9408.

Hoge, R.D., Atkinson, J., Gill, B., Crelier, G.R., Marrett, S., Pike, G.B., 1999c. Stimulus-dependent BOLD and perfusion dynamics in human V1. Neuroimage 9, 573-585.

Holder, C.A., Muthupillai, R., Mukundan, S., Eastwood, J.D., Hudgins, P.A., 2000. Diffusion-weighted MR imaging of the normal human spinal cord in vivo. AJNR Am J Neuroradiol 21, 1799-1806.

Hosey, T., Williams, G., Ansorge, R., 2005. Inference of multiple fiber orientations in high angular resolution diffusion imaging. Magn Reson Med 54, 1480-1489.

Houghton, I.T., Cronin, M., Redfern, P.A., Utting, J.E., 1973. The analgesic effect of halothane. Br J Anaesth 45, 1105-1110.

Hu, D., Yan, L., Liu, Y., Zhou, Z., Friston, K.J., Tan, C., Wu, D., 2005. Unified SPM-ICA for fMRI analysis. Neuroimage 25, 746-755.

Hu, X., Le, T.H., Parrish, T., Erhard, P., 1995. Retrospective estimation and correction of physiological fluctuation in functional MRI. Magn Reson Med 34, 201-212.

Hudson, L.C., Hamilton, W.P., 1993. Atlas of feline anatomy for veterinarians. Saunders, Philadelphia, Pa.

Huettel, S.A., Song, A.W., McCarthy, G., 2004. Functional Magnetic Resonance Imaging. Sinauer Associates Inc., Sunderland, MA.

Hulvershorn, J., Bloy, L., Gualtieri, E.E., Leigh, J.S., Elliott, M.A., 2005. Spatial sensitivity and temporal response of spin echo and gradient echo bold contrast at 3 T using peak hemodynamic activation time. Neuroimage 24, 216-223.

Huppert, T.J., Hoge, R.D., Diamond, S.G., Franceschini, M.A., Boas, D.A., 2006. A temporal comparison of BOLD, ASL, and NIRS hemodynamic responses to motor stimuli in adult humans. Neuroimage 29, 368-382.

Jankowska, E., 1992. Interneuronal relay in spinal pathways from proprioceptors. Prog Neurobiol 38, 335-378.

Jasanoff, A., 2007. Bloodless FMRI. Trends Neurosci 30, 603-610.

Jasdzewski, G., Strangman, G., Wagner, J., Kwong, K.K., Poldrack, R.A., Boas, D.A., 2003. Differences in the hemodynamic response to event-related motor and visual paradigms as measured by near-infrared spectroscopy. Neuroimage 20, 479-488.

Jenkinson, M., 2003. Fast, automated, N-dimensional phase-unwrapping algorithm. Magn Reson Med 49, 193-197.

Jeong, E.K., Kim, S.E., Guo, J., Kholmovski, E.G., Parker, D.L., 2005. High-resolution DTI with 2D interleaved multislice reduced FOV single-shot diffusion-weighted EPI (2D ss-rFOV-DWEPI). Magn Reson Med 54, 1575-1579.

Jeong, E.K., Kim, S.E., Kholmovski, E.G., Parker, D.L., 2006. High-resolution DTI of a localized volume using 3D single-shot diffusion-weighted STimulated echo-planar imaging (3D ss-DWSTEPI). Magn Reson Med 56, 1173-1181.

Jespersen, S.N., Kroenke, C.D., Ostergaard, L., Ackerman, J.J., Yablonskiy, D.A., 2007. Modeling dendrite density from magnetic resonance diffusion measurements. Neuroimage 34, 1473-1486.

Jian, B., Vemuri, B.C., 2007. A unified computational framework for deconvolution to reconstruct multiple fibers from diffusion weighted MRI. IEEE Trans Med Imaging 26, 1464-1471.

Jiang, W., Drew, T., 1996. Effects of bilateral lesions of the dorsolateral funiculi and dorsal columns at the level of the low thoracic spinal cord on the control of locomotion in the adult cat. I. Treadmill walking. J Neurophysiol 76, 849-866.

Jobsis, F.F., 1977. Noninvasive, infrared monitoring of cerebral and myocardial oxygen sufficiency and circulatory parameters. Science 198, 1264-1267.

Jochimsen, T.H., Norris, D.G., Moller, H.E., 2005. Is there a change in water proton density associated with functional magnetic resonance imaging? Magn Reson Med 53, 470-473.

Johansen-Berg, H., Behrens, T.E., 2006. Just pretty pictures? What diffusion tractography can add in clinical neuroscience. Curr Opin Neurol 19, 379-385.

Jones, D.K., 2004. The effect of gradient sampling schemes on measures derived from diffusion tensor MRI: a Monte Carlo study. Magn Reson Med 51, 807-815.

Jones, D.K., Griffin, L.D., Alexander, D.C., Catani, M., Horsfield, M.A., Howard, R., Williams, S.C., 2002a. Spatial normalization and averaging of diffusion tensor MRI data sets. Neuroimage 17, 592-617.

Jones, D.K., Williams, S.C., Gasston, D., Horsfield, M.A., Simmons, A., Howard, R., 2002b. Isotropic resolution diffusion tensor imaging with whole brain acquisition in a clinically acceptable time. Hum Brain Mapp 15, 216-230.

Jones, R.S., 1979. Injectable anaesthetic agents in the cat: a review. J Small Anim Pract 20, 345-352.

Julien, C., 2006. The enigma of Mayer waves: Facts and models. Cardiovascular Research 70, 12-21.

Kahle, W., Frotscher, M., 2005. Taschenatlas der Anatomie. 3. Nervensystem und Sinnesorgane, 9 ed.

Kannurpatti, S.S., Biswal, B.B., 2004. Effect of anesthesia on CBF, MAP and fMRI-BOLD signal in response to apnea. Brain Res 1011, 141-147.

Karlsborg, M., Rosenbaum, S., Wiegell, M., Simonsen, H., Larsson, H., Werdelin, L., Gredal, O., 2004. Corticospinal tract degeneration and possible pathogenesis in ALS evaluated by MR diffusion tensor imaging. Amyotroph Lateral Scler Other Motor Neuron Disord 5, 136-140.

Kato, H., Izumiyama, M., Koizumi, H., Takahashi, A., Itoyama, Y., 2002. Near-infrared spectroscopic topography as a tool to monitor motor reorganization after hemiparetic stroke: a comparison with functional MRI. Stroke 33, 2032-2036.

Kerschensteiner, M., 2007. Strategies for axonal repair in central nervous system diseases. J Neurol 254 Suppl 1, I29-I32.

Kharbanda, H.S., Alsop, D.C., Anderson, A.W., Filardo, G., Hackney, D.B., 2006. Effects of cord motion on diffusion imaging of the spinal cord. Magn Reson Med 56, 334-339.

Kim, J.H., Budde, M.D., Liang, H.F., Klein, R.S., Russell, J.H., Cross, A.H., Song, S.K., 2006. Detecting axon damage in spinal cord from a mouse model of multiple sclerosis. Neurobiol Dis 21, 626-632.

Kim, J.H., Loy, D.N., Liang, H.F., Trinkaus, K., Schmidt, R.E., Song, S.K., 2007a. Noninvasive diffusion tensor imaging of evolving white matter pathology in a mouse model of acute spinal cord injury. Magn Reson Med 58, 253-260.

Kim, J.H., Trinkaus, K., Ozcan, A., Budde, M.D., Song, S.K., 2007b. Postmortem delay does not change regional diffusion anisotropy characteristics in mouse spinal cord white matter. NMR Biomed 20, 352-359.

Kim, S.-H., Cohen, A.S., 1998. On the Behrens-Fisher Problem: A Review. J Educ Behav Stat 23, 356-377.

Kinoshita, M., Yamada, K., Hashimoto, N., Kato, A., Izumoto, S., Baba, T., Maruno, M., Nishimura, T., Yoshimine, T., 2005. Fiber-tracking does not accurately estimate size of fiber bundle in pathological condition: initial neurosurgical experience using neuronavigation and subcortical white matter stimulation. Neuroimage 25, 424-429.

Kinoshita, Y., Ohnishi, A., Kohshi, K., Yokota, A., 1999. Apparent diffusion coefficient on rat brain and nerves intoxicated with methylmercury. Environ Res 80, 348-354.

Klapka, N., Hermanns, S., Straten, G., Masanneck, C., Duis, S., Hamers, F.P., Muller, D., Zuschratter, W., Muller, H.W., 2005. Suppression of fibrous scarring in spinal cord injury of rat promotes long-distance regeneration of corticospinal tract axons, rescue of primary motoneurons in somatosensory cortex and significant functional recovery. Eur J Neurosci 22, 3047-3058.

Kollias, S.S., Kwiecinski, S., Summers, P., 2004. Functional MR Imaging of the Human Cervical Spinal Cord. In: Proceedings of the American Society of Neuroradiology, 227.

Komisaruk, B.R., Mosier, K.M., Liu, W.C., Criminale, C., Zaborszky, L., Whipple, B., Kalnin, A., 2002. Functional localization of brainstem and cervical spinal cord nuclei in humans with fMRI. AJNR Am J Neuroradiol 23, 609-617.

Kornelsen, J., Mackey, S., 2007. Potential clinical applications for spinal functional MRI. Curr Pain Headache Rep 11, 165-170.

Kornelsen, J., Stroman, P.W., 2004. fMRI of the lumbar spinal cord during a lower limb motor task. Magn Reson Med 52, 411-414.

Kornelsen, J., Stroman, P.W., 2007. Detection of the neuronal activity occurring caudal to the site of spinal cord injury that is elicited during lower limb movement tasks. Spinal Cord 45, 485-490.

Kozlowski, P., Liu, J., Yung, A.C., Tetzlaff, W., 2008. High-resolution myelin water measurements in rat spinal cord. Magn Reson Med 59, 796-802.

Krueger, G., Glover, G.H., 2001. Physiological noise in oxygenation-sensitive magnetic resonance imaging. Magn Reson Med 46, 631-637.

Krzyzak, A.T., Jasinski, A., Weglarz, W.P., Adamek, D., Sagnowskil, P., Baj, M., 2005. Visualisation of the extent of damage in a rat spinal cord injury model using MR microsopy of the water diffusion tensor. Acta Neurobiol Exp (Wars) 65, 255-264.

Kubicki, M., Maier, S.E., Westin, C.F., Mamata, H., Ersner-Hershfield, H., Estepar, R., Kikinis, R., Jolesz, F.A., McCarley, R.W., Shenton, M.E., 2004. Comparison of single-shot echo-planar and line scan protocols for diffusion tensor imaging. Acad Radiol 11, 224-232.

Kwong, K.K., Belliveau, J.W., Chesler, D.A., Goldberg, I.E., Weisskoff, R.M., Poncelet, B.P., Kennedy, D.N., Hoppel, B.E., Cohen, M.S., Turner, R., et al., 1992. Dynamic magnetic resonance imaging of human brain activity during primary sensory stimulation. Proc Natl Acad Sci U S A 89, 5675-5679.

Kybic, J., Thevenaz, P., Nirkko, A., Unser, M., 2000. Unwarping of unidirectionally distorted EPI images. IEEE Trans Med Imaging 19, 80-93.

Lammertse, D., Dungan, D., Dreisbach, J., Falci, S., Flanders, A., Marino, R., Schwartz, E., 2007. Neuroimaging in traumatic spinal cord injury: an evidence-based review for clinical practice and research. J Spinal Cord Med 30, 205-214.

Landman, B.A., Farrell, J.A., Jones, C.K., Smith, S.A., Prince, J.L., Mori, S., 2007. Effects of diffusion weighting schemes on the reproducibility of DTI-derived fractional anisotropy, mean diffusivity, and principal eigenvector measurements at 1.5T. Neuroimage 36, 1123-1138.

Lange, N., Strother, S.C., Anderson, J.R., Nielsen, F.A., Holmes, A.P., Kolenda, T., Savoy, R., Hansen, L.K., 1999. Plurality and resemblance in fMRI data analysis. Neuroimage 10, 282-303.

Lawrence, J., Stroman, P.W., Bascaramurty, S., Jordan, L.M., Malisza, K.L., 2004. Correlation of functional activation in the rat spinal cord with neuronal activation detected by immunohistochemistry. Neuroimage 22, 1802-1807.

Lawrence, J., Stroman, P.W., Malisza, K.L., 2007. Comparison of functional activity in the rat cervical spinal cord during alpha-chloralose and halothane anesthesia. Neuroimage 34, 1665-1672.

Lawrence, J., Stroman, P.W., Malisza, K.L., 2008a. Functional MRI of the cervical spinal cord during noxious and innocuous thermal stimulation in the alpha-chloralose- and halothane-anesthetized rat. Magn Reson Imaging 26, 1-10.

Lawrence, J.M., Stroman, P.W., Kollias, S.S., 2008b. Functional magnetic resonance imaging of the human spinal cord during vibration stimulation of different dermatomes. Neuroradiology 50, 273-280.

Lazar, M., Alexander, A.L., 2003. An error analysis of white matter tractography methods: synthetic diffusion tensor field simulations. Neuroimage 20, 1140-1153.

Lazar, N.A., Luna, B., Sweeney, J.A., Eddy, W.F., 2002. Combining brains: a survey of methods for statistical pooling of information. Neuroimage 16, 538-550.

Le Bihan, D., Breton, E., Lallemand, D., Grenier, P., Cabanis, E., Laval-Jeantet, M., 1986. MR imaging of intravoxel incoherent motions: application to diffusion and perfusion in neurologic disorders. Radiology 161, 401-407.

Le Bihan, D., Mangin, J.F., Poupon, C., Clark, C.A., Pappata, S., Molko, N., Chabriat, H., 2001. Diffusion tensor imaging: concepts and applications. J Magn Reson Imaging 13, 534-546.

Le Bihan, D., Urayama, S., Aso, T., Hanakawa, T., Fukuyama, H., 2006. Direct and fast detection of neuronal activation in the human brain with diffusion MRI. Proc Natl Acad Sci U S A 103, 8263-8268.

Le Roux, P., 2002. Non-CPMG Fast Spin Echo with full signal. J Magn Reson 155, 278-292.

Lee, J.W., Kim, J.H., Kang, H.S., Lee, J.S., Choi, J.Y., Yeom, J.S., Kim, H.J., Chung, H.W., 2006. Optimization of acquisition parameters of diffusion-tensor magnetic resonance imaging in the spinal cord. Invest Radiol 41, 553-559.

Li, G., Ng, M.C., Wong, K.K., Luk, K.D., Yang, E.S., 2005. Spinal effects of acupuncture stimulation assessed by proton density-weighted functional magnetic resonance imaging at 0.2 T. Magn Reson Imaging 23, 995-999.

Liao, R., Krolik, J.L., McKeown, M.J., 2005. An information-theoretic criterion for intrasubject alignment of FMRI time series: motion corrected independent component analysis. IEEE Trans Med Imaging 24, 29-44.

Lilja, J., Endo, T., Hofstetter, C., Westman, E., Young, J., Olson, L., Spenger, C., 2006. Blood oxygenation level-dependent visualization of synaptic relay stations of sensory pathways along the neuroaxis in response to graded sensory stimulation of a limb. J Neurosci 26, 6330-6336.

Lin, C.P., Wedeen, V.J., Chen, J.H., Yao, C., Tseng, W.Y., 2003. Validation of diffusion spectrum magnetic resonance imaging with manganese-enhanced rat optic tracts and ex vivo phantoms. Neuroimage 19, 482-495.

Lindberg, P.G., Skejo, P.H., Rounis, E., Nagy, Z., Schmitz, C., Wernegren, H., Bring, A., Engardt, M., Forssberg, H., Borg, J., 2007. Wallerian degeneration of the corticofugal tracts in chronic stroke: a pilot study relating diffusion tensor imaging, transcranial magnetic stimulation, and hand function. Neurorehabil Neural Repair 21, 551-560.

Liu, J.Z., Brown, R.W., Yue, G.H., 2002. A dynamical model of muscle activation, fatigue, and recovery. Biophys J 82, 2344-2359.

Liu, Z.M., Schmidt, K.F., Sicard, K.M., Duong, T.Q., 2004. Imaging oxygen consumption in forepaw somatosensory stimulation in rats under isoflurane anesthesia. Magn Reson Med 52, 277-285.

Logothetis, N.K., 2002. The neural basis of the blood-oxygen-level-dependent functional magnetic resonance imaging signal. Philos Trans R Soc Lond B Biol Sci 357, 1003-1037.

Logothetis, N.K., Pauls, J., Augath, M., Trinath, T., Oeltermann, A., 2001. Neurophysiological investigation of the basis of the fMRI signal. Nature 412, 150-157.

Loy, D.N., Kim, J.H., Xie, M., Schmidt, R.E., Trinkaus, K., Song, S.K., 2007. Diffusion tensor imaging predicts hyperacute spinal cord injury severity. J Neurotrauma 24, 979-990.

Lu, K., Jr, Ghorbel, F.H., Ware, D.L., Zwischenberger, J.B., Bidani, A., 2003. Whole-Body Gas Exchange in Human Predicted by a Cardiopulmonary Model. Cardiovascular Engineering V3, 1-19.

Lu, Y., Aldroubi, A., Gore, J.C., Anderson, A.W., Ding, Z., 2006. Improved fiber tractography with Bayesian tensor regularization. Neuroimage 31, 1061-1074.

Lund, T., Madsen, K., Sidaros, K., Luo, W.-L., Nichols, T., 2006. Non-white noise in fMRI: Does modelling have an impact? Neuroimage 29, 54-66.

Lundell, H., Cohen-Adad, J., 2009. Point spread function mapping for distortion correction of spinal cord diffusion weighted MRI. In: 17th Annual Meeting of the International Society for Magnetic Resonance in Medicine (ISMRM), Honolulu, Hawaii.

Mac Donald, C.L., Dikranian, K., Bayly, P., Holtzman, D., Brody, D., 2007. Diffusion tensor imaging reliably detects experimental traumatic axonal injury and indicates approximate time of injury. J Neurosci 27, 11869-11876.

Mackey, S., Ludlow, D., Knierim, K., Hanelin, J., Glover, G., 2003. FMRI Activation in the Human Cervical Spinal Cord to Noxious Thermal Stimulation. In: Proceedings of the American Pain Society, 750.

Madi, S., Flanders, A.E., Vinitski, S., Herbison, G.J., Nissanov, J., 2001. Functional MR imaging of the human cervical spinal cord. AJNR Am J Neuroradiol 22, 1768-1774.

Madi, S., Hasan, K.M., Narayana, P.A., 2005. Diffusion tensor imaging of in vivo and excised rat spinal cord at 7 T with an icosahedral encoding scheme. Magn Reson Med 53, 118-125.

Maes, F., Vandermeulen, D., Suetens, P., 1999. Comparative evaluation of multiresolution optimization strategies for multimodality image registration by maximization of mutual information. Med Image Anal 3, 373-386.

Maier, S.E., 2007. Examination of spinal cord tissue architecture with magnetic resonance diffusion tensor imaging. Neurotherapeutics 4, 453-459.

Maier, S.E., Mamata, H., 2005. Diffusion tensor imaging of the spinal cord. Ann N Y Acad Sci 1064, 50-60.

Maieron, M., Bodurka, J., Birn, R., Porro, C.A., Bandettini, P., 2007a. Breath-hold-induced MRI signal changes in the spinal cord imply BOLD contrast. In: 13th Annual Meeting of the Organization for Human Brain Mapping (HBM), Chicago, USA, S91.

Maieron, M., Iannetti, G.D., Bodurka, J., Tracey, I., Bandettini, P.A., Porro, C.A., 2007b. Functional responses in the human spinal cord during willed motor actions: evidence for side- and rate-dependent activity. J Neurosci 27, 4182-4190.

Majcher, K., Tomanek, B., Jasinski, A., Foniok, T., Stroman, P.W., Tuor, U.I., Kirk, D., Hess, G., 2006. Simultaneous functional magnetic resonance imaging in the rat spinal cord and brain. Exp Neurol 197, 458-464.

Majcher, K., Tomanek, B., Tuor, U.I., Jasinski, A., Foniok, T., Rushforth, D., Hess, G., 2007. Functional magnetic resonance imaging within the rat spinal cord following peripheral nerve injury. Neuroimage 38, 669-676.

Malisza, K.L., Stroman, P.W., 2002. Functional imaging of the rat cervical spinal cord. J Magn Reson Imaging 16, 553-558.

Malonek, D., Dirnagl, U., Lindauer, U., Yamada, K., Kanno, I., Grinvald, A., 1997. Vascular imprints of neuronal activity: relationships between the dynamics of cortical blood flow, oxygenation, and volume changes following sensory stimulation. Proc Natl Acad Sci U S A 94, 14826-14831.

Malonek, D., Grinvald, A., 1996. Interactions between electrical activity and cortical microcirculation revealed by imaging spectroscopy: implications for functional brain mapping. Science 272, 551-554.

Mamata, H., De Girolami, U., Hoge, W.S., Jolesz, F.A., Maier, S.E., 2006. Collateral nerve fibers in human spinal cord: visualization with magnetic resonance diffusion tensor imaging. Neuroimage 31, 24-30.

Mandeville, J.B., Marota, J.J., 1999. Vascular filters of functional MRI: spatial localization using BOLD and CBV contrast. Magn Reson Med 42, 591-598.

Mangin, J.F., Poupon, C., Clark, C., Le Bihan, D., Bloch, I., 2002. Distortion correction and robust tensor estimation for MR diffusion imaging. Med Image Anal 6, 191-198.

Mao, J., Price, D.D., Coghill, R.C., Mayer, D.J., Hayes, R.L., 1992. Spatial patterns of spinal cord [14C]-2-deoxyglucose metabolic activity in a rat model of painful peripheral mononeuropathy. Pain 50, 89-100.

Marcus, M.L., Heistad, D.D., Ehrhardt, J.C., Abboud, F.M., 1977. Regulation of total and regional spinal cord blood flow. Circ Res 41, 128-134.

Marrelec, G., Benali, H., Ciuciu, P., Pélégrini-Issac, M., Poline, J.B., 2003. Robust Bayesian estimation of the hemodynamic response function in event-related BOLD fMRI using basic physiological information. Hum Brain Mapp 19, 1-17.

Marrelec, G., Ciuciu, P., Pélégrini-Issac, M., Benali, H., 2004. Estimation of the hemodynamic response in event-related functional MRI: Bayesian networks as a framework for efficient Bayesian modeling and inference. IEEE Trans Med Imaging 23, 959-967.

Martin, C., Martindale, J., Berwick, J., Mayhew, J., 2006. Investigating neural-hemodynamic coupling and the hemodynamic response function in the awake rat. Neuroimage 32, 33-48.

Mattiello, J., Basser, P.J., Le Bihan, D., 1997. The b matrix in diffusion tensor echo-planar imaging. Magn Reson Med 37, 292-300.

Mayer, S., 1876. Studies about the physiology of heart and blood vessels [Studien zur Physiologie des Herzens und der Blutgefässe]. Sitzungsbericht der mathematisch-naturwissenschaftlichen Classe 74, 281-307.

McDonald, J.W., Belegu, V., 2006. Demyelination and remyelination after spinal cord injury. J Neurotrauma 23, 345-359.

McKeown, M.J., Makeig, S., Brown, G.G., Jung, T.P., Kindermann, S.S., Bell, A.J., Sejnowski, T.J., 1998. Analysis of fMRI data by blind separation into independent spatial components. Hum Brain Mapp 6, 160-188.

Melhem, E.R., Itoh, R., Jones, L., Barker, P.B., 2000. Diffusion tensor MR imaging of the brain: effect of diffusion weighting on trace and anisotropy measurements. AJNR Am J Neuroradiol 21, 1813-1820.

Menon, R.S., 2002. Postacquisition suppression of large-vessel BOLD signals in high-resolution fMRI. Magn Reson Med 47, 1-9.

Meyer, F.G., 2003. Wavelet-based estimation of a semiparametric generalized linear model of fMRI time-series. IEEE Trans Med Imaging 22, 315-322.

Miezin, F.M., Maccotta, L., Ollinger, J.M., Petersen, S.E., Buckner, R.L., 2000. Characterizing the hemodynamic response: effects of presentation rate, sampling procedure, and the possibility of ordering brain activity based on relative timing. Neuroimage 11, 735-759.

Miner, J.R., Burton, J.H., 2007. Clinical practice advisory: Emergency department procedural sedation with propofol. Ann Emerg Med 50, 182-187, 187 e181.

Moffitt, M.A., Dale, B.M., Duerk, J.L., Grill, W.M., 2005. Functional magnetic resonance imaging of the human lumbar spinal cord. J Magn Reson Imaging 21, 527-535.

Moller, M., Frandsen, J., Andersen, G., Gjedde, A., Vestergaard-Poulsen, P., Ostergaard, L., 2007. Dynamic changes in corticospinal tracts after stroke detected by fibretracking. J Neurol Neurosurg Psychiatry 78, 587-592.

Morgan, V.L., Pickens, D.R., Hartmann, S.L., Price, R.R., 2001. Comparison of functional MRI image realignment tools using a computer-generated phantom. Magn Reson Med 46, 510-514.

Mori, S., Zhang, J., 2006. Principles of diffusion tensor imaging and its applications to basic neuroscience research. Neuron 51, 527-539.

Mukherjee, P., Hess, C.P., Xu, D., Han, E.T., Kelley, D.A., Vigneron, D.B., 2008. Development and initial evaluation of 7-T q-ball imaging of the human brain. Magn Reson Imaging 26, 171-180.

Mukkamala, R., Cohen, R.J., 2001. A forward model-based validation of cardiovascular system identification. Am J Physiol Heart Circ Physiol 281.

Murphy, B.P., Zientara, G.P., Huppi, P.S., Maier, S.E., Barnes, P.D., Jolesz, F.A., Volpe, J.J., 2001. Line scan diffusion tensor MRI of the cervical spinal cord in preterm infants. J Magn Reson Imaging 13, 949-953.

Nair, D.G., 2005. About being BOLD. Brain Res Brain Res Rev 50, 229-243.

Nair, G., Tanahashi, Y., Low, H.P., Billings-Gagliardi, S., Schwartz, W.J., Duong, T.Q., 2005. Myelination and long diffusion times alter diffusion-tensor-imaging contrast in myelin-deficient shiverer mice. Neuroimage 28, 165-174.

Namiki, A., Collins, J.G., Kitahata, L.M., Kikuchi, H., Homma, E., Thalhammer, J.G., 1980. Effects of halothane on spinal neuronal responses to graded noxious heat stimulation in the cat. Anesthesiology 53, 475-480.

Narayana, P., Abbe, R., Liu, S.J., Johnston, D., 1999a. Does loss of gray- and white-matter contrast in injured spinal cord signify secondary injury? In vivo longitudinal MRI studies. Magn Reson Med 41, 315-320.

Narayana, P., Fenyes, D., Zacharopoulos, N., 1999b. In vivo relaxation times of gray matter and white matter in spinal cord. Magn Reson Imaging 17, 623-626.

Narayana, P.A., Grill, R.J., Chacko, T., Vang, R., 2004. Endogenous recovery of injured spinal cord: longitudinal in vivo magnetic resonance imaging. J Neurosci Res 78, 749-759.

Neema, M., Stankiewicz, J., Arora, A., Guss, Z.D., Bakshi, R., 2007. MRI in Multiple Sclerosis: What's Inside the Toolbox? Neurotherapeutics 4, 602-617.

Nencka, A.S., Rowe, D.B., 2007. Reducing the unwanted draining vein BOLD contribution in fMRI with statistical post-processing methods. Neuroimage 37, 177-188.

Nevo, U., Hauben, E., Yoles, E., Agranov, E., Akselrod, S., Schwartz, M., Neeman, M., 2001. Diffusion anisotropy MRI for quantitative assessment of recovery in injured rat spinal cord. Magn Reson Med 45, 1-9.

Ng, M.C., Wong, K.K., Li, G., Lai, S., Yang, E.S., Hu, Y., Luk, K.D., 2006. Proton-density-weighted spinal fMRI with sensorimotor stimulation at 0.2 T. Neuroimage 29, 995-999.

Ng, M.C., Wu, E.X., Lau, H.F., Hu, Y., Lam, E.Y., Luk, K.D., 2008. Cervical spinal cord BOLD fMRI study: modulation of functional activation by dexterity of dominant and non-dominant hands. Neuroimage 39, 825-831.

Ni, H., Kavcic, V., Zhu, T., Ekholm, S., Zhong, J., 2006. Effects of number of diffusion gradient directions on derived diffusion tensor imaging indices in human brain. AJNR Am J Neuroradiol 27, 1776-1781.

Nicoll, R.A., Madison, D.V., 1982. General anesthetics hyperpolarize neurons in the vertebrate central nervous system. Science 217, 1055-1057.

Nix, W., Capra, N.F., Erdmann, W., Halsey, J.H., 1976. Comparison of vascular reactivity in spinal cord and brain. Stroke 7, 560-563.

Noebauer-Huhmann, I.M., Glaser, C., Dietrich, O., Wallner, C.P., Klinger, W., Imhof, H., Schoenberg, S.O., 2006. MR imaging of the cervical spine: assessment of image quality with parallel imaging compared to non-accelerated MR measurements. Eur Radiol.

Nunes, R.G., Jezzard, P., Behrens, T.E., Clare, S., 2005. Self-navigated multishot echo-planar pulse sequence for high-resolution diffusion-weighted imaging. Magn Reson Med 53, 1474-1478.

O'connell, J.E.A., 1943. The vascular factor in intracranial pressure and the maintenance of the cerebrospinal fluid circulation. Brain 66, 204-228.

Oakes, T.R., Johnstone, T., Ores Walsh, K.S., Greischar, L.L., Alexander, A.L., Fox, A.S., Davidson, R.J., 2005. Comparison of fMRI motion correction software tools. Neuroimage 28, 529-543.

Ogawa, S., Lee, T.M., Kay, A.R., Tank, D.W., 1990. Brain magnetic resonance imaging with contrast dependent on blood oxygenation. Proc Natl Acad Sci U S A 87, 9868-9872.

Ogawa, S., Menon, R.S., Kim, S.G., Ugurbil, K., 1998. On the characteristics of functional magnetic resonance imaging of the brain. Annu Rev Biophys Biomol Struct 27, 447-474.

Ohgiya, Y., Oka, M., Hiwatashi, A., Liu, X., Kakimoto, N., Westesson, P.L., Ekholm, S.E., 2007a. Diffusion tensor MR imaging of the cervical spinal cord in patients with multiple sclerosis. Eur Radiol 17, 2499-2504.

Ohgiya, Y., Oka, M., Hiwatashi, A., Liu, X., Kakimoto, N., Westesson, P.L., Ekholm, S.E., 2007b. Diffusion tensor MR imaging of the cervical spinal cord in patients with multiple sclerosis. Eur Radiol.

Ong, H.H., Wright, A.C., Wehrli, S.L., Souza, A., Schwartz, E.D., Hwang, S.N., Wehrli, F.W., 2008. Indirect measurement of regional axon diameter in excised mouse spinal cord with q-space imaging: simulation and experimental studies. Neuroimage 40, 1619-1632.

Ono, J., Harada, K., Takahashi, M., Maeda, M., Ikenaka, K., Sakurai, K., Sakai, N., Kagawa, T., Fritz-Zieroth, B., Nagai, T., et al., 1995. Differentiation between dysmyelination and demyelination using magnetic resonance diffusional anisotropy. Brain Res 671, 141-148.

Oouchi, H., Yamada, K., Sakai, K., Kizu, O., Kubota, T., Ito, H., Nishimura, T., 2007. Diffusion anisotropy measurement of brain white matter is affected by voxel size: underestimation occurs in areas with crossing fibers. AJNR Am J Neuroradiol 28, 1102-1106.

Oppenheim, C., Ducreux, D., Rodrigo, S., Hodel, J., Tourdias, T., Charbonneau, F., Pierrefitte, S., Meder, J., 2007. [Diffusion tensor imaging and tractography of the brain and spinal cord]. J Radiol 88, 510-520.

Ozanne, A., Krings, T., Facon, D., Fillard, P., Dumas, J.L., Alvarez, H., Ducreux, D., Lasjaunias, P., 2007. MR diffusion tensor imaging and fiber tracking in spinal cord arteriovenous malformations: a preliminary study. AJNR Am J Neuroradiol 28, 1271-1279.

Pagani, E., Bammer, R., Horsfield, M.A., Rovaris, M., Gass, A., Ciccarelli, O., Filippi, M., 2007. Diffusion MR imaging in multiple sclerosis: technical aspects and challenges. AJNR Am J Neuroradiol 28, 411-420.

Pagani, M., Montano, N., Porta, A., Malliani, A., Abboud, F.M., Birkett, C., Somers, V.K., 1997. Relationship between spectral components of cardiovascular variabilities and direct measures of muscle sympathetic nerve activity in humans. Circulation 95, 1441-1448.

Papadakis, N.G., Xing, D., Huang, C.L., Hall, L.D., Carpenter, T.A., 1999. A comparative study of acquisition schemes for diffusion tensor imaging using MRI. J Magn Reson 137, 67-82.

Park, E., Velumian, A.A., Fehlings, M.G., 2004. The role of excitotoxicity in secondary mechanisms of spinal cord injury: a review with an emphasis on the implications for white matter degeneration. J Neurotrauma 21, 754-774.

Parkes, L.M., Schwarzbach, J.V., Bouts, A.A., Deckers, R.H., Pullens, P., Kerskens, C.M., Norris, D.G., 2005. Quantifying the spatial resolution of the gradient echo and spin echo BOLD response at 3 Tesla. Magn Reson Med 54, 1465-1472.

Parrish, T.B., Gitelman, D.R., LaBar, K.S., Mesulam, M.M., 2000. Impact of signal-to-noise on functional MRI. Magn Reson Med 44, 925-932.

Pattany, P.M., Puckett, W.R., Klose, K.J., Quencer, R.M., Bunge, R.P., Kasuboski, L., Weaver, R.G., 1997. High-resolution diffusion-weighted MR of fresh and fixed cat spinal cords: evaluation of diffusion coefficients and anisotropy. AJNR Am J Neuroradiol 18, 1049-1056.

Pattinson, K.T., Rogers, R., Mayhew, S.D., Tracey, I., Wise, R.G., 2007. Pharmacological FMRI: measuring opioid effects on the BOLD response to hypercapnia. J Cereb Blood Flow Metab 27, 414-423.

Pearson, K.G., Rossignol, S., 1991. Fictive motor patterns in chronic spinal cats. J Neurophysiol 66, 1874-1887.

Peled, S., Yeshurun, Y., 2001. Superresolution in MRI: application to human white matter fiber tract visualization by diffusion tensor imaging. Magn Reson Med 45, 29-35.

Peles, S., Miranda, A., Shaker, R., Sengupta, J.N., 2004. Acute nociceptive somatic stimulus sensitizes neurones in the spinal cord to colonic distension in the rat. J Physiol 560, 291-302.

Peng, H., Arfanakis, K., 2007. Diffusion tensor encoding schemes optimized for white matter fibers with selected orientations. Magn Reson Imaging 25, 147-153.

Perlbarg, V., Bellec, P., Anton, J.L., Pelegrini-Issac, M., Doyon, J., Benali, H., 2007. CORSICA: correction of structured noise in fMRI by automatic identification of ICA components. Magn Reson Imaging 25, 35-46.

Perrin, M., Poupon, C., Rieul, B., Leroux, P., Constantinesco, A., Mangin, J.F., Lebihan, D., 2005. Validation of q-ball imaging with a diffusion fibre-crossing phantom on a clinical scanner. Philos Trans R Soc Lond B Biol Sci 360, 881-891.

Pfefferbaum, A., Sullivan, E.V., Adalsteinsson, E., Garrick, T., Harper, C., 2004. Postmortem MR imaging of formalin-fixed human brain. Neuroimage 21, 1585-1595.

Piché, M., Cohen-Adad, J., Kosh Nejad, M., Perlbarg, V., Xie, G., Beaudoin, G., Benali, H., Rainville, P., 2008. Characterization of cardiac-related noise in fMRI of the cervical spinal cord. Magn Reson Imaging (in press).

Pierpaoli, C., Basser, P.J., 1996. Toward a quantitative assessment of diffusion anisotropy. Magn Reson Med 36, 893-906.

Pipe, J.G., 1999. Motion correction with PROPELLER MRI: application to head motion and free-breathing cardiac imaging. Magn Reson Med 42, 963-969.

Pipe, J.G., Zwart, N., 2006. Turboprop: improved PROPELLER imaging. Magn Reson Med 55, 380-385.

Plank, C., Koller, A., Mueller-Mang, C., Bammer, R., Thurnher, M.M., 2007. Diffusion-weighted MR imaging (DWI) in the evaluation of epidural spinal lesions. Neuroradiology 49, 977-985.

Porro, C.A., Cavazzuti, M., Galetti, A., Sassatelli, L., Barbieri, G.C., 1991. Functional activity mapping of the rat spinal cord during formalin-induced noxious stimulation. Neuroscience 41, 655-665.

Porszasz, R., Beckmann, N., Bruttel, K., Urban, L., Rudin, M., 1997. Signal changes in the spinal cord of the rat after injection of formalin into the hindpaw: characterization using functional magnetic resonance imaging. Proc Natl Acad Sci U S A 94, 5034-5039.

Poser, B.A., Norris, D.G., 2007. Fast spin echo sequences for BOLD functional MRI. Magma 20, 11-17.

Posse, S., Wiese, S., Gembris, D., Mathiak, K., Kessler, C., Grosse-Ruyken, M.L., Elghahwagi, B., Richards, T., Dager, S.R., Kiselev, V.G., 1999. Enhancement of BOLD-contrast sensitivity by single-shot multi-echo functional MR imaging. Magn Reson Med 42, 87-97.

Poupon, C., Poupon, F., Roche, A., Cointepas, Y., Dubois, J., Mangin, J.F., 2007. Real-time MR diffusion tensor and Q-ball imaging using Kalman filtering. Conf Med Image Comput Comput Assist Interv 10, 27-35.

Poustchi-Amin, M., Mirowitz, S.A., Brown, J.J., McKinstry, R.C., Li, T., 2001. Principles and applications of echo-planar imaging: a review for the general radiologist. Radiographics 21, 767-779.

Praamstra, P., Kourtis, D., Kwok, H.F., Oostenveld, R., 2006. Neurophysiology of implicit timing in serial choice reaction-time performance. J Neurosci 26, 5448-5455.

Preiss, G., Polosa, C., 1974. Patterns of sympathetic neuron activity associated with Mayer waves. Am J Physiol 226, 724-730.

Prince, S., Kolehmainen, V., Kaipio, J.P., Franceschini, M.A., Boas, D., Arridge, S.R., 2003. Time-series estimation of biological factors in optical diffusion tomography. Phys Med Biol 48, 1491-1504.

Pruessmann, K.P., Weiger, M., Scheidegger, M.B., Boesiger, P., 1999. SENSE: sensitivity encoding for fast MRI. Magn Reson Med 42, 952-962.

Purcell, E.M., Pound, R.V., Bloembergen, N., 1946. Nuclear Magnetic Resonance Absorption in Hydrogen Gas. Physical Review 70, 986-987.

Pypendop, B.H., Ilkiw, J.E., Imai, A., Bolich, J.A., 2003. Hemodynamic effects of nitrous oxide in isoflurane-anesthetized cats. Am J Vet Res 64, 273-278.

Raichle, M.E., 2001. Cognitive neuroscience. Bold insights. Nature 412, 128-130.

Raj, D., Anderson, A.W., Gore, J.C., 2001. Respiratory effects in human functional magnetic resonance imaging due to bulk susceptibility changes. Phys Med Biol 46, 3331-3340.

Ramu, J., Herrera, J., Grill, R., Bockhorst, T., Narayana, P., 2008. Brain fiber tract plasticity in experimental spinal cord injury: diffusion tensor imaging. Exp Neurol 212, 100-107.

Raya, J.G., Dietrich, O., Reiser, M.F., Baur-Melnyk, A., 2005. Techniques for diffusion-weighted imaging of bone marrow. Eur J Radiol 55, 64-73.

Reese, T.G., Heid, O., Weisskoff, R.M., Wedeen, V.J., 2003. Reduction of eddy-current-induced distortion in diffusion MRI using a twice-refocused spin echo. Magn Reson Med 49, 177-182.

Reinsberg, S.A., Doran, S.J., Charles-Edwards, E.M., Leach, M.O., 2005. A complete distortion correction for MR images: II. Rectification of static-field inhomogeneities by similarity-based profile mapping. Phys Med Biol 50, 2651-2661.

Richardson, C.A., Flecknell, P.A., 2005. Anaesthesia and post-operative analgesia following experimental surgery in laboratory rodents: are we making progress? Altern Lab Anim 33, 119-127.

Ries, M., Jones, R.A., Dousset, V., Moonen, C.T., 2000. Diffusion tensor MRI of the spinal cord. Magn Reson Med 44, 884-892.

Roberts, K.C., Tran, T.T., Song, A.W., Woldorff, M.G., 2007. Component structure of event-related fMRI responses in the different neurovascular compartments. Magn Reson Imaging 25, 328-334.

Robertson, R.L., Maier, S.E., Mulkern, R.V., Vajapayam, S., Robson, C.D., Barnes, P.D., 2000. MR line-scan diffusion imaging of the spinal cord in children. AJNR Am J Neuroradiol 21, 1344-1348.

Robertson, S.A., Taylor, P.M., 2004. Pain management in cats--past, present and future. Part 2. Treatment of pain--clinical pharmacology. J Feline Med Surg 6, 321-333.

Robson, M.D., Gore, J.C., Constable, R.T., 1997. Measurement of the point spread function in MRI using constant time imaging. Magn Reson Med 38, 733-740.

Roemer, P.B., Edelstein, W.A., Hayes, C.E., Souza, S.P., Mueller, O.M., 1990. The NMR phased array. Magn Reson Med 16, 192-225.

Rogers, R., Wise, R.G., Painter, D.J., Longe, S.E., Tracey, I., 2004. An investigation to dissociate the analgesic and anesthetic properties of ketamine using functional magnetic resonance imaging. Anesthesiology 100, 292-301.

Ronen, I., Ugurbil, K., Kim, D.S., 2005. How does DWI correlate with white matter structures? Magn Reson Med 54, 317-323.

Rossignol, S., 2006a. Plasticity of connections underlying locomotor recovery after central and/or peripheral lesions in the adult mammals. Philos Trans R Soc Lond B Biol Sci 361, 1647-1671.

Rossignol, S., 2006b. Plasticity of connections underlying locomotor recovery after central and/or peripheral lesions in the adult mammals. Philos Trans R Soc Lond B Biol Sci 361, 1647-1671.

Rossignol, S., Chau, C., Brustein, E., Giroux, N., Bouyer, L., Barbeau, H., Reader, T.A., 1998. Pharmacological activation and modulation of the central pattern generator for locomotion in the cat. Ann N Y Acad Sci 860, 346-359.

Rossignol, S., Schwab, M., Schwartz, M., Fehlings, M.G., 2007. Spinal cord injury: time to move? J Neurosci 27, 11782-11792.

Roth, Y., Ocherashvilli, A., Daniels, D., Ruiz-Cabello, J., Maier, S.E., Orenstein, A., Mardor, Y., 2008. Quantification of water compartmentation in cell suspensions by diffusion-weighted and T(2)-weighted MRI. Magn Reson Imaging 26, 88-102.

Rousseeuw, J., Croux, C., 1993. Alternatives to the median absolute deviation. J Am Stat Assoc 88, 1273-1283.

Saritas, E., Lee, J., Cunningham, C., Nishimura, D., Han, E., 2008. High-Resolution Axial DWI of the Spinal Cord with Reduced-FOV Single-Shot EPI. In: 16th Annual Meeting of the International Society for Magnetic Resonance in Medicine (ISMRM), Toronto, Canada, 760.

Sarlls, J., Pierpaoli, C., 2008a. High-resolution Diffusion Tensor Imaging at 3T with Radial-FSE. In: 16th Annual Meeting of the International Society for Magnetic Resonance in Medicine (ISMRM), Toronto, Canada, 758.

Sarlls, J.E., Newbould, R.D., Altbach, M.I., Gmitro, A.F., Seeger, J., Trouard, T.P., 2005. Isotropic diffusion weighting in radial fast spin-echo magnetic resonance imaging. Magn Reson Med 53, 1347-1354.

Sarlls, J.E., Pierpaoli, C., 2008b. Diffusion-weighted radial fast spin-echo for high-resolution diffusion tensor imaging at 3T. Magn Reson Med 60, 270-276.

Sasaki, S., Yazawa, I., Miyakawa, N., Mochida, H., Shinomiya, K., Kamino, K., Momose-Sato, Y., Sato, K., 2002. Optical imaging of intrinsic signals induced by peripheral nerve stimulation in the in vivo rat spinal cord. Neuroimage 17, 1240-1255.

Schmahmann, J.D., Pandya, D.N., Wang, R., Dai, G., D'Arceuil, H.E., de Crespigny, A.J., Wedeen, V.J., 2007. Association fibre pathways of the brain: parallel observations from diffusion spectrum imaging and autoradiography. Brain 130, 630-653.

Schmithorst, V.J., Dardzinski, B.J., Holland, S.K., 2001. Simultaneous correction of ghost and geometric distortion artifacts in EPI using a multiecho reference scan. IEEE Trans Med Imaging 20, 535-539.

Schneider, E., Glover, G., 1991. Rapid in vivo proton shimming. Magn Reson Med 18, 335-347.

Schroeter, M.L., Kupka, T., Mildner, T., Uludağ, K., von Cramon, D.Y., 2006. Investigating the post-stimulus undershoot of the BOLD signal--a simultaneous fMRI and fNIRS study. Neuroimage 30, 349-358.

Schroth, G., Klose, U., 1992. Cerebrospinal fluid flow. II. Physiology of respiration-related pulsations. Neuroradiology 35, 10-15.

Schwab, M.E., 2004. Nogo and axon regeneration. Curr Opin Neurobiol 14, 118-124.

Schwartz, E.D., Chin, C.L., Shumsky, J.S., Jawad, A.F., Brown, B.K., Wehrli, S., Tessler, A., Murray, M., Hackney, D.B., 2005a. Apparent diffusion coefficients in spinal cord transplants and surrounding white matter correlate with degree of axonal dieback after injury in rats. AJNR Am J Neuroradiol 26, 7-18.

Schwartz, E.D., Cooper, E.T., Chin, C.L., Wehrli, S., Tessler, A., Hackney, D.B., 2005b. Ex vivo evaluation of ADC values within spinal cord white matter tracts. AJNR Am J Neuroradiol 26, 390-397.

Schwartz, E.D., Cooper, E.T., Fan, Y., Jawad, A.F., Chin, C.L., Nissanov, J., Hackney, D.B., 2005c. MRI diffusion coefficients in spinal cord correlate with axon morphometry. Neuroreport 16, 73-76.

Schwartz, E.D., Duda, J., Shumsky, J.S., Cooper, E.T., Gee, J., 2005d. Spinal cord diffusion tensor imaging and fiber tracking can identify white matter tract disruption and glial scar orientation following lateral funiculotomy. J Neurotrauma 22, 1388-1398.

Schwartz, E.D., Flanders, A.E., 2007. Spinal Trauma: Imaging, Diagnosis, And Management. Lippincott Williams & Wilkins, Philadelphia.

Schwartz, E.D., Shumsky, J.S., Wehrli, S., Tessler, A., Murray, M., Hackney, D.B., 2003. Ex vivo MR determined apparent diffusion coefficients correlate with motor recovery mediated by intraspinal transplants of fibroblasts genetically modified to express BDNF. Exp Neurol 182, 49-63.

Schwartz, E.D., Yezierski, R.P., Pattany, P.M., Quencer, R.M., Weaver, R.G., 1999. Diffusion-weighted MR imaging in a rat model of syringomyelia after excitotoxic spinal cord injury. AJNR Am J Neuroradiol 20, 1422-1428.

Schwartz, M., Yoles, E., 2006. Immune-based therapy for spinal cord repair: autologous macrophages and beyond. J Neurotrauma 23, 360-370.

Sen, P.N., Basser, P.J., 2005. A model for diffusion in white matter in the brain. Biophys J 89, 2927-2938.

Shanmuganathan, K., Gullapalli, R.P., Zhuo, J., Mirvis, S.E., 2008. Diffusion Tensor MR Imaging in Cervical Spine Trauma. AJNR Am J Neuroradiol 29, 655-659.

Shen, H., Tang, Y., Huang, L., Yang, R., Wu, Y., Wang, P., Shi, Y., He, X., Liu, H., Ye, J., 2007. Applications of diffusion-weighted MRI in thoracic spinal cord injury without radiographic abnormality. Int Orthop 31, 375-383.

Sicard, K., Shen, Q., Brevard, M.E., Sullivan, R., Ferris, C.F., King, J.A., Duong, T.Q., 2003. Regional cerebral blood flow and BOLD responses in conscious and anesthetized rats under basal and hypercapnic conditions: implications for functional MRI studies. J Cereb Blood Flow Metab 23, 472-481.

Sicard, K.M., Duong, T.Q., 2005. Effects of hypoxia, hyperoxia, and hypercapnia on baseline and stimulus-evoked BOLD, CBF, and CMRO2 in spontaneously breathing animals. Neuroimage 25, 850-858.

Silver, X., Ni, W.X., Mercer, E.V., Beck, B.L., Bossart, E.L., Inglis, B., Mareci, T.H., 2001. In vivo 1H magnetic resonance imaging and spectroscopy of the rat spinal cord using an inductively-coupled chronically implanted RF coil. Magn Reson Med 46, 1216-1222.

Skare, S., Andersson, J.L., 2005. Correction of MR image distortions induced by metallic objects using a 3D cubic B-spline basis set: application to stereotactic surgical planning. Magn Reson Med 54, 169-181.

Skare, S., Li, T., Nordell, B., Ingvar, M., 2000. Noise considerations in the determination of diffusion tensor anisotropy. Magn Reson Imaging 18, 659-669.

Skare, S., Newbould, R.D., Clayton, D.B., Albers, G.W., Nagle, S., Bammer, R., 2007. Clinical multishot DW-EPI through parallel imaging with considerations of susceptibility, motion, and noise. Magn Reson Med 57, 881-890.

Smirnakis, S.M., Schmid, M.C., Weber, B., Tolias, A.S., Augath, M., Logothetis, N.K., 2007. Spatial specificity of BOLD versus cerebral blood volume fMRI for mapping cortical organization. J Cereb Blood Flow Metab 27, 1248-1261.

Smith, A.M., Lewis, B.K., Ruttimann, U.E., Ye, F.Q., Sinnwell, T.M., Yang, Y., Duyn, J.H., Frank, J.A., 1999. Investigation of low frequency drift in fMRI signal. Neuroimage 9, 526-533.

Smith, S., McNab, J., Miller, K., 2008. Partial-Volume Modelling in Diffusion MRI. In: 16th Annual Meeting of the International Society for Magnetic Resonance in Medicine (ISMRM), Toronto, Canada, 137.

Smith, S.M., Jenkinson, M., Woolrich, M.W., Beckmann, C.F., Behrens, T.E., Johansen-Berg, H., Bannister, P.R., De Luca, M., Drobnjak, I., Flitney, D.E., Niazy, R.K., Saunders, J., Vickers, J., Zhang, Y., De Stefano, N., Brady, J.M., Matthews, P.M., 2004. Advances in functional and structural MR image analysis and implementation as FSL. Neuroimage 23 Suppl 1, S208-219.

Song, A.W., Fichtenholtz, H., Woldorff, M., 2002a. BOLD signal compartmentalization based on the apparent diffusion coefficient. Magn Reson Imaging 20, 521-525.

Song, A.W., Woldorff, M.G., Gangstead, S., Mangun, G.R., McCarthy, G., 2002b. Enhanced spatial localization of neuronal activation using simultaneous apparent-diffusion-coefficient and blood-oxygenation functional magnetic resonance imaging. Neuroimage 17, 742-750.

Song, S.K., Sun, S.W., Ramsbottom, M.J., Chang, C., Russell, J., Cross, A.H., 2002c. Dysmyelination revealed through MRI as increased radial (but unchanged axial) diffusion of water. Neuroimage 17, 1429-1436.

Song, S.K., Yoshino, J., Le, T.Q., Lin, S.J., Sun, S.W., Cross, A.H., Armstrong, R.C., 2005. Demyelination increases radial diffusivity in corpus callosum of mouse brain. Neuroimage 26, 132-140.

Spuentrup, E., Buecker, A., Koelker, C., Guenther, R.W., Stuber, M., 2003. Respiratory motion artifact suppression in diffusion-weighted MR imaging of the spine. Eur Radiol 13, 330-336.

Srivastava, G., Crottaz-Herbette, S., Lau, K.M., Glover, G.H., Menon, V., 2005. ICA-based procedures for removing ballistocardiogram artifacts from EEG data acquired in the MRI scanner. Neuroimage 24, 50-60.

Stanisz, G.J., Odrobina, E.E., Pun, J., Escaravage, M., Graham, S.J., Bronskill, M.J., Henkelman, R.M., 2005. T1, T2 relaxation and magnetization transfer in tissue at 3T. Magn Reson Med 54, 507-512.

Stefanovic, B., Warnking, J., Rylander, K., Pike, B., 2006. The effect of global cerebral vasodilation on focal activation hemodynamics. Neuroimage 30, 726-734.

Stejskal, E.O., Tanner, J.E., 1965. Spin Diffusion Measurements: Spin Echoes in the Presence of a Time-Dependent Field Gradient. J Chem Phys 42, 288-292.

Stracke, C.P., Pettersson, L.G., Schoth, F., Moller-Hartmann, W., Krings, T., 2005. Interneuronal systems of the cervical spinal cord assessed with BOLD imaging at 1.5 T. Neuroradiology 47, 127-133.

Stroman, P.W., 2005. Magnetic resonance imaging of neuronal function in the spinal cord: spinal FMRI. Clin Med Res 3, 146-156.

Stroman, P.W., 2006. Discrimination of errors from neuronal activity in functional MRI of the human spinal cord by means of general linear model analysis. Magn Reson Med 56, 452-456.

Stroman, P.W., Figley, C.R., Cahill, C.M., 2008a. Spatial normalization, bulk motion correction and coregistration for functional magnetic resonance imaging of the human cervical spinal cord and brainstem. Magn Reson Imaging 26, 809-814.

Stroman, P.W., Kornelsen, J., Bergman, A., Krause, V., Ethans, K., Malisza, K.L., Tomanek, B., 2004. Noninvasive assessment of the injured human spinal cord by means of functional magnetic resonance imaging. Spinal Cord 42, 59-66.

Stroman, P.W., Kornelsen, J., Lawrence, J., 2005a. An improved method for spinal functional MRI with large volume coverage of the spinal cord. J Magn Reson Imaging 21, 520-526.

Stroman, P.W., Kornelsen, J., Lawrence, J., Malisza, K.L., 2005b. Functional magnetic resonance imaging based on SEEP contrast: response function and anatomical specificity. Magn Reson Imaging 23, 843-850.

Stroman, P.W., Krause, V., Frankenstein, U.N., Malisza, K.L., Tomanek, B., 2001a. Spin-echo versus gradient-echo fMRI with short echo times. Magn Reson Imaging 19, 827-831.

Stroman, P.W., Krause, V., Malisza, K.L., Frankenstein, U.N., Tomanek, B., 2001b. Characterization of contrast changes in functional MRI of the human spinal cord at 1.5 T. Magn Reson Imaging 19, 833-838.

Stroman, P.W., Krause, V., Malisza, K.L., Frankenstein, U.N., Tomanek, B., 2002a. Extravascular proton-density changes as a non-BOLD component of contrast in fMRI of the human spinal cord. Magn Reson Med 48, 122-127.

Stroman, P.W., Krause, V., Malisza, K.L., Frankenstein, U.N., Tomanek, B., 2002b. Functional magnetic resonance imaging of the human cervical spinal cord with stimulation of different sensory dermatomes. Magn Reson Imaging 20, 1-6.

Stroman, P.W., Lee, A.S., Pitchers, K.K., Andrew, R.D., 2008b. Magnetic resonance imaging of neuronal and glial swelling as an indicator of function in cerebral tissue slices. Magn Reson Med 59, 700-706.

Stroman, P.W., Malisza, K.L., Onu, M., 2003a. Functional magnetic resonance imaging at 0.2 Tesla. Neuroimage 20, 1210-1214.

Stroman, P.W., Nance, P.W., Ryner, L.N., 1999. BOLD MRI of the human cervical spinal cord at 3 tesla. Magn Reson Med 42, 571-576.

Stroman, P.W., Ryner, L.N., 2001. Functional MRI of motor and sensory activation in the human spinal cord. Magn Reson Imaging 19, 27-32.

Stroman, P.W., Tomanek, B., Krause, V., Frankenstein, U.N., Malisza, K.L., 2002c. Mapping of neuronal function in the healthy and injured human spinal cord with spinal fMRI. Neuroimage 17, 1854-1860.

Stroman, P.W., Tomanek, B., Krause, V., Frankenstein, U.N., Malisza, K.L., 2003b. Functional magnetic resonance imaging of the human brain based on signal enhancement by extravascular protons (SEEP fMRI). Magn Reson Med 49, 433-439.

Stroman, P.W., Tomanek, B., Malisza, K.L., 2003c. Functional magnetic resonance imaging of the human brain and spinal cord by means of signal enhancement by extavascular protons. Conc Magn Reson 16, 28-34.

Studholme, C., Constable, R.T., Duncan, J.S., 2000. Accurate alignment of functional EPI data to anatomical MRI using a physics-based distortion model. IEEE Trans Med Imaging 19, 1115-1127.

Summers, P., Staempfli, P., Jaermann, T., Kwiecinski, S., Kollias, S., 2006. A preliminary study of the effects of trigger timing on diffusion tensor imaging of the human spinal cord. AJNR Am J Neuroradiol 27, 1952-1961.

Tachtsidis, I., Elwell, C.E., Leung, T.S., Lee, C.W., Smith, M., Delpy, D.T., 2004. Investigation of cerebral haemodynamics by near-infrared spectroscopy in young healthy volunteers reveals posture-dependent spontaneous oscillations. Physiol Meas 25, 437-445.

Tator, C.H., Fehlings, M.G., 1991. Review of the secondary injury theory of acute spinal cord trauma with emphasis on vascular mechanisms. J Neurosurg 75, 15-26.

Thivard, L., Pradat, P.F., Lehericy, S., Lacomblez, L., Dormont, D., Chiras, J., Benali, H., Meininger, V., 2007. Diffusion tensor imaging and voxel based morphometry study in amyotrophic lateral sclerosis: relationships with motor disability. J Neurol Neurosurg Psychiatry 78, 889-892.

Thomalla, G., Glauche, V., Koch, M.A., Beaulieu, C., Weiller, C., Rother, J., 2004. Diffusion tensor imaging detects early Wallerian degeneration of the pyramidal tract after ischemic stroke. Neuroimage 22, 1767-1774.

Thomas, C.G., Harshman, R.A., Menon, R.S., 2002. Noise reduction in BOLD-based fMRI using component analysis. Neuroimage 17, 1521-1537.

Thuret, S., Moon, L.D., Gage, F.H., 2006. Therapeutic interventions after spinal cord injury. Nat Rev Neurosci 7, 628-643.

Thurnher, M.M., Bammer, R., 2006a. Diffusion-weighted magnetic resonance imaging of the spine and spinal cord. Semin Roentgenol 41, 294-311.

Thurnher, M.M., Bammer, R., 2006b. Diffusion-weighted MR imaging (DWI) in spinal cord ischemia. Neuroradiology 48, 795-801.

Tournier, J.D., Calamante, F., Connelly, A., 2007. Robust determination of the fibre orientation distribution in diffusion MRI: non-negativity constrained super-resolved spherical deconvolution. Neuroimage 35, 1459-1472.

Tournier, J.D., Calamante, F., Gadian, D.G., Connelly, A., 2004. Direct estimation of the fiber orientation density function from diffusion-weighted MRI data using spherical deconvolution. Neuroimage 23, 1176-1185.

Triantafyllou, C., Hoge, R.D., Krueger, G., Wiggins, C.J., Potthast, A., Wiggins, G.C., Wald, L.L., 2005. Comparison of physiological noise at 1.5 T, 3 T and 7 T and optimization of fMRI acquisition parameters. Neuroimage 26, 243-250.

Tsuchiya, K., Fujikawa, A., Suzuki, Y., 2005. Diffusion tractography of the cervical spinal cord by using parallel imaging. AJNR Am J Neuroradiol 26, 398-400.

Tsuchiya, K., Katase, S., Fujikawa, A., Hachiya, J., Kanazawa, H., Yodo, K., 2003. Diffusion-weighted MRI of the cervical spinal cord using a single-shot fast spin-echo technique: findings in normal subjects and in myelomalacia. Neuroradiology 45, 90-94.

Tuch, D.S., 2004. Q-ball imaging. Magn Reson Med 52, 1358-1372.

Tuch, D.S., Reese, T.G., Wiegell, M.R., Makris, N., Belliveau, J.W., Wedeen, V.J., 2002. High angular resolution diffusion imaging reveals intravoxel white matter fiber heterogeneity. Magn Reson Med 48, 577-582.

Tuch, D.S., Reese, T.G., Wiegell, M.R., Wedeen, V.J., 2003. Diffusion MRI of complex neural architecture. Neuron 40, 885-895.

Tuch, D.S., Wisco, J.J., Khachaturian, M.H., Ekstrom, L.B., Kotter, R., Vanduffel, W., 2005. Q-ball imaging of macaque white matter architecture. Philos Trans R Soc Lond B Biol Sci 360, 869-879.

Turner, R., 2002. How much cortex can a vein drain? Downstream dilution of activation-related cerebral blood oxygenation changes. Neuroimage 16, 1062-1067.

Uchida, H., Kishikawa, K., Collins, J.G., 1995. Effect of propofol on spinal dorsal horn neurons. Comparison with lack of ketamine effects. Anesthesiology 83, 1312-1322.

Ueki, M., Mies, G., Hossmann, K.A., 1992. Effect of alpha-chloralose, halothane, pentobarbital and nitrous oxide anesthesia on metabolic coupling in somatosensory cortex of rat. Acta Anaesthesiol Scand 36, 318-322.

Valsasina, P., Agosta, F., Caputo, D., Stroman, P.W., Filippi, M., 2008. Spinal fMRI during proprioceptive and tactile tasks in healthy subjects: activity detected using cross-correlation, general linear model and independent component analysis. Neuroradiology.

Valsasina, P., Rocca, M.A., Agosta, F., Benedetti, B., Horsfield, M.A., Gallo, A., Rovaris, M., Comi, G., Filippi, M., 2005. Mean diffusivity and fractional anisotropy histogram analysis of the cervical cord in MS patients. Neuroimage 26, 822-828.

Van de Moortele, P.F., Pfeuffer, J., Glover, G.H., Ugurbil, K., Hu, X., 2002. Respiration-induced B0 fluctuations and their spatial distribution in the human brain at 7 Tesla. Magn Reson Med 47, 888-895.

van Gelderen, P., de Zwart, J.A., Starewicz, P., Hinks, R.S., Duyn, J.H., 2007. Real-time shimming to compensate for respiration-induced B0 fluctuations. Magn Reson Med 57, 362-368.

Vargas, M.I., Delavelle, J., Jlassi, H., Rilliet, B., Viallon, M., Becker, C.D., Lovblad, K.O., 2008. Clinical applications of diffusion tensor tractography of the spinal cord. Neuroradiology 50, 25-29.

Vazquez, A.L., Cohen, E.R., Gulani, V., Hernandez-Garcia, L., Zheng, Y., Lee, G.R., Kim, S.G., Grotberg, J.B., Noll, D.C., 2006. Vascular dynamics and BOLD fMRI: CBF level effects and analysis considerations. Neuroimage 32, 1642-1655.

Vielle, B., 2005. Mathematical analysis of Mayer waves. J Math Biol 50, 595-606.

Voss, H.U., Watts, R., Uluğ, A.M., Ballon, D., 2006. Fiber tracking in the cervical spine and inferior brain regions with reversed gradient diffusion tensor imaging. Magn Reson Imaging 24, 231-239.

Waller, A., 1850. Experiments on the section of glossopharyngeal and hypoglossal nerves of the frog and observations of the alternatives produced thereby in the structure of their primitive fibers. Philos Trans R Soc Lond B Biol Sci 140, 423.

Wang, F.N., Huang, T.Y., Lin, F.H., Chuang, T.C., Chen, N.K., Chung, H.W., Chen, C.Y., Kwong, K.K., 2005. PROPELLER EPI: an MRI technique suitable for diffusion tensor imaging at high field strength with reduced geometric distortions. Magn Reson Med 54, 1232-1240.

Watabe, N., Tominaga, T., Shimizu, H., Koshu, K., Yoshimoto, T., 1999. Quantitative analysis of cerebrospinal fluid flow in patients with cervical spondylosis using cine phase-contrast magnetic resonance imaging. Neurosurgery 44, 779-784.

Wedeen, V.J., Hagmann, P., Tseng, W.Y., Reese, T.G., Weisskoff, R.M., 2005. Mapping complex tissue architecture with diffusion spectrum magnetic resonance imaging. Magn Reson Med 54, 1377-1386.

Werring, D.J., Toosy, A.T., Clark, C.A., Parker, G.J., Barker, G.J., Miller, D.H., Thompson, A.J., 2000. Diffusion tensor imaging can detect and quantify corticospinal tract degeneration after stroke. J Neurol Neurosurg Psychiatry 69, 269-272.

Wheeler-Kingshott, C.A., Hickman, S.J., Parker, G.J., Ciccarelli, O., Symms, M.R., Miller, D.H., Barker, G.J., 2002. Investigating cervical spinal cord structure using axial diffusion tensor imaging. Neuroimage 16, 93-102.

Wiegell, M.R., Larsson, H.B., Wedeen, V.J., 2000. Fiber crossing in human brain depicted with diffusion tensor MR imaging. Radiology 217, 897-903.

Wiggins, G.C., Triantafyllou, C., Potthast, A., Reykowski, A., Nittka, M., Wald, L.L., 2006. 32-channel 3 Tesla receive-only phased-array head coil with soccer-ball element geometry. Magn Reson Med 56, 216-223.

Wilm, B.J., Gamper, U., Henning, A., Pruessmann, K.P., Kollias, S.S., Boesiger, P., 2008. Diffusion-weighted imaging of the entire spinal cord. NMR Biomed.

Wilm, B.J., Svensson, J., Henning, A., Pruessmann, K.P., Boesiger, P., Kollias, S.S., 2007. Reduced field-of-view MRI using outer volume suppression for spinal cord diffusion imaging. Magn Reson Med 57, 625-630.

Wilson, J.L., Jenkinson, M., de Araujo, I., Kringelbach, M.L., Rolls, E.T., Jezzard, P., 2002. Fast, fully automated global and local magnetic field optimization for fMRI of the human brain. Neuroimage 17, 967-976.

Wirth, E.D., 3rd, Mareci, T.H., Beck, B.L., Fitzsimmons, J.R., Reier, P.J., 1993. A comparison of an inductively coupled implanted coil with optimized surface coils for in vivo NMR imaging of the spinal cord. Magn Reson Med 30, 626-633.

Wise, R.G., Ide, K., Poulin, M.J., Tracey, I., 2004. Resting fluctuations in arterial carbon dioxide induce significant low frequency variations in BOLD signal. Neuroimage 21, 1652-1664.

Woods, R.P., Grafton, S.T., Holmes, C.J., Cherry, S.R., Mazziotta, J.C., 1998. Automated image registration: I. General methods and intrasubject, intramodality validation. J Comput Assist Tomogr 22, 139-152.

Worsley, K.J., Friston, K.J., 1995. Analysis of fMRI time-series revisited--again. Neuroimage 2, 173-181.

Worsley, K.J., Liao, C.H., Aston, J., Petre, V., Duncan, G.H., Morales, F., Evans, A.C., 2002. A general statistical analysis for fMRI data. Neuroimage 15, 1-15.

Wright, M., 1982. Pharmacologic effects of ketamine and its use in veterinary medicine. J Am Vet Med Assoc 180, 1462-1471.

Xu, D., Henry, R.G., Mukherjee, P., Carvajal, L., Miller, S.P., Barkovich, A.J., Vigneron, D.B., 2004. Single-shot fast spin-echo diffusion tensor imaging of the brain and spine with head and phased array coils at 1.5 T and 3.0 T. Magn Reson Imaging 22, 751-759.

Xu, D., Mori, S., Solaiyappan, M., van Zijl, P.C., Davatzikos, C., 2002. A framework for callosal fiber distribution analysis. Neuroimage 17, 1131-1143.

Yamamori, Y., Kishikawa, K., Collins, J.G., 1995. Halothane effects on low-threshold receptive field size of rat spinal dorsal horn neurons appear to be independent of supraspinal modulatory systems. Brain Res 702, 162-168.

Yodh, A., Chance, B., 1995. Spectroscopy and imaging with diffusing light. Physics Today 48, 34-40.

Yoshizawa, T., Nose, T., Moore, G.J., Sillerud, L.O., 1996. Functional magnetic resonance imaging of motor activation in the human cervical spinal cord. Neuroimage 4, 174-182.

Zaitsev, M., Hennig, J., Speck, O., 2004. Point spread function mapping with parallel imaging techniques and high acceleration factors: fast, robust, and flexible method for echo-planar imaging distortion correction. Magn Reson Med 52, 1156-1166.

Zang, Y., Jia, F., Weng, X., Li, E., Cui, S., Wang, Y., Hazeltine, E., Ivry, R., 2003. Functional organization of the primary motor cortex characterized by event-related fMRI during movement preparation and execution. Neurosci Lett 337, 69-72.

Zarahn, E., Aguirre, G.K., D'Esposito, M., 1997. Empirical analyses of BOLD fMRI statistics. I. Spatially unsmoothed data collected under null-hypothesis conditions. Neuroimage 5, 179-197.

Zeng, H., Constable, R.T., 2002. Image distortion correction in EPI: comparison of field mapping with point spread function mapping. Magn Reson Med 48, 137-146.

Zhan, W., Yang, Y., 2006. How accurately can the diffusion profiles indicate multiple fiber orientations? A study on general fiber crossings in diffusion MRI. J Magn Reson 183, 193-202.

Zhang, J., Huan, Y., Qian, Y., Sun, L., Ge, Y., 2005a. Multishot diffusion-weighted imaging features in spinal cord infarction. J Spinal Disord Tech 18, 277-282.

Zhang, J., Jones, M., Deboy, C., Reich, D., Hoffman, P., Sheikh, K., Mori, S., Calabresi, P., 2008. Temporal Changes in Axial and Radial Diffusivities in a Rat Model of Wallerian Degeneration in the Spinal Cord. In: 16th Annual Meeting of the International Society for Magnetic Resonance in Medicine (ISMRM), Toronto, Canada, 3400.

Zhang, J.S., Huan, Y., Sun, L.J., Ge, Y.L., Zhang, X.X., Chang, Y.J., 2007. Temporal evolution of spinal cord infarction in an in vivo experimental study of canine models characterized by diffusion-weighted imaging. J Magn Reson Imaging 26, 848-854.

Zhang, Y., Brooks, D.H., Franceschini, M.A., Boas, D.A., 2005b. Eigenvector-based spatial filtering for reduction of physiological interference in diffuse optical imaging. J Biomed Opt 10, 011014.

Zhao, F., Tai, C., Wang, J., Roppolo, J.R., de Groat, W.C., Kim, S.G., 2006a. Functional Imaging of Cat Spinal Cord by CBV-weighted fMRI. In: Proceedings 14th Scientific Meeting, International Society for Magnetic Resonance in Medicine, 2127.

Zhao, F., Wang, P., Hendrich, K., Ugurbil, K., Kim, S.G., 2006b. Cortical layer-dependent BOLD and CBV responses measured by spin-echo and gradient-echo fMRI: insights into hemodynamic regulation. Neuroimage 30, 1149-1160.

Zhao, F., Wang, P., Kim, S.G., 2004. Cortical depth-dependent gradient-echo and spin-echo BOLD fMRI at 9.4T. Magn Reson Med 51, 518-524.

Zhao, F., Williams, M., Meng, X., Welsh, D.C., Coimbra, A., Crown, E.D., Cook, J.J., Urban, M.O., Hargreaves, R., Williams, D.S., 2008. BOLD and blood volume-weighted fMRI of rat lumbar spinal cord during non-noxious and noxious electrical hindpaw stimulation. Neuroimage 40, 133-147.

Zhao, X., Bodurka, J., Jesmanowicz, A., Li, S.J., 2000. B(0)-fluctuation-induced temporal variation in EPI image series due to the disturbance of steady-state free precession. Magn Reson Med 44, 758-765.